

**Solid-state NMR of (membrane) protein complexes:  
Novel methods and applications**

Dissertation  
zur Erlangung des Doktorgrades  
der Mathematisch-Naturwissenschaftlichen Fakultäten  
der Georg-August-Universität zu Göttingen

vorgelegt von  
Ovidiu-Cristian Andronesi  
aus Bukarest

Göttingen 2006

D7

Referent: Prof. Dr. Tim Salditt

Korreferent: Prof. Dr. Christian Griesinger

Tag der mündlichen Prüfung: 18 April 2006



*Motto:* 'I am interested how God thinks, the rest are details.'

A. Einstein

# Contents

<b>Contents</b>	<b>i</b>
<b>Acknowledgments</b>	<b>v</b>
<b>Publication list</b>	<b>viii</b>
<b>Abbreviations</b>	<b>x</b>
<b>Symbols</b>	<b>xi</b>
<b>Abstract</b>	<b>xii</b>
<b>Zusammenfassung</b>	<b>xiii</b>
<b>1 General introduction</b>	<b>1</b>
<b>2 Principles of NMR spectroscopy and its biological applications</b>	<b>5</b>
2.1 Fundamentals of nuclear magnetic resonance . . . . .	5
2.2 Quantum mechanical description of NMR . . . . .	8
2.2.1 Equation of motion . . . . .	8
2.2.2 NMR Interactions . . . . .	9

---

2.2.3	Tensor rotations . . . . .	11
2.3	Basic solid-state NMR techniques . . . . .	12
2.3.1	Magic angle spinning . . . . .	12
2.3.2	Cross polarization . . . . .	15
2.3.3	Recoupling techniques . . . . .	17
2.4	Multidimensional NMR spectroscopy . . . . .	19
2.5	Protein structure and dynamics . . . . .	20
2.5.1	Protein structure determination . . . . .	20
2.5.2	Protein dynamics . . . . .	26
<b>3</b>	<b>MAS of membrane proteins in oriented lipid bilayers</b>	<b>29</b>
3.1	Introduction . . . . .	29
3.2	Theory . . . . .	33
3.3	Numerical Simulations . . . . .	37
3.4	Pulse sequences for MAS of oriented samples . . . . .	42
3.5	$^{15}\text{N}$ CSA recoupling of Gramicidin A and WALP23 . . . . .	46
3.6	Orientation and local structure of WALP23 . . . . .	49
3.7	Conclusions . . . . .	52
<b>4</b>	<b>Structure and dynamics of free and bound Phospholamban</b>	<b>55</b>
4.1	Introduction . . . . .	55
4.2	Existing models of free PLN . . . . .	57
4.3	Dynamics-based spectral editing . . . . .	59
4.4	Multidimensional experiments . . . . .	62
4.5	Analysis of structure and dynamics of free PLN . . . . .	72

---

4.6	Structural model of free PLN . . . . .	73
4.7	SERCA-bound PLN . . . . .	75
4.8	Conclusions . . . . .	81
<b>5</b>	<b>Structural model of Alzheimer's-like intraneuronal fibrils</b>	<b>83</b>
5.1	Introduction . . . . .	83
5.2	Assignment of the core and flexible domains . . . . .	87
5.3	Secondary, tertiary and quaternary distance constraints . . . . .	89
5.4	Minimal structural unit of K19 PHFs . . . . .	92
5.5	Structural model . . . . .	95
5.6	Conclusions . . . . .	99
<b>6</b>	<b>Summary and outlook</b>	<b>101</b>
<b>A</b>	<b>Spherical tensors and rotations</b>	<b>105</b>
A.1	Irreducible spherical tensors for NMR interactions . . . . .	105
A.2	Euler rotations and reduced Wigner elements . . . . .	106
<b>B</b>	<b>MAS on oriented samples</b>	<b>107</b>
B.1	AHT for $^{15}\text{N}$ CSA recoupling . . . . .	107
B.2	$^{31}\text{P}$ spinning sidebands . . . . .	111
B.3	GAMMA simulation programs . . . . .	112
B.4	1D and 2D BRUKER pulse programs . . . . .	122
<b>C</b>	<b>PLN assignment and experimental conditions</b>	<b>127</b>
C.1	Scalar-coupling based pulse programs . . . . .	127

C.2	3D HCC experiment . . . . .	134
C.3	Assignment table . . . . .	135
C.4	Sample preparation . . . . .	137
C.5	Dipolar-coupling based pulse sequences . . . . .	139
<b>D</b>	<b>K19 PHFs assignment table and model validation</b>	<b>143</b>
D.1	Assignment table . . . . .	143
D.2	Experimental conditions . . . . .	147
D.3	Chemical shifts analysis . . . . .	148
D.4	CHHC analysis . . . . .	149
D.5	Pulse program for the water-edited NCA experiment . . . . .	150
	<b>List of Tables</b>	<b>152</b>
	<b>List of Figures</b>	<b>152</b>
	<b>Index</b>	<b>155</b>
	<b>Bibliography</b>	<b>157</b>
	<b>Curriculum Vitae</b>	<b>189</b>
	<b>Lebenslauf</b>	<b>190</b>

## Acknowledgments

I am very grateful to many people that have inspired me and contributed to my education. Specially, I would like to thank to:

Prof. dr. Tim Salditt for accepting me as an external PhD student in the Physics Faculty of Georg-August University, Göttingen, and his advice during my studies. Also, all members of the PhD comity that red and evaluated this thesis.

Prof. dr. Christian Griesinger for accepting me in his NMR department at Max Planck Institute for Biophysical Chemistry, Göttingen, all scientific support and interest in my research. It was a great advantage to work in such an environment, having access to the most modern equipment and coming in contact with so many challenging projects. Equally for the nice atmosphere, including the yearly departmental excursions.

Dr. Marc Baldus for all guidance during my PhD studies from the level of introducing me to the field of solid-state NMR up to exploring the limits of what the modern instrumentation can do. My first contact with NMR was in the lab of Prof. de Groot from Leiden University where I spent few months during my master studies and at the end of my stay I met Marc who gave me a short introduction in GAMMA and impressed me with the style the he just brought fresh from MIT. At that time, I have seen the very promising applications of solid-state NMR to biology. I was happy for the opportunity to become a PhD student in the group that Marc started in Göttingen and be involved in development of new methods and applications for the study of membrane proteins. These years have been a fruitful and stimulating experience.

Prof. dr. Huub J. M. de Groot from Gorlaeus Laboratories, Leiden University, The Netherlands, for giving me the first chance to work with NMR. I spent many nice moments in Leiden in the company of his family.

Dr. Stefan Becker for many discussions about molecular biology and importance of function-structure relationship. In particular, for the very interesting Phospholamban project that he proposed and all efforts that he pursued during its study.

The group of Prof. dr. Eckhard Mandelkow from Max-Planck-Unit for Structural Molecular Biology in Hamburg for the protein Tau paired helical filaments. In particular, Dr. Martin von Bergen for his constant support and interest that considerably motivated and inspired this project.

Brigitta Angerstein that always helped me in dealing with the most challenging samples - membrane proteins reconstituted in oriented lipid bilayers. Her expertise and 'magic' hands finally made the samples to orient, roll and spin. Not last, for her friendly and carrying feelings.

Dr. Sorin Luca, my former colleague and friend at the beginning of PhD, now at NIH Bethesda. His support with spectrometer and computer simulations helped me a lot to get started on oriented samples. Besides this, for all our extra activities.

Dr. Colan E. Hughes, for the very clear way he made me understand phase cycle and coherence transfer pathways. Apart from this, he was well informed on various topics and discussions with him were always interesting.

Dr. Henrike Heise, for cooperation during the development of pulse sequences to study dynamics of membrane proteins. Not less important, for sharing with me all her experience on protein fibrils.

Karsten Seidel, the group expert in structure calculation, for all contribution in Phospholamban and Tau paired helical filaments projects, and for cheerful character.

Adam Lange, my officemate and 'buddy' during three years, for the daily support and friendly company. Our many discussions kept us on track.

Manuel Etzkorn, for nice collaboration on interesting membrane proteins. His relaxing attitude made things work easier.

Robert Schneider, the last PhD 'acquisition' of the group and pleasant presence in the office for the last year. Lars Sonnenberg, that was part of the initial team in Göttingen as a diploma student and became soon the rotational resonance specialist.

All other members of the department, in particular Nils Lakomek, Dr. Christophe Fares and Dr. Pierre Montaville with whom I had many entertaining activities. Dr. Laurent Verdier for introduction in INSIGHT.

Dr. Mirela and Dante Neculai, with whom I collaborated on one of my first projects, and I spent many nice moments in Göttingen.

My former professors in Romania. My mathematics teacher in gymnasium, Stefan Smarandache, who inspired us the spirit of competition and from whom I remember the nice lessons of geometry. My professor of quantum electronics, Liviu Giurgiu, who was my mentor during physics studies. Prof. dr. Eugenia Kovacs, from the biophysics department of medical school in Bucharest where I started my carrier.

Last but not least, I am very grateful to all members of my family. My mother that encouraged me continuously. My father who was my model and opened my mind for physics. My sister Diana, that brought her happiness and joy during summer visits in Göttingen. My future wife Anca who shared with me the last months of this PhD and gave me the strength to finish it.

**After all, science and PhD are fun.**

Als Schüler mit einer Leidenschaft für Physik las ich viele Bücher über die Geschichte der Physik. Darin tauchte der Name eines Ortes besonders oft auf: Göttingen. Vielleicht war es wegen der großen Forscher und ihrer Leistungen, die in diesen Büchern beschrieben wurden, daß ich Physiker werden wollte. Zu dieser Zeit hätte ich aber nie gedacht, daß ich an einem Ort promovieren würde, dessen Name so *'resoniert'* wie Göttingen.

Ich hoffe, ich kann etwas von dem Geist mit mir nehmen, der Größen wie Gauss, Planck oder Heisenberg genährt hat.

Este o experiență deosebită contactul cu oamenii altor țări și culturi. Pe lângă realizările din timpul doctoratului am avut ocazia să mă confrunt cu multe situații. Mai ales, am înțeles ca oamenii au aceleași bucurii și probleme peste tot. Mi-au dat putere în momentele dificile învățăturile, amintirile și imaginile dragi de acasă. Sper că am reușit să le îmbogățesc cu altele noi. Mă gândesc cu speranță și bucurie la timpul când vom putea face acasă lucruri ca cele descrise în această teză.

Cuvintele sunt prea puține să le mulțumesc tuturor celor care m-au ajutat și au fost alături de mine, mai ales familiei, vă datorez enorm.

**Ovidiu-Cristian Andronesi,  
Göttingen, March 2006**



## Publication list

This thesis is based on the following papers:

### Chapter 3

- [1] O. C. Andronesi, J. R. Pfeifer, L. Al-Momani, S. Ozdirekcan, D. T. S. Rijkers, B. Angerstein, S. Luca, U. Koert, J. A. Killian, and M. Baldus. Probing membrane protein orientation and structure using fast magic-angle-spinning solid-state NMR. *Journal of Biomolecular NMR*, 30(3):253-265, 2004.

### Chapter 4

- [2] O. C. Andronesi, S. Becker, K. Seidel, H. Heise, H. S. Young, and M. Baldus. Determination of membrane protein structure and dynamics by magic-angle-spinning solid-state NMR spectroscopy. *Journal of the American Chemical Society*, 127(37):12965-12974, 2005.
- [3] H. Heise, W. Hoyer, S. Becker, O. C. Andronesi, D. Riedel, and M. Baldus. Molecular-level secondary structure, polymorphism, and dynamics of full-length alpha-synuclein fibrils studied by solid-state NMR. *Proceedings of the National Academy of Sciences of the United States of America*, 102(44):15871-15876, 2005.
- [4] M. Etzkorn et al. Molecular structure and intrinsic dynamics of a 7-transmembrane protein receptor in native membranes seen by solid-state NMR. *manuscript in preparation*.

### Chapter 5

- [5] O. C. Andronesi et al. Structural model of Alzheimer's-like paired helical filaments from neuronal tau derived from solid-state NMR spectroscopy. *manuscript in preparation*.

In addition, I have been involved in several projects:

- [6] A. M. Neculai, D. Neculai, H. W. Roesky, J. Magull, M. Baldus, O. Andronesi and M. Jansen. Stabilization of a diamagnetic (ScBr)-Br-I molecule in a sandwich-like structure. *Organometallics*, 21(13):2590-2592, 2002.
- [7] C. E. Hughes, S. Olejniczak, J. Helinski, W. Ciesielski, M. Repisky, O. Andronesi, M. J. Potrzebowski and M. Baldus. Probing structure in the polymorphic domain of the L-enantiomer of N-benzoyl-phenylalanine by means of 2D solid-state NMR spectroscopy and DFT calculations. *Journal of Physical Chemistry B*, 109(49):23175-23182, 2005.
- [8] S. S. Kumar, H. W. Roesky, O. Andronesi, M. Baldus and R. F. Winter. Synthesis and electrochemical behavior of the ferrocenyl units assembled on imidoalane and carbaalane clusters. *Inorganica Chimica Acta*, 358(7):2349-2354, 2005.

I have contributed to the book chapter:

- [9] O. C. Andronesi, H. Heise, and M. Baldus. Determining Protein 3D structure by Magic-Angle-Spinning NMR. *Handbook of Modern Magnetic Resonance*. Webb, G., Ed., Kluwer Academic Publishers London, 2006, in press.

## Abbreviations

<b>AHT</b>	Average Hamiltonian Theory
<b>CP</b>	Cross Polarization
<b>CSA</b>	Chemical Shielding Anisotropy
<b>DMPC</b>	Dimyristoyl Phosphatidyl Choline
<b>DOPC</b>	Dioleoyl Phosphatidyl Choline
<b>DQ</b>	Double Quantum
<b>EM</b>	Electron Microscopy
<b>EPR</b>	Electron Paramagnetic Resonance
<b>INEPT</b>	Insensitive Nuclei Enhanced by Polarization Transfer
<b>LAB</b>	Laboratory Frame
<b>lsNMR</b>	liquid-state Nuclear Magnetic Resonance
<b>MAS</b>	Magic Angle Spinning
<b>MD</b>	Molecular Dynamics
<b>NMR</b>	Nuclear Magnetic Resonance
<b>NOESY</b>	Nuclear Overhauser Effect Spectroscopy
<b>PAS</b>	Principal Axis System
<b>PLN</b>	Phospholamban
<b>PHFs</b>	Paired Helical Filaments
<b>RAS</b>	Rotor Axis System
<b>R.f.</b>	Radio frequency
<b>SD</b>	Spin diffusion
<b>SERCA</b>	Sarco-Endoplasmic Reticulum Ca-ATPase
<b>SQ</b>	Single Quantum
<b>SR</b>	Sarcoplasmic Reticulum
<b>ssNMR</b>	solid-state Nuclear Magnetic Resonance
<b>TOBSY</b>	Total Through Bond Spectroscopy

## Symbols

$\hat{A}_{k,q}^{\Lambda}$	Space spherical tensors for interaction $\Lambda$
$B_0$	Static magnetic field
$B_1$	R.f. field
$\hat{D}$	Dipolar coupling tensor
$d_{p,q}^{(k)}$	Reduced Wigner elements
$\gamma$	Nuclear gyromagnetic ratio
$\hat{H}_{\Lambda}$	Hamiltonian operator for interaction $\Lambda$
$\bar{H}^{(0)}$	Zeroth order Average Hamiltonian
$\hat{I}_{x,y,z}$	Cartesian spin operators
$\hat{I}_{+/-}$	Shift (raising/lowering) spin operators
$J$	Scalar coupling constant
$J^2(\omega_0)$	Spectral density function
$M_0$	Magnetization of nuclear spins at thermal equilibrium
$\omega_L, \omega_0$	Larmor frequency
$\omega_r$	MAS spinning rate
$\omega_{rf}$	R.f. field strength
$\omega_1, \omega_2$	Chemical shift (in ppm) axes in multidimensional spectra
$\hat{\rho}$	Density matrix operator
$\hat{\sigma}$	Chemical shielding tensor
$T_1$	Spin-lattice (longitudinal) relaxation time
$T_2$	Spin-spin (transverse) relaxation time
$\hat{T}_{k,q}^{\Lambda}$	Spin spherical tensors for interaction $\Lambda$
$\tau_i$	Internal correlation time

# Abstract

The main purpose of this thesis is the development of methods for high-resolution MAS solid-state NMR and its application to membrane proteins and protein fibrils (i.e. protein complexes). The thesis is organized in six chapters, including a general introduction in Chapter 1 that sets solid-state NMR spectroscopy in the context of structural biology.

Chapter 2 contains an introduction of NMR, focusing on the most important concepts, techniques and biological applications. Chapter 3 presents new pulse sequences for fast MAS on oriented samples of membrane peptides in aligned lipid bilayers. Here, the orientation and structure of selectively labeled, well-known examples of membrane peptides (Gramicidin A and WALP23) are investigated. Due to the high-resolution achieved at fast MAS, the same experiments can be applied on uniformly labeled proteins.

The main part of the thesis (Chapters 4 and 5) is devoted to the study of structure and dynamics of uniformly labeled proteins. In Chapter 4 the membrane protein Phospholamban, an important regulator of the cardiac function and drug target in heart failure, is investigated when free in the lipid membrane and bound to its regulatory partner, the sarco-endoplasmic Ca-ATPase (SERCA). A new concept that uses dynamics-based spectral editing is introduced and proven. Chapter 5 extends the previous strategy to the study of the paired helical filaments prepared from a three repeat construct (K19) of the protein Tau involved in Alzheimer's Disease. Novel water-edited experiments are used to probe the supramolecular arrangement of the monomers inside the fibril. A model of the minimal structural unit of the fibrils is proposed.

Chapter 6 contains final conclusions, summarizes the main results of this thesis and proposes future directions. In addition, four appendixes with supplementary information are provided for Chapters 2-5.

# Zusammenfassung

Der Hauptzweck dieser Arbeit ist die Entwicklung von Methoden für hochauflösende MAS-Festkörper-NMR und ihre Anwendung auf Membranproteine und Proteinfibrillen (also Proteinkomplexe). Die Arbeit ist in sechs Kapitel gegliedert, einschließlich einer allgemeinen Einführung in Kapitel 1, das die Festkörper-NMR-Spektroskopie in den Kontext der Strukturbiochemie einbettet.

Kapitel 2 enthält eine Einführung in die NMR-Spektroskopie, wobei der Schwerpunkt auf den wichtigsten Konzepten, Techniken und biologischen Anwendungen liegt. Kapitel 3 stellt neue Pulssequenzen für schnelles MAS an orientierten Membranpeptiden in definiert ausgerichteten Lipiddoppelschichten vor. Hier werden Orientierung und Struktur von selektiv markierten, gut bekannten Membranpeptiden (Gramicidin A und WALP23) untersucht. Aufgrund der hohen Auflösung, die bei schnellem MAS erreicht wird, können dieselben Experimente auf uniform markierte Proteine angewendet werden.

Der Hauptteil dieser Arbeit (Kapitel 4 und 5) ist der Untersuchung von Struktur und Dynamik uniform isotoopenmarkierter Proteine gewidmet. In Kapitel 4 wird das Membranprotein Phospholamban, ein wichtiger regulierender Faktor der Herzfunktion und Ziel von Medikamenten gegen Herzversagen, sowohl als freies membranständiges Protein als auch im an seinen regulatorischen Partner, die sarco-endoplasmatische Calcium-ATPase (SERCA), gebundenen Zustand untersucht. Ein neues Konzept, das spektrales Editieren auf der Basis von Dynamik verwendet, wird eingeführt und überprüft. Kapitel 5 erweitert die bisherige Strategie auf die Untersuchung von gepaarten helikalen Filamenten, die aus einem Drei-Repeat-Konstrukt (K19) des Proteins Tau, das an der Entstehung der Alzheimer-Krankheit beteiligt ist, hergestellt wurden.

Neuartige wassereditierte Experimente werden verwendet, um die supramolekulare Anordnung der Monomere in der Fibrille zu erforschen. Ein Modell der minimalen Struktureinheit der Fibrillen wird vorgestellt.

Kapitel 6 enthält abschließende Folgerungen, faßt die Hauptresultate dieser Arbeit zusammen und macht Vorschläge für die weitere Forschung. Zusätzliche Informationen zu den Kapiteln 2 bis 5 finden sich in vier Kapiteln im Anhang.

# Chapter 1

## General introduction

The three-dimensional structures and dynamics of proteins are among the most valuable contribution of biophysics to the knowledge of biological systems. Such information can explain key effector roles of proteins: enzymes, receptors, ion channels, pumps, exchangers, or the cytoskeleton. Understanding how proteins work is not only a fundamental problem, but serves also as a scientific basis in the attempt to control or correct their function. Rational drug design is extensively using '*Structure-Activity-Relationship*' (SAR) in the search of more specific and efficient medicines. Because of their large complexity, proteins represent a challenging task for physical and computational structural techniques, fueling their progress and interdisciplinarity with chemistry, biology and medicine.

Since its discovery in 1946 by Bloch [1] and Purcell [2] (Nobel prize for physics in 1952), nuclear magnetic resonance (NMR) has developed into a major spectroscopic and imaging technique with important applications in physics, chemistry, biology and medicine, acknowledged during the last two decades by three Nobel prizes (R. R. Ernst 1991 [3] and K. Wüthrich 2002 [4] for chemistry and P. C. Lauterbur [5] together with P. Mansfield [6] for medicine in 2003). As a result, today NMR spectroscopy is one of



the most important tool in structural biology besides X-ray crystallography. This is documented by the growing number of deposited structures each year [7] in the protein data banks (PDB), or assignments in the biological magnetic resonance data bank (BMRB). Moreover, combination of complementary methods (e.g., X-ray and NMR or EM and NMR) is required in challenging cases [8, 9].

While the majority of the NMR structures have been obtained by liquid-state NMR (lsNMR) on soluble proteins, solid-state NMR (ssNMR) spectroscopy can be the method of choice for high-resolution studies of membrane proteins or protein fibrils. These two types of samples pose problems for both lsNMR<sup>1</sup> and X-ray because of their insoluble nature or resistance to form crystals. Hence, only about 90 membrane proteins and less than 10 protein fibrils structures have been deposited to date (March 2006) from a total of 32519 PDB entries (proteins only), despite very high interest in these systems.

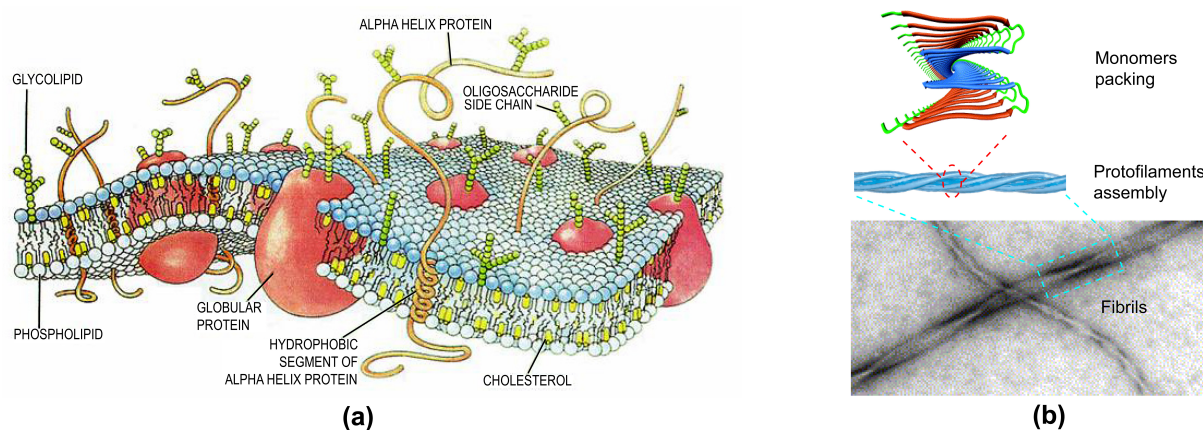


Figure 1.1: (a) Model of the cell membrane showing major components such as lipids and proteins, and (b) EM micrograph of protein fibrils with details of their supramolecular arrangement.

<sup>1</sup>lsNMR can study membrane proteins in lipid micelles [10, 11].

---

Membrane proteins account for almost 30% of the genome of an organism, having crucial functions (receptors, ion channels, pumps, exchangers, vesicle fusion), and as such they represent about 50% of all pharmaceutical drug targets [12]. In addition to normal constitutive fibrils such as collagen or myofibrils, abnormal ordered aggregates of proteins (‘*amyloids*’) have received major attention in the last years due to medical evidence of their implication in many degenerative diseases, among the most known being type-II diabetes, Alzheimer’s, or Parkinson’s disease [13, 14, 15].

Important advantage of ssNMR, regarding sample preparation, is the fact that it does not require solubilization or crystallization. For example, membrane proteins can be studied in lipid bilayers that are similar to cell membranes. Also, compared to other structural methods with atomic (X-ray diffraction or neutron scattering [16]) or near atomic resolution (cryo-EM [17]) that can be applied on the same systems, ssNMR is a non-destructive technique.

Solid-state NMR spectroscopy is becoming an active method in the field of ‘*structural proteomics*’. Advancement in hardware technology (probeheads, pulse generators) have provided the resolution and sensitivity necessary for structural characterization of biomolecules, and very elaborate multidimensional experiments have been proposed. However, further development is needed to find the most successful combination of experiments for automating the procedures and creating a high-throughput method.

Two main directions have emerged: (i) randomly oriented samples in combination with magic angle spinning (MAS, [18]) as reviewed in [19, 20], and (ii) oriented samples under static [21, 22] or spinning conditions [23, 24]. The scalability of the first approach to study larger proteins is straightforward.

From the early MAS solid-state NMR studies of selectively labeled proteins targeting key residues [25], successful applications have been recently shown on uniformly labeled proteins [26, 27, 28], aiming to complete 3D structure determination. Although, these last results represent a proof of principle obtained on test cases of small-size proteins in microcrystalline form, they serve as useful steps in developing a general methodology applicable to uniformly labeled membrane proteins and protein fibrils.

Progress obtained so far has enabled the structural study of high-affinity complexes of large membrane proteins (GPCRs) with ligands of significant medical and pharmaceutical interest [29]. Lately, the ability to probe molecular interfaces and specific interactions [30, 31] has also been demonstrated, with promising applications in studies of drug-target complexes by ssNMR. Altogether, these unique merits of ssNMR have motivated and inspired the research performed in this thesis.

# Chapter 2

## Principles of NMR spectroscopy and its biological applications

### 2.1 Fundamentals of nuclear magnetic resonance

The phenomenon of nuclear magnetic resonance [1, 2, 32] is based on the interaction of the nuclear spins<sup>1</sup> situated in a constant magnetic field ( $\vec{B}_0$ ) with a periodic magnetic field ( $\vec{B}_1$ ).

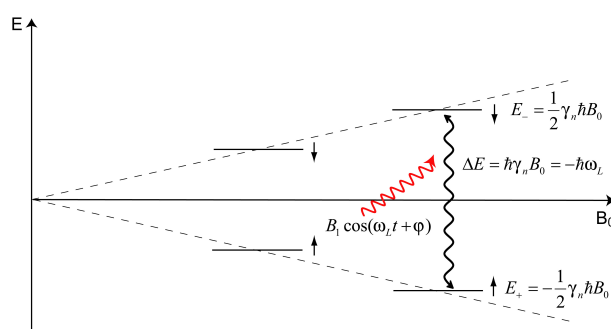


Figure 2.1: Phenomenon of nuclear magnetic resonance: Zeeman levels and NMR transitions.

---

<sup>1</sup>Only nuclei with non-zero spin number are detectable by NMR. For biomolecular NMR applications  $^1\text{H}$ ,  $^{13}\text{C}$ ,  $^{15}\text{N}$  and  $^{31}\text{P}$  one-half spins ( $I = 1/2$ ) are the most important.

In the case of spins  $1/2$ , the Zeeman interaction determined by the static magnetic field  $\vec{B}_0$  produces two energy levels corresponding to the spin-up  $|\uparrow\rangle$  and spin-down  $|\downarrow\rangle$  eigenstates. Resonant transitions between these states will be induced (absorption and stimulated emission) by a coherent oscillating field  $\vec{B}_1$  that has the frequency<sup>2</sup> equal to the Larmor frequency  $\omega_L = \gamma_n B_0$  ( $\gamma_n$  is the nuclear gyromagnetic ratio, shortly  $\gamma$  ratio). Among all nuclei, protons ( $^1\text{H}$ ) have the largest  $\gamma$  ratio, while  $^{13}\text{C}$  and  $^{15}\text{N}$  have ratios that are 4 and 10 times smaller, respectively.  $^1\text{H}$  nuclei have also the highest natural abundance in biomolecules. As a result, they are the most sensitive nuclei for detection in NMR<sup>3</sup>.

Pulsed Fourier Transformed (FT) NMR spectroscopy is currently the most successful and versatile form of NMR spectroscopy [33].

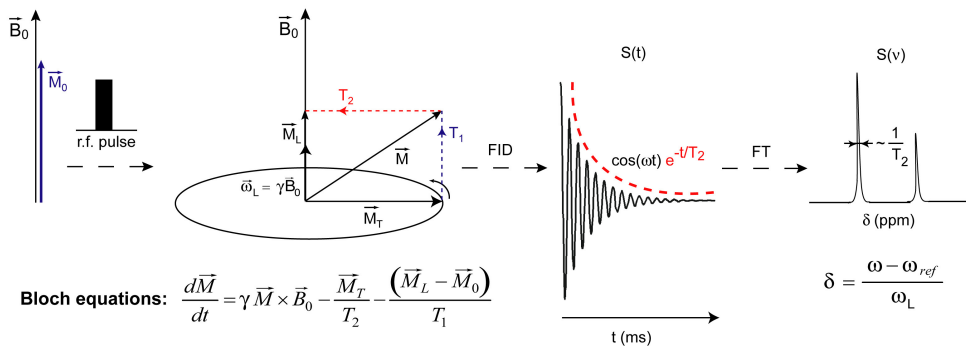


Figure 2.2: Pulsed Fourier-transformed NMR: the thermal equilibrium magnetization  $\vec{M}_0$  is flipped in the transverse plane by the r.f. pulse where the free precession of the transverse magnetization  $\vec{M}_T$  around  $\vec{B}_0$  field determines the free-induction-decay (FID) signal  $S(t)$  that, by Fourier transformation (FT), yields the NMR spectrum  $S(\nu)$  (conventionally given in  $\delta$  [ppm] scale). The longitudinal magnetization  $\vec{M}_L$  is recovered with the relaxation time  $T_1$  while the transverse magnetization decays with the relaxation time  $T_2$  as described by the Bloch equations.

<sup>2</sup>The frequency of the periodic field falls in the radio-frequency (r.f.) range (MHz) for NMR and  $B_1$  is called the r.f. field.

<sup>3</sup>Hence, in NMR the intensity of the  $B_0$  field is usually specified by the  $^1\text{H}$  Larmor frequency (i.e. 900 MHz at 21.4 T - commercially, the highest available field at the moment).

In FTNMR, the r.f. field is applied in pulses of defined length, amplitude, phase and offset frequency (amplitude, phase or offset frequency can be modulated) that are separated by periods of free evolution as defined by the pulse sequence. The classical theory of NMR given by the phenomenological Bloch equations [34, 35] (see Figure 2.2) describes the evolution of the total magnetization vector  $\vec{M}$  under the influence of r.f. and  $\vec{B}_0$  fields and two relaxation times:  $T_1$  for longitudinal (spin-lattice) relaxation and  $T_2$  for transverse (spin-spin) relaxation. In NMR the relaxation caused by spontaneous or induced emission is negligibly small and the main mechanisms are the non-adiabatic ( $T_1$ ) or adiabatic ( $T_2$ ) coupling with a thermal bath (lattice) and the loss of phase coherence ( $T_2$ ) [36, 37, 38]. The full-width at half-maximum (FWHM) of the NMR line is given by the inverse of the transverse  $T_2$  relaxation time. In solid-state NMR, the  $T_2$  relaxation times are in general shorter than in liquid-state NMR [32] leading to broader lines and reduced spectral resolution (see further discussions in § 2.3 and § 2.5.2).

For an ensemble of nuclear spins at thermal equilibrium (temperature  $T$ ), the Boltzmann distribution approximates well the populations of the spin eigenstates. For nuclear magnetism, the paramagnetic contribution is most important [32] and the thermal equilibrium magnetization of an ensemble of  $N_s$  nuclear spins can be calculated as  $M_0 = \frac{N_s \gamma \hbar I(I+1)}{3k_B T} B_0$  (Curie law, '*high temperature approximation*'). Together with instrument dependent parameters (e.g., quality factor of the probe coil  $Q$ ) and number of averaged scans ( $N_{scans}$ ) this determines the signal-to-noise ratio (SNR) of NMR [39]:

$$SNR \propto (N_{scans})^{1/2} Q N_s \gamma^{5/2} \left( \frac{B_0}{T} \right)^{3/2} T_2 \quad (2.1)$$

showing how sensitivity increases at high fields and low temperatures.

The classical Bloch formalism of NMR (suitable for isolated spins) does not contain an adequate description of the internal spin interactions, which are the basis of the detailed structural and dynamical information obtained from NMR. These are properly defined in a quantum mechanical formalism (see § 2.2.2). However, the r.f. fields can be further treated classically [32].

## 2.2 Quantum mechanical description of NMR

### 2.2.1 Equation of motion

Generally, for diamagnetic<sup>4</sup> molecules the nuclear degrees of freedom can be treated separately from those of electrons and a statistical ensemble of  $N_s$  nuclear spins in a mixed quantum state can be described by a density operator [33]:

$$\hat{\rho}(t) = \sum_{k=1}^{N_s} p_k \sum_i \sum_j c_{ki}(t) c_{kj}^*(t) |i\rangle \langle j| \quad (2.2)$$

where  $p_k$  represents the probability that spin  $k$  is found in the state specified by the  $c_{ki}$  complex coefficients in the orthonormal base  $\{|i\rangle\}$ . The diagonal elements  $\rho_{ii}$  of the density matrix represent populations of the pure-states  $|i\rangle$ , while off-diagonal terms  $\rho_{ij}$  are coherences (coherent superpositions) of  $|i\rangle$  and  $|j\rangle$  that can be associated with (coherent) transitions between them.

Considering  $N_s$  one-half nuclear spins at thermal equilibrium in the  $\vec{B}_0$  field (along  $z$ ), the density matrix can be approximated (*high temperature approximation*) to:

$$\hat{\rho}_{eq} = \frac{1}{2^{N_s}} \left( \hat{1} + \frac{\hbar \gamma_n B_0}{k_B T} \sum_{k=1}^{N_s} \hat{I}_{z,k} \right) \quad (2.3)$$

where  $\hat{1}$  is the identity matrix and  $\hat{I}_{z,k}$  is the Pauli matrix for the  $z$  spin operator of spin  $k$ .

The time evolution of the spin system under the action of a Hamiltonian  $\hat{\mathcal{H}}(t)$  is given by the Liouville von Neumann equation of motion (not including relaxation):

$$\frac{d}{dt} \hat{\rho}(t) = -\frac{i}{\hbar} [\hat{\mathcal{H}}(t), \hat{\rho}(t)] \quad (2.4)$$

The formal solution for equation of motion can be written using Dyson's time-ordering operator  $\mathcal{T}$ :

$$\hat{\rho}(t) = \mathcal{T} \left\{ e^{-\frac{i}{\hbar} \int_0^t \hat{\mathcal{H}}(t') dt'} \right\} \hat{\rho}(0) \mathcal{T} \left\{ e^{\frac{i}{\hbar} \int_0^t \hat{\mathcal{H}}(t') dt'} \right\} \quad (2.5)$$

---

<sup>4</sup>Referring to the electronic magnetism - the discussions and applications presented in this thesis are restricted to molecules without paramagnetic centers which is often the case for biomolecules.

The expectation value of the observable operator ( $\hat{\mathcal{A}}$ ) that corresponds to the measured physical quantity ( $A$ ) is given by:

$$\langle A \rangle = Tr\{\hat{\rho}\hat{\mathcal{A}}\} \quad (2.6)$$

Simple transformation rules of the product operator formalism [33] allow to calculate the evolution of the density matrix (Equation 2.5) under the effect of r.f pulses or NMR interactions. For Hamiltonians that are constant in time, exact calculations can be performed. In the case of periodic Hamiltonians (often encountered in NMR), analytical methods such as average Hamiltonian theory (AHT) [40] (see Chapter 3) or Floquet theory [41] allow to calculate the system evolution (Equation 2.5) for time steps equal to one period. For arbitrary time-dependent Hamiltonians only numerical results can be obtained, using simulations platforms such as GAMMA [42, 43] or SIMPSON [44].

### 2.2.2 NMR Interactions

Magnetic resonance experiments can be described by a simplified spin Hamiltonian that contains only nuclear spin operators and phenomenological constants resulting from the reduction of the complete molecular Hamiltonian. It is common to classify the NMR interactions as: (1) external spin interactions - the Zeeman interaction ( $\hat{\mathcal{H}}_Z$ ) with  $\vec{B}_0$  field and the r.f. interaction ( $\hat{\mathcal{H}}_{rf}$ ) with  $\vec{B}_1$  field, and (2) internal spin interactions - chemical shielding ( $\hat{\mathcal{H}}_{CS}$ ), dipolar coupling ( $\hat{\mathcal{H}}_D$ ), scalar coupling ( $\hat{\mathcal{H}}_J$ ) and quadrupolar coupling ( $\hat{\mathcal{H}}_Q$ ). The total spin Hamiltonian  $\hat{\mathcal{H}}$  is obtained from:

$$\hat{\mathcal{H}} = \hat{\mathcal{H}}_Z + \hat{\mathcal{H}}_{rf} + \hat{\mathcal{H}}_{CS} + \hat{\mathcal{H}}_D + \hat{\mathcal{H}}_J + \hat{\mathcal{H}}_Q \quad (2.7)$$

Usually, in NMR the strength of an interaction is specified in frequency units. At high fields the strongest interaction is the Zeeman interaction in the range of 0-900 MHz, chemical shielding (in the absence of paramagnetic centers) and dipolar couplings are in the order of 0-100 kHz (122 kHz for  $^1\text{H}$  at 1 Å). The scalar coupling is the weakest internal



interaction 0-200 Hz (for  $^1\text{H}$ ,  $^{13}\text{C}$ ,  $^{15}\text{N}$  in proteins), while the quadrupolar interaction (only for  $I > 1/2$ ) is the strongest internal interaction up to few MHz (not considered further). R.f. fields comparable to the strength of internal interactions (up to 120 kHz in solid-state NMR described in the following) can be applied, allowing to manipulate them efficiently. Additionally, magic-angle-spinning (see § 2.3.1) enhances further these possibilities in solid-state NMR.

Hamiltonians of the internal interactions relevant in the context of this thesis are summarized in the table bellow, according to the definitions used in [40, 45].

Interaction	Origin	Hamiltonian
R.f.	External r.f. field	$\hat{\mathcal{H}}_{rf} = -B_1 \sum_{k=1}^N \gamma_k \hbar (\hat{I}_{kx} \cos \varphi + \hat{I}_{ky} \sin \varphi) B_1 \cos(\omega_L t + \varphi)$
Chemical shielding	Electrons shielding the nucleus	$\hat{\mathcal{H}}_{CS} = \sum_{k=1}^N \gamma_k \hbar \hat{I}_k \tilde{\sigma}_k \vec{B}_0$
Dipolar coupling	Through-space (direct) dipole-dipole	$\hat{\mathcal{H}}_D = \sum_{i<k}^N \hat{I}_i \tilde{D}_{ik} \hat{I}_k = \frac{1}{2} \sum_{i<k}^N \frac{\gamma_i \gamma_k \hbar}{r_{ik}^3} [1 - 3 \cos^2 \theta_{ik}] (3 \hat{I}_{iz} \hat{I}_{kz} - \hat{I}_i \hat{I}_k)$
Scalar coupling	Through-bond (indirect) electron mediated	$\hat{\mathcal{H}}_J = 2\pi \sum_{i<k}^N \hat{I}_i \tilde{J}_{ik} \hat{I}_k$

Table 2.1: Hamiltonians of the r.f. interaction and of the internal interactions:  $\tilde{\sigma}$  represents the chemical shielding tensor,  $\tilde{D}$  the dipolar coupling tensor and  $\tilde{J}$  the scalar coupling tensor. The r.f. interaction is defined in the rotating frame (i.e. the frame rotating with the Larmor frequency around  $\vec{B}_0$ ) where it is time-independent.

Conventionally, NMR measurements and calculations are made in the rotating frame (see table) that eliminates the Zeeman interaction term (containing no structural information).

### 2.2.3 Tensor rotations

In the solid state, the NMR interactions are anisotropic (the size of the interaction depends of the molecule orientation in the magnetic field) and often transformations (Euler rotations) between different reference frames are necessary (§ 3.2). This task becomes simpler when the Hamiltonians are expressed using irreducible spherical tensors [45]:

$$\hat{\mathcal{H}}_{\Lambda} = \sum_{k=0}^2 \sum_{q=-k}^k (-1)^q \hat{A}_{k,q}^{\Lambda} \hat{T}_{k,-q}^{\Lambda} \quad (2.8)$$

where  $\hat{A}_{k,q}^{\Lambda}$  and  $\hat{T}_{k,-q}^{\Lambda}$  correspond to the space and spin tensors, respectively, for the interaction  $\Lambda$  (CS, D, Q, J). Wigner rotation matrices can be employed to perform Euler rotations of the space coordinates:

$$(x, y, z) \xrightarrow{R(\alpha, \beta, \gamma)} (x', y', z') \\ \hat{A}'_{k,q} = R(\alpha, \beta, \gamma) \hat{A}_{k,q} R^{-1}(\alpha, \beta, \gamma) = \sum_{p=-k}^k \hat{A}_{k,p} D_{p,q}^{(k)}(\alpha, \beta, \gamma) \quad (2.9)$$

where  $D_{p,q}^{(k)} = e^{-ip\alpha} d_{p,q}^{(k)}(\beta) e^{-iq\gamma}$  and  $d_{p,q}^{(k)}$  are the reduced Wigner elements. Definitions of  $\hat{A}_{k,q}^{\Lambda}$ ,  $\hat{T}_{k,-q}^{\Lambda}$ , Euler angles and reduced Wigner elements are provided in Appendix A.

Equation 2.8 can be simplified if one considers that, at high fields, it is justified to retain only the secular part of the internal Hamiltonians (elements with  $q = 0$  in Equation 2.8 that commute with  $\hat{\mathcal{H}}_Z$  in the laboratory frame - '*high field approximation*') [40, 45]. For randomly oriented samples, integration over all possible orientations has to be performed in order to reproduce the experimental lineshapes.

Euler transformations can be performed also in the spin space to mimic the effect of r.f. pulses. By rotating the spin coordinates of the Hamiltonians, the NMR interactions can be expressed in the interaction frame (defined by the r.f. field) where the calculations are simpler. The well established theory and the possibility for arbitrary spin manipulations via r.f. pulse sequences or sample spinning are important advantages of NMR spectroscopy compared to other forms of spectroscopy.

## 2.3 Basic solid-state NMR techniques

Most of the experimental techniques used in solid-state NMR have been developed to achieve (1) line-narrowing, (2) signal enhancement or (3) selective recoupling of spin interactions. Solid-state NMR is characterized by intrinsic broad lines due to the anisotropy of NMR interactions and short  $T_2$  relaxation times. Anisotropically broadened lineshapes affect mainly randomly oriented (sometimes called '*powder*') samples<sup>5</sup> that are also the most interesting for biological applications.

There are line-narrowing methods that average-out anisotropic interactions either in real space (magic-angle-spinning) [46, 47] or in spin-space (Lee-Goldburg [48, 46] or WAHUHA [40] based r.f. pulse sequences). Short  $T_2$  relaxation times and wide-lines are particular problems for strongly coupled proton networks ('*homogeneous broadening*'), as often encountered in organic solids. Improved resolution can be achieved either by detecting rare hetero-nuclei like  $^{13}\text{C}$  or  $^{15}\text{N}$  at the cost of sensitivity, or by diluting (deuteration) the proton bath. Techniques that increase sensitivity when detecting heteronuclei use isotope labeling ( $^{13}\text{C}, ^{15}\text{N}$ ) and polarization transfer from protons. Although MAS is very helpful in improving the resolution of solid-state NMR spectra, useful structural information contained in the dipolar couplings or chemical shielding anisotropy (CSA) is lost and pulse sequences that reintroduce ('*recouple*') these interactions under MAS have been designed (see § 2.3.3).

### 2.3.1 Magic angle spinning

Magic-angle-spinning (MAS), first proposed by Andrew [18] and Lowe [49], relates to sample spinning about an axis that is inclined by an angle  $\theta$  to the static magnetic field  $\vec{B}_0$ . If  $\theta$  equals  $54.44^\circ$  ('*magic angle*') the second rank tensor interactions ( $k = 2$  in Equation 2.8) can be averaged out [40, 45]. The effect of MAS is evident especially in

---

<sup>5</sup>Single crystals or oriented samples can have sharper lines due to the presence of only one or a reduced number, respectively, of molecular orientations.

the case of powder samples where it can provide high resolution spectra. As a result, the experimental study of non-soluble materials that do not crystallize (polymers, glasses) or that are hard to crystallize (membrane proteins in their lipid environment), and hence cannot be studied by other high-resolution methods (i.e. X-ray crystallography and liquid-state NMR) becomes possible. When spinning the sample, all internal interactions become time-dependent resulting in spectra that contain spinning sidebands separated by the spinning rate  $\omega_r$ . If the spinning rate is larger than the anisotropy of the NMR interactions ( $\omega_r \geq 3 \times \text{anisotropy}$ ), these can be averaged out efficiently over the NMR time-scale. In this regime, high-resolution solid-state NMR spectra are obtained, characterized by vanishingly small spinning sidebands well separated from the central line.

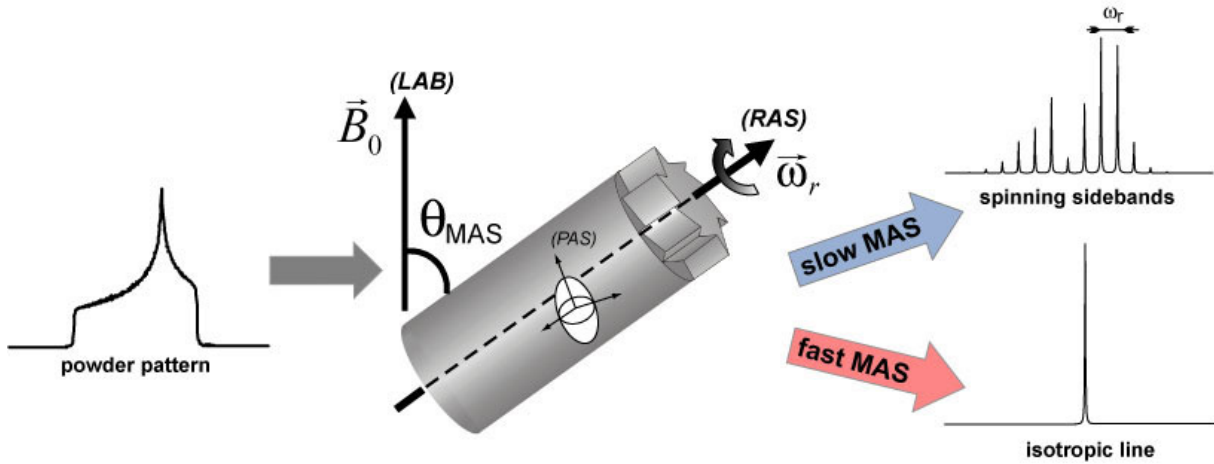


Figure 2.3: Magic angle spinning: the rotor inclined by the magic angle ( $\theta_{MAS} = 54.44^\circ$ ) from  $\vec{B}_0$  rotates with the  $\omega_r$  and leads to a narrowing of the broad powder pattern to an isotropic line and spinning sidebands. The measured spectrum in the laboratory frame (LAB) can be calculated through two consecutive Euler rotations of the NMR interactions from the principal axis system (PAS) via the rotor axis system (RAS).

Sample spinning renders the space part of the interactions periodic. Because at high fields  $\gamma B_0$  (MHz)  $\gg \omega_r$  (kHz), only the secular terms must be taken in account in the system Hamiltonian<sup>6</sup>:

$$\hat{\mathcal{H}}^{LAB,\Lambda}(t) = \hat{A}_{00}^{LAB,\Lambda} \hat{T}_{00}^\Lambda + \hat{A}_{10}^{LAB,\Lambda}(t) \hat{T}_{10}^\Lambda + \hat{A}_{20}^{LAB,\Lambda}(t) \hat{T}_{20}^\Lambda \quad (2.10)$$

The antisymmetric part  $A_{10}$  does not contribute to the spectrum in first order and the isotropic part  $A_{00}^{LAB,\Lambda}$  is invariant under rotations ( $A_{00}^{LAB,\Lambda} = A_{00}^{PAS,\Lambda}$ ). Hence, only the modulation of rank 2 component  $A_{20}^{LAB,\Lambda}$  under MAS has to be analyzed. The space components in the LAB frame can be obtained from the PAS diagonal tensor (molecule dependent and assumed to be known) via two successive Euler rotations:

$$PAS \xrightarrow{(\alpha, \beta, \gamma)} RAS \xrightarrow{(\omega_r t, \theta, 0)} LAB \quad (2.11)$$

$$A_{20}^{LAB,\Lambda}(t) = \sum_{q=-2}^2 \sum_{p=-2}^2 A_{2,p}^{PAS,\Lambda} D_{p,q}^{(2)}(\alpha, \beta, \gamma) D_{q,0}^{(2)}(\omega_r t, \theta, 0)$$

Using the properties of the Wigner matrices and of the PAS components ( $A_{2,\pm 1} = 0$ ,  $A_{22} = A_{2,-2}$ ) Equation 2.11 can be cast into:

$$\begin{aligned} A_{20}^{LAB,\Lambda}(t) = & \left[ \frac{1}{2}(3 \cos^2 \beta - 1) A_{20}^{PAS,\Lambda} + \sqrt{\frac{3}{2}} \cos 2\alpha \sin^2 \beta A_{22}^{PAS,\Lambda} \right] \frac{1}{2}(3 \cos^2 \theta - 1) + \\ & + C_1^\Lambda \cos(\omega_r t) + S_1^\Lambda \sin(\omega_r t) + C_2^\Lambda \cos(2\omega_r t) + S_2^\Lambda \sin(2\omega_r t) \end{aligned} \quad (2.12)$$

It can be seen that for the magic angle condition ( $3 \cos^2 \theta - 1 = 0$ ) the time-independent part of  $A_{20}^{LAB,\Lambda}$  vanishes, while the time-dependent part is averaged-out over the rotor period. If the spinning speed is larger than the interaction, efficient averaging over the NMR time-scale can be achieved. Thus, under fast MAS only the isotropic part  $A_{00}^\Lambda T_{00}^\Lambda$  from Equation 2.10 survives, yielding the same Hamiltonian as in the high-resolution liquid-state NMR. This is easily obtainable for hetero-nuclei at the available

---

<sup>6</sup>Equation 2.10 is written in the laboratory frame of the space part  $\hat{A}_{k,q}^\Lambda$  and the rotating frame of the spin part  $\hat{T}_{k,-q}^\Lambda$ .

MAS rates, while for strongly coupled protons the resolution is only partially improved. Better results can be obtained for protons by averaging the homonuclear dipolar interaction in the spin space with tailored r.f. sequences (i.e. WAHUHA type [40, 50, 51], Lee-Goldburg type [48, 52, 53], or DUMBO [54]).

### 2.3.2 Cross polarization

Sensitivity of  $^{13}\text{C}$  or  $^{15}\text{N}$  detection is worse compared to protons due to smaller  $\gamma$  ratios, lower natural abundances and longer spin-lattice relaxation times. Cross polarization (Hartmann and Hahn [55], Pines [56]) is the main technique to increase sensitivity by transferring magnetization from the abundant proton bath to the rare heteronuclei. In addition, it provides a means for spectral editing and obtaining information about spatial proximity. This scheme employs simultaneous irradiation (double-resonance) of the protons and heteronuclei with two matched r.f. fields  $\omega_{1I} = \omega_{1S}$  (Hartmann-Hahn condition, I abundant spins, S rare spins).

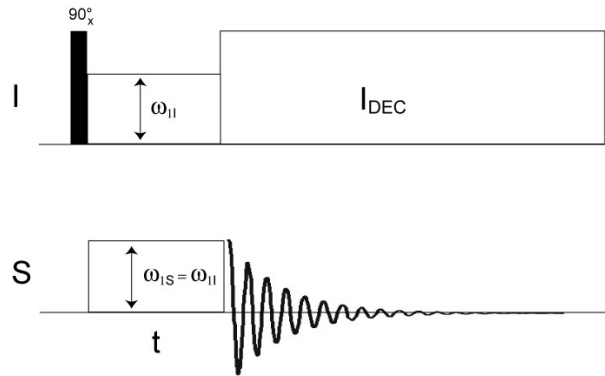


Figure 2.4: Direct cross-polarization experiment: transverse magnetization of abundant I spins is created first by the  $90^\circ$  pulse, which is spin locked by the  $\omega_{1I}$  r.f. field. A contact with the proton bath is established by applying an r.f. field on the rare S spins at the Hartmann-Hahn condition  $\omega_{1S} = \omega_{1I}$ . After the contact time  $t$  the S spins are observed under r.f decoupling of the I spins.

In the doubly rotating frame<sup>7</sup> the energy difference becomes equal for protons and heteronuclei for matched r.f. fields, hence energy conserving flip-flop transitions are possible due to the heteronuclear dipolar Hamiltonian  $\hat{\mathcal{H}}_{IS}^D = D_{IS}[\hat{I}_+\hat{S}_- + \hat{I}_-\hat{S}_+]$  (interaction frame).

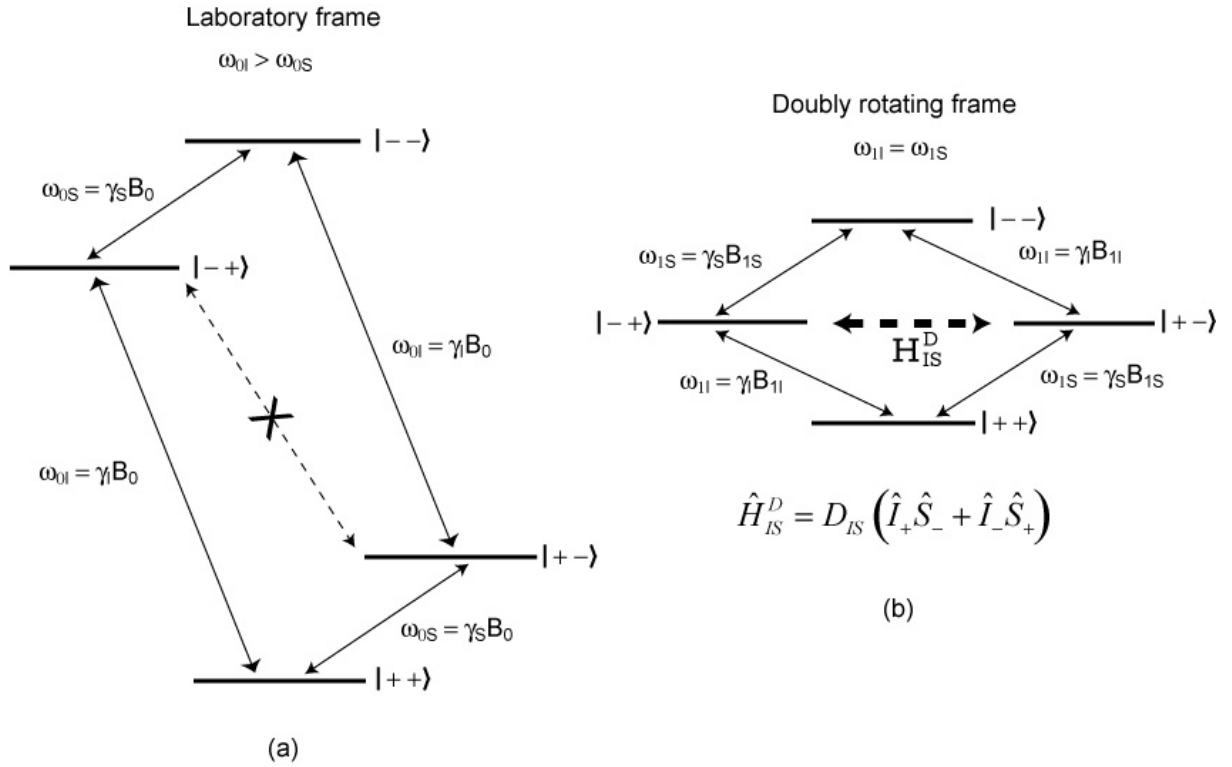


Figure 2.5: Energy level diagram for an I-S spin pair: (a) in the laboratory frame, (b) in the doubly rotating frame energy exchange during CP is possible between the two nuclei with a net magnetization transfer from I to S.

On thermodynamic grounds a net energy (magnetization) transfer from the high temperature proton reservoir to the low temperature rare nuclei reservoir takes place until a thermodynamic equilibrium is reached. In a simple model (Pines [56]) the net magne-

<sup>7</sup>The frame that rotates at Larmor frequency for I spins and Larmor frequency for S spins.

tization gain ( $\eta$ ) of the S spins in a single cross-polarization contact can be calculated:

$$\eta = \frac{\gamma_I}{\gamma_S} \frac{1}{1 + \epsilon} \quad (2.13)$$

where  $\epsilon = N_S S(S + 1)/N_I I(I + 1)$  and  $N_S$  and  $N_I$  are the number of S and I spins, respectively (due to spin-lattice relaxation the gain is higher in multiple scans).

Under MAS conditions, this simple description of CP is not valid and the matching conditions are given by  $\omega_{1I} - \omega_{1S} = \pm\omega_r, \pm 2\omega_r$  where only one of the terms in Equation 2.12 is recoupled. The  $\pm 1$  conditions are more efficient (*'finger pattern'*).

The above considerations are valid for rigid solids. In the case of biological samples that exhibit a high degree of molecular mobility, cross-polarization can become ineffective. Different strategies are discussed later (Chapter 4) to overcome these limitations.

### 2.3.3 Recoupling techniques

As discussed, MAS provides high-resolution spectra for solid-state NMR by averaging out chemical shift anisotropies and dipolar couplings. For the purpose of structure determination, these interactions contain, however, useful information providing orientational or distance constraints [20, 57]. It is possible to recouple some of these interactions with the aid of r.f. pulse sequences. Especially for dipolar recoupling, a lot of progress has been made resulting in a variety of (i) homonuclear broadband (RFDR [58], RIL-ZQT/DQT [59], HORROR [60], MELODRAMA [61], DRAMA [62], symmetry-based R and C sequences [63]) or chemical-shift selective (rotational resonance [64], R2TR [65]) and (ii) heteronuclear (REDOR [66], TEDOR [67], symmetry-based R and C sequences [68]) recoupling pulse sequences.

There is a common principle underlying the design of these recoupling pulse sequences [69]. If r.f. pulses are applied synchronized with the MAS period it is possible to interfere with the MAS averaging effect. In the case of MAS alone, the average Hamiltonian over one-rotor period vanishes ( $\overline{H}^{\Lambda,(0)}$  first-order average Hamiltonian), while in



the presence of rotor synchronized r.f. pulses a non-zero average Hamiltonian over the sequence cycle  $N\tau_r$  is obtained.

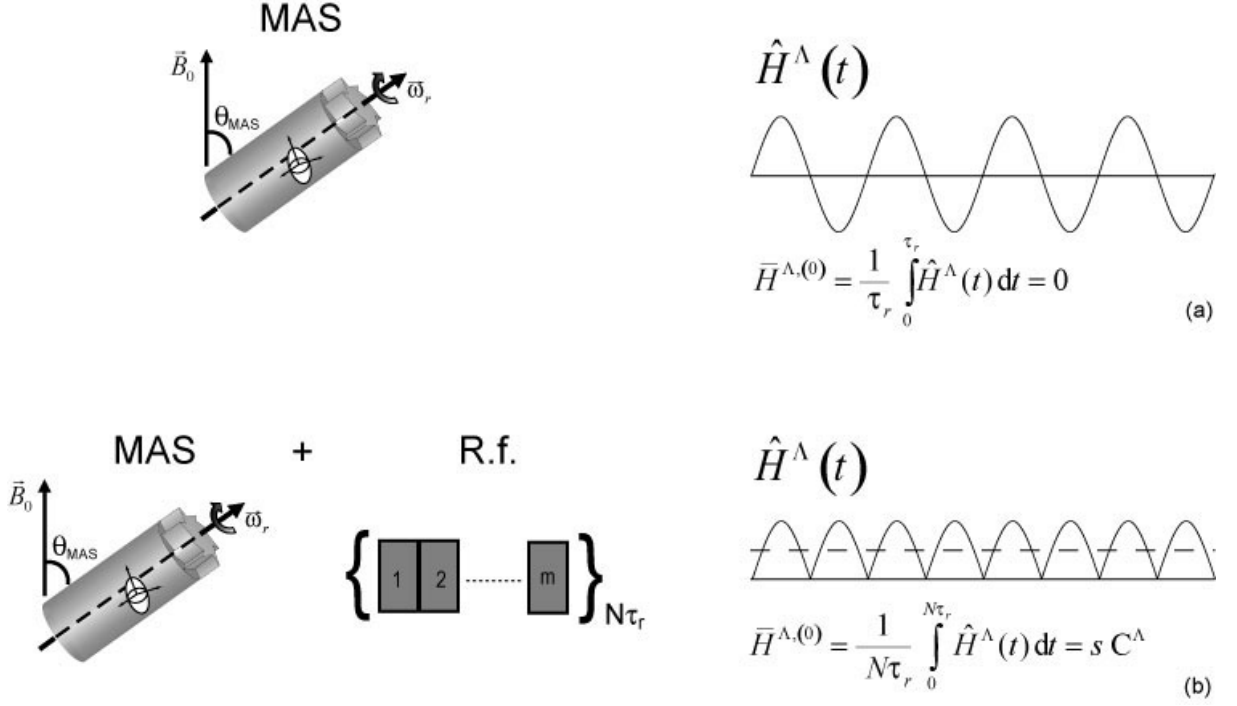


Figure 2.6: Recoupling of the interaction  $\hat{H}^\Lambda$ : (a) averaged-out by MAS, and (b) reintroduced by rotor synchronized r.f. pulses.

However, only a scaled interaction  $sC^\Lambda$  ( $C^\Lambda$  the size of the interaction when integrated over the powder orientations) is recovered and the scaling factor  $s$  is a measure of the recoupling sequence efficiency. Due to the fact that the spin tensors ( $\hat{T}_{kq}^\Lambda$ , Equation 2.8) of each NMR interactions are different, it is possible to construct r.f. sequences that recouple only one interaction and not the others (in zeroth order AHT). For the dipolar interaction, double-quantum ( $\hat{\mathcal{H}}_{DQ}^D = D_{IS}[\hat{I}_{1+}\hat{I}_{2+} + \hat{I}_{1-}\hat{I}_{2-}]$ ) [59, 60, 61, 62, 63] or zero-quantum ( $\hat{\mathcal{H}}_{ZQ}^D = D_{IS}[\hat{I}_{1+}\hat{I}_{2-} + \hat{I}_{1-}\hat{I}_{2+}]$ ) [64, 58, 59] Hamiltonians can be constructed. Applications for the CSA recoupling are presented in the Chapter 3.

## 2.4 Multidimensional NMR spectroscopy

Multidimensional NMR spectroscopy [70, 71, 72, 33, 73, 74, 75] is essential for the study of macromolecules such as proteins since it is not possible to resolve in a single dimension all resonances even for high-resolution spectra of liquid-state NMR. Adding new dimensions helps in disentangling the complicated protein spectra, especially when signals of different nuclei are correlated and recorded in separate dimensions. The general scheme of the 2D NMR spectroscopy is outlined in the Figure 2.7.

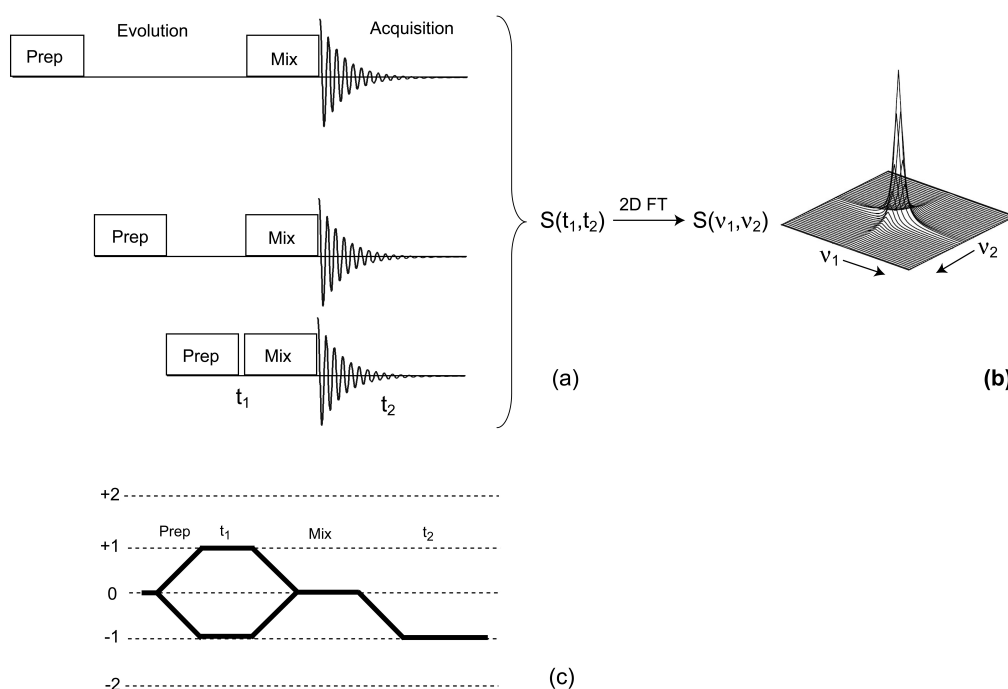


Figure 2.7: Two-dimensional NMR spectroscopy: the 2D NMR experiment consists of four different periods: preparation (Prep), evolution ( $t_1$  - also called indirect detected dimension), mixing (Mix) and acquisition ( $t_2$  - direct detected dimension). The evolution period is systematically incremented and a collection of FIDs,  $S(t_1, t_2)$  is recorded (a). The two-dimensional spectrum  $S(\nu_1, \nu_2)$  is obtained by 2D FT of the  $S(t_1, t_2)$  (b). Phase cycling of the preparation and mixing units selects the desired coherence transfer pathways (c).

Preparation periods usually contain various types of excitation ( $90^\circ$  pulse, CP, INEPT, DQ,  $T_2$  filtered) and during mixing blocks different recoupling or magnetization transfer sequences can be applied. The length of preparation and mixing units are fixed, while the evolution time is systematically incremented. Single- (SQ), zero- (ZQ), double- (DQ) or multiple-quantum (MQ, i.e. TQ or more) coherences can be observed in the indirect dimension while during acquisition only SQ can be recorded. Different types of signals such as SQ, ZQ or DQ can be selected by phase cycling the preparation and mixing blocks [76]. Phase sensitive detection in the indirect dimensions is possible by recording both *sin* and *cos* components of the magnetization (TPPI [77] or States [78] schemes).

For 3D or higher dimensional experiments different approaches such as non-linear sampling schemes with projection-reconstruction of the NMR spectrum [79], Hadamard spectroscopy [80] or G-matrix NMR [81] have been proposed to reduce the total acquisition time. Also, single-scan schemes are developing [82] for ultrafast (ms) multidimensional NMR spectroscopy.

## 2.5 Protein structure and dynamics

### 2.5.1 Protein structure determination

Proteins are biopolymers characterized by four structural levels [83]: (1) primary structure given by the amino acid sequence, (2) secondary structure defined by the local conformation of the backbone, (3) tertiary structure represented by the spatial proximity of the secondary elements and (4) quaternary structure that specifies the packing of several polypeptide chains.

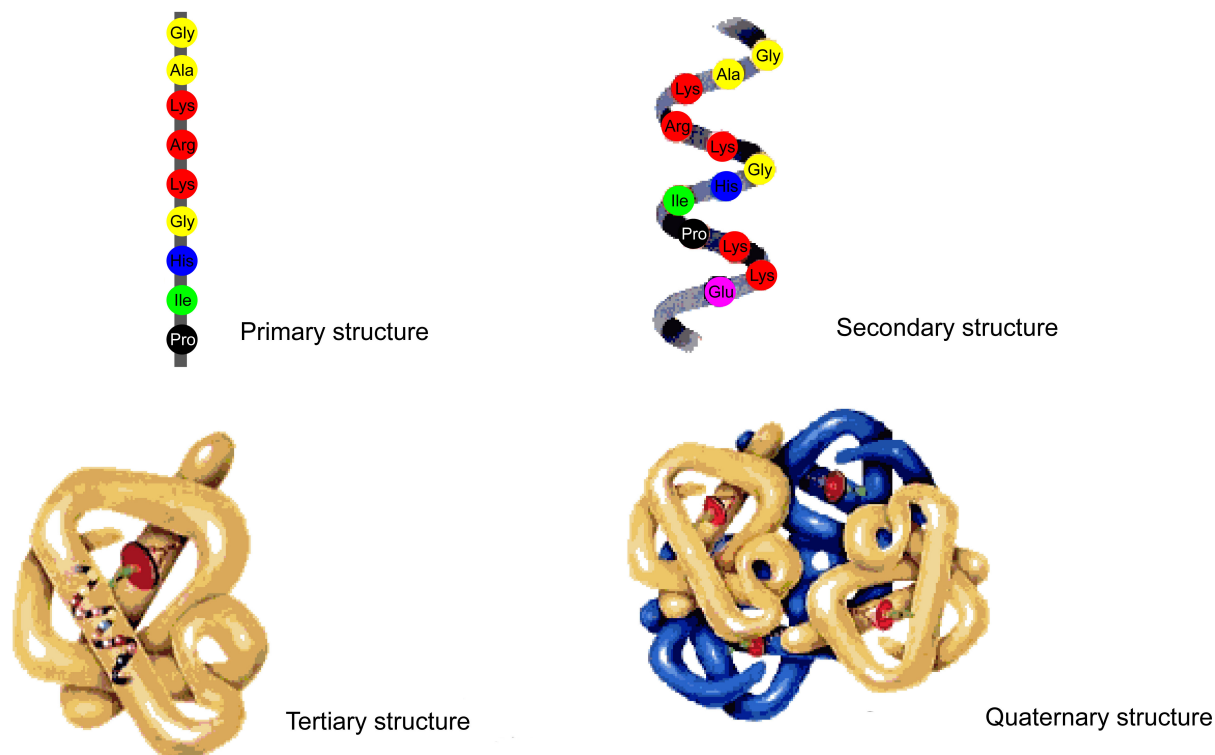


Figure 2.8: Structural levels of proteins: primary, secondary, tertiary and quaternary.

Assuming that sample and measured data are available, there are three main steps [84] in the strategy of protein structure determination by NMR: (1) sequential assignment, (2) collection of structural constraints and (3) structure calculation (see Figure 2.9).

During sequential assignment each of the resonances in the NMR spectra are attributed to residues from the primary sequence of the protein (see conventions in [85] and BMRB). Assigning the resonances is the critical step in the strategy of Figure 2.9 due to limited resolution and spectral overlap. In the end, the quality of the determined structures depends on the number of correct assignments.

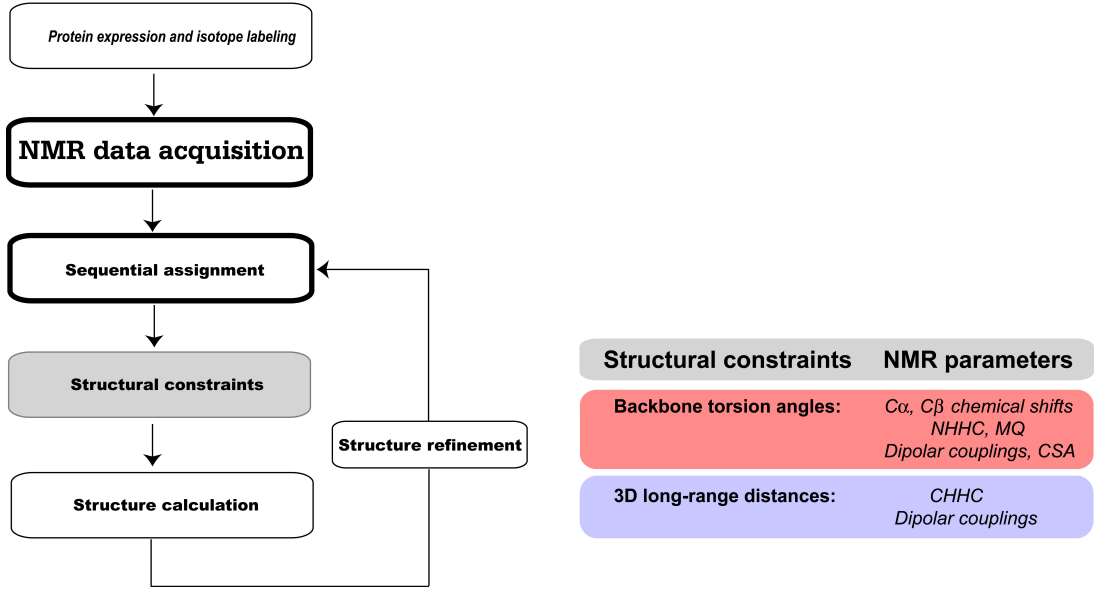


Figure 2.9: Strategy of NMR protein structure determination and the parameters associated with structural constraints, particularly for solid-state NMR [20, 57] which is the aim of this thesis.

Structural constraints (e.g., angles or distances) are obtained from measured parameters via theoretical or empirical relationships and they define in the context of solid-state NMR: (1) the local structure (such as  $^{13}C\alpha$  and  $^{13}C\beta$  chemical shifts [86], see Figure 2.10, or NHHC [30]) and (2) the global 3D fold (such as CHHC [87]). Structure calculation uses the determined constraints together with the known covalent topology of each residue most often in restrained molecular dynamics protocols (CNS [88], XPLOR [89]) containing NMR specific force fields. For example, restrained potential energy used in XPLOR is defined as a sum of covalent (first four terms) and non-covalent (the last two terms contain NMR restrains) contribution:

$$\begin{aligned}
 E_{pot} = & \sum_{bonds} k_b(r - r_0)^2 + \sum_{angles} k_\theta(\theta - \theta_0)^2 + \sum_{dihedrals} k_\phi(1 + \cos(n\phi + \delta))^2 + \\
 & + \sum_{impropers} k_\phi(\phi - \delta)^2 + \sum_{non-bonded} k_{repel}(max(o, (sR)^2 - R^2))^2 + \\
 & + \sum_{distance\ restr.} k_d\delta_d^2 + \sum_{angle\ restr.} k_a\delta_a^2
 \end{aligned} \tag{2.14}$$

Starting from an extended polypeptide chain, potential energy (Equation 2.14) is minimized and the ensemble of 10-20 lowest energy conformations are selected to represent the NMR derived protein structure. Refinement and validation of the structure can be done iteratively [90, 91].

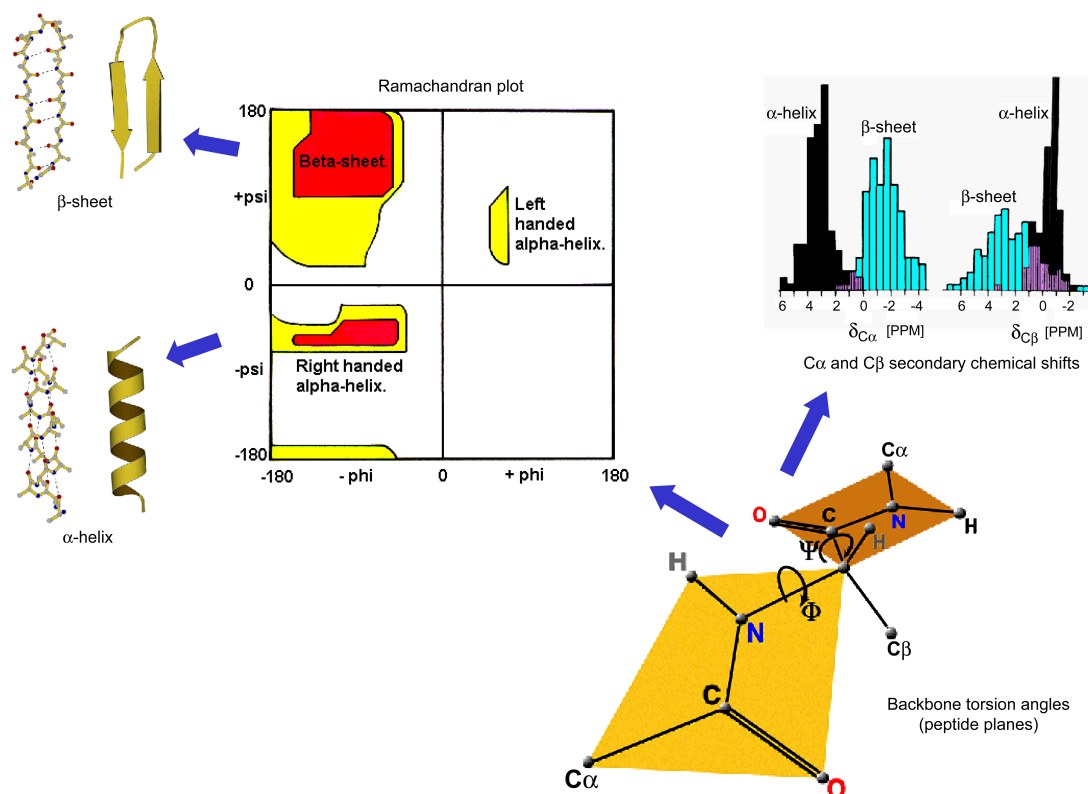


Figure 2.10: Elements of protein secondary structure ( $\alpha$ -helix and  $\beta$ -sheet) defined by the backbone torsion angles ( $\phi$  and  $\psi$ ) and empirical correlations with  $^{13}\text{C}\alpha$  and  $^{13}\text{C}\beta$  secondary chemical shifts [92, 93, 86].

Liquid-state NMR has constantly developed methods since the first protein structure determination in 1985 by Wüthrich [94] and currently, a large toolbox of multidimensional NMR experiments [39, 95], labeling schemes [96], automated or semi-automated programs [84, 90, 97, 91] exist for sequential assignment and structure calculation. Proteins up to 30 kDa can be routinely studied by liquid-state NMR and successful appli-

cations have been demonstrated for proteins with molecular weights up to 100 kDa [98]. This limitation in liquid-state NMR appears due to the increase of the correlation time ( $\tau_c$ , see Figure 2.12) with the molecular weight (‘*correlation-time problem*’) that shortens the transverse relaxation time ( $T_2 \propto \tau_c^{-1}$ ) and degrades spectral resolution. The problem becomes even more apparent in the case of membrane proteins where the size of the lipid-protein assemblies (micelles, bicelles, liposomes) can easily reach or exceed the above limits even for small proteins.

The situation is different in solid-state NMR. Here, the proteins are often immobilized on the NMR time scale. As a result, solid-state NMR is less sensitive to the correlation-time problem and the resolution will not degrade with increasing molecular weights. Instead it will be determined by the available MAS rate ( $T_2 \propto \omega_r^2$ , see Equations 2.15-2.16), the structural heterogeneity (static disorder) and the degree of spectral overlap. In addition, fast internal dynamics (see § 2.5.2 and Chapter 4) may improve resolution. Although, a routine methodology for solid-state NMR does not exist yet as in the case of liquid-state NMR, much progress has been recently realized.

The current strategy for uniformly labeled proteins in MAS solid-state NMR relies heavily on  $^{13}\text{C}$  (detected) and  $^{15}\text{N}$  nuclei, making isotope labeling mandatory [99].

The residues type are identified in ( $^{13}\text{C},^{13}\text{C}$ ) homonuclear correlation spectra (SQ/SQ or DQ/SQ) based on the unique spin connectivities and distinct  $^{13}\text{C}$  chemical shifts of each residue, while sequential assignment is obtained from combination of heteronuclear NCACX and NCOCX spectra that link neighbour residues via the common amide  $^{15}\text{N}$  nucleus [62, 20] (see Figure 2.11). Sequential assignments can be probed also in CC correlation spectra under specific, so called ‘*weak coupling conditions*’ [100], or in NN correlations when possible [101]. To improve resolution and obtain long range constraints in spin diffusion [102, 103] spectra, special  $^{13}\text{C}$  labeling schemes have been proposed [26].

Most often, protons are used in solid-state NMR for signal enhancement via cross-polarization as opposed to liquid-state NMR where  $^1\text{H}$  is the detect nucleus and provides important distance constraints and assignments from NOESY experiments [104]. How-

ever, a variety of methods have been developed to obtain more information from the protons either by indirect detection of the  $^1\text{H} - ^1\text{H}$  distances in CHHC [105, 87] (probe 3D structure) and NHHC [30] (probe secondary structure and molecular interfaces) experiments, or by decoupling sequences that improve proton resolution [48, 54].

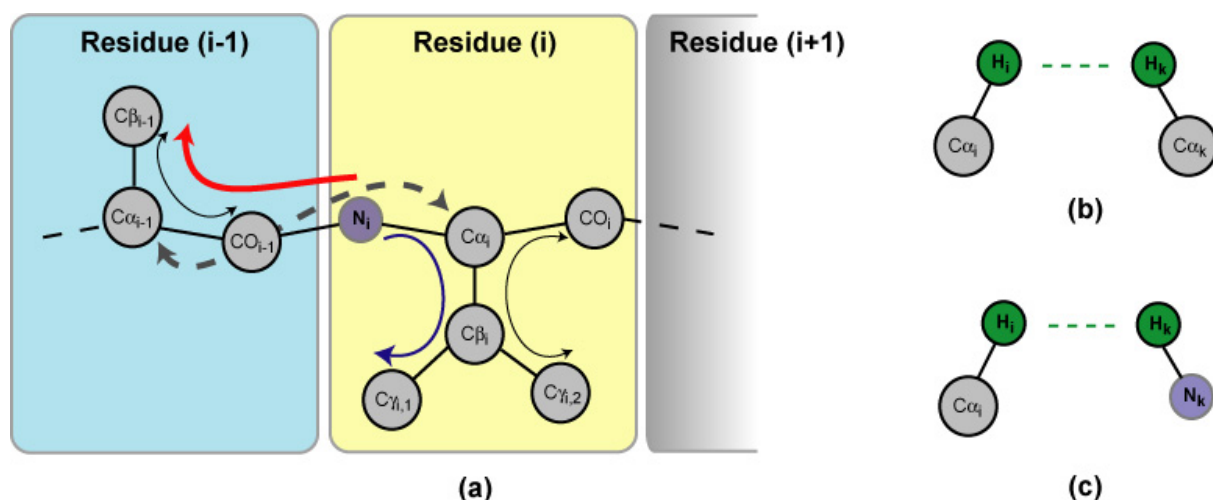


Figure 2.11: Correlation experiments for uniformly labeled proteins in MAS solid-state NMR: (a) CC residue type (black) or sequential (dashed) assignment, intra-residue NCACX (blue) and sequential inter-residue NCOCX (red), (b) indirect detected non-trivial  $^1\text{H} - ^1\text{H}$  distances in CHHC, or (c) NHHC experiments.

MAS experiments on uniformly [ $^{13}\text{C}$ ,  $^{15}\text{N}$ ] labeled proteins in different preparations, including (1) microcrystals [106, 107, 108, 109, 27, 110], (2) proteoliposomes [111], or (3) fibrils [112, 113] have shown that sufficient resolution can be obtained in 2D and 3D spectroscopy for the assignment of proteins up to 150 residues. In addition to MAS, the use of oriented samples has proven to be helpful for structure determination of membrane proteins reconstituted in macroscopically aligned lipid bilayers [114, 115, 22]. Here, separated-local-fields experiments such as PISEMA [116, 117, 118] on  $^{15}\text{N}$  labeled membrane proteins correlate  $^{15}\text{N}$  CSA and  $^{15}\text{N} - ^1\text{H}$  dipolar-coupling interactions and produce peak patterns that are diagnostic of secondary structure and orientation.



## 2.5.2 Protein dynamics

One important advantage of the NMR spectroscopy over X-ray crystallography or other types of spectroscopy is the ability to study protein dynamics over a wide range of time-scales and motional modes [119, 120]. Dynamics consist of: (1) external (translation and rotational diffusion) and (2) internal (local and domain reorientations) degrees of freedom.

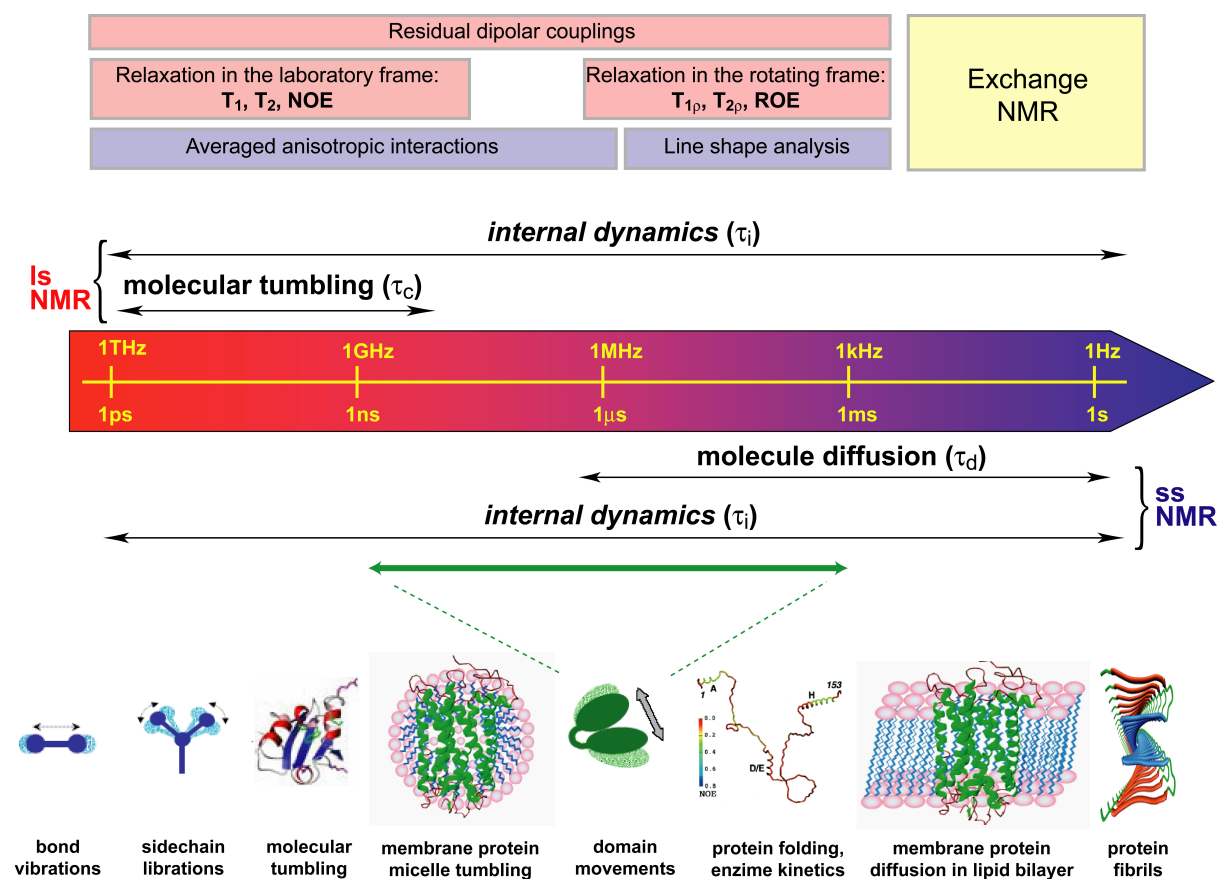


Figure 2.12: Protein dynamics: NMR parameters, time scales, type of motions and the associated physical, chemical and biological events. Domain movements relevant in the context of Chapters 4-5 are highlighted.

Internal dynamics, highly important for protein function, are characterized by motional time-scale (fast ps-ns, intermediate  $\mu$ s-ms and slow ms-s), amplitude and mode (localized - bond vibrations, chemical group rotations, peptide-plane librations, aromatic ring flips; or extended - random reorientation of whole domains). Different motions can be present simultaneously in the same sample. For example integral membrane proteins can have very different dynamics in the transmembrane domains (intermediate-time and small-amplitude librations) as compared to the connecting loops or N and C termini (fast and large amplitude motions).

In liquid-state NMR where fast molecular tumbling averages completely the anisotropic interactions, protein dynamics are usually investigated through relaxation mechanisms and one of the most employed method to fit experimental with theoretical derived spectral density functions is the Lipari-Szabo model-free approach [121, 122].

On the other hand, in solid-state NMR the anisotropy of nuclear spin interactions is only partially averaged by internal dynamics. Localized dynamics has been mostly probed for a long time by solid-state NMR through line-shape analysis [123, 124]. However, fast movements of larger domains have been less explored. Fast and large amplitude dynamics can scale-down or even average-out the anisotropic part of NMR interactions. In particular, strong  $^1\text{H} - ^1\text{H}$  dipolar interactions are reduced to such a degree where protons no longer form a strongly coupled solid spin network. In this situation, their interactions can be completely averaged-out by MAS. Hence the only relevant interactions remaining are the isotropic chemical shifts and scalar couplings. CSA and dipolar couplings will manifest only in the relaxation rates, similar to liquid-state NMR. For example, the transverse relaxation rate for proton homonuclear dipolar coupling interaction is given given by the relationship ( '*weak collision limit*' ) [45, 125]:

$$\frac{1}{T_{2II}} = \frac{1}{5} I(I+1) D^2 [ 3J^2(0) + 5J^2(\omega_{0I}) + 2J^2(2\omega_{0I}) ] \quad (2.15)$$

where  $I = 1/2$  is the spin number,  $D = \mu\gamma_I^2\hbar/4\pi r^3$  the dipolar coupling constant ( $r$

distance between the spins) and  $J^2$  the spectral density functions (contribution of  $k = 2$  terms from Equation 2.8).

Spectral density functions are a measure of the energy existing at multiples ( $m = 0, 1, 2$ ) of Larmor frequency  $\omega_{0I}$  due to random molecular motion and are modulated by the spinning rate  $\omega_r$  in the presence of MAS [45]:

$$J^2(m\omega_{0I}) = (-1)^m \frac{1}{4\pi} \sum_{m'=-2}^2 \left[ d_{mm'}^{(2)}(\beta) \right]^2 \frac{\tau_i}{1 + (m\omega_{0I} - m'\omega_r)^2 \tau_i^2} \quad (2.16)$$

where  $d_{mm'}^{(2)}(\beta)$  are the reduced Wigner elements ( $\beta = 90^\circ$  for  $T_2$  relaxation) and  $\tau_i$  the (internal) correlation time of the internal motions. For rigid solids  $\omega_{0I}\tau_i \gg \omega_r\tau_i \gg 1$  while for very flexible domains  $1 \gg \omega_{0I}\tau_i \gg \omega_r\tau_i$  (in addition for solids, always  $\omega_{0I}\tau_d \gg 1$ , see Figure 2.12). In the last case, internal correlation time  $\tau_i$  and order parameter can be calculated based on the relaxation time measurements [121, 122].

Also in the presence of large dynamics, dipolar-coupling based cross polarization or recoupling techniques of solid-state NMR become ineffective, hence interactions that are not averaged out by mobility such as scalar couplings have to be used for polarization transfers (INEPT [126] or TOBSY [127]). This can be used as a powerful mechanism for spectral editing (see § 4.3). An important advantage is the improved proton resolution, opening the way to the use of proton dimension in multidimensional ssNMR experiments. Results based on these principles are demonstrated for membrane proteins in Chapter 4.

# Chapter 3

## MAS of membrane proteins in oriented lipid bilayers

### 3.1 Introduction

In addition to the tertiary (quaternary) fold, membrane proteins can be characterized by their overall orientation in the lipid membrane. Both features play crucial roles in determining the protein function and are likely to be stabilized through a complex network of interactions, including hydrophobic protein residues and lipid fatty-acid chains. Factors such as lipid composition, lipid to peptide (L/P) ratio [128], hydrophobic mismatch or inter-facial anchoring [129] have been discovered as important modulators of protein structure and function. Because MAS solid-state NMR has the ability to study membrane proteins reconstituted in model (*'bio-mimicking'*) lipid membranes, it is highly desirable to develop methods that can determine both orientation and conformation of such systems.

Solid-state NMR has long been utilized to examine membrane protein structure in lipid bilayers at atomic resolution, complementary to techniques such as X-ray and neutron scattering techniques [130]. Liquid-state NMR (see, e.g. Ref. [131]) has also

been employed to study membrane proteins solubilized in detergents or micells. While the 3D structure of proteins can be investigated by MAS solid-state NMR in randomly oriented samples, the study of protein orientation relative to the membrane requires samples that have a defined axis of orientation ( '*macroscopically uniaxially oriented samples*' ). In particular, investigations using static, macroscopically oriented samples have become an invaluable tool for the study of peptides and proteins interacting with phospholipid bilayers [132, 114, 133]. Absolute orientational constraints derived from these studies are potentially more accurate [134] in defining the protein structure than qualitatively estimated distances [104], and have been adopted also in liquid-state NMR through the use of residual dipolar couplings on weakly oriented proteins in liquid crystalline media [135, 136]. As of to date, solid-state NMR studies on static oriented samples have led to several high-resolution 3D structures of membrane-interacting short peptides such as Gramicidin A [137], trans-membrane helices of larger systems as the M2 channel-lining segments of nicotinic acetylcholine and NMDA receptors [115] or, most recently, the coat protein of fd filamentous bacteriophage particles [138].

On the other hand, MAS solid-state NMR [18] has successfully been used to probe structural aspects in membrane proteins for a long time [139, 19, 69, 140, 141]. For example, MAS-based solid-state NMR methods have been employed to probe individual structural parameters such as the local backbone conformation [142, 143] and monomer-monomer contacts [144, 145, 146] in membrane-embedded peptides, or the entire backbone conformation of a uniformly labeled peptide ligand bound to its G-protein coupled receptor [29]. In addition to the detection of local structural aspects, MAS-based methods are available to probe the overall orientation of the peptide in the membrane, for example by employing heteronuclear dipolar recoupling experiments under MAS [147]. Alternatively, experiments that combine MAS and macroscopic sample orientation have given additional insight into molecular structure ranging from oriented polymers [148, 149] to protein fibers [150].

Since model lipid membranes are well known to orient on solid supports under appropriate hydration and temperature conditions [128], the above concepts could be extended for the structural study of membrane peptides and proteins [151, 24]. Here,  $^{15}\text{N}$ ,  $^{13}\text{C}$  or  $^2\text{H}$  NMR spectroscopy on isotope-labeled peptides has often been used to probe molecular orientation in a membrane environment. Because of technical limitations or due to the fact that structural parameters have been extracted from a spinning side band analysis of anisotropic interactions [152, 153, 154], fast MAS and the concomitant gain in spectral resolution and sensitivity could, thus far, not be exploited. Signal to noise considerations are, however, often of critical importance and may represent a strong determinant as to whether solid-state NMR based investigations of membrane proteins by static or MAS-related experiments are feasible. Moreover, polarization transfer schemes that can provide the basis for further structural investigations are most effective at fast MAS rates and ultrahigh magnetic fields where signal overlap due to spinning sidebands and line-width modulations due to unwanted recoupling effects can be minimized. Compared to structural studies using statically aligned samples [155, 156, 118], MAS based methods may offer an increase in sensitivity and better control of experimental parameters such as hydration level and temperature over extended time periods. Moreover, such techniques can be readily employed on conventional MAS probe heads.

These aspects provide a strong incentive to establish a general set of NMR experiments that allows for the extraction of a variety of structural parameters of membrane embedded peptides at the highest achievable MAS rates. In the following, I am particularly interested in incorporating the detection of macroscopic peptide orientation into standard two-dimensional ( $^{13}\text{C}/^{15}\text{N}$ ) assignment methods. Hence, signal dephasing due to an orientation-dependent chemical shielding interaction or polarization transfer methods using dipolar through-space interactions [20] can be used to encode molecular orientation in high spectral resolution. Both types of signal modulation schemes are also sensitive to local structural parameters such as backbone conformation or hydrogen-bonding. In the following, I demonstrate how MAS ssNMR r.f. recoupling schemes (see § 2.3.3) can be

combined to probe both protein structural parameters (orientation and backbone conformation) in standard 1D or 2D NMR experiments.

Experimental results are shown for two types of trans-membrane peptides, Gramicidin A and WALP23, as examples of the two major backbone conformations found in proteins,  $\beta$ -sheet and  $\alpha$ -helix, respectively. While Gramicidin A is a channel-forming antibiotic peptide naturally produced [157, 158], WALP23 represents a member of the family of Trp-flanked peptides synthetically designed [129] to mimic  $\alpha$ -helical trans-membrane segments of intrinsic membrane proteins. Both peptides have been well characterized by solid-state NMR using static, macroscopically oriented samples. Gramicidin A incorporates into phospholipid membranes as a right-handed  $\beta$  6.5 helix [137, 159, 158]. WALP peptides have been shown to adopt an  $\alpha$ -helical conformation in model membranes [129, 160, 161, 162]. These peptides were reconstituted into model DMPC bilayers and mechanically oriented onto thin poly-ether-ether-ketone (PEEK) films [163, 24]. Subsequently the polymer films were rolled in the form of a cylinder and placed in the MAS rotor (see Figure 3.1 (ii)).

## 3.2 Theory

Average Hamiltonian theory [40] has previously been used to describe the effect of CSA and dipolar recoupling under MAS for the case of randomly oriented samples. Using spherical tensor notation, the spin tensor components and rank 0 space tensor elements (such as the isotropic chemical shift) remain unchanged if one considers the problem of a macroscopically oriented system subjected to MAS. The functional dependence of the higher rank space tensor elements on the molecular orientation for each interaction ( $\Lambda$ ) can be obtained from a succession of 4 Euler transformations [164] between five different reference frames <sup>1</sup>:

$$\begin{aligned}
 PAS & \xrightarrow{(\alpha_\Lambda, \beta_\Lambda, 0^\circ)} MOL \\
 MOL & \xrightarrow{(\varphi, \theta, 0^\circ)} MEM \\
 MEM & \xrightarrow{(\varphi_R, \theta_R, 0^\circ)} RAS \\
 RAS & \xrightarrow{(\omega_R t, \theta_{MAS}, 0^\circ)} LAB
 \end{aligned} \tag{3.1}$$

In the principal axis system (PAS), the anisotropic interaction  $\Lambda$  of interest (CSA, dipolar, quadrupolar) depends on the anisotropy  $\delta_\Lambda$  and the asymmetry  $\eta_\Lambda$  and can be represented by the following set of rank 2 spherical space tensor components [45, 20]:

$$\begin{aligned}
 A_{20}^{PAS, \Lambda} &= \sqrt{\frac{3}{2}} \delta_\Lambda \\
 A_{2\pm 2}^{PAS, \Lambda} &= \frac{1}{2} \eta_\Lambda
 \end{aligned} \tag{3.2}$$

In the present analysis,  $\delta_\Lambda$  refers to the anisotropic  $^{15}\text{N}$  chemical shielding (CSA) and the heteronuclear (i.e.  $^{15}\text{N}-^{13}\text{C}\alpha$ ) or homonuclear (i.e.  $^{13}\text{C}\alpha-^{13}\text{C}\beta$ ) dipolar (D) interactions. The quadrupolar interaction (i.e.  $^2\text{H}$ ) has been extensively used by others [151, 161] and

---

<sup>1</sup>The last rotation in a frame transformation is equivalent with the first rotation of the next transformation, thus one rotation can be skipped by setting the corresponding Euler angle to  $0^\circ$ .



is beyond the aim of the current work.

Figure 3.1 summarizes the relationship between the laboratory frame (LAB, Z axis along the static magnetic field  $\vec{B}_0$ ), the rotor axis system (RAS, Z axis along the rotor axis), the membrane frame (MEM, Z axis along the membrane normal  $\vec{n}$  and, also known as the sample director frame in the polymer literature [165]), the molecular frame (MOL, Z axis along molecule symmetry axis  $\vec{a}$ ), and the principal axis system (PAS, characterized by the tensor diagonal elements defined above in Equation 3.2 and the angles  $\alpha_A$  and  $\beta_A$  for each interaction). For example,  $\beta_{CSA}$ ,  $\beta_{D-NH}$ ,  $\beta_{D-NC\alpha}$  and  $\beta_{D-C\alpha C\beta}$  are shown in Figure 3.1 (iii). The Z axis  $\vec{a}$  of the MOL frame can be chosen to coincide with the molecular symmetry axis, for example in the case of an  $\alpha$ -helix (WALP23) or  $\beta$ -helix (Gramicidin A):

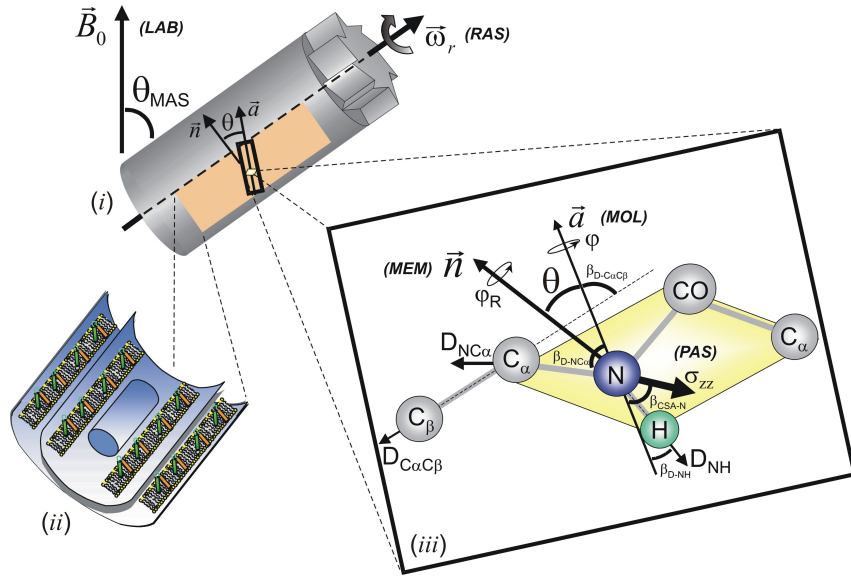


Figure 3.1: Reference frames used to describe the MAS experiments on oriented samples: (i) the MAS rotor oriented at magic angle  $\theta_{MAS} = 54.44^\circ$  with respect to the static magnetic field  $B_0$ , (ii) the reconstituted peptides and lipid bilayers oriented onto rolled polymer films, (iii) NMR interactions and their orientation in the peptide plane.

The general approach of oriented samples assumes knowledge of the PAS tensor elements (Equation 3.2) and their orientation in the peptide plane (i.e. the angles  $\alpha_\Lambda$  and  $\beta_\Lambda$  of the first transformation in Equation 3.1)<sup>2</sup>. By measuring the interactions in the laboratory frame and using the transformations of Equation 3.1 the molecular orientation of interest (i.e. the tilt  $\theta$  and azimuthal  $\varphi$  angles in the second transformation from Equation 3.1) can be recovered. The other angles present in Equation 3.1 (third and fourth transformations) are defined by the experimental method and are known.

In explicit form, the rank 2 spherical space tensor components of each reference frame are obtained through Euler rotations of the preceding frame components in Equation 3.1 and can be expressed using the standard set of reduced Wigner elements of rank 2 [45, 20]:

$$\begin{aligned} A_{2M}^{RAS,\Lambda} &= \sum_{m'=-2}^2 A_{2m'}^{MEM,\Lambda} e^{-im'\varphi_R} d_{m'M}(\theta_R) \\ A_{2n}^{MEM,\Lambda} &= \sum_{n'=-2}^2 A_{2n'}^{MOL,\Lambda} e^{-in'\varphi} d_{n'n}(\theta) \\ A_{2l}^{MOL,\Lambda} &= \sum_{l'=-2}^2 A_{2l'}^{PAS,\Lambda} e^{-il'\alpha_\Lambda} d_{l'l}(\beta_\Lambda) \end{aligned} \quad (3.3)$$

Based on Equations 3.3, the general expression of the relevant space components in the RAS frame can be calculated from the known PAS components:

$$A_{2M}^{RAS,\Lambda} = \sum_{m'=-2}^2 \sum_{n'=-2}^2 \sum_{l'=-2}^2 A_{2l'}^{PAS,\Lambda} e^{-i(l'\alpha_\Lambda + n'\varphi + m'\varphi_R)} d_{l'n'}(\beta_\Lambda) d_{n'm'}(\theta) d_{m'M}(\theta_R) \quad (3.4)$$

where M represents the possible space tensor components recoupled by the r.f. scheme, i.e.  $M = \pm 1$  or  $M = \pm 2$ . For symmetric tensors such as found for the dipolar coupling ( $A_{2\pm 2}^{PAS,D} = 0$ ) or for CSA tensors (i.e.  $^{15}\text{N}$ ) with very small asymmetry parameters ( $A_{2\pm 2}^{PAS,CSA} \ll A_{20}^{PAS,CSA}$ ), the NMR measurements are unaffected by the angle  $\alpha_\Lambda$  (see

---

<sup>2</sup>One strong assumption is that PAS orientation and size are relatively fixed for a given residue type in proteins with similar backbone conformations.

Appendix B.1 for details). In general, the angle  $\beta_\Lambda$  is fixed by the molecular structure and has been investigated in a variety of model compounds<sup>3</sup>. In the case of an  $\alpha$ -helix the  $^{15}\text{N} - ^1\text{H}$  dipolar vector approximately coincides with the helix axis and  $\beta_{\text{CSA-N}}$  angles in the range  $[15^\circ, 20^\circ]$  are usually found<sup>4</sup> [166], while for  $\beta$ -helices (such as in the case of Gramicidin A) the  $^{15}\text{N} - ^1\text{H}$  bonds are no longer oriented parallel to the molecular Z axis (see Figure 3.1) hence the PAS orientations in the peptide plane frame [167] and in the MOL frame do not coincide anymore. The signal modulation (see also Equation B.6) is thus determined by the tilt angle  $\theta$  between molecular ( $\vec{a}$ ) and membrane frame directors ( $\vec{n}$ ), and the azimuthal angle  $\varphi$  that defines a rotation around the molecular frame director ( $\vec{a}$ ).

If PAS and MOL frame coincide ( $\beta_\Lambda = 0^\circ$ ), Equation 3.4 reduces to:

$$A_{2M}^{RAS,\Lambda} = \delta_\Lambda \sqrt{\frac{3}{2}} \sum_{m'=-2}^2 d_{0m'}(\theta) d_{m'M}(\theta_R) e^{-im'\varphi_R} \quad (3.5)$$

The angle  $\theta_R$  describes the orientation of the membrane normal relative to the rotor fixed axis system. Watts and coworkers [151, 153] have proposed a macroscopic alignment for MAS using glass plates where  $\theta_R = 0^\circ$ . In this case, Equation 3.5 can be further simplified to:

$$A_{2M}^{RAS,\Lambda} = \frac{3}{4} \delta_\Lambda \begin{cases} \sin(2\theta) e^{\mp i\varphi_R}, & M = \pm 1 \\ \sin^2(\theta) e^{\mp i\varphi_R}, & M = \pm 2 \end{cases} \quad (3.6)$$

indicating a simple geometrical dependence of the anisotropic recoupling element on the tilt angle  $\theta$  [168]. Note that for  $\theta = 0^\circ$ , i.e. a trans-membrane orientation, the recoupling element vanishes for both conditions.

For the case considered in this thesis where lipid bilayers are oriented onto a cylinder wrapped from thin PEEK [24] ( $\theta_R = 90^\circ$ , see Figure 3.1 (ii)), Equation 3.5 can

---

<sup>3</sup>The orientation and size of the space components of dipolar interaction for two bonded nuclei is given by the bond direction and length, while the CSA space tensor has to be measured on model compounds.

<sup>4</sup>The  $\sigma_{zz}$  component of  $^{15}\text{N}$  CSA tensor lies in the peptide plane that includes also the  $^{15}\text{N} - ^1\text{H}$  bond.

be evaluated to:

$$A_{2M}^{RAS,\Lambda} = \frac{3}{4}\delta_{\Lambda} \begin{cases} \sin(2\theta) \cos(\varphi_R) \pm i \sin^2(\theta) \sin(2\varphi_R), & M = \pm 1 \\ \frac{1}{2} [\sin^2(\theta) \cos(\varphi_R) + 3 \cos^2(\theta) - 1 \mp 2i \sin(2\theta) \sin(\varphi_R)], & M = \pm 2 \end{cases} \quad (3.7)$$

Contrary to the previous case the  $M = \pm 2$  condition predicts here a signal modulation also for the trans-membrane orientation, and this will be exploited in the case of  $^{15}\text{N}$  CSA recoupling.

As discussed in further details in the Appendix B.1, an analytical description of the signal intensity can be obtained by constructing the zeroth order average Hamiltonian [40] from Equation 3.4 for a given interaction  $\Lambda$  and space number  $M$ . For the case of Equations 3.4-3.7, the analytical result fully agrees with a numerical study, employing a piece-wise constant Hamiltonian. However the complexity of analytical calculations increase rapidly with the number of variables considered and for the general case described by Equations 3.3 and 3.4, quantum-mechanical simulations were performed using the GAMMA [43] software to elucidate the signal modulation under the influence of the proposed r.f. schemes.

### 3.3 Numerical Simulations

Numerical simulations for the r.f. recoupling of anisotropic interactions under MAS have been performed to study: (1) the dependence of the signal evolution as a function of the tilt angle  $\theta$  for various values of  $\beta_{\Lambda}$  (assuming cylindrical symmetry for the angle  $\varphi$  around the molecular director axis  $\vec{a}$ ), (2) the influence of the azimuthal angle  $\varphi$  upon the signal and (3) compare the theoretical results to experimental data. The angular distribution (*mosaic spread*) around an average molecular tilt angle  $\theta$  was approximated by a Gaussian distribution  $g(\theta, \Delta)$  (Equation B.6) in all numerical studies. The standard deviation  $\Delta$  was determined experimentally from a  $^{31}\text{P}$  spinning sideband analysis (see Figure B.2).

In Figure 3.2, predictions of the signal modulations due to  $^{15}\text{N}$  CSA and  $^{15}\text{N} - ^{13}\text{C}\alpha$  (NC) or  $^{13}\text{C}\alpha - ^{13}\text{C}\beta$  (CC) dipolar interactions for both  $M = \pm 1$  and  $M = \pm 2$  conditions are shown. In all cases, the signal was computed as a function of the molecular tilt angle ranging from  $0^\circ$  to  $90^\circ$  in steps of ten degrees, for one ( $^{15}\text{N}$  CSA) or two (NC, CC dipolar) distinct values of  $\beta_\Lambda$ .

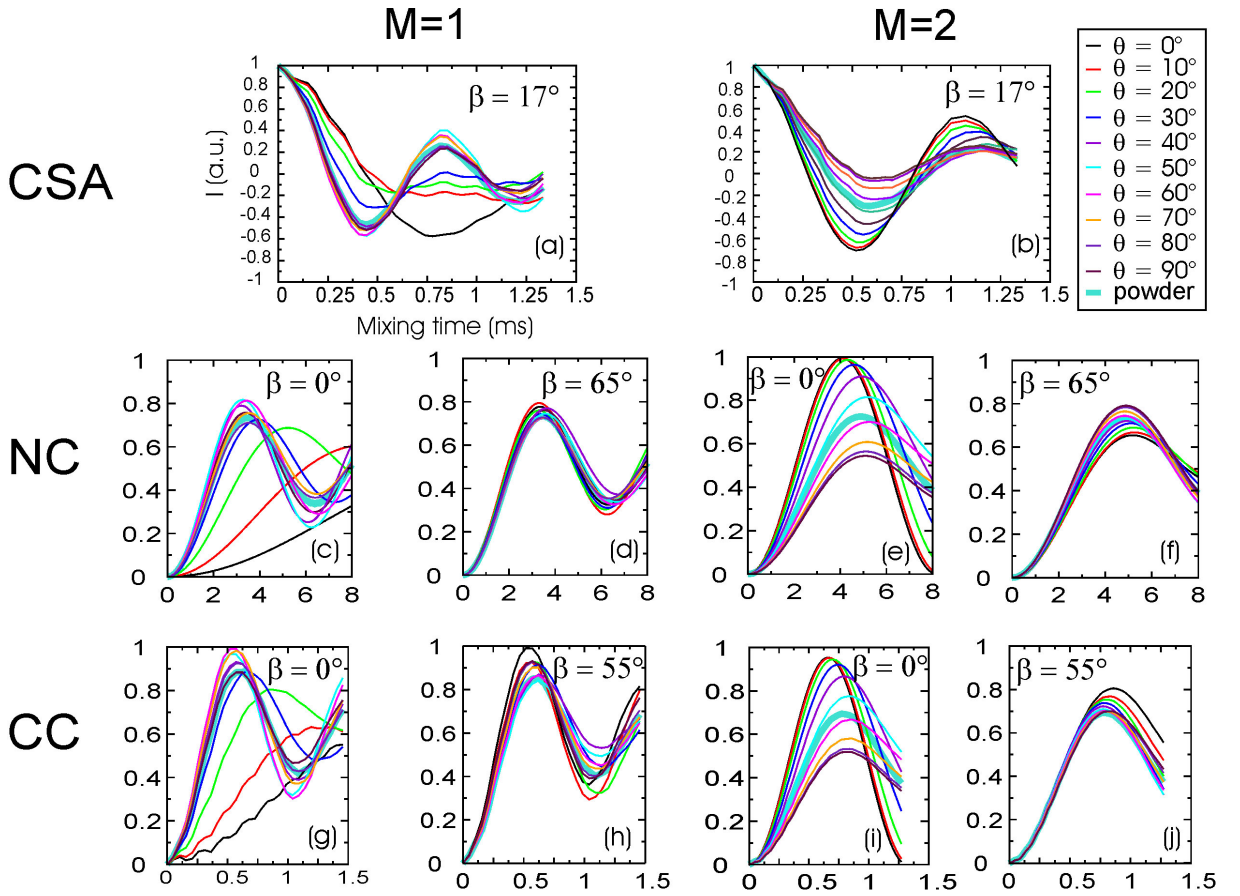


Figure 3.2: Recoupling of the  $M = 1$  and  $M = 2$  space components for anisotropic NMR interactions for different tilt angles  $\theta$ : (a,b)  $^{15}\text{N}$  CSA, (c-f)  $^{15}\text{N} - ^{13}\text{C}\alpha$  heteronuclear dipolar interaction and (g-j)  $^{13}\text{C}\alpha - ^{13}\text{C}\beta$  homonuclear dipolar interaction. Simulations corresponding to unoriented (powder) samples are shown for comparison by the thick curves.

In particular, the molecular geometry relevant for an ideal  $\alpha$ -helix was considered with the  $\vec{a}$  axis of MOL frame along the  $^{15}\text{N} - ^1\text{H}$  bonds, i.e.  $\beta_{CSA-N} = 17^\circ$ . PAS values of the  $^{15}\text{N}$  CSA tensor ( $\sigma_{xx} = 57$ ,  $\sigma_{yy} = 57$ ,  $\sigma_{zz} = 220$  in ppm) were taken from the literature [24]. In addition, results are displayed for different orientations of the dipolar vectors  $^{15}\text{N} - ^{13}\text{C}\alpha$  and  $^{13}\text{C}\alpha - ^{13}\text{C}\beta$  in the molecular frame (i.e.  $\beta_{D-NC\alpha} = 0^\circ$  (c,e),  $\beta_{D-NC\alpha} = 65^\circ$  (d,f),  $\beta_{D-C\alpha C\beta} = 0^\circ$  (g,i) and  $\beta_{D-C\alpha C\beta} = 55^\circ$  (h,j)) where the non-zero values again correspond to angles typically found for an  $\alpha$ -helical geometry. The zero angles have been purposely chosen to illustrate the angular dependences given in Equations 3.4-3.7. For CSA dephasing the recoupling sequences  $R18_2^7$  ( $M = \pm 1$ ) [63] and  $R18_2^5$  ( $M = \pm 2$ ) [169] were assumed (details of the sequences are given in § 3.4 and § 3.5). Dipolar recoupling was established for NC using cross polarization ( $M = \pm 1$  and  $M = \pm 2$ ) [55, 56, 170] and in the case of CC the DQ r.f. schemes such as POST-C7 ( $M = \pm 1$ , see also experiments in § 3.6) [171] or  $C8_1^3$  ( $M = \pm 2$ ) [63]. For the CSA case (MAS = 6 kHz, Figure 3.2 (a,b)), the signal modulation represents the dephasing of longitudinal magnetization, (i.e.  $\sigma_0 = D_{CSA} = I_z$ , see Equation B.6). For NC and CC transfer, the buildup of single-quantum (SQ,  $\sigma_0 = I_x$  and  $D_{NC} = S_x$ ) or double-quantum (DQ,  $\sigma_0 = I_{z1}$  and  $D_{CC} = I_{z2}$ ) coherence, respectively, is monitored. Numerical results for NC (MAS = 5 kHz, Figure 3.2 (c-f)) and CC dipolar recoupling (MAS = 5.5 kHz, Figure 3.2 (g-j)) are shown. Standard one-bond distances have been considered for the NC (1.45 Å) and CC (1.5 Å) dipolar couplings. In all simulations, a Gaussian mosaic spread of  $\Delta = \pm 8^\circ$  for the angle  $\theta$  was assumed. Simulations assuming random (powder) orientation are included for reference (thick line). One spin (CSA) or two spins systems (NC, CC) were considered and the signal intensity was averaged over 277 different orientations of  $\varphi_R$  and 209 different values of  $\varphi$  between  $0^\circ$  to  $360^\circ$  according to the method proposed by Cheng et al. [172] (see Equation B.6). To account for the mosaic spread, the tilt angle was linearly varied in the range  $[\theta \pm \Delta]$  (50 orientations for  $\Delta = \pm 8^\circ$ ). For the calculation of the piecewise-constant Hamiltonian, the time step over which the Hamiltonian was considered constant was set to  $0.55 \mu s$  (5.5 kHz MAS, POST-C7) or

$0.46 \mu s$  (6 kHz MAS,  $R18_2^5$ ) (corresponding to  $1^\circ$  of MAS rotation at the given spinning rate). The GAMMA simulation program for  $R18_2^5$  is given in Appendix B.3.

For all considered schemes, recoupling of the  $M = 1$  components leads to a limited sensitivity of the signal modulation to the molecular tilt angle  $\theta$ . Variations in the dipolar recoupling NC or CC signal buildup (at the  $M = 1$  condition) are seen for a small range of peptide orientations ( $\theta \in [0^\circ, 30^\circ]$ ) and only in the degenerate cases  $\beta_{D-NC\alpha} = 0^\circ$  or  $\beta_{D-C\alpha C\beta} = 0^\circ$ , respectively (Figure 3.2 (c,g)). In contrast,  $M = 2$  CSA dephasing exhibits a desired monotonic dependence on the molecular orientation through the whole range  $\theta \in [0^\circ, 90^\circ]$  (Figure 3.2 (b)).

A more detailed analysis is presented in Figure 3.3, where the  $^{15}\text{N}$  CSA dephasing behavior at the minimum intensity (i.e. a dephasing time of 0.55 ms for  $M = 2$  recoupling condition with  $R18_2^5$  at 6 kHz MAS, Figure 3.2 (b)) is displayed as a function of the Euler angles  $\theta$  and  $\beta_{CSA-N}$ , extending the analysis beyond the  $\alpha$ -helix case treated before.

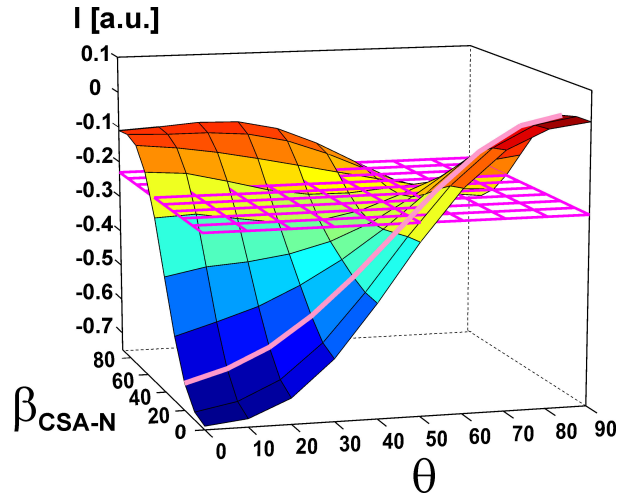


Figure 3.3: Plot of the minimum intensity of the  $^{15}\text{N}$  CSA dephasing curve ( $M = 2$ , Figure 3.2 (b)) for the entire  $[\beta_{CSA-N}, \theta]$  space, assuming cylindrical symmetry around the azimuthal angle  $\varphi$ . The case of an oriented  $\alpha$ -helix ( $\beta_{CSA-N} = 17^\circ$ ) is highlighted. The grid plane indicates results for a powder sample.

In agreement with Figure 3.2 (b), the signal intensity is very sensitive to the molecular orientation for the case of an  $\alpha$ -helix ( $\beta_{CSA-N} = 17^\circ$ , highlighted) and in generally this holds true for the whole range of  $\beta_{CSA-N} \in [0^\circ, 40^\circ]$ . Interestingly, the dephasing signal at the considered mixing time vanishes for an in-plane orientation of the  $\alpha$ -helix ( $\theta = 90^\circ$ ) and becomes strongly negative for a trans-membrane orientation. In summary, when describing the influence of the tilt angle three main ranges of orientations,  $[0^\circ, 20^\circ]$ ,  $[20^\circ, 70^\circ]$  and  $[70^\circ, 90^\circ]$  can be distinguished. The strongest variation for the case of an  $\alpha$ -helix is observed for tilt angles  $\theta \in [20^\circ, 70^\circ]$ .

Numerical simulations also permit to estimate the influence of the azimuthal angle  $\varphi$ . In Figure 3.4, simulations assuming the CSA dephasing time of Figure 3.3 and PAS values and orientation of an  $\alpha$ -helix are shown for variable values of  $\varphi$  and helix tilt angle  $\theta$ .

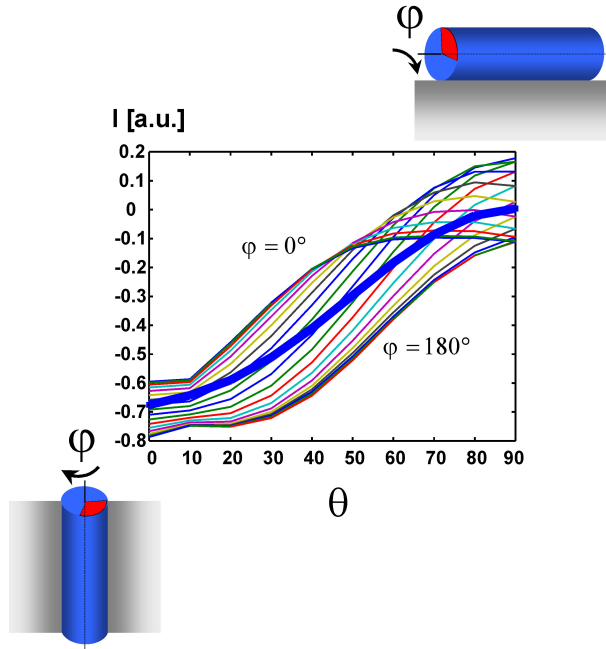


Figure 3.4: Variation of the minimum intensity of the  $^{15}\text{N}$  CSA dephasing curve ( $M = 2$ , Figure 3.2 (b)) in case of an  $\alpha$ -helix ( $\beta_{CSA-N} = 17^\circ$ ) as a function of the tilt  $\theta$  and azimuthal  $\varphi$  angles, the case of cylindrical symmetry is indicated by the bold line.



As expected, the signal intensities vary around the average (assuming cylindrical symmetry, indicated in bold) value. For the considered case of CSA dephasing (shown in Figure 3.4), but also for additional calculations referring to NC and CC transfers (data not shown), deviations are most significant for helix tilt angles larger than  $10^\circ$  and will be neglected for the analysis of the experimental data presented in the following<sup>5</sup>.

The results of Figure 3.2 and Figure 3.3 suggest a possible combination of a CSA dephasing and dipolar transfer unit in which *only one* of the transfer units, namely the CSA dephasing block, is sensitive to the peptide orientation and where the dipolar transfer dynamics are (for a general case of  $\beta_{D-NC\alpha}, \beta_{D-C\alpha C\beta} \geq 10^\circ$ ) largely insensitive to the overall molecular orientation in the membrane: Such a behavior should be expected if one combines a CSA ( $M = 2$ ) dephasing unit with dipolar NC and CC ( $M = 1$ ) transfer schemes. In the following section such a generalized scheme for the case of unoriented tri-peptide and two membrane-embedded model peptides is exemplified.

### 3.4 Pulse sequences for MAS of oriented samples

In Figure 3.5 one-dimensional NMR experiments to detect anisotropic interactions under MAS conditions are proposed. Anisotropic chemical shielding interactions (CSA) are recoupled using a set of symmetry based r.f. schemes introduced by Levitt and coworkers [63]. These, so called,  $R18_2^5$  and  $R18_1^7$  (for  $M = 2$  CSA recoupling) schemes involve multiple repetitions of rotor-synchronized R elements ( $180^\circ$  pulse) with phase switches  $\phi = \pm 50^\circ$  and  $\phi = \pm 70^\circ$ , respectively [169, 173] (for a general  $RN_n^\nu$  symmetry sequence specified by the N, n and  $\nu$  symmetry numbers, the relationship between the MAS frequency ( $\omega_r$ ), the amplitude ( $\omega_{rf}$ ) and the phase ( $\phi$ ) of the r.f. field, and the number (N) of R elements ( $180_\phi^\circ 180_{-\phi}^\circ$ ) per rotor period  $\tau_r$  is shown in Figure 3.5 (b)). After the initial  $^1\text{H}$  to  $^{15}\text{N}$  CP polarization transfer,  $^{15}\text{N}$  Z magnetization is created for longitu-

---

<sup>5</sup>In order to refine both parameters, more than one data set is necessary, i.e. several uniquely labeled samples or one multiply (uniformly) labeled sample.

dinal CSA recoupling, while simultaneously the  $^1\text{H}$  are decoupled. In the 0<sup>th</sup> order AHT the only interaction that is selected by the  $R18_2^5$  and  $R18_1^7$  symmetries is the (scaled) CSA, while the homonuclear dipolar couplings are averaged to zero (amide  $^{15}\text{N} - ^{15}\text{N}$  homonuclear dipolar couplings are negligible). In addition, R sequences seem to be less sensitive to r.f. field inhomogeneity. This superior behaviour allows for a more accurate estimation of the desired structural parameters by CSA recoupling in the presence of R symmetry sequences than using simple spin-lock rotary resonance recoupling. To decrease the influence of r.f. heating (mainly due to  $^1\text{H}$  decoupling) and other probehead performance related parameters, the experiments were conducted in a constant-time manner as indicated in Figure 3.5 (a) where  $T_c$  was set to 2 ms (in general a  $^1\text{H}$  r.f. field decoupling of 83 kHz has been employed under continuous-wave (CW) or TPPM schemes [174]). After CSA recoupling, the  $^{15}\text{N}$  magnetization is flipped back to the transverse plane for detection and  $^1\text{H}$  are further decoupled during acquisition.

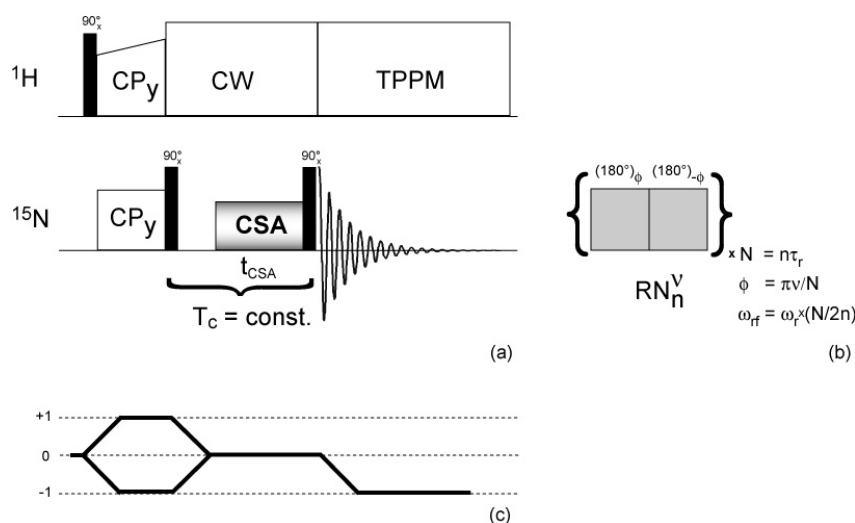


Figure 3.5: 1D  $^{15}\text{N}$  CSA recoupling experiment: (a) pulse sequence with time constant implementation, (b) detail of the internal parameters of the general  $RN_n^V$  symmetry sequences used for CSA recoupling, (c)  $^{15}\text{N}$  coherence-transfer pathways. The 1D Bruker pulse program is given in Appendix B.4.

The extension to 2D NMR spectroscopy is shown in Figure 3.6 where the signal modulation after  $^{15}\text{N}$  CSA recoupling is followed by a  $t_1$  evolution and then transferred to  $^{13}\text{C}$  to take advantage of the increased spectral dispersion and the secondary structure information contained in  $^{13}\text{C}$  chemical shifts. For this purpose,  $^{15}\text{N} - ^{13}\text{C}\alpha$  transfer can be established under SPECIFIC CP condition [170] and magnetization can be further relayed to  $^{13}\text{C}\beta$  via longitudinal mixing schemes such as spin diffusion (zero quantum, ZQ) [103, 33] or DQ (POST-C7 [171], SPC5 [175]) . Phase cycling ensures longitudinal mixing for both CSA and CC blocks, together with spin-temperature alternation of the  $^1\text{H} - ^{15}\text{N}$  CP and SPECIFIC CP in order to eliminate directly excited  $^{15}\text{N}$  and  $^{13}\text{C}$  signal. Experimentally, the  $^1\text{H} - ^{15}\text{N}$  CP (1 ms) was established using 40 kHz (ramped 100-80%)  $^1\text{H}$  and 35 kHz  $^{15}\text{N}$  r.f. fields, while for the  $^{15}\text{N} - ^{13}\text{C}\alpha$  SPECIFIC CP (3 ms), 20 kHz  $^{15}\text{N}$  and 15 kHz (ramped 80-100%)  $^{13}\text{C}\alpha$  r.f. fields were used. The TPPI scheme [33] was employed for the  $^{15}\text{N}$  CP spin-lock field and the  $90^\circ$  pulses preceding  $t_1$  evolution to ensure phase-sensitive detection of this dimension.

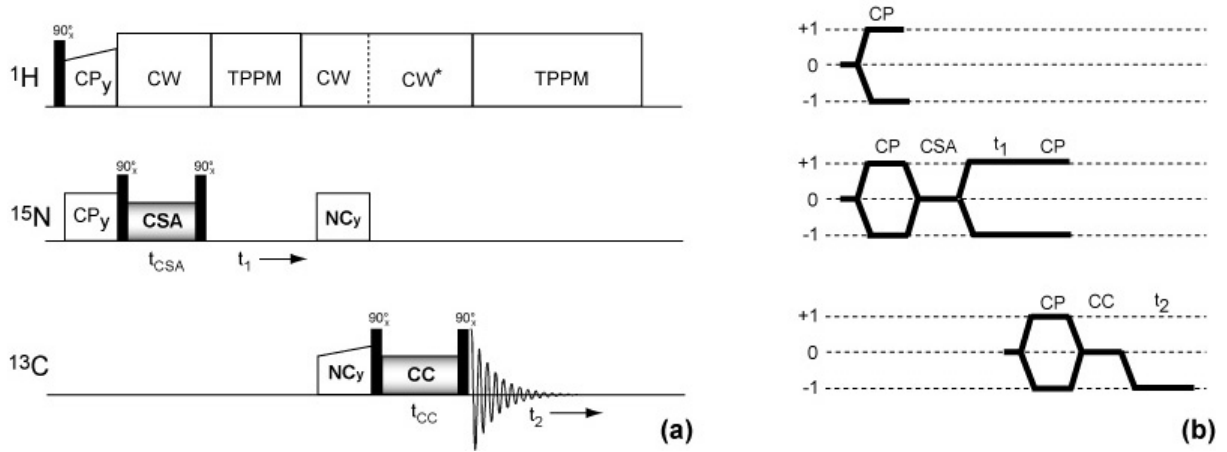


Figure 3.6: 2D  $^{15}\text{N}/^{13}\text{C}$  correlation experiment to probe simultaneously the peptide orientation ( $^{15}\text{N}$  CSA) and backbone conformation ( $^{13}\text{C}$  chemical shifts): (a) block diagram of the pulse sequence, (b) coherence-transfer pathways for longitudinal mixing during CSA and CC blocks. The 2D Bruker pulse program is given in Appendix B.4.

First, the accuracy with which the CSA signal dephasing can be monitored in a constant-time experiment (Figure 3.5 (a)) was investigated for a randomly oriented sample. In Figure 3.7 (a), the  $^{15}\text{N}$  CSA dephasing ( $M = 2$ ) curve is shown for residue Gly3 of the U- $^{15}\text{N}$ ,  $^{13}\text{C}$  labeled tripeptide Ala-Gly-Gly. Numerical simulations were scaled by a mono-exponential relaxation function (relaxation time of 2 ms) and  $^{15}\text{N}$  CSA tensor values previously obtained for AcGlyGlyNH<sub>2</sub> [176] were used. The agreement between simulation and experiment is good and, as indicated by the thin reference lines, significantly differs from predictions assuming a trans-membrane ( $\theta = 0^\circ$ , green) or in plane ( $\theta = 90^\circ$ , blue) oriented peptide.

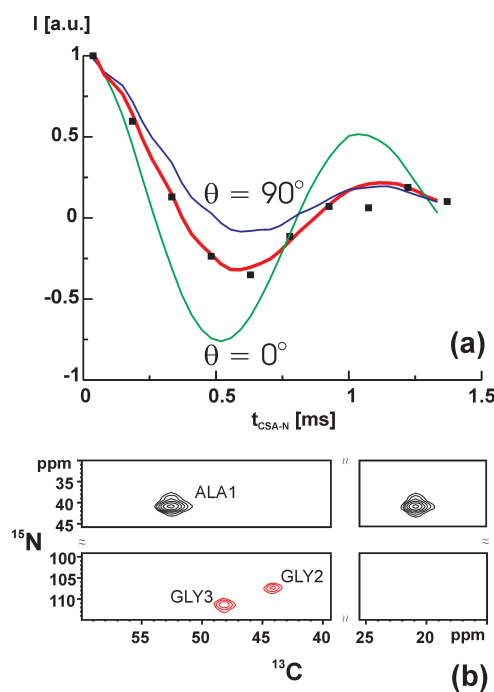


Figure 3.7: Experimental results on the U- $^{15}\text{N}$ ,  $^{13}\text{C}$  labeled AGG: (a)  $^{15}\text{N}$  CSA dephasing for Gly3 ( $CSA = R18_2^5$ , 6 kHz MAS, 600 MHz  $^1\text{H}$  magnetic field) in red simulations assuming a powder sample and comparison to trans-membrane ( $\theta = 0^\circ$ ) and in-plane ( $\theta = 90^\circ$ ) orientations, (b) 2D  $^{15}\text{N}/^{13}\text{C}$  using  $t_{CSA} = 0.55$  ms ( $R18_2^5$ ), NC SPECIFIC CP (4 ms) and spin diffusion for the CC block (5 ms). Negative signal intensities (Gly2/3) are indicated by red contour levels.

In addition, Figure 3.7 (b) demonstrates the application of the 2D approach to encode anisotropic  $^{15}\text{N}$  CSA dephasing in a standard 2D NC correlation experiment. Again, as a control a uniformly labeled powder sample of AGG was considered. The CSA  $R18_2^5$  dephasing time was set to 0.55 ms giving rise of negative signal  $^{15}\text{N}$  modulations (red contour levels) for all NH groups that are characterized by sizable  $^{15}\text{N}$  CSA tensor values (i.e. Gly2 and Gly3). On the other hand,  $^{15}\text{N}$  nucleus such as the  $\text{NH}_3$  group of the N terminus (i.e. Ala1), where motional averaging leads to a strong reduction of  $\delta_{\text{CSA-N}}$  (Equation 3.2), is only weakly affected by the dephasing block and hence occurs with positive signal intensity in the 2D spectrum. After NC and CC transfer, these signal modulations are encoded on both  $^{13}\text{C}\alpha$  and  $^{13}\text{C}\beta$  chemical shifts, as visible in Figure 3.2 (b). For a zero-quantum (ZQ) ( $^{13}\text{C}$ ,  $^{13}\text{C}$ ) transfer, such as the spin diffusion transfer block [102] utilized in Figure 3.6,  $^{13}\text{C}\alpha$  and  $^{13}\text{C}\beta$  resonances are characterized by the same sign of the 2D signal amplitude. 64  $t_1$  increments with 128 scans were recorded using a NC transfer time of 4 ms and a SD mixing time of 5 ms.

### 3.5 $^{15}\text{N}$ CSA recoupling of Gramicidin A and WALP23

1D  $^{15}\text{N}$  CSA dephasing experiments (Figure 3.5) were conducted on oriented samples of U- $^{13}\text{C}$ ,  $^{15}\text{N}$ ]-Ala3 labeled Gramicidin A ( $\text{HCO-VGAL}\underline{\text{A}}\underline{\text{V}}\underline{\text{V}}(\underline{\text{W}}\underline{\text{L}})_3\text{W-CONHCH}_2\text{-CH}_2\text{OH}$ , D-amino acids are underlined) and U- $^{13}\text{C}$ ,  $^{15}\text{N}$ ]-Leu6,Ala7 labeled WALP23 (acetyl-GWW(LA) $_8$ LWWA-amide) in hydrated DMPC lipid bilayers, using the  $R18_1^7$  (Figure 3.8 (a), MAS = 5 kHz) and  $R18_2^5$  (Figure 3.8 (b), MAS = 6 kHz), respectively. Both samples contained 3 mg of labeled peptide at L/P ratios of 8:1 (Gramicidin A), or 16:1 (WALP23) (for details of sample preparation see Ref. [177]). The lipid bilayer orientation has been checked for all samples by measuring  $^{31}\text{P}$  spinning sidebands in the lipid liquid crystalline phase of DMPC (40 °C) and compared to a Floquet MAS sideband simulation (see Figure B.2 and GAMMA program in Appendix B.3). Gaussian mosaic spreads of  $\pm 12^\circ$  and  $\pm 8^\circ$  have been found for the Gramicidin A and WALP23, respectively. In order

to maximize the signal to noise ratio (see Equation 2.1) and prevent the averaging of the NMR interactions due to mobility at higher temperatures, experiments were performed at  $-15^\circ\text{C}$ . A fast-freezing procedure, as described in [177], has been employed to ensure that the lipid bilayer and the peptide orientation are preserved and to prevent the formation of ice crystals. The MAS rotors were transferred in the pre-cooled probehead. The sample hydration level and orientation were stable over a long period of time (as checked by  $^{31}\text{P}$ ), without the need of rehydration over the time frame of solid-state NMR experiments.

Gramicidin A has been shown to adopt a head to head dimer structure in DMPC bilayers [137]. As a result, the  $^{15}\text{N}$  signals of both monomer units are identical in frequency units and, for reasons of molecular symmetry, lead to analogous signal modulations in Figure 3.8 (a). For the numerical simulations, CSA PAS tensor values (Equation 3.2) as reported by Cross et al. [167] were used. In the case of Ala3 of Gramicidin A [167] the  $^{15}\text{N} - ^1\text{H}$  dipolar vector is oriented  $20^\circ$  away from the  $\beta$ -helix axis, while the  $\sigma_{zz}$  axis of the  $^{15}\text{N}$  CSA PAS is tilted by another  $20^\circ$  with respect to the  $^{15}\text{N} - ^1\text{H}$  bond. Hence,  $\beta_{\text{CSA-N}}$  as given in Figure 3.1 (iii) can vary in the range of  $[0^\circ, 40^\circ]$ . Indeed, a numerical grid search for  $\beta_{\text{CSA-N}} \in [0^\circ, 40^\circ]$  and  $\theta \in [0^\circ, 90^\circ]$  lead to the best fit of the experimental data for the pair  $\beta_{\text{CSA-N}} = 40^\circ$  and  $\theta = 0^\circ$ . Cylindrical symmetry for the azimuthal angle  $\varphi$  has been assumed. All simulations included the same relaxation time as in Figure 3.7 (a) and assumed a gaussian mosaic spread ( $\Delta$ ) of  $\pm 12^\circ$ . For each of the 15 dephasing values shown ( $t_{\text{CSA}}$  increment time of  $88\mu\text{s} = 8\pi$  pulses, and constant-time  $T_c$  was fixed at 2 ms), 1536 scans were averaged at 600 MHz  $^1\text{H}$  resonance frequency.

Good agreement between numerical results and the NMR experiment is also observed for U- $^{13}\text{C}$ ,  $^{15}\text{N}$ -Leu6,Ala7 labeled WALP23 sample (10 dephasing values, 1k scans). Notably, the signal modulation is significantly more pronounced than in the powder sample of AGG or in the case of Gramicidin A. Assuming an  $\alpha$ -helix conformation (i.e.  $\beta_{\text{CSA-N}} = 17^\circ$ ) and typical  $^{15}\text{N}$  CSA PAS values for alanine and leucine ( $^{15}\text{N}$  CSA values as given in Ref. [24]), the experimental data are best described if  $\theta = 5^\circ$  ( $\Delta = \pm 8^\circ$  gaussian mosaic spread was included), a value that is very close to results obtained using

samples macroscopically oriented on glass plates [162].

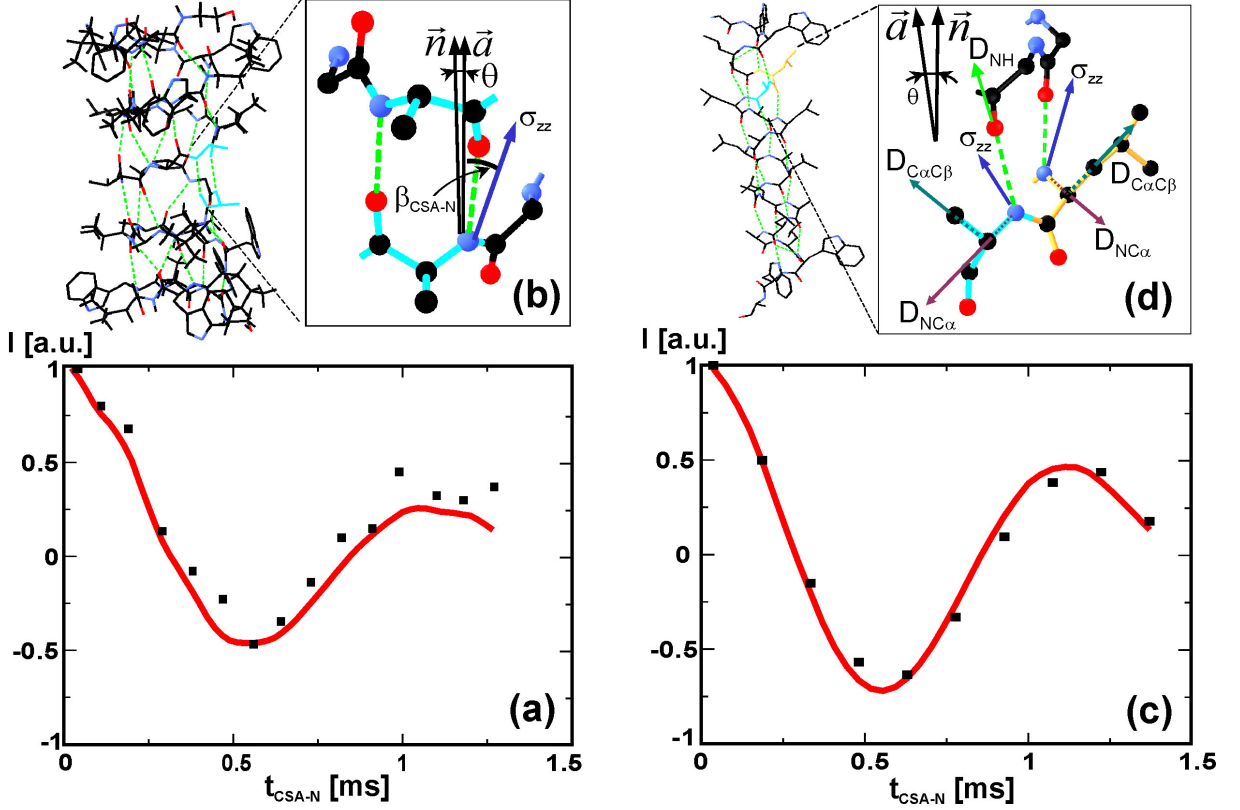


Figure 3.8:  $^{15}\text{N}$  CSA recoupling experiments (Figure 3.5) on Gramicidin A and WALP23 in DMPC oriented lipid bilayers: (a)  $^{15}\text{N}$  CSA dephasing of U- $^{13}\text{C}$ ,  $^{15}\text{N}$ -Ala3 labeled Gramicidin A using the  $R18_1^7$  sequence (5 kHz MAS, 600 MHz  $^1\text{H}$  field), 15 dephasing values (black squares) and simulations ( $\beta_{\text{CSA-N}} = 40^\circ$ ,  $\theta = 0^\circ$ ,  $\Delta = \pm 12^\circ$ , red line) are shown. (b) The  $\beta$ -helix structure [137] of Gramicidin A in the lipid bilayer with a close-up around one of the two Ala3 residues and the relevant interactions. (c)  $^{15}\text{N}$  CSA dephasing of U- $^{13}\text{C}$ ,  $^{15}\text{N}$ -Leu6,Ala7 doubly labeled WALP23 using the  $R18_2^5$  sequence (6 kHz MAS, 600 MHz  $^1\text{H}$  field). 10 dephasing values are shown (black squares) and for comparison, simulations ( $\beta_{\text{CSA-N}} = 17^\circ$ ,  $\theta = 5^\circ$ ,  $\Delta = \pm 8^\circ$ , red line) are included. (d) The  $\alpha$ -helical structure of WALP23 in lipid bilayer generated within Insight II (Biosym Technologies, CA) focusing on the Leu6-Ala7 moiety and the relevant interactions. Experiments have been done at  $-15^\circ\text{C}$  (a,c).

In addition, the GALA approach [161] using deuterated alanine residues in oriented bilayers leads to a helix tilt angle of  $5.5^\circ$  of WALP23 in DMPC. Within the resolution of experiments (see also Figure 3.2 (b)), both values reported in [161, 162] are in good agreement with the WALP23 data obtained under MAS (Figure 3.8 (c)). For Gramicidin A (Figure 3.8 (a)) experimental data follow less the simulated curve than in the case of WALP23. This can be related to lower symmetry of the  $R18_1^7$  (one rotor period) sequence compared to  $R18_2^5$  (two rotor periods) and larger mosaic spread. However tilt angles larger than  $0^\circ$  would make the second maximum (at  $T_{\text{CSA-N}} = 1$  ms) of the simulated curve to deviate even more from the experimental points (see Figure 3.2 (b)).

In the case of doubly-labeled WALP23 peptide, a 1D  $^{15}\text{N}$  CSA dephasing experiment is not sufficient to probe individual residues. As shown in the next section extension to the  $^{13}\text{C}$  dimension and the use of the residue and conformation specific  $^{13}\text{C}$  chemical shift values [92, 178, 86] allows to assign the residues and probe the local  $\alpha$ -helical conformation.

### 3.6 Orientation and local structure of WALP23

The use of the 2D  $^{15}\text{N}/^{13}\text{C}$  experiment from Figure 3.6 allows for simultaneous determination of the orientation and local backbone structure of U- $^{13}\text{C}$ ,  $^{15}\text{N}$ -Leu6,Ala7 labeled WALP23 reconstituted in oriented DMPC lipid bilayers. Based on simulations of Figure 3.2 the  $M = 2$   $^{15}\text{N}$  CSA recoupling condition is combined with  $M = 1$  recoupling of the  $^{15}\text{N} - ^{13}\text{C}\alpha$  and  $^{13}\text{C}\alpha - ^{13}\text{C}\beta$  dipolar interactions in order to render only one of the interactions (i.e.  $^{15}\text{N}$  CSA) orientation dependent. For the  $^{13}\text{C}\alpha - ^{13}\text{C}\beta$  magnetization transfer the DQ POST-C7 [171] pulse sequence is employed due to superior performance on hydrated lipid bilayer samples compared to the ZQ spin diffusion, used in the case of dry AGG powder sample (Figure 3.7 (b)). As a consequence the double-quantum block leads to antiphase  $^{13}\text{C}\beta$  resonances [59] (see Figure 3.10).



In order to check first the validity of predictions from Figure 3.2 (h), DQ buildups for an oriented and unoriented sample of WALP23 were compared. In Figure 3.9 (b,c) results from DQ buildups using POST-C7 sequence are shown.

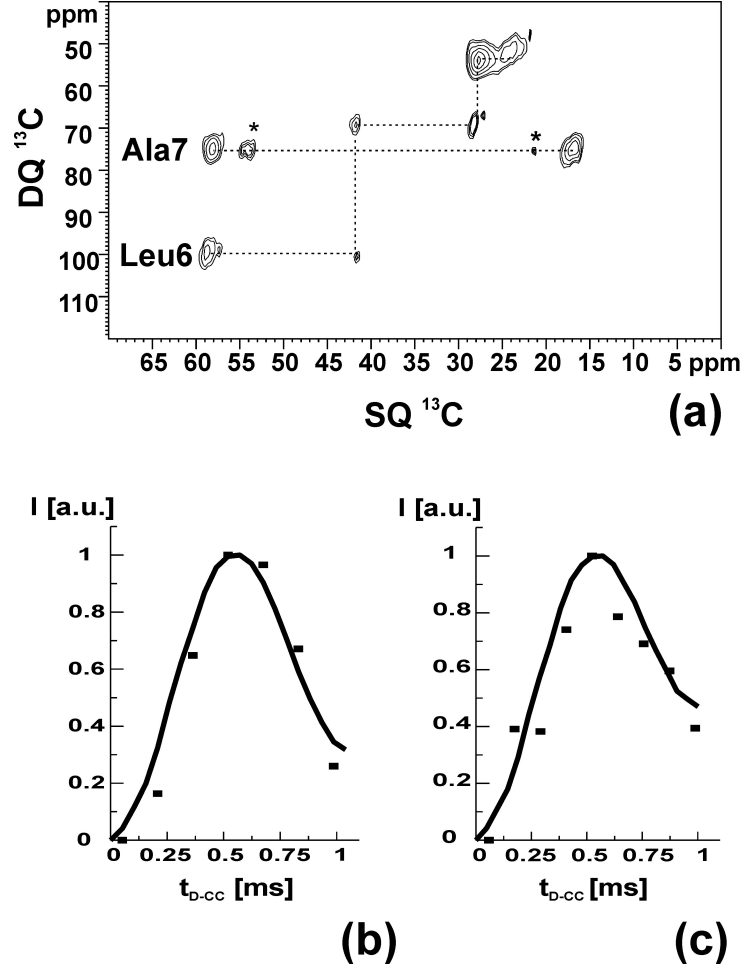


Figure 3.9:  $^{13}\text{C}$  DQ (POST-C7 sequence [171]) solid-state NMR spectroscopy of WALP23 in oriented DMPC lipid bilayers (5.5 kHz MAS, 600 MHz  $^1\text{H}$  field): (a) 2D  $^{13}\text{C}$  DQ/SQ spectrum (DQ excitation and reconversion times were set to 0.6 ms, 48  $t_1$  increments with 512 scans were recorded, spinning sidebands are indicated by asterisk). (b) Comparison between the experimental  $^{13}\text{C}$  DQ buildup of oriented WALP23 ( $^{13}\text{C}\beta$  peak of Ala7 is shown) and numerical predictions (solid line) assuming a  $^{13}\text{C}\alpha - ^{13}\text{C}\beta$  distance of 1.5 Å,  $\beta_{D-CC} = 55^\circ$  and a Gaussian spread  $\Delta$  of  $\pm 8^\circ$ . (c)  $^{13}\text{C}$  DQ buildup of WALP23 in randomly oriented liposomes.

In line with the theoretical and numerical analysis, the ( $^{13}\text{C}\alpha$ ,  $^{13}\text{C}\beta$ ) DQ recoupling for  $M = 1$  is - within the limits of the experimental sensitivity - identical for both preparations and indicates that the transfer dynamics are not sensitive to the macroscopic sample orientation.

Figure 3.9 (a) shows the 2D DQ/SQ spectrum obtained on the oriented sample and has been used to confirm  $^{13}\text{C}$  assignment, following the specific spin network connectivity of each labeled residue Leu6 and Ala7. The  $^{13}\text{C}\alpha$  and  $^{13}\text{C}\beta$  chemical shifts of both residues have been used to probe the local backbone conformation.

Calculation of secondary chemical shifts for both residues [86] indicates an  $\alpha$ -helical conformation. A subsequent structural analysis based on TALOS [93] predicts the  $\alpha$ -helical backbone torsion angles:  $\Phi = -66.85^\circ \pm 6.79^\circ$ ,  $\Psi = -41.24^\circ \pm 8.63^\circ$  for Leu6 and  $\Phi = -68.8^\circ \pm 15.37^\circ$ ,  $\Psi = -18.26^\circ \pm 31.67^\circ$  for Ala7 (see Figure 2.10).

As can be easily noticed, DQ spectroscopy selects only the signal of the  $^{13}\text{C}$  labeled peptide while natural abundance  $^{13}\text{C}$  of lipids or polymer are filtered out. Furthermore, experimental buildups (data not shown) of the  $^{15}\text{N} - ^{13}\text{C}\alpha$  cross polarization for  $M = 1$  condition show no dependence on the orientation.

In Figure 3.10, the use of  $^{13}\text{C}$  encoded  $^{15}\text{N}$  CSA dephasing experiment (Figure 3.6) is demonstrated whenever  $^{13}\text{C}$  resonance assignments (obtained from Figure 3.9 (a)) are available and an additional  $^{15}\text{N}$  evolution dimension such as used for AGG is not necessary ( $t_1 = 0$  in Figure 3.6) or precluded by signal to noise considerations.

In the case of U- $[^{13}\text{C}, ^{15}\text{N}]$ -Leu6,Ala7 labeled WALP23, two 1D experiments for  $^{15}\text{N}$  CSA dephasing times of 0 ms and 0.55 ms are shown. In both cases, the application of a DQ  $^{13}\text{C}\alpha - ^{13}\text{C}\beta$  transfer (SPC5 DQ sequence, [175]) was used to detect  $^{13}\text{C}\beta$  resonances that are unambiguously resolved ( $^{13}\text{C}\alpha$  signals of Leu6 and Ala7 overlap). For each residue, the relative ratio of  $^{13}\text{C}\beta$  signals is determined by orientation dependent  $^{15}\text{N}$  signal modulation, leading to similar tilt angle as previously obtained [161, 162].

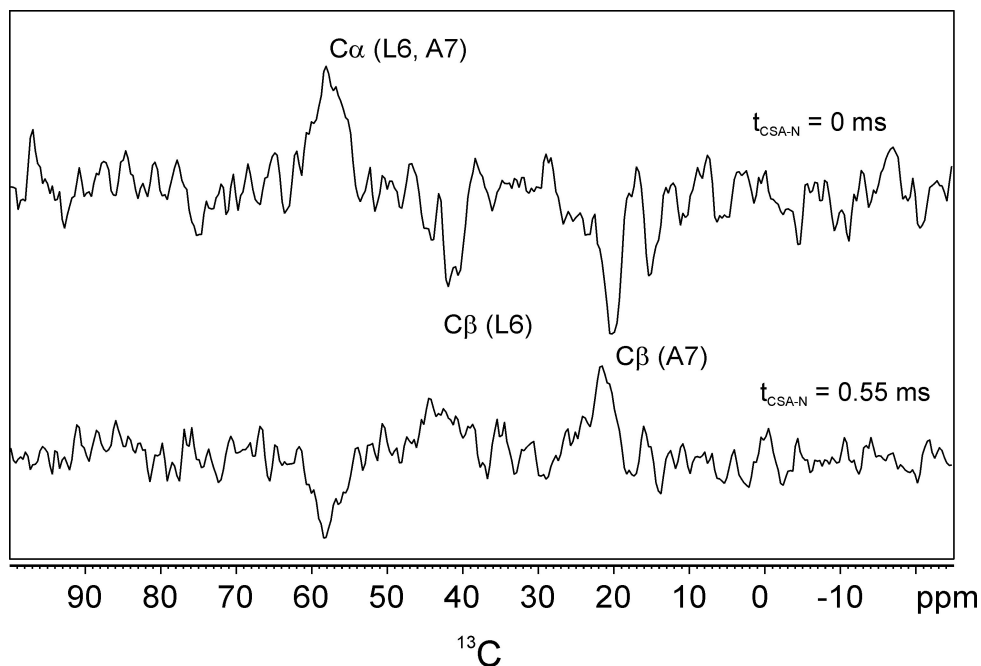


Figure 3.10: Structure and orientation of WALP23 in DMPC lipid bilayers:  $^{13}\text{C}\alpha$  and  $^{13}\text{C}\beta$  chemical shifts are indicative of secondary structure, while signal intensities detected after 0 ms and 0.55 ms  $^{15}\text{N}$  CSA dephasing times probe orientation (in Figure 3.6:  $t_1 = 0$ ,  $\text{CSA} = R18_2^5$ ,  $\text{NC} = \text{SPECIFIC CP}$  (4 ms),  $\text{CC} = \text{DQ SPC5}$  (0.8 ms)). For each spectrum 48k scans were recorded at  $-15^\circ\text{C}$ , 6 kHz MAS and 600 MHz  $^1\text{H}$  magnetic field.

### 3.7 Conclusions

A general approach to study membrane proteins in oriented lipid bilayers under fast magic angle spinning has been introduced. The presented methods simultaneously yield structural constraints for the local backbone conformation and the overall orientation of the polypeptide interacting with a model membrane environment. Notably, both structural parameters can be probed separately within the same NMR scheme.

The advantages of fast MAS scheme relate to increased resolution, signal-to-noise and possibility to work with multiply or uniformly labeled proteins as compared to previous methods that study oriented samples at slow MAS [151]. From analysis of spinning sidebands in the last case, proteins that are labeled to only one position can be investigated.

Moreover, the presented NMR method can be readily extended to include techniques that measure non-trivial structural constraints under MAS conditions from ( $^1\text{H}$ ,  $^1\text{H}$ ) transfer steps [105, 108], from monitoring the dephasing of multiple-quantum coherence or by determining internuclear distances using chemical shift-selective transfer methods [65, 179, 180].

The accuracy with which the molecular orientation can be detected depends on experimental parameters such as overall sensitivity and the molecular symmetry. The numerical analysis presented in § 3.3 suggests that the polypeptide orientation in the membrane can be determined with an accuracy of  $\pm 10^\circ$  throughout the entire range of  $\theta \in [0^\circ, 90^\circ]$ .

The precision could further be improved by a combined analysis of several residues in a multiply-labeled peptide or by incorporating structural constraints obtained from an analysis of the dipolar  $^{15}\text{N} - ^1\text{H}$  interactions. The same approach also permits restriction of the number of possible solutions in cases where a cylindrical symmetry around the azimuthal angle  $\varphi$  cannot be assumed (see Figure 3.4). In principle,  $^{15}\text{N}$  dephasing curves could be individually monitored for different residues of a uniformly labeled peptide, by performing a series of 2D  $^{15}\text{N}/^{13}\text{C}$  experiments at various CSA recoupling times, as shown in Figure 3.10.

Similar to experiments that rely on the structural analysis of  $^{15}\text{N}$  resonance shifts and  $^{15}\text{N} - ^1\text{H}$  dipolar couplings in static aligned samples [155, 156, 118], the data interpretation must in general include mosaic spread effects. Both static and MAS methods for oriented samples rely on previous knowledge of the  $^{15}\text{N}$  CSA PAS values and orientation relative to the peptide plane.

The discussed concept permits structural studies using a single NMR sample and can be probed in a standard MAS setup. Using the alignment technique proposed by Bechinger et al. [24], oriented samples can be readily prepared and the functional dependence of the NMR data resulting from the proposed r.f. schemes is particularly sensitive to molecular orientations at or close to the membrane normal, a situation most likely to occur for trans-membrane segments of ion channels, pumps, transporters or G-protein coupled receptors.

# Chapter 4

## Structure and dynamics of free and bound Phospholamban

### 4.1 Introduction

Phospholamban (PLN) is a 52-residue membrane protein<sup>1</sup> that plays an important role in regulating cardiac contractility. It is abundantly found in the membrane of the sarcoplasmic reticulum (SR) of myocytes where it modulates the activity of the sarco-endoplasmic reticulum Ca-ATPase (SERCA2a) in response to  $\beta$ -adrenergic stimuli. Hence, it influences the kinetics of cytosolic calcium ( $[Ca^{2+}]_i$ ) transients during the cardiac cycle [181]: at submicromolar diastolic  $[Ca^{2+}]_i$  concentrations, PLN binds to and inhibits SERCA2a, while for micromolar systolic  $[Ca^{2+}]_i$  levels the complex dissociates and the inhibition is relieved. Physiologically, the inhibition is two- to three-fold diminished by the phosphorylation of Ser16 (PKA) or Thr17 (Ca<sup>2+</sup>/CAM kinase) residues of PLN in conditions of  $\beta$ -adrenergic stimulation, thus enhancing the relaxation rate (*lusitropic effect*) and contractility (*positive inotropic effect*) of the cardiac muscle. The particular

---

<sup>1</sup>Primary sequence of human PLN: MEKVQYLTRS AIRRASTIEM PQQARQKLQN LFINFCLILI CLLLICIIVM LL

position of PLN at the intersection of two major signal-transduction pathways ( $\text{Ca}^{2+}$  and  $\beta$ -adrenergic) in myocytes makes correct PLN function critical for the cardiac cycle<sup>2</sup>.

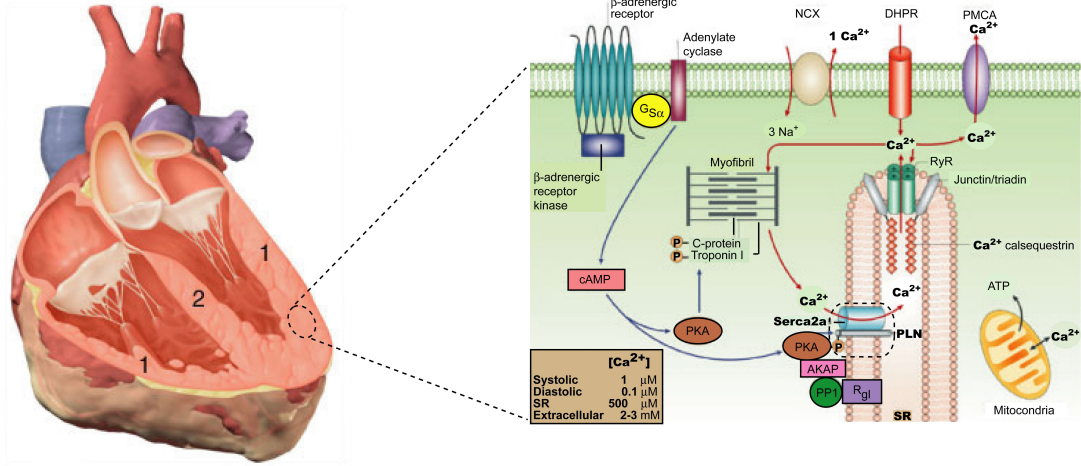


Figure 4.1: Heart function and calcium regulation: PLN is at the intersection of two major signal transduction pathways  $\text{Ca}^{2+}$  (red) and  $\beta$ -adrenergic (blue) (modified from [181]).

In humans with a PLN-null genotype early-onset *dilated cardiomyopathy* has been documented [181]. On the other hand, super-inhibitory (mutated) forms [182] or less phosphorylated PLN [181] are involved in *hypertrophied cardiomyopathy*. Hence, in these cases controlling PLN-SERCA2a interaction is thought to be a possible treatment for heart failure and prevent myocardial remodeling.

Structural studies of the PLN-SERCA2a complex are a prerequisite for a *rational drug design*. To date, no high resolution structure of SERCA-PLN has been reported. At first, knowledge about the non-interacting partners is required. Here, I present a new strategy developed for MAS solid-state NMR to study structure and dynamics of free phospholamban in lipid membranes close to physiological conditions. The proposed method can be of wider applicability in the context of membrane proteins or protein fibrils. Finally, SERCA-bound PLN is investigated and compared to the free PLN.

<sup>2</sup>Either loss or gain of the PLN inhibitory role is able to severely impair heart function [181, 182].

## 4.2 Existing models of free PLN

According to biochemical assays (i.e., SDS-PAGE), wild-type phospholamban associates through a '*leucine zipper*' into homopentamers [183, 184], believed to be the storage form of PLN in SR membranes and alternatively proposed to form a  $\text{Ca}^{2+}$  channel. On the other hand, the stoichiometry of the ATPase-activity [185, 186] indicates that monomeric form of PLN is responsible for the functional inhibition of SERCA. An equilibrium between the storage-pentameric pool and the inhibitory-monomeric form is supposed to exist in SR membranes. The equilibrium is influenced by many factors both *in-vivo* and *in-vitro*. The monomeric form can be stabilized in a fully functional form by mutating the three cysteines (Cys36, Cys41 and Cys46) into Ala36, Phe41 and Ala46 [187], resulting in the AFA-PLN mutant. To avoid the complicated situation of an inhomogeneous sample where different *multimers* would coexist, the AFA-PLN mutant was selected for this study.

From the analysis of the primary sequence it was suggested [181] that PLN is organized in three domains: (1) the cytosolic domain Ia (residues 1-20) largely hydrophilic and containing the phosphorylation sites, (2) the cytosolic domain Ib (residues 21-30) comprising many basic residues and (3) the highly hydrophobic transmembrane domain II (residues 31-52) that traverses the SR membrane. To date the only existing high-resolution structures, obtained by liquid-state NMR spectroscopy in organic solvents [188, 189] or micelles [190], indicate the existence of two  $\alpha$ -helical regions (residues 4-16 and 22-50) which are connected by a semiflexible  $\beta$ (III) turn (residues 17-21). Furthermore AFA-PLN in solution adopts an overall '*L-shape*' 3D fold with an average angle of approximately  $80^\circ$  between the two  $\alpha$ -helices, implying that the cytoplasmic PLN helix would be associated with the SR membrane when free and unbound to SERCA2a. The same '*L-shape*' has been derived [191] from ssNMR measurements of selectively labeled PLN in oriented lipid bilayers. The last conclusion is, however, based on very limited information (one labeled residue) and assumes rigid-body dynamics for domain Ia. On



the other hand, mutagenesis studies [192] that do not show an  $\alpha$ -helical pattern in the cytoplasmic domain and biophysical measurements [193, 187] performed under more appropriate lipid membrane conditions imply that PLN dynamics of domain Ia play an important role in the functional interaction of PLN with Ca-ATPase. Evidence that the cytoplasmic domain of PLN may indeed adopt, at least transiently, an unstructured conformation when reconstituted in lipid membranes comes from a large number of different spectroscopic techniques such as FTIR on wild type PLN [194], FRET [195] or EPR measurements of selectively spin-labeled AFA-PLN mutants [196]. Results of the latter experiments suggest that the cytoplasmic domain of AFA-PLN exists in a dynamic equilibrium between a moderately stable conformation (supposedly  $\alpha$ -helical) and a significantly populated unstructured ensemble. To answer which of the currently existing models describe the structure of PLN, I conducted solid-state NMR experiments on uniformly labeled PLN in lipid bilayers.

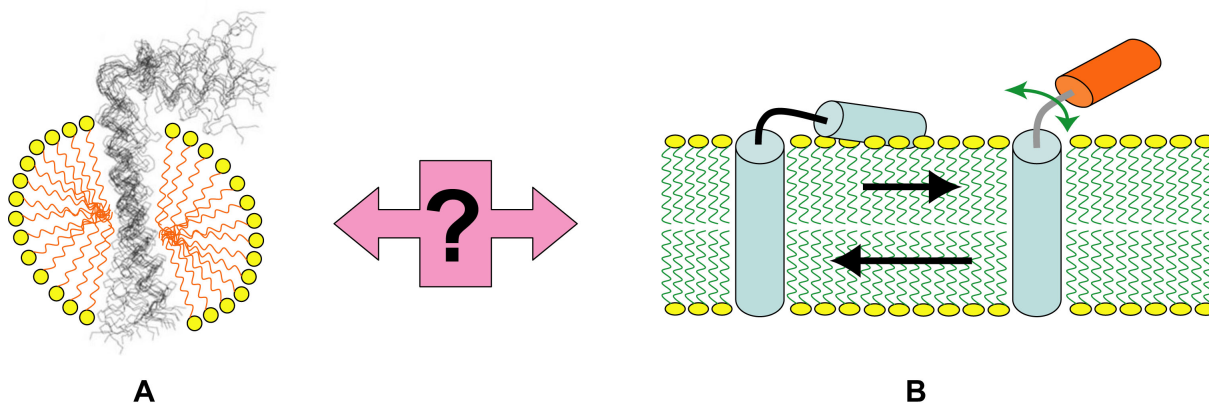


Figure 4.2: Models for dynamics and structure of phospholamban: (A) '*L-shape*' according to liquid-state NMR in DPC micelles, (B) two different dynamical populations for the cytoplasmic domain probed by EPR in DOPC lipid membranes.

## 4.3 Dynamics-based spectral editing

Previous solid-state NMR studies on PLN have used specifically labeled samples to probe either local secondary structure elements under MAS [197, 198] or domain orientation in static, macroscopically aligned samples [191]. PLN dynamics have also been investigated by relaxation rates in liquid-state NMR [199] or by a lineshape analysis of the anisotropic  $^2\text{H}$  quadrupolar interaction in solid-state NMR [200, 201].

Traditionally, solid-state NMR has been more focused on measuring dynamics at selected sites mainly by  $^2\text{H}$  quadrupolar interaction of methyl groups [123, 124]. More recently, the influence of dynamics on relaxation has been also exploited by including a transverse relaxation filter in a CP experiment [202] and applied onto membrane proteins labeled by residue-type.

Here, a general methodology for multidimensional MAS solid-state NMR on uniformly [ $^{13}\text{C}$ ,  $^{15}\text{N}$ ] labeled membrane proteins reconstituted in hydrated liposomes is proposed to probe structure and dynamics along the complete polypeptide sequence. The strategy is believed to be advantageous especially in the presence of fast (ns) and large amplitude motions.

The sample has been prepared following standard procedures for membrane protein lipid reconstitution as detailed in [111]. In particular, different L/P ratios (20:1 and 100:1) and different lipids (DMPC-D67 or 4:1 mixture of DOPC/DOPE) have been investigated. All measurements have been done in the liquid crystalline phase at temperatures of 30 °C (DMPC) or 5 °C (DOPC/DOPE). The results are similar and in the following those obtained for DMPC reconstitution are presented. A comparison between different sample preparations is given in Appendix C.4.

For the study presented in the following, two extreme cases can be imagined that form the principle of *dynamics-based spectral editing*<sup>3</sup>.

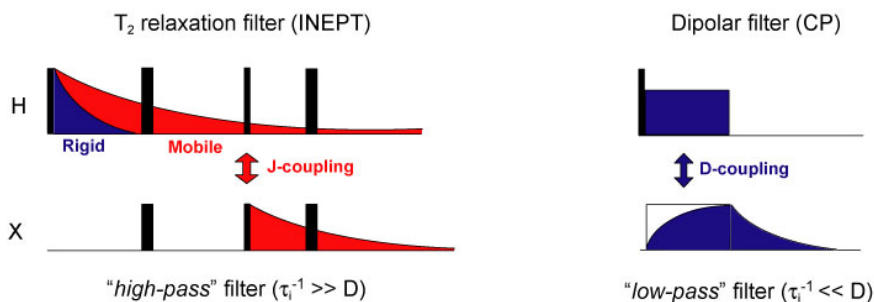


Figure 4.3: Principle of dynamics-based spectral editing: (1) the fast decaying signal (blue) of rigid protons is filtered-out during INEPT [126] and only the slow relaxing signal (red) resulting from mobile  $^1\text{H}$  is selected  $\rightarrow$  'high-pass' filter, while (2) during CP [55] only the signal from rigid  $^1\text{H}$  is efficiently transferred  $\rightarrow$  'low-pass' filter.

Dynamics are very important for  $^1\text{H}$  dipole-dipole interactions that provide the most efficient transverse relaxation mechanism and can not be completely suppressed by MAS for rigid solids. In the presence of fast (ns) and large amplitude motions of a protein domain the dipolar interactions are considerably reduced while the scalar-couplings are unaffected. When combined with MAS, the transverse relaxation times (see Equations 2.15-2.16) are improved to a value where J-coupling based INEPT [126] polarization-transfer becomes possible and in the same time dipolar-coupling based CP [55, 56] (§ 2.3.2) or recoupling methods (§ 2.3.3) of solid-state NMR are largely inefficient. On the other hand for rigid domains in the absence of fast overall isotropic molecular tumbling, the dipolar-couplings are preserved, allowing solid-state NMR transfers. These two mutually excluding dynamical regimes provide a straightforward way for signal filtration and spectral editing.

<sup>3</sup>In addition, an intermediate dynamic regime can exist and may be probed by a 'band-pass' filter that combines a  $^1\text{H}$   $T_2$  filter with long CP such as used in [202, 113].

In the case of PLN, direct experimental evidence of the mechanisms described above results by comparing the  $^{13}\text{C}$ -detected 1D spectra obtained with different excitation schemes, CP or INEPT, for the same sample under identical experimental conditions.

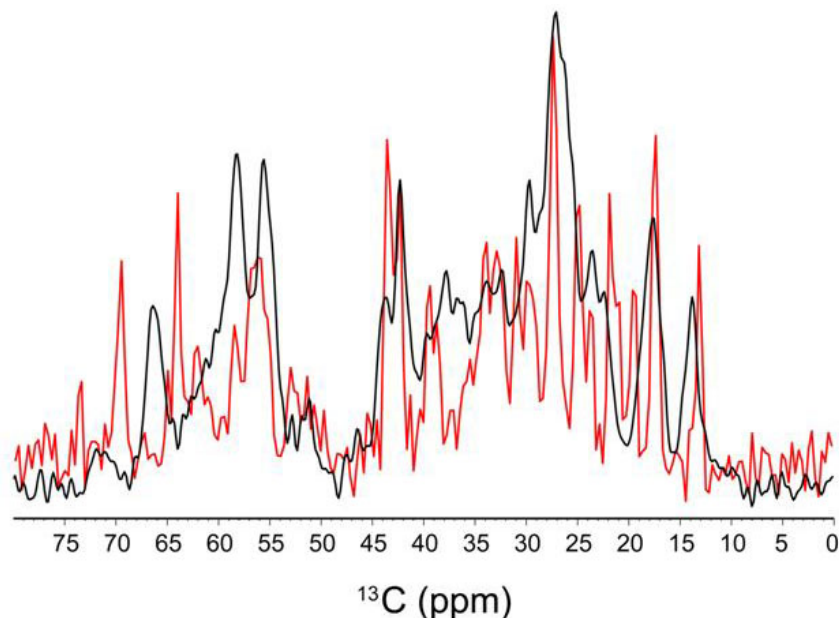


Figure 4.4: Overlay of  $^{13}\text{C}$ -detected 1D spectra of U- $[^{13}\text{C}, ^{15}\text{N}]$  AFA-PLN in DMPC-D67 hydrated lipid bilayers recorded at 30 °C, 600 MHz  $^1\text{H}$  Larmor frequency and 11 kHz MAS with CP (black) or INEPT (red) excitation, respectively (both spectra were processed the same way).

Different signals are obtained, and specially in the  $^{13}\text{C}\alpha$  region ([70 – 45] ppm) this is indicative of different residue types and, or backbone conformation. In addition, natural abundance  $^{13}\text{C}$  signal from lipids can contribute differently in the two experiments. However, the differences in the 1D experiments may result also from selection of peptide populations with different mobility (as pointed out by EPR) that could coexist for example in situations such as incorrect reconstitution of membrane protein into liposomes or protein aggregation. In the next section it is proven how scalar-coupling based polarization transfers and solid-state NMR recoupling methods can be combined and applied to the same sample.

## 4.4 Multidimensional experiments

A complete set of multidimensional double- and triple-channel NMR experiments can be designed for (1) residue type identification, (2) sequential assignment and (3) long range distance-constraints of mobile membrane protein segments under MAS solid-state NMR conditions.

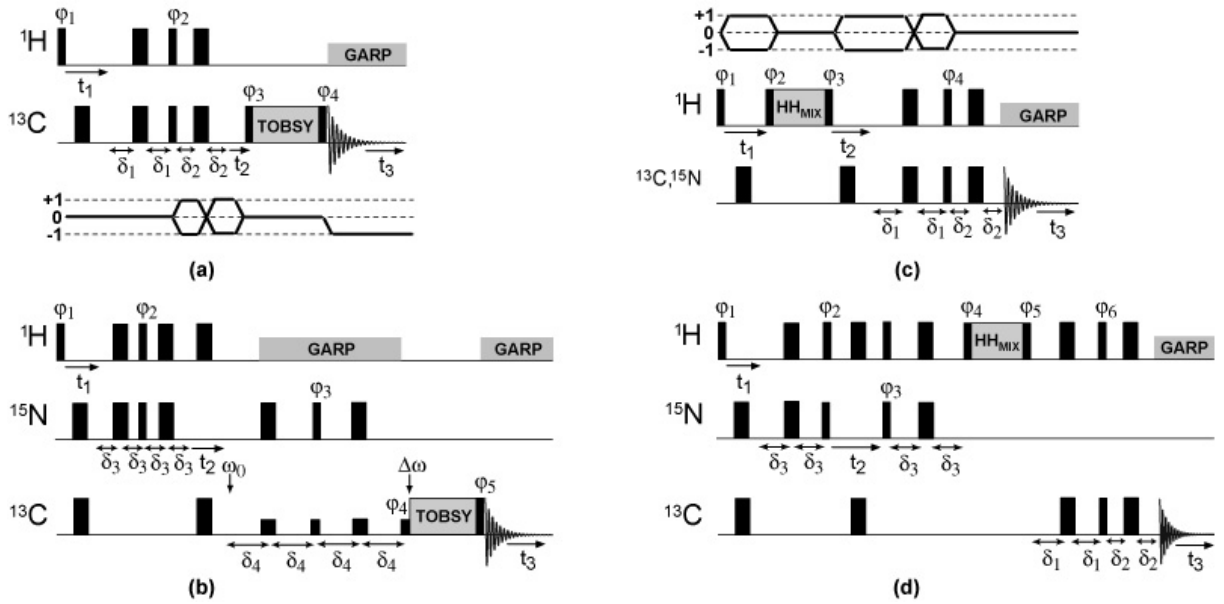


Figure 4.5: Double- and triple-channel pulse sequences for multidimensional NMR experiments to detect mobile protein segments under MAS conditions: (a) HCC for residue type identification, (b) HNCACB or HNCOCACB for sequential assignment, (c) HHC or HHN and (d) HN(HH)C or HC(HH)C for long-range distance constraints. Narrow and wide black rectangles correspond to  $90^\circ$  and  $180^\circ$  pulses, respectively. Indicated phases  $\phi_i$  are cycled in steps of  $180^\circ$ , except for  $\phi_4$  in (a) and  $\phi_5$  in (b) that are cycled in steps of  $90^\circ$  (coherence transfer pathways are shown for  $^{13}\text{C}$  (a) and  $^1\text{H}$  (c)). Refocused INEPT is used to obtain in-phase signals with the spin-echo delays given by the one bond J-couplings:  $\delta_{1,3,4} = 1/(4 \times {}^1J_{\text{HC,HN,NC}})$  or  $\delta_2 = 1/(6 \times {}^1J_{\text{HC}})$ . Bruker pulse programs are given in Appendix C.1.

HCC, HNCACB and HNCOCACB experiments depicted in Figure 4.5 (a,b) employ only *'through-bond'* couplings and combine hetero-nuclear polarization transfer (i.e. refocused INEPT [126]) with MAS synchronized solid-state NMR sequences for homo-nuclear mixing (i.e. TOBSY [203, 127]). The latter mixing scheme minimizes artifacts due to residual dipolar couplings as might result for proteins that exhibit localized domain dynamics in the absence of overall isotropic molecular tumbling. Long-range, *'through-space'* distance constraints from HHC, HHN, HN(HH)C or HC(HH)C experiments<sup>4</sup> shown in Figure 4.5 (c,d) can be obtained via NOESY [104, 204] cross-relaxation mediated  $^1\text{H} - ^1\text{H}$  magnetization exchange. The presented pulse sequences are designed for heteronuclei detection as opposed to proton detection in liquid-state NMR. This is mainly due to the poor water suppression on probe-heads that are not equipped with gradients, conventionally most of solid-state probe-heads being optimized for  $^{13}\text{C}$  detection. Although  $^{13}\text{C}$  detection has lower sensitivity compared to  $^1\text{H}$  detection, a benefit could be the increased spectral dispersion of the  $^{13}\text{C}$  dimension. Because of the  $^{13}\text{C} - ^{13}\text{C}$  scalar couplings, splitting of the resonances can occur, with the largest effect on the  $^{13}\text{C}'$  peaks. In special cases where water suppression or relaxation is favorable,  $^1\text{H}$  detection can be employed.

Homo-nuclear  $^{13}\text{C} - ^{13}\text{C}$  through-bond mixing without reintroduction of dipolar couplings has been demonstrated [203, 127] for rigid rotating solids. Recent implementations [205] based on the symmetry principles have robust broad-band transfer. In particular the  $P9_3^1$  sequence [205] was selected for the TOBSY unit because it shows good performance in the 5-10 kHz MAS regime with regard of both r.f. power deposition ( $\omega_{r.f.} = 6 \times \omega_{MAS}$ ) and transfer efficiency. An INADEQUATE [206] type of transfer as in liquid-state NMR was not successful because of unfavorable  $^{13}\text{C}$  relaxation times. Due to the weak  $^1\text{H}$  dipolar interactions and the high  $^{13}\text{C}$  r.f. fields applied (50 kHz at 8.333 kHz MAS) proton decoupling during TOBSY is not necessary. Moreover only low-power

---

<sup>4</sup>Conventional notation from liquid-state NMR has been adopted, where nuclei inside brackets have no evolution and are used only as relay nuclei.

(10 kHz)  $^1\text{H}$  decoupling with GARP sequence [207] for the J coupling interaction was necessary during acquisition or  $^{15}\text{N} - ^{13}\text{C}$  INEPT. Most experiments have been realized at 8.333 kHz MAS due to the easy setup and sustainable long-time power deposition on the sample and the r.f. coil during the TOBSY unit. For MAS rates in the range 5-10 kHz an improvement in the line-width can not be detected, although a slight improvement in signal-to-noise ratio ( $\approx 5\%$ ) can be observed due to better polarization transfer efficiency during the INEPT steps. The signal-to-noise ratio is considerably increased ( $\geq 50\%$ ) for fast spinning (10 kHz) when compared to slow (1 kHz) or non-spinning conditions.

A critical issue is the specific  $^{15}\text{N} - ^{13}\text{C}'$  or  $^{15}\text{N} - ^{13}\text{C}\alpha$  INEPT transfer. To obtain the selective transfer, weak (10kHz) pulses are applied on resonance ( $\omega_0$ ) for  $^{13}\text{C}'$  or  $^{13}\text{C}\alpha$ . The  $^{13}\text{C}$  carrier is shifted ( $\Delta\omega$ ) in the middle of  $^{13}\text{C}' - ^{13}\text{C}\alpha$  region for the HNCOCACB experiment while it is kept unchanged in the HNCACB experiment. In the current implementation of the HNCACB experiment, the  $^{13}\text{C}\alpha$  signal of Glycine residues will appear anti-phase because it is the only residue type that has a primary  $^{13}\text{C}\alpha$ . However in the HNCOCACB all signals will be in-phase because for all residue types the  $^{13}\text{C}'$  are primary carbons. Also, due to additional relaxation during the  $^{15}\text{N} - ^{13}\text{C}$  transfers, less correlations might result than expected from the HCC experiment.

A last observation refers to the HHC experiment where intra-lipid crosspeaks can result in the presence of a large lipid background and have to be distinguished from intra-peptide transfers. However this experiment has the ability to probe either water exposure or lipid-protein contacts. When the  $^1\text{H}$  dispersion is limited or intra-protein crosspeaks overlap with intra-lipid ones, the experiment can be run as HN(HH)C or HC(HH)C ( $^{15}\text{N}$  or  $^{13}\text{C}$  edited NOESY in both dimensions).

Distinct molecular entities (either two dynamical PLN domains or populations and lipids) that may contribute differently to the 1D spectra of Figure 4.4 can be in detail analyzed by comparing a 2D  $^1\text{H}/^{13}\text{C}$ -INEPT heteronuclear spectrum (scalar-coupling) with a 2D  $^{13}\text{C}/^{13}\text{C}$ -DQ/SQ homonuclear spectrum (dipolar-coupling).

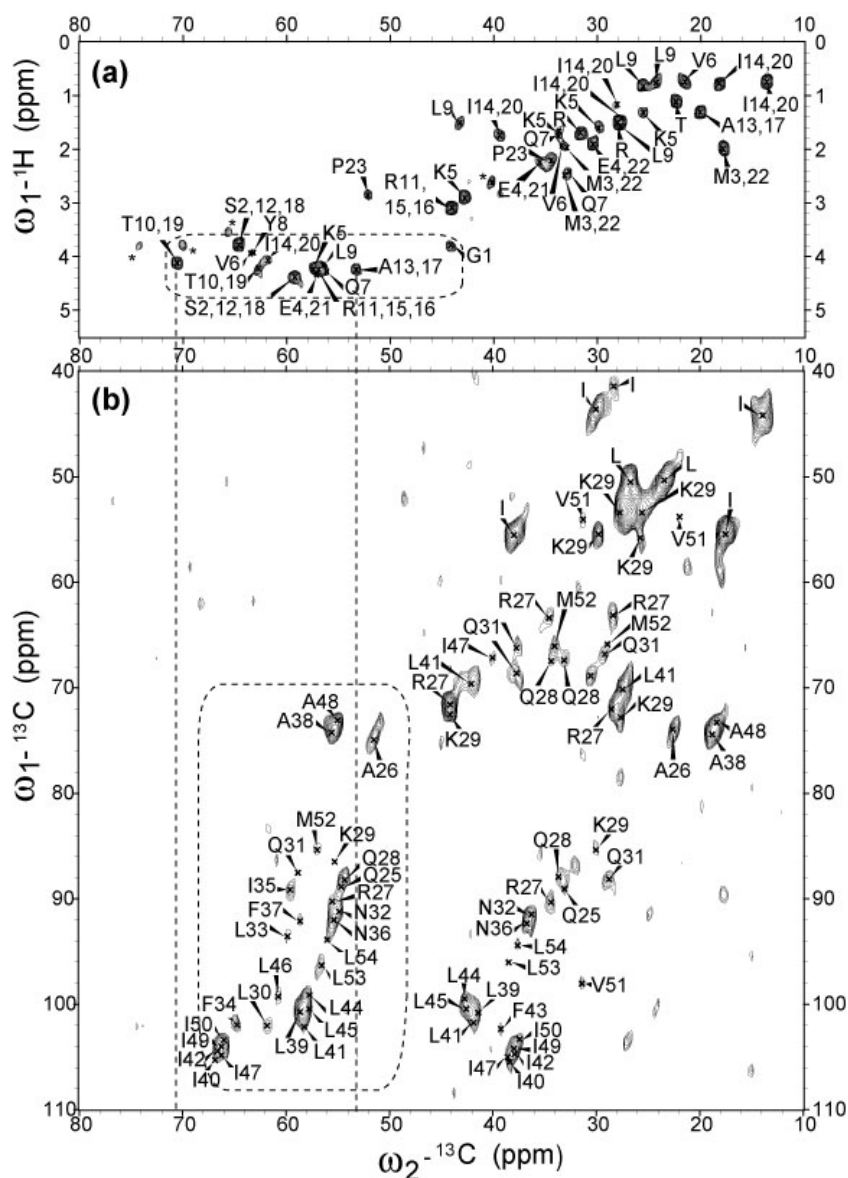


Figure 4.6: 2D spectra of U- $^{13}\text{C}$ ,  $^{15}\text{N}$ ] AFA-PLN in DMPC-D67 hydrated lipid bilayers (30 °C, 600 MHz  $^1\text{H}$  field): (a)  $^1\text{H}/^{13}\text{C}$ -INEPT ( $^1J_{\text{CH}} = 155$  Hz, 10 ppm  $^1\text{H}$  spectral width, 64  $t_1$ , 640 scans, 10kHz GARP decoupling, 9 kHz MAS) and (b)  $^{13}\text{C}/^{13}\text{C}$ -DQ/SQ ( $t_{\text{CP}} = 250$   $\mu\text{s}$ ,  $t_{\text{DQexc}} = t_{\text{DQrec}} = 534$   $\mu\text{s}$  SPC5 [175], 55  $t_1$  incremented by 1/4 rotor period, 1360 scans, 70 kHz SPINAL64 decoupling [208], 7.5 kHz MAS). FT: QSINE = 3.5 window function and linear prediction. Dashed lines point to different residue types (T) or shifts for the same residues (A), dashed boxes enclose the  $^{13}\text{C}\alpha$  regions, lipid contribution is marked as asterisk in (a).



Residues G, S, T, Y and P that are present only in the cytoplasmic domain Ia and have very characteristic  $^{13}\text{C}$  chemical shifts can be found only in the INEPT excited spectrum (Figure 4.6 (a)), while F residues, present only in the transmembrane domain, are obtained only in the CP-DQ excited spectrum (Figure 4.6 (b)).

Moreover, similar residue types such as A, I, L and V that are present in both domains and can be identified in both spectra. The existence of distinct  $^{13}\text{C}\alpha$  and  $^{13}\text{C}\beta$  shifts suggests different backbone conformations.

These results clearly speak in favor of a signal selection mechanism based on mobility of two different dynamical domains within the same PLN molecule, rather than the existence of different PLN populations.

Two other qualitative aspects in the spectra of Figure 4.6 (a,b) are also notable. As expected,  $^1\text{H}$  line widths are largely reduced and range between 0.15 ppm and 0.35 ppm in contrast to typical featureless lines of rigid solids. This is indicative of molecular mobility that leads to significant reduction of dipolar interactions and a concomitant increase in proton  $T_2$  relaxation times. However, the single-quantum  $^{13}\text{C}$  line widths (0.5 - 1 ppm) are comparable in the two experiments, confirming that MAS can provide high resolution solid-state NMR spectra for uniformly labeled  $^{13}\text{C}$  proteins.

Furthermore, intra-residue  $^{13}\text{C} - ^{13}\text{C}$  correlations for residue-type assignment are obtained with good resolution and dispersion in the 2D H(C)C experiment. When spectral overlap or resolution precludes unambiguous residue-type identification, the experiment can be performed as a 3D HCC. Slices from a 3D HCC spectrum are presented in Appendix C.2.

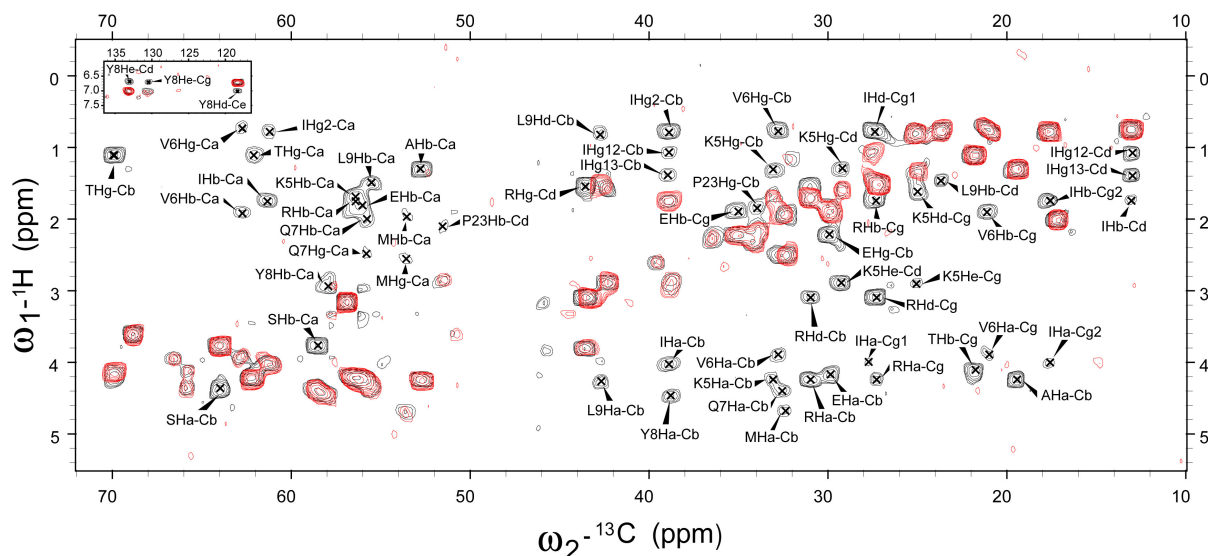


Figure 4.7: 2D H(C)C spectrum of U- $^{13}\text{C}$ ,  $^{15}\text{N}$ ] AFA-PLN in DMPC-D67 hydrated lipid bilayers recorded at 30 °C and 600 MHz  $^1\text{H}$  Larmor frequency:  $P9_3^1$  TOBSY for 6 ms and 50 kHz  $^{13}\text{C}$  r.f. field at 8.333 kHz MAS. Only the crosspeaks (black) resulting from the  $^{13}\text{C} - ^{13}\text{C}$  transfer are indicated. Overlaid in red is shown the 2D HC spectrum obtained with refocused INEPT (Figure 4.6 (a)). The aromatic region containing the Y8 crosspeaks is shown as an insert.

$^{15}\text{N}$  chemical shifts of each amino acid type can be further obtained from the 2D (H)NCACB experiment. Finally, the 2D (H)NCOCACB experiment correlates the  $^{15}\text{N}$  chemical shifts of each residue with the  $^{13}\text{C}$  chemical shifts of the preceding one. Particularly, narrow  $^{15}\text{N}$  line-widths (0.5 ppm) and good dispersion of the (H)NCOCACB spectrum allow a complete sequential walk along the backbone in the cytoplasmic domain using only 2D spectra. Where necessary, 3D implementations are straightforward and limited only by experimental time.

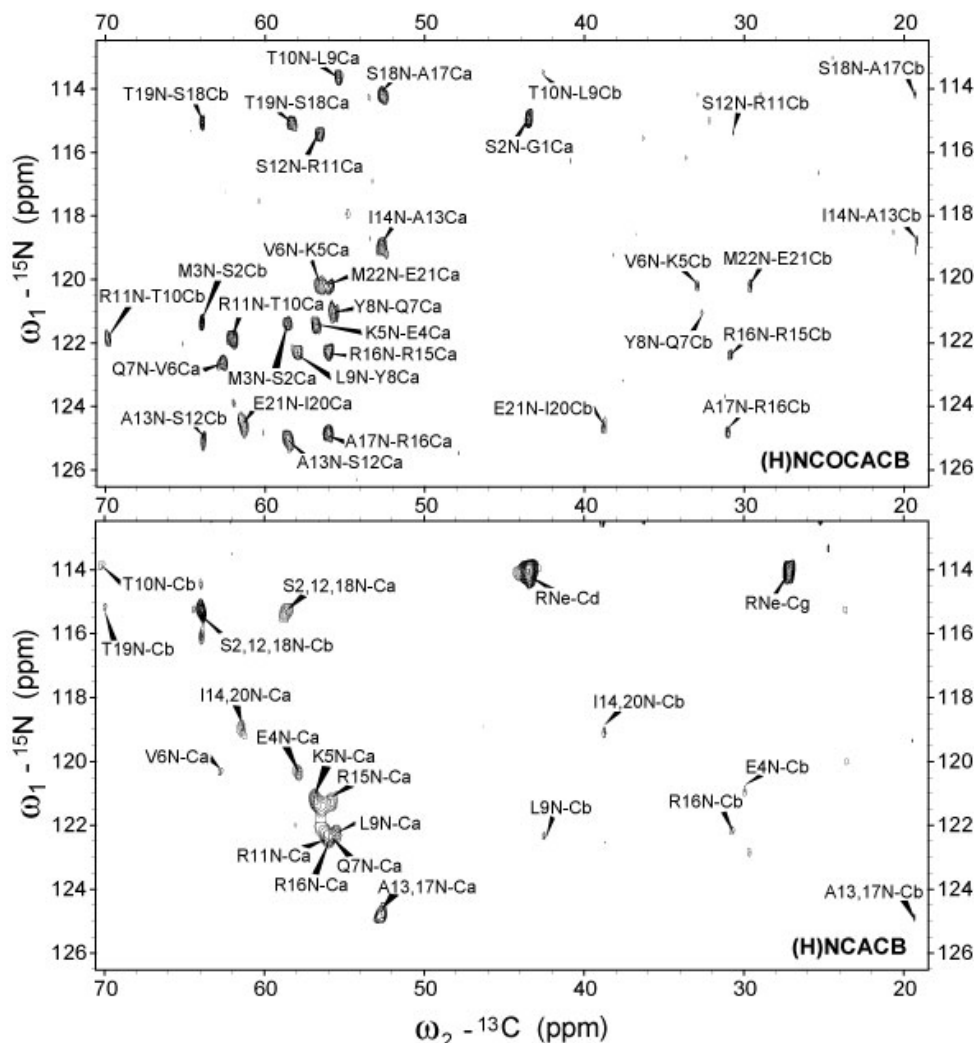


Figure 4.8: 2D (H)NCACB and (H)NCOCACB INEPT-TOBSY spectra (30 °C, 800 MHz  $^1\text{H}$  field, 8.33 kHz MAS):  $^1J_{\text{HN}} = 93$  Hz,  $^1J_{\text{NC}} = 19$  Hz, TOBSY mixing time of 6 ms and 8.5 ms for  $^{13}\text{C}\alpha - ^{13}\text{C}\beta$  and  $^{13}\text{C}' - ^{13}\text{C}\alpha/^{13}\text{C}\beta$  transfers, respectively.

Assignments for the transmembrane domain residues follow the same approach combining the 2D  $^{13}\text{C}/^{13}\text{C}$ -DQ/SQ from Figure 4.6 (b) with 2D NCA and NCOCA spectra obtained with SPECIFIC CP [170] for selective  $^{15}\text{N} - ^{13}\text{C}\alpha/^{13}\text{C}'$  heteronuclear-dipolar transfers and double-quantum  $^{13}\text{C}' - ^{13}\text{C}\alpha$  homonuclear dipolar transfer. Pulse sequences are provided in Appendix C.5, including Bruker pulse program for the 2D  $^{13}\text{C}/^{13}\text{C}$ -DQ/SQ experiment.

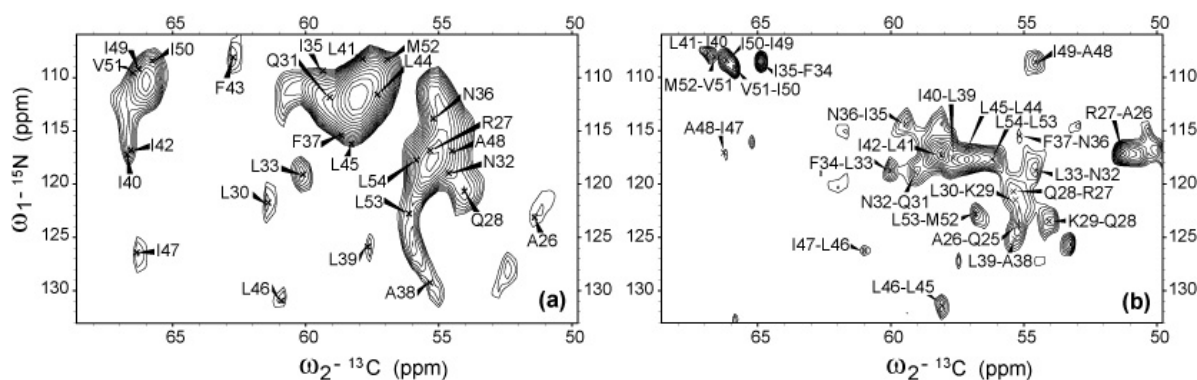


Figure 4.9: 2D NCA (a) and NCOCA (b) dipolar-coupling based spectra recorded at 30 °C, 600 MHz  $^1\text{H}$  Larmor frequency and 7.5 kHz MAS. Matched r.f. fields during SPECIFIC CP were 25 kHz ( $^{15}\text{N}$ ) and 17.5 kHz ( $^{13}\text{C}$ ) for 5 ms (NCA) or 3 ms (NCO), the  $^{13}\text{C}' - ^{13}\text{C}\alpha$  transfer was realized under DQ SPC5 conditions for 1.06 ms mixing time and 37.5 kHz  $^{13}\text{C}$  r.f. field.

The  $^{15}\text{N}$  line-width (1-2 ppm) in the dipolar-coupling spectra is considerable broader than the one resulting in the scalar-coupling spectra. Conformational heterogeneity or interference between proton decoupling and relaxation mechanisms can be responsible for increased line-width of  $^{15}\text{N}$  in the transmembrane domain. Also, for a mainly  $\alpha$ -helical conformation the dispersion of the  $^{15}\text{N}$  resonances is reduced. As a consequence of both increased spectral overlap and reduced resolution some ambiguity results for the sequential assignment of the transmembrane domain.

Through-space contacts can be probed for the cytoplasmic domain by employing the NOESY type experiments from Figure 4.5 (c,d). In particular the existence of an  $\alpha$ -helical conformation can be probed in the H(H)N experiment where  $H_{N(i+1)} - H_{N(i)}$  contacts are diagnostic for an  $\alpha$ -helix. The 2D HN spectrum ( $^{15}\text{N}$ -detected HSQC) is used as the finger-print of a protein in liquid-state NMR. When compared to the 2D H(H)N no crosspeaks supporting the existence of an  $\alpha$ -helical cytoplasmic domain are found.

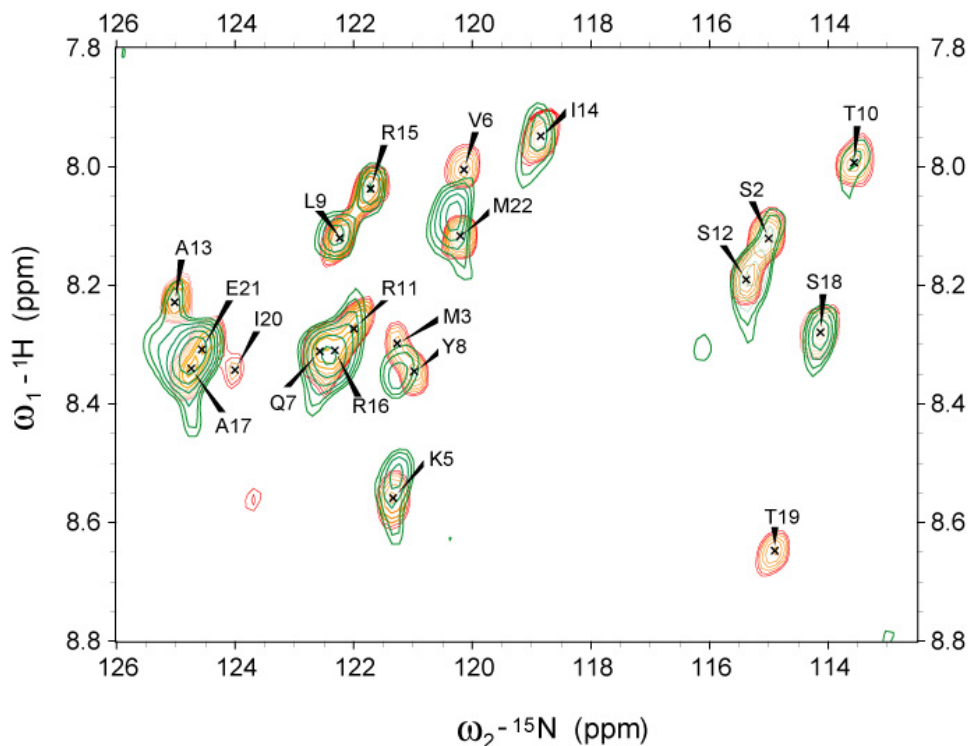


Figure 4.10: Overlay of the 2D HN-INEPT (red) and H(H)N INEPT-NOESY (green) spectra of free U- $^{13}\text{C}$ ,  $^{15}\text{N}$ ] AFA-PLN in DMPC-D67 hydrated lipid bilayers (30 °C, 800 MHz  $^1\text{H}$  field, 8.33 kHz MAS). No crosspeaks consistent with an  $\alpha$ -helix can be detected in the NOESY experiment (200 ms NOESY time).

To exclude possible spectral overlap in the 2D H(H)N spectrum and to probe different 3D folds of the cytoplasmic domain the H(H)C and (H)N(HH)C experiments have been used. In both experiments only trivial sequential contacts are obtained that are consistent with a highly dynamical and unstructured domain where a fixed long-range distance does not exist. In the 2D H(H)C experiment water-exchange crosspeaks (4.75 ppm  $^1\text{H}$ ) indicate that the cytoplasmic domain is located outside of the core of the lipid membrane and water exposed.

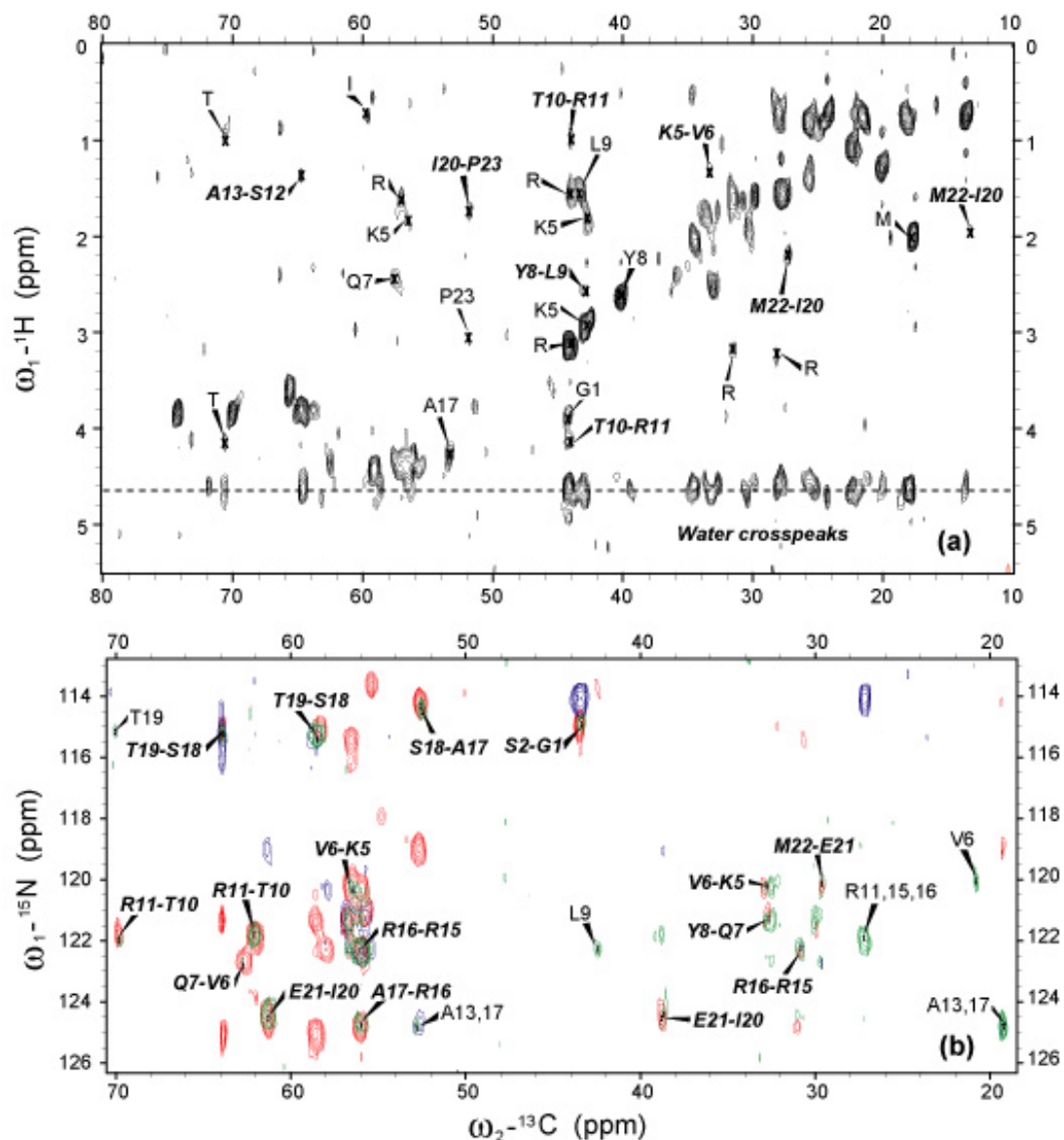


Figure 4.11: 2D NOESY experiments: (a) H(H)C with 300 ms  $^1\text{H} - ^1\text{H}$  mixing time, (b) (H)N(HH)C (green, 200 ms NOESY time) compared with 2D (H)NCACB (blue) and (H)NCOCACB (red). Water crosspeaks in (a) indicate water accessibility and in (b) the (H)N(HH)C is largely similar with the (H)NCOCACB, probing only sequential contacts (*italic*), as expected for an unstructured domain.

## 4.5 Analysis of structure and dynamics of free PLN

The assignments obtained for AFA-PLN in DMPC-D67 lipid bilayers are summarized in the table given in Appendix C.3. The  $^{13}\text{C}\alpha$  and  $^{13}\text{C}\beta$  chemical shifts sensitive to backbone conformation [92] are used to calculate the secondary chemical shifts ( $\Delta\delta = ({}^{13}\text{C}\alpha_{\text{exp}} - {}^{13}\text{C}\alpha_{\text{rc}}) - ({}^{13}\text{C}\beta_{\text{exp}} - {}^{13}\text{C}\beta_{\text{rc}})$ ) as defined for solid-state NMR purpose [86]. The  $\Delta\delta$  values are highly correlated with the secondary structure. In general positive deviations are found for  $\alpha$ -helices and negative values for  $\beta$ -sheets. A plot of the secondary chemical shifts along AFA-PLN backbone and comparison to the secondary structure obtained by liquid-state NMR in DPC micelles is shown below.

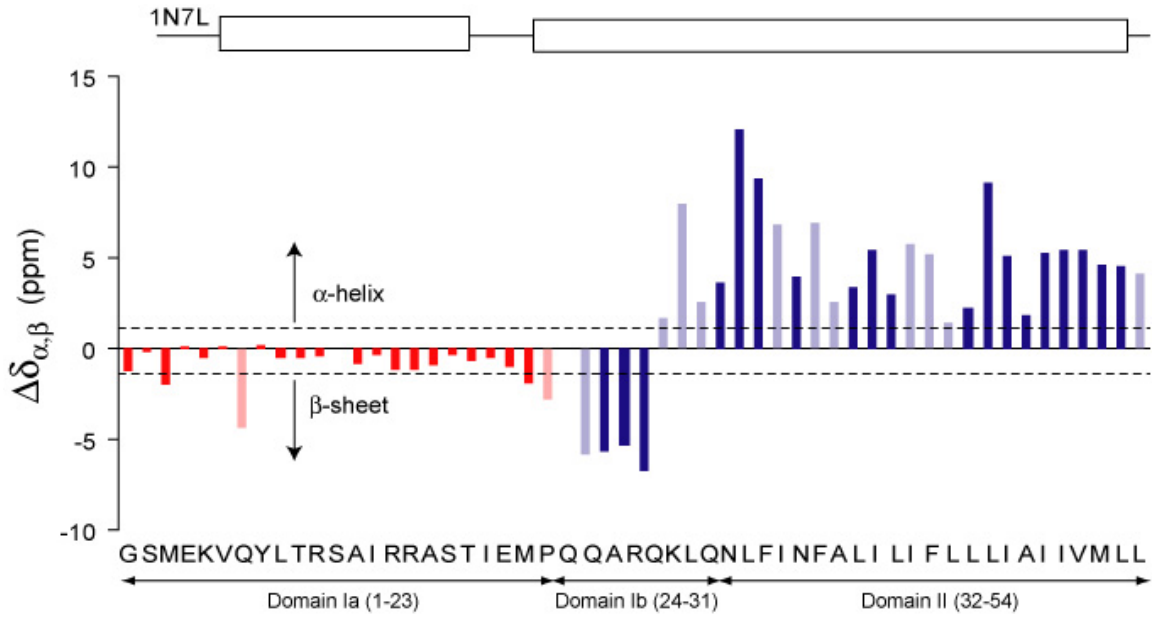


Figure 4.12: Secondary chemical shifts of AFA-PLN in DMPC-D67 hydrated lipid bilayers as obtained by solid-state NMR: red corresponds to mobile residues, blue to rigid residues, dark and light colors to ambiguous and unambiguous assignments, respectively, dashed lines at  $\pm 1$  ppm indicate cutoff values for  $\alpha$ -helix and  $\beta$ -sheet. Secondary structure of AFA-PLN in DPC micelles according to liquid-state NMR [190] is given above the plot with rectangles representing  $\alpha$ -helices.

For the cytoplasmic domain Ia (residues 1-23)<sup>5</sup>, mostly small and negative secondary chemical shifts are found. This can be expected for an unstructured and highly dynamic domain that can sample with equal probability the whole backbone conformational space. The  $\beta$ -sheet region of the Ramachandran plot is larger than the  $\alpha$ -helix region (see Figure 2.10) and on average the domain spends more time in the  $\beta$ -sheet conformation, resulting in  $\beta$ -sheet like chemical shifts [204]. In accord with the results of the NOESY experiments, this clearly indicates the lack of conformation and high dynamics for the cytoplasmic domain.

The transmembrane domain II (residues 32-54) is characterized by large and positive deviations from the random coil values which are consistent with a stable  $\alpha$ -helix. Interestingly, in the cytoplasmic domain Ib (residues 24-31) secondary chemical shifts have greater dispersion, with large negative (25-28) and positive (29-31) values. Notably, the values for the <sup>25</sup>QARQ<sup>28</sup> show  $\beta$ -sheet character in qualitative agreement to early FTIR experiments [194]. However, direct interpretation of the secondary chemical shifts in terms of secondary structure has to be carefully considered since two particular aspects of domain Ib can influence the observed values: (1) it contains many basic residues that are likely to be positively charged at neutral pH and (2) it traverses the water-lipid interface realized by the zwitterionic phosphocholine headgroups.

## 4.6 Structural model of free PLN

To construct a structural model of AFA-PLN in DMPC lipid bilayers, backbone dihedral angles predicted by the TALOS [93] program from the measured chemical shifts are combined with the NOESY constraints in a simulated annealing protocol of CNS [88] version 1.1 with the PROTEIN-ALLHDG parameter file [209]. Square-well potentials were employed to represent experimental constraints in the simulation (see Equation 2.14). No constraint force was applied for proton-proton distances below 5 Å, and back-

---

<sup>5</sup>GS residues are added to the domain numbering of [181]



bone torsion angle deviations from the TALOS prediction within a range given by the prediction RMSD for both angles (*'flat bottoms'*). As starting conformation for all simulations, an extended strand of AFA-PLN was generated from the amino acid sequence.

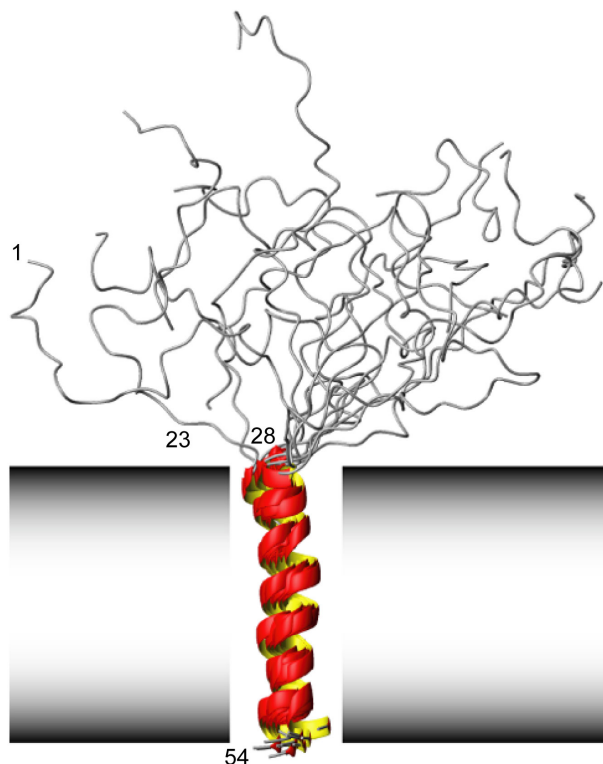


Figure 4.13: Structural model of AFA-PLN in DMPC lipid bilayers according to MAS solid-state NMR. While the transmembrane  $\alpha$ -helix (residues 30-53) is buried in the membrane, the cytoplasmic N terminus (residues 1-23) exhibits a high degree of molecular disorder and is in close contact to the aqueous environment. An ensemble of 15 lowest energy structures was selected to represent the molecular conformation of the PLN monomer.

The structure calculation protocol consisted of three stages: (1) High-temperature annealing in torsion angle space, in 2000 time steps of 0.015 ps at 50000 K. (2) Slow-cool annealing in torsion angle space, in 4000 steps of 0.015 ps, and temperature reduction from 50000 K to zero in steps of 250 K. (3) Final conjugate gradient minimization in 10 cycles of 200 steps each. Distance constraints were invoked by force constants of 300

kcal mol<sup>-1</sup> Å<sup>-2</sup> during annealing, and halved for conjugate gradient minimization. Ambiguities in the assignments of methylene and methyl protons were accounted for by sum averaging over all possible contacts. From the TALOS analysis, a total of 28 ( $\phi, \psi$ ) pairs of backbone angle constraints were included. A set of 200 structures was calculated starting with different initial velocities. Structures with a cytoplasmic domain that penetrates the lipid bilayer were excluded during the calculations. An ensemble of 15 structures with the lowest energy, which are in agreement with the membrane geometry, was selected to represent the molecular conformation of the PLN monomer. A stable transmembrane  $\alpha$ -helix and a highly disordered cytoplasmic domain results. The structures were aligned along backbone atoms of residues L30 to L53. In this ensemble, no distance or angle restraint violation of more than 0.2 Å or 2° occurred.

## 4.7 SERCA-bound PLN

Up to date no high resolution structure of PLN-SERCA complex is available. However, SERCA function and structure have been studied in detail and the main results are summarized in the following.

SERCA2a is a P-type ATPase [210, 211] responsible for removing 70% of myoplasmic calcium ( $[Ca^{2+}]_i$ ). Calcium translocation across the SR membrane is realized via an enzymatic cycle with six intermediates (see Figure 4.14 (b)). PLN is believed to bind in the E2 conformation of SERCA [212, 213]. PLN shifts the ATPase activity towards lower pCa values and, as a result, slows down calcium pumping. Activity test of the sample prepared for solid-state NMR investigation shows a typical inhibition curve (see Figure 4.14 (b)).

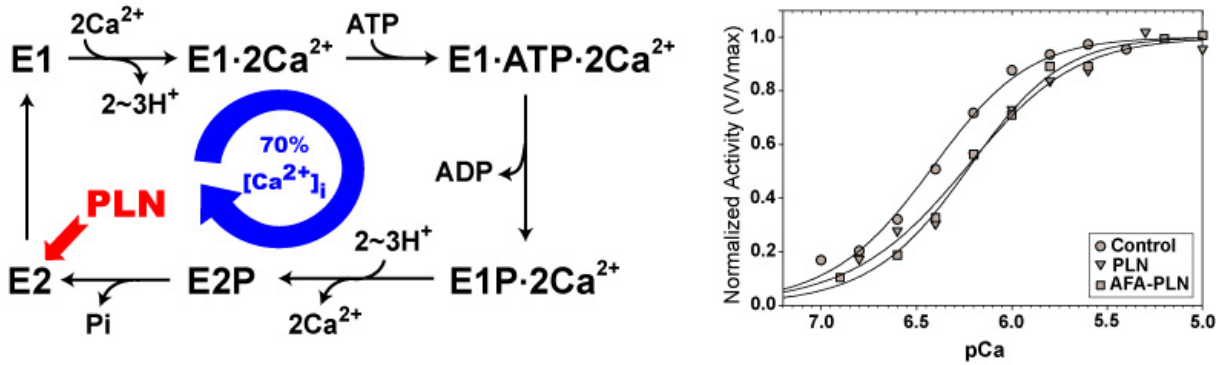


Figure 4.14: Function and regulation of SERCA: left - enzymatic cycle, SERCA pumps out 70% of internal calcium  $[Ca^{2+}]_i$ , PLN is believed to bind to SERCA in E2 state; right - activity test of the sample prepared for solid-state NMR study.

The skeletal muscle isoform of Ca-ATPase (SERCA1a) has been recently structurally characterized by X-ray crystallography in different intermediate states [214, 215] and serves as a model for SERCA2a. According to these, SERCAs(1a,2a) are large membrane proteins (110 kDa, approx. 1000 residues) with a complex molecular architecture organized in a transmembrane (TM) domain of 10 helices (M1-M10) and three cytoplasmic domains: a nucleotide binding domain (N), a phosphorylation domain (P) and an actuator domain (A). Four of the TM helices (M2-M5) extend into the cytoplasm to form the 'stalk', connecting TM with A and P domains.

Calcium pumping is accompanied by major structural changes: (1) two  $Ca^{2+}$  binding sites are provided by residues of M4, M5, M6 and M8, the movement of helix M4 is essential during translocation, (2) the compact cytoplasmic head (N,A,P) opens upon  $Ca^{2+}$  binding, domain A undergoing the largest reorientation during the cycle. A proton ( $H_3O^+$ ) countertransport is postulated to take place.

The PLN transmembrane domain (II) has been cross-linked to M2 and M4, suggesting a possible binding site for PLN and a mechanism for inhibition of calcium transport. A similar reaction has been shown between the PLN cytoplasmic domain (Lys3) and the N domain (Lys400) of SERCA [216]. Attempts to obtain more precise structural

information about the complex have been made using cryo-EM [217, 218], but have failed to identify PLN. Also, the complex has resisted crystallization efforts for X-ray. Recently, mapping of the interaction surface has been tried through liquid-state NMR by titrating SERCA together with AFA-PLN [219]. The observed chemical shift perturbations of the exchangeable PLN (an intermediate between unbound and bound state) have been mapped onto an existing molecular dynamics (MD) model of the complex [213].

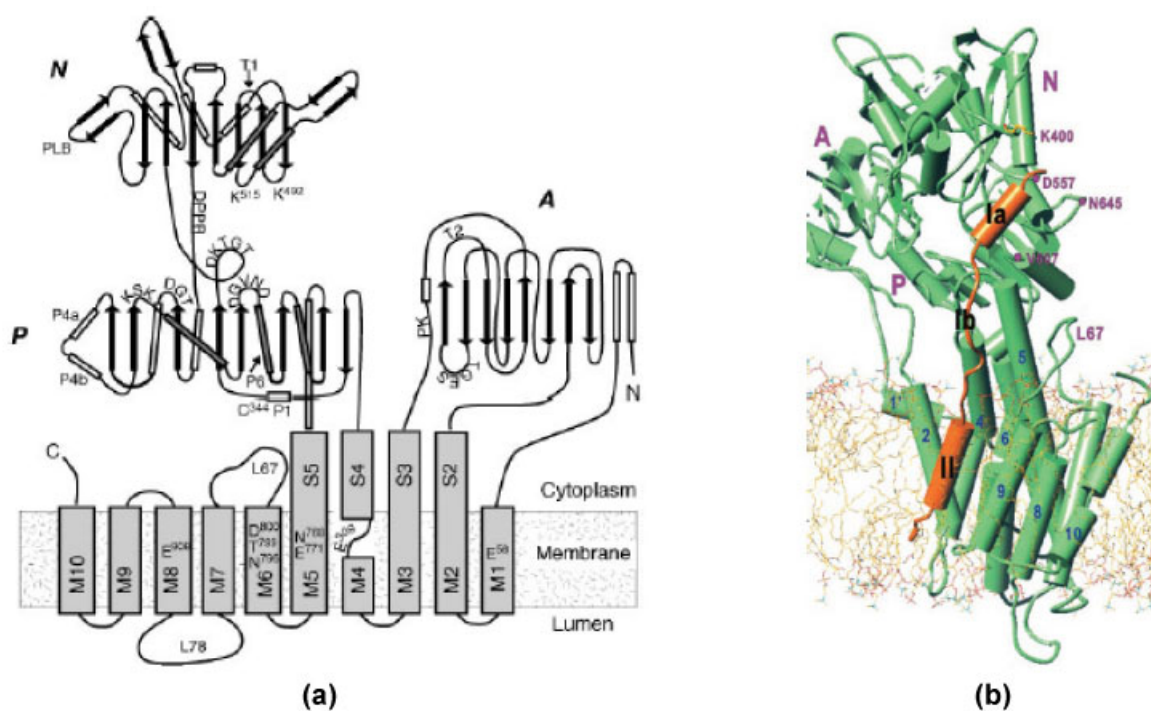


Figure 4.15: Model of SERCA and SERCA-PLN complex: (a) domain organization of SERCA [210] and (b) MD model of PLN-SERCA complex (PLN orange, SERCA green) [213].

To date, MD models [212, 213] offer the only detailed picture of the PLN-SERCA complex. In both models elongated conformations (50-60 Å) of PLN result. The first model identifies M6 as the most important SERCA binding partner of the PLN transmembrane helix. The C terminal end of PLN traverses only half of the membrane and this concurs with a narrower winding of the PLN helix between Asn27 and Ile33. The cy-

toplasmic helix is not affected. According to the second model, bound PLN has a shorter transmembrane helix (Leu31-Val50) that sits in a groove formed by M2, M4, M6 and M9. The cytoplasmic helix unwinds slightly (Val4-Ile12) and is accommodated by a  $\beta$ -hairpin of the N domain. The two helices are connected through a long unstructured stretch of residues (Arg13-Asn30).

Because ssNMR does not require crystallization or solubility, it can be employed for high-resolution structural characterization of SERCA-bound PLN. This section presents results obtained on U- $^{13}\text{C}$ ,  $^{15}\text{N}$ ] AFA-PLN reconstituted in the presence of unlabeled SERCA1a in DOPC liposomes (molar ratio 1:1:160). The value reported [220] for specific PLN-SERCA interaction in lipid bilayers (dissociation constant  $K_d \leq 20 \mu\text{M}$ ) indicate a weaker binding as compared to similar solid-state NMR studies of high affinity ( $K_d \approx n\text{M}$ ) membrane protein complexes, such as kalitoxin (KTX) bound to KcsA potassium channel [221] or neurotensin (NT) in complex with NTS-1 receptor [29].

First, the same approach as for the free PLN (see § 4.3) has been used to investigate internal dynamics. Recording a 2D HC INEPT spectrum in the liquid crystalline phase of lipids ( $T = 5^\circ\text{C}$  for DOPC) revealed only lipid signals (see Figure 4.16 (a)), indicating the fact that the cytoplasmic domain of PLN is immobilized upon SERCA binding. Hence in the following, only experiments based on dipolar coupling polarization transfer have been employed (see Appendix C.5). In order to profit from the increased signal-to-noise ratio at low temperatures (see Equation 2.1), the complex has been studied at  $-30^\circ\text{C}$ .

A comparison of 2D CC-DQ/SQ spectra between free and bound PLN shows considerable changes for residues located mainly in domain Ib and beginning of domain II (see Figure 4.16 (b)), the same region that is predicted by MD studies [212, 213] to be the most affected upon binding. Unambiguous assignments of bound PLN are necessary to distinguish between static disorder (as suggested in [213]) or an increase in  $\alpha$ -helical character (consistent with model from [212]) of this region. Both situations can explain at the moment the spectrum from Figure 4.16 (b).

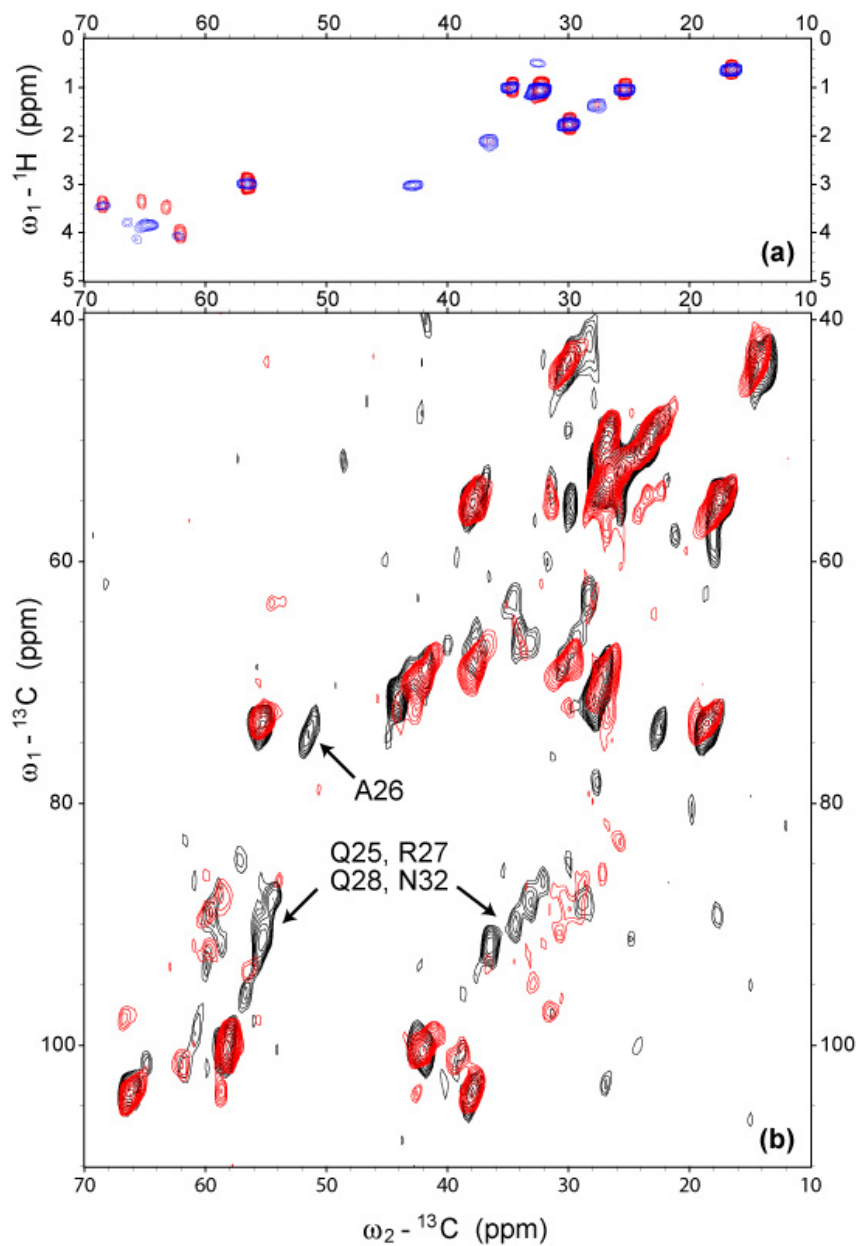


Figure 4.16: Dynamics of the SERCA-bound AFA-PLN: (a) comparison of 2D HC-INEPT spectra of SERCA-bound AFA-PLN in DOPC (red) and mixture of only (4:1) DOPC/DOPE (blue), (b) comparison of 2D CC-DQ/SQ spectra of free AFA-PLN (black) and SERCA-bound AFA-PLN (red, DQ with R14<sub>2</sub><sup>6</sup> [63] at 10 kHz MAS, 600 MHz <sup>1</sup>H field).

In addition, CC spin diffusion spectra reveal contribution of the cytoplasmic residues. Specially for Thr, Ser and Pro that can be unambiguously identified, dispersion of chemical shifts seems to indicate different conformations: extended for S18,T19-P23 region and more  $\alpha$ -helical around T10-S12.

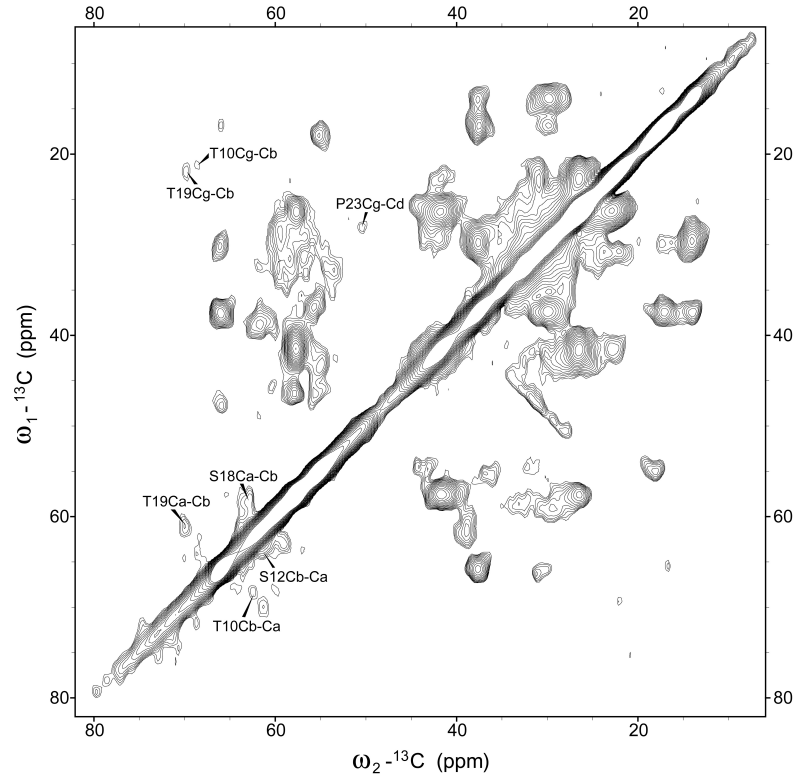


Figure 4.17: 2D CC spin diffusion spectrum of SERCA-bound AFA-PLN (5 ms mixing time, 11kHz MAS, 600  $^1\text{H}$  MHz). Distinct cytoplasmic residues can be identified.

Experiments that provide sequential assignment (NCACX, NCOCACX and CC under weak recoupling conditions [110]) will offer a more detailed picture about the conformation of SERCA-bound PLN. Specially, experiments that probe water accessibility (see § 5.3) could be useful to determine how much of the PLN transmembrane helix is actually embedded in the lipid membrane, as pointed by the MD model from [212]. Limited signal to noise and resolution make data acquisition and analysis more time consuming and tedious.

## 4.8 Conclusions

Structural results obtained for the C-terminal segment of free phospholamban corroborate earlier NMR studies in organic solvents and detergent micelles [189, 190], although a shorter (residues 30-53) stable  $\alpha$ -helix is detected. The helix found by ssNMR would span correctly the thickness of the DMPC lipid bilayer, while the one indicated by lsNMR would exceed this limit. On the other hand, results differ for the N-terminal end (residues 1-23) where a highly flexible, water exposed and unstructured domain is found. Here, three aspects are important to be highlighted. (1) The findings for the cytoplasmic domain are in agreement with other biophysical [196, 195] and biochemical [192, 222, 223] experiments, indicating important dynamics when PLN is reconstituted in lipid bilayers. (2) A highly dynamical cytoplasmic domain can be essential for PLN functional interactions with multiple partners on the relatively fast time scale required for the tight (*'beat-to-beat'*) regulation of the cardiac cycle. As such, functional tests indicate that mainly the transmembrane domain is responsible for SERCA inhibition [223, 224], while the cytoplasmic domain *'fine-tunes'* this interaction. In addition, a disordered cytoplasmic segment Thr8-Pro21 could enhance the accessibility of the cytoplasmic  $^{13}\text{RRAST}^{17}$  sequence to enzymatic interactions and could hence facilitate phosphorylation of Ser16 and Thr17 [192, 222]. (3) Results can be largely influenced by sample preparation and experimental conditions. Specially the L/P ratio, lipid type, lyophilization, hydration level and temperature are responsible for the correct fold and insertion of a membrane protein in a well formed liquid-crystalline lipid bilayer. In order to check the effect of all these factors, different samples have been prepared as described in detail in [111] (results are shown in Appendix C.4). The most sensitive property to various sample conditions is expected to be the dynamics and this has been checked in a series of 2D HC INEPT experiments (see Figure C.2). In particular, L/P ratios in the range 20:1 to 100:1 have been shown to give similar results. Also, different lipid types like DMPC and DOPC/DOPE (4:1 mixture, mimicking closest SR membranes) do not affect neither the dynamics of the



cytoplasmic domain, nor the  $\alpha$ -helix of the transmembrane domain. The formation of a liquid-crystalline lipid bilayer has been probed by  $^{31}\text{P}$  spinning-sidebands (see Figure C.3). The experimental conditions and sample preparation used for solid-state NMR studies are closer to the physiological conditions than those employed in liquid-state NMR. (4) However, the existence of a further population of membrane-associated PLN containing an  $\alpha$ -helical cytoplasmic domain as suggested by EPR [187] cannot be ruled out at present. In the case of a moderately stable helix that undergoes a conformational exchange on the intermediate time scale ( $\mu\text{s}$ - $\text{ms}$ ) the proposed experiments might not be sensitive. Different experiments [202] that could be sensitive in this regime have been tried but failed to capture such a state, possibly due to exchange broadening. Measurements at lower temperatures can be tried to check further this possibility.

In conclusion, monitoring through-space and through-bond polarization transfer by two complementary sets of experiments under MAS solid-state NMR conditions are shown here to provide not only access to the study of structure and dynamics under close to physiological conditions, but also to simplify the spectroscopic analysis. The proposed method is likely to be applicable to larger membrane proteins (e.g. rhodopsins [225]) or amyloid fibrils (see Chapter 5) where internal dynamics over a large time scale ( $\text{ns}$ - $\text{s}$ ) may exist.

Preliminary studies of the PLN-SERCA complex indicate that the cytoplasmic domain of PLN is immobilized and can be probed only by dipolar coupling based experiments. A comparison between 2D CC-DQ/SQ spectra of free and SERCA-bound PLN indicates that the most perturbed parts are domain Ib and beginning of domain II. The observed changes can be explained either by static disorder or an increase of  $\alpha$ -helix character. In addition, 2D CC spin diffusion spectra show that key residues of domain Ia, such as Ser or Thr, have large chemical shift dispersion and suggest different conformations, going from more  $\alpha$ -helical (T10-S12) to more extended (S18,T19-P23). Further experiments probing sequential assignment and hydration will allow a more detailed picture of SERCA-bound PLN conformation.

# Chapter 5

## Structural model of Alzheimer's-like intraneuronal fibrils

### 5.1 Introduction

Protein tau is one of the key microtubule-associated proteins (MAP) in neurons [226]. Apart of its physiological function, the binding to and stabilization of microtubules, tau forms in many *tauopathies* [227, 228] pathological aggregates, such as neurofibrillary tangles (NFTs) or neuropil threads (NPTs). The most prevalent<sup>1</sup> neurodegenerative disorder [229] - Alzheimer's disease (AD) - has two histological hallmarks in the brain: (1) the intra-neuronal NFTs containing paired helical filaments (PHFs) or straight filaments (SFs) assembled from the hyperphosphorylated tau protein [230, 231], and (2) the extra-cellular senile plaques consisting of filaments of the A $\beta$ -peptide [232]. The relationship between these pathological pathways and the events that trigger them is still a matter of debate [233, 234]. Controversy also exists on whether these protein aggregates are responsible for the neurodegenerative process or they represent the harmless dead-end

---

<sup>1</sup>15 million people are estimated world-wide to have AD today, and the number is predicted to increase by three-fold in the next 50 years.

of more aggressive oligomeric intermediates [235]. However, the clinical progression and diagnosis of AD is highly correlated with the brain distribution of the intra-neuronal tau PHFs ('*Braak stages*' - Braak 1991, [236]). Investigating the molecular mechanisms of tau polymerization and the structure of PHFs, hence may offer important information in the search for inhibitory conditions or compounds preventing PHFs or oligomers formation. As a result, degeneration of neurons in Alzheimer's disease may be slowed down or even reversed.

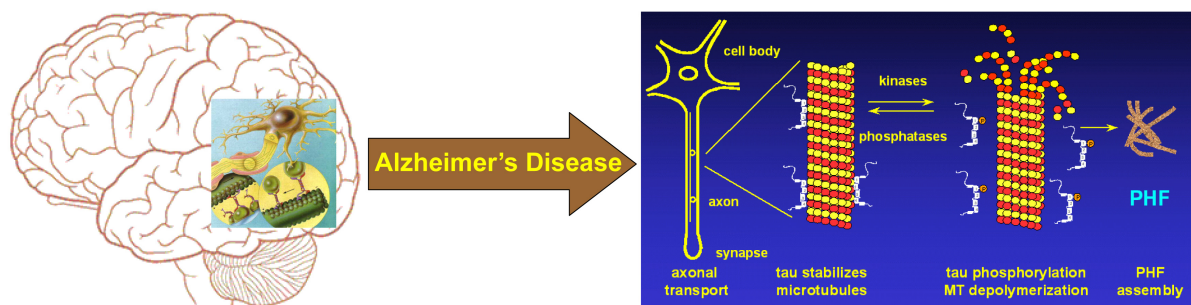


Figure 5.1: Intraneuronal pathogenic mechanisms associated with dysfunction of tau protein in Alzheimer's Disease.

There are six tau isoforms in the human brain that are developmentally regulated [237]. The longest isoform htau40 consists of 441 residues and contains several important domains (see Figure 5.2 (a)) such as the four pseudo-repeats R1-R4 (each  $\approx 31$  aa's long, the second repeat R2 may be absent due to alternative splicing) which together with their proline-rich flanking regions (P1,P2) constitute the '*microtubule binding domain*' (MBD). At present, little is known about the molecular details of tau's PHFs. In contrast to the  $A\beta_{1-40}$  peptide, the MAP tau is a highly soluble protein largely devoid of hydrophobic residues and contains an excess of positively charged amino acids (the same is true for K19 construct, see Figure 5.2 (a)). The lack of hydrophobic amino acids and the net charge at physiological pH explains the '*natively unfolded*' character of soluble tau protein.

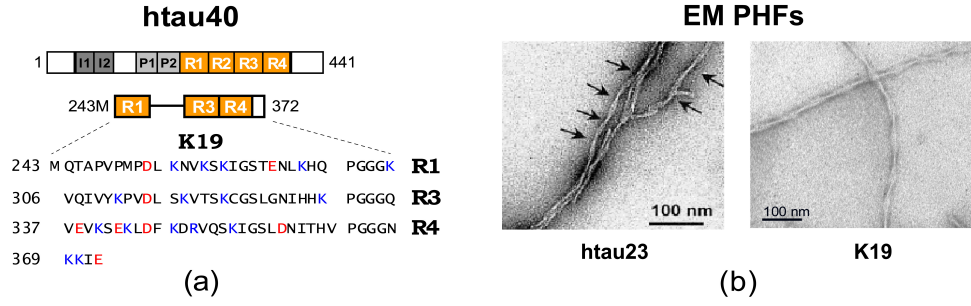


Figure 5.2: Comparison of htau40 and K19 construct: (a) domains of htau40 (R1-R4 microtubule binding repeats) and primary sequence of K19 (in red negatively- and in blue positively-charged residues), (b) EM of PHFs from htau23 (fetal isoform of tau, missing R2) and K19.

As probed by thioflavin fluorescence, CD and FTIR measurements, in-vitro aggregation of tau is highly accelerated by the addition of polyanions that contain an extended negative charge (e.g. heparin, MW = 6 kDa) [238, 231] and leads to a conformational switch from mostly random coil to a beta-sheet structure in regions, known as the '*hexapeptide motifs*' [239, 240] of the second (R2) and third (R3) microtubule binding repeats. These stretches are arranged in the form of cross- $\beta$  structure [241, 239, 242] homologous to other amyloidogenic peptides and proteins [243]. Beside the importance of the hexapeptides it is elusive which amino acids are involved in beta structure and how the strands are oriented.

Structural studies have been tried using several methods. EM micrographs on full length tau filaments purified from AD brains or assembled in-vitro (see Figure 5.2 (b)) reveal a '*core*' region and a '*fuzzy coat*' [244]. X-ray powder diffraction patterns contain the '*cross- $\beta$* ' peaks indicating a core formed by  $\beta$ -strands perpendicular to the fibril long axis [240]. Protease digestion studies further determined that the core of PHF is mainly built from the microtubule binding domains. More specific information on the PHFs fibril core packing has been limited to EPR studies using spin labels mainly within the third repeat (residues 301-320) and residues 400-404 of the C terminus. According to Ref. [245], these results speak in favor of increased protein dynamics for residues 400-404 and  $\beta$ -strands in R3 that stack parallel along the fibrils axis and are connected by inter-

molecular hydrogen-bonds.

Significant progress has been achieved in using MAS solid-state NMR [18] to characterize amyloid fibrils [246, 247, 112, 113]. 3D structures have been obtained for a ten-residue peptide fragment of Transthyretin [247] and for the  $A\beta_{1-40}$  peptide [246] in fibrillar form. Compared to  $\alpha$ -synuclein, the largest amyloid protein thus far studied by ssNMR [113], the spectroscopic study of full length tau PHFs is complicated by its size.

The length and residue composition of full htau40 sequence is challenging even for structural characterization of tau monomers in solution by liquid-state NMR [248]. Although, attempts of studying full length tau PHFs by liquid-state NMR alone [249], or in combination with HR-MAS [250] have been made, these did not provide 3D structural constraints of the fibril core, identifying only residues that are relaxation broadened. For these reasons, most structural studies have been performed on smaller constructs that preserve the key functions of tau (e.g. microtubule binding studied in solution by lsNMR [251, 252]) and aggregation.

For a structural investigation by ssNMR, *bona-fide* PHFs prepared from the three-repeat-domain construct K19 (R1, R3 and R4 in total 99 residues, see Figure 5.2 (a)) and displaying all the major features of PHFs purified from AD brains (see Figure 5.2 (b)) were chosen. Structure and dynamics of PHFs grown from uniformly [ $^{13}\text{C}$ ,  $^{15}\text{N}$ ] labeled K19 in the presence of heparin (4:1 molar ratio) were studied by combination of MAS solid-state NMR methods that permit structural analysis of immobilized proteins [20, 57] with techniques that probe different degrees of molecular mobility (see Chapter 4, [111]). Centrifuged PHFs were carefully washed twice with polymerization buffer to minimize the content of free monomers and enable the observation of the flexible parts of PHFs via experiments described in § 4.4. In order to probe first the tertiary structure of K19 monomers inside the fiber, molecular dilution was used by growing PHFs from a mixture of labeled and unlabeled (1:10) K19. The quaternary (supramolecular) arrangement of monomers inside PHFs has been obtained through a novel approach that can monitor molecular topology in protein fibrils relative to a mobile aqueous environment indepen-

dent of the molecular dilution. The experimental conditions for the spectra shown in the following are given in the table from § D.2.

## 5.2 Assignment of the core and flexible domains

As described in the previous chapter (see § 4.3 and § 4.4), dipolar and scalar coupling based experiments have been used to separate contribution of the flexible and core parts of K19 PHFs.

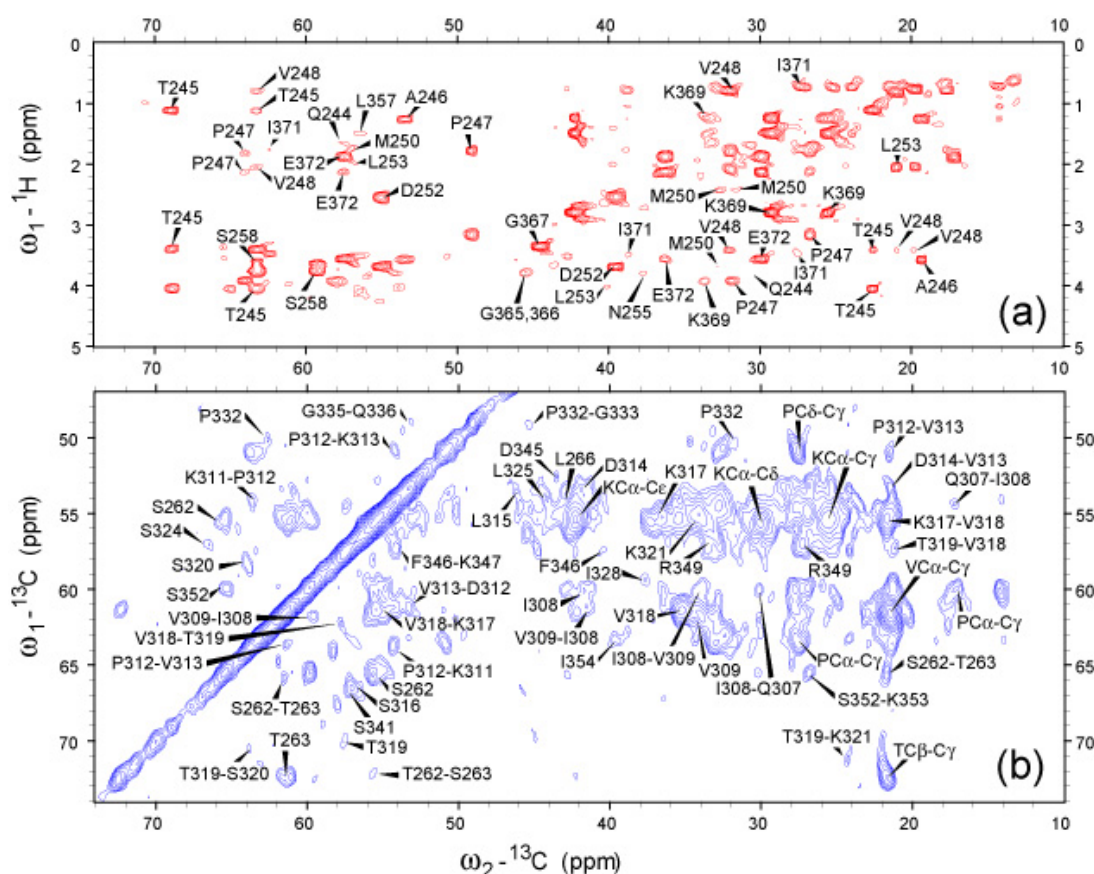


Figure 5.3: Flexible vs. rigid segments of K19 PHFs: (a) 2D H(C)C INEPT-TOBSY spectrum contains flexible residues, (b) 2D CC spin diffusion spectrum shows core residues (only crosspeaks are assigned).

Further identification of the residues present in spectra of Figure 5.3 (a,b) can be made through NC sequential assignment experiments. Again, dipolar vs. scalar coupling transfers enable spectroscopic filtration based on internal dynamics.

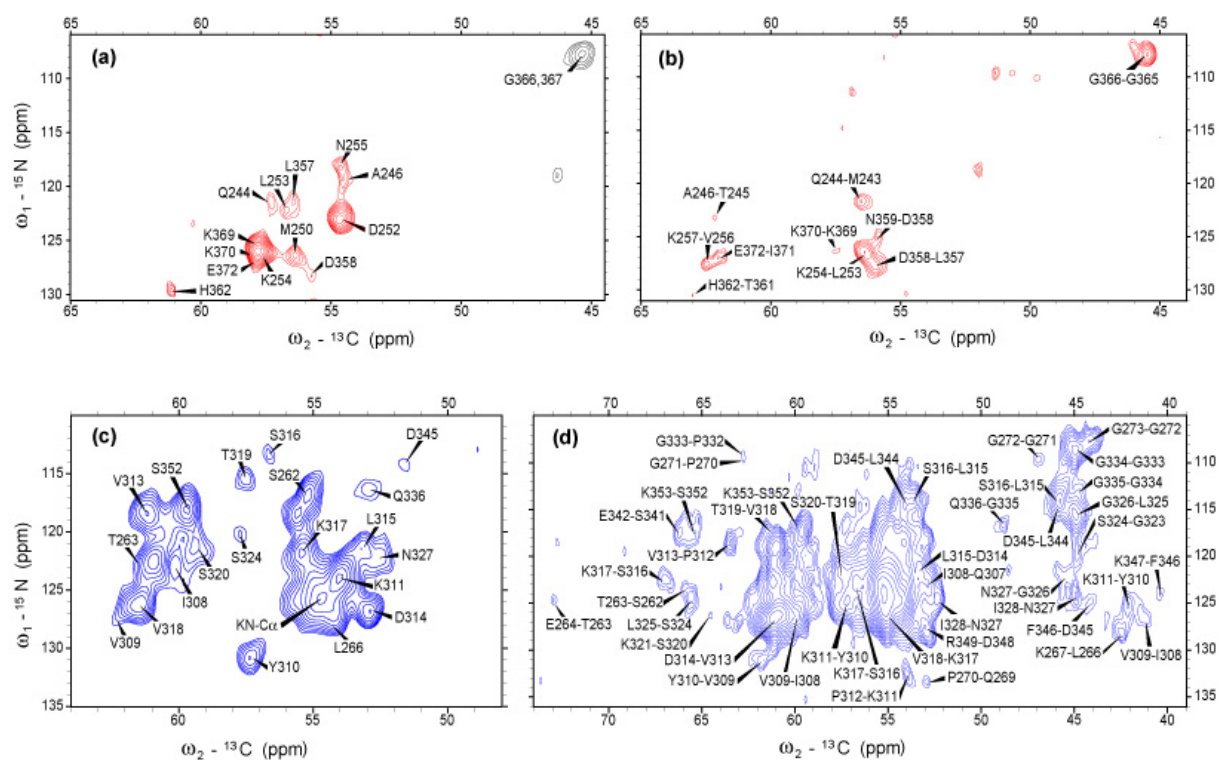


Figure 5.4: Sequential assignment: scalar coupling (H)NCA (a) and (H)NCOCA (b) or dipolar coupling based NCA (c) and NCOCX (d) spectra. Note, in (a) black contours indicate negative  $^{13}\text{C}\alpha$  peaks for glycines (the only residues with primary  $^{13}\text{C}\alpha$ ), resulting from the N – C $\alpha$  INEPT.

The through-bond correlation spectra (Figure 5.4 (a,b)) are dominated by the flexible segments of the fibrils. The fraction of free tumbling monomers has been sufficiently reduced by repeated washing of the pelleted fibrils. This might also indicate that K19 PHFs are relatively stable over a long period of time. By contrast, in the case of  $\alpha$ -synuclein fibrils the use of such an approach has been precluded by the presence of a large proportion of free monomers [113], either because of sample preparation or fibril stability.

Due to sequence composition, where 5 residues (Lys, Gly, Val, Ser, Pro) constitute approx. 60% of primary structure, complete sequential assignment remains difficult. Analysis of the above spectra has confirmed that both N and C termini are mobile (first and last 18 residues, respectively) and have led to unambiguous assignment of 20 residues in the flexible termini and 43 amino acids in the core region. A complete assignment table is given in § D.1.

### 5.3 Secondary, tertiary and quaternary distance constraints

The 3D fold of the core region and supramolecular (quaternary) packing are investigated next. Constraints for the tertiary structure and the possible arrangement of monomers in the fibril have been obtained from a novel water-edited 2D NCA experiment.

To take advantage of fibrils hydration, polarization exchange between protons of the external hydration water and protein  $^1\text{H}$  is possible [253, 254]. The pulse sequence and the underlying principle are shown in Figure 5.5. Thus, a  $^1\text{H}$   $T_2$  relaxation filter [202] selects first water protons with long transverse relaxation times (green box outside the core region that is shown in black before and white after the filter removed the initial magnetization). Subsequently, during a spin diffusion time, polarization transfer from



The diagram illustrates the NCA-HN experiment pulse sequence and chemical shift ranges. At the top, three green squares represent the magnetization states: a black circle (all  $^1\text{H}$  magnetization), a white circle (all  $^{15}\text{N}$  magnetization), and a grey circle (mixed magnetization). The pulse sequence for  $^1\text{H}$  (top) includes an initial pulse  $x$ , two pulses with phases  $\phi_1$  and  $\phi_2$  separated by delays  $\delta$ , a mixing time  $t_{\text{MIX-HH}}$ , a pulse  $x$  followed by a pulse  $y$  with a phase shift, a cross-polarization (CP) block, and a detection block (DEC). The  $^{15}\text{N}$  sequence (middle) features a  $\phi_{\text{TPPI}}$  CP block followed by a time interval  $t_1$  and a  $\phi_3$  CP block. The  $^{13}\text{C}$  sequence (bottom) includes a  $\phi_4$  CP block followed by a time interval  $t_2$  and a detection block. At the bottom, a chemical structure of a polymer chain is shown with chemical shift ranges for  $^1\text{H}$  (+1 to -1 ppm) and  $^{13}\text{C}$  (0 to 100 ppm) indicated.

Figure 5.5: Pulse sequence of the water edited NCA experiment: a  $^1\text{H}$   $T_2$  filter and  $^1\text{H} - ^1\text{H}$  spin diffusion time precede the NCA SPECIFIC CP [170] ( $180^\circ$  and  $90^\circ$  pulses are shown as wide and narrow rectangles). Phase cycle:  $\phi_1$  and  $\phi_4$  are cycled in steps of  $90^\circ$ ,  $\phi_2$  and  $\phi_3$  in steps of  $180^\circ$  and  $\phi_{rec} = \phi_4 + \phi_3 - \phi_2 + 2\phi_1$ . The working principle is depicted above (see also [113]) and coherence transfer pathways for  $^1\text{H}$  are shown below the sequence (Bruker pulse program is given in Appendix D.5).

Comparison of the water edited and conventional NCA spectra indicates that the fibril core is largely devoid of mobile water and residues in the third repeat R3 are water

protected. As discussed in the next section, this protection is consistent with a minimal structural unit of the fibril core represented by an antiparallel dimer formed by lateral assembly of two monomers along the third repeat (see Figure 5.8 and Figure 5.9 (a,b)).

In addition, intramolecular contacts have been probed by indirect detected  $^1\text{H} - ^1\text{H}$  distances in CHHC (sensitive to the 3D fold [87]) and NHHC (diagnostic for  $\beta$ -strands [30]) experiments. The CHHC spectrum is consistent with a fold back (*' $\beta$ -hairpin'* like) of the R4 repeat onto the R3 repeat.

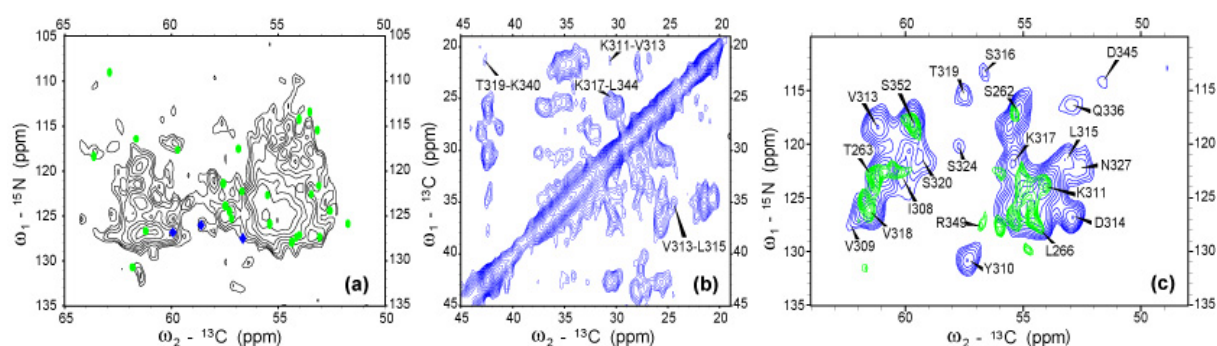


Figure 5.6: Secondary, tertiary and quaternary distance constraints for the PHF core: (a) 2D NHHC, (b) 2D CHHC, and (c) 2D water-edited NCA.

Details of Figure 5.6 (a-c) are as following: in (a) the NHHC spectrum is compared with intraresidue  $\text{N}_i\text{C}\alpha_i$  (blue) or sequential interresidue  $\text{N}_{i+1}\text{C}\alpha_i$  (green) correlations that are predicted for H-H distances present in  $\beta$ -strands (see next section) and using the assignments given § D.1, in (b) R3-R4 inter-strand (unambiguous T319C $\gamma$ -K340C $\epsilon$  or ambiguous K317C $\delta$ -L344C $\delta$ ) or  $i - (i + 2)$  R3 intra-strand (K311C $\delta$ -V313C $\gamma$  and V313C $\beta$ -L315C $\delta$ ) contacts are indicated, and in (c) the comparison between water-edited (green) and conventional (blue) NCA spectra. More discussions are made in § 5.4 and § 5.5.

## 5.4 Minimal structural unit of K19 PHFs

A summary of all structural constraints resulting from ssNMR spectra of Figure 5.3 (a,b), Figure 5.4 (a-d) and Figure 5.6 (a-c) is given in the figure below (b-e).

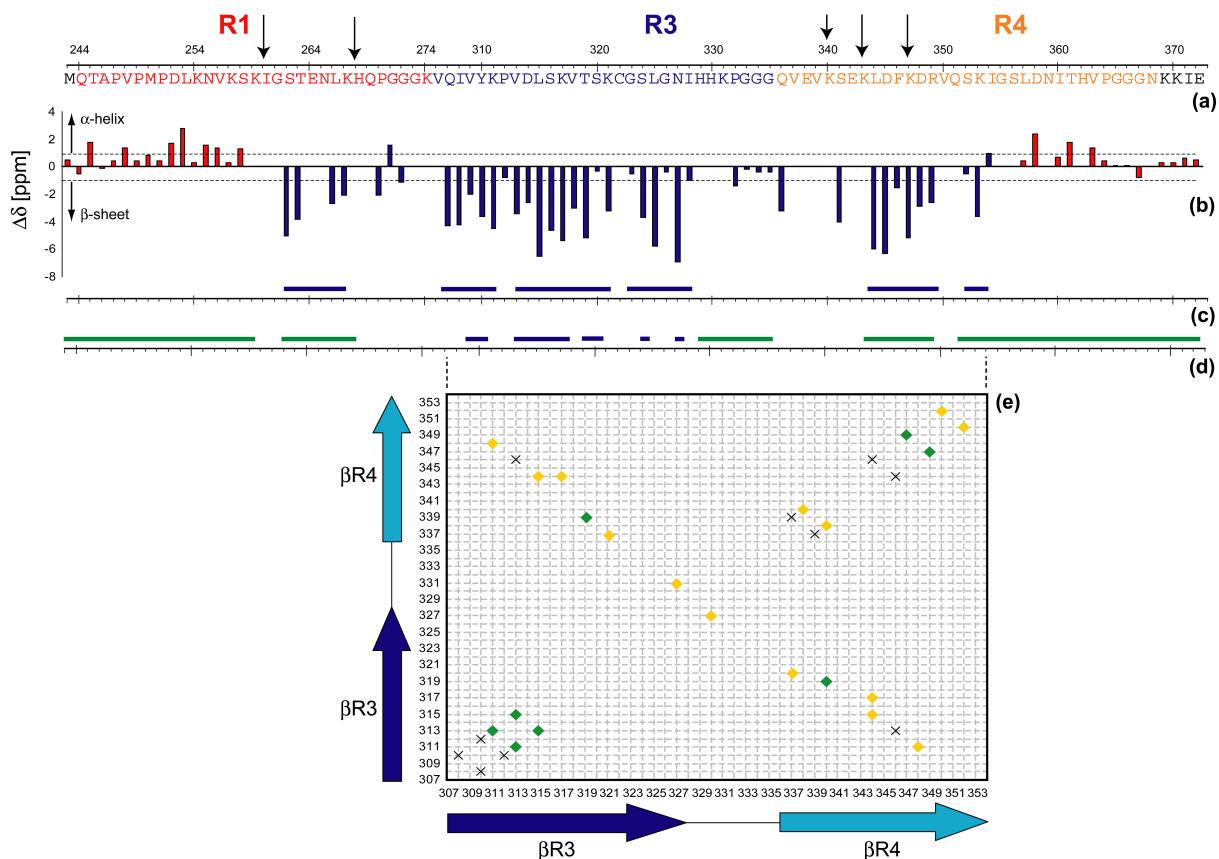


Figure 5.7: Structural constraints: (a) K19 primary sequence and arrows indicating protease digestion sites, (b) secondary chemical shifts [86], diagnostic of the secondary structure (red and blue indicate flexible and rigid residues, respectively), (c) beta-strands consistent with the NHHK (blue stretches), (d) water protected (blue) or exposed regions (green), and (e) tertiary contacts consistent with CHHC (green - unambiguously assigned peaks, yellow - peaks overlapped by intra-residue contribution, crosses - missing peaks or close to the diagonal).

As defined in [86, 92], secondary chemical shifts of the core region (blue bars in Figure 5.7 (b))<sup>2</sup> indicate three main  $\beta$ -strand regions: (1) the short stretch 262-267 (abbreviated  $\beta$ R1) at the end of first repeat, (2) residues 306-328 that form  $\beta$ R3 in third repeat and (3) the segment 336-354 that constitute  $\beta$ R4 in fourth repeat. Secondary chemical shifts of the mobile N and C termini show mostly random coil character, with a slight  $\alpha$ -helical propensity for residues closer to the core (252-258 and 358-363, respectively).

In addition, as indicated in Figure 5.7 (c) the  $\beta$ -strands are confirmed by short  $H_N^{(i+1)} - H_\alpha^{(i)}$  distances ( $< 2.7 \text{ \AA}$ ) that are probed indirectly in the NHHc spectrum (Figure 5.6 (a)) under experimental conditions such as given in Appendix D.2. Note that  $\beta$ R3 contains the hexapeptide motif  $^{306}\text{VQIVYK}^{311}$  identified previously [239]. These strands also contain residues V306-L315 and Q336-D345 that exhibited a nascent  $\beta$ -structure in soluble K19 monomers [252]. Notably, a similar correlation between K19 monomers and PHFs cannot be obtained for  $\beta$ R1 and is not seen for the remaining segments of R3 and R4. Furthermore, the connecting segments  $\beta$ R1- $\beta$ R3 and  $\beta$ R3- $\beta$ R4 consist of PGGGX motifs that exhibit ssNMR data typically found for protein loops or turns.

The water-edited NCA experiment indicates that within the core only  $\beta$ R3 is water protected. Additionally, dynamic experiments probe that the flexible N and C termini are hydrated (see Figure 5.7 (d)). While  $\beta$ R4 is similar in length to  $\beta$ R3 and can shield it from the outside,  $\beta$ R1 is significantly shorter than  $\beta$ R3. Hence, a molecular arrangement where  $\beta$ R3 is entirely water protected by intramonomer rigid segments is not possible. Instead, complete protection of  $\beta$ R3 can be achieved if two K19 monomer units constitute to the fibril core. As indicated in Figure 5.8 water protection of  $\beta$ R3 can then be realized by a  $\beta$ -hairpin like fold of the  $\beta$ R3- $\beta$ R4 within one monomer unit and, at the same time, the presence of a second K19 unit juxtaposed to the first one.

The validity of these conclusions were further tested by a CHHC correlation experiment that indirectly records proton-proton contacts relevant for the 3D fold of K19

---

<sup>2</sup>Only values exceeding the natural line width i.e.  $|\Delta\delta| > 1 \text{ ppm}$  are considered significant.

monomers. Contacts indicated in Figure 5.7 (e) are consistent with the fold back of  $\beta$ R4 on  $\beta$ R3. Moreover, the  $\beta$ R3- $\beta$ R4 hairpin fold would also suggest the formation of intra-monomer salt bridges K311-D348, K317-E342, and K321-E342 (see Figure 5.8).

Based on the solid-state NMR restraints presented above, the minimal structural unit for K19 PHFs is proposed to be formed by K19 antiparallel dimers that are stacked on top of each other along the fibril long axis. A dimer model mapped on the primary sequence of K19 is shown below. Reasons for antiparallel arrangement are further discussed in the next section.

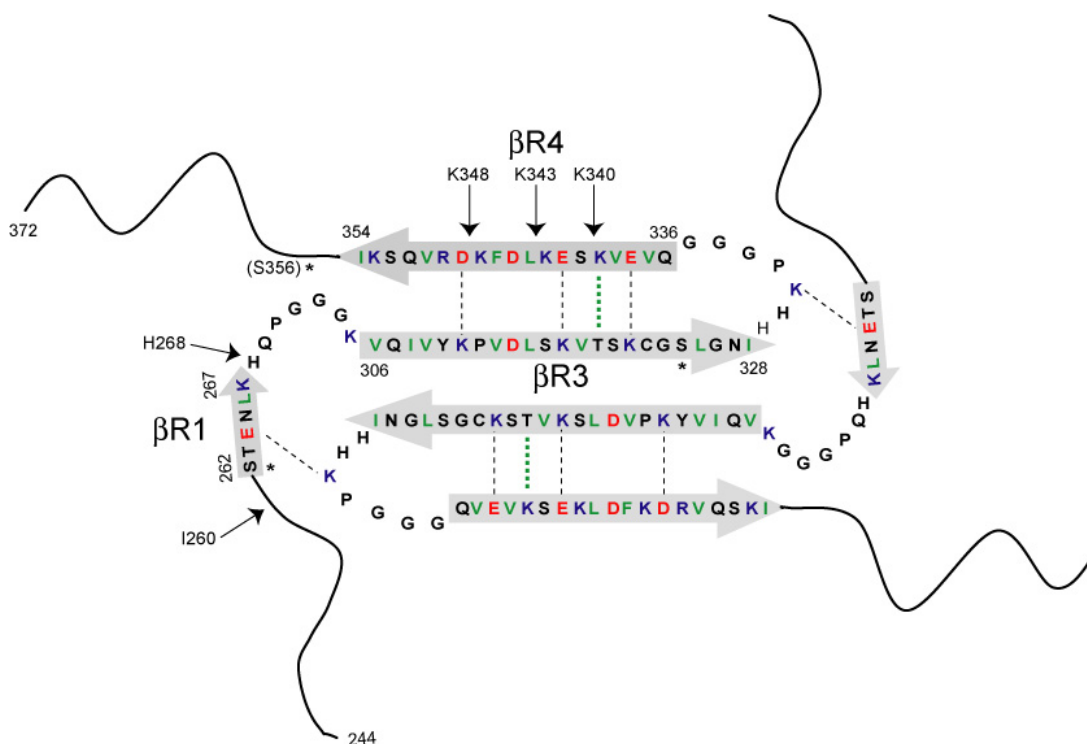


Figure 5.8: Minimal structural unit of K19 PHFs that fulfills solid-state NMR constraints of Figure 5.7 is represented by an antiparallel dimer (dashed lines indicate possible salt-bridges (black) or H-H contacts (green) observed in CHHC spectrum of Figure 5.6 (b)). Colored residues: positively- (blue), negatively-charged (red) and hydrophobic (green). Arrows indicate protease digestion sites and asterisks mark phosphorylation positions.

## 5.5 Structural model

A three-dimensional structural model of K19 PHFs in agreement with the experimental findings, as outlined in Figure 5.8, was generated using CNS (Brunger, [88]), and visualized in PyMol (DeLano Scientific, CA [255]).

A simulated annealing protocol using torsion angle and Cartesian dynamics was employed to obtain the desired fibril arrangement. (1) Parallel  $\beta$ -sheets derived from secondary chemical shift analysis were modeled using idealized backbone torsion angles and by hydrogen bond restraints according to: (i) square-well potentials were defined around  $\Phi = 114^\circ$  and  $\Psi = -119^\circ$ , and allowing for a variation of  $\pm 30^\circ$  without penalty to the energy target function, (ii) hydrogen bonds were enforced by restraints representing an attractive force between H-O pairs for distances exceeding 2 Å, and a repulsive force for backbone N-C distances below 3.9 Å, favoring planarity. (2) Salt bridges as indicated in Figure 5.8 were implemented by attractive potentials for  $N\zeta - O\epsilon$  distances above 2.8 Å. Additionally, a distance constraint was set between T319 – O $\gamma$ 1 and K340 – H $\zeta$ , in line with a possible hydrogen bond. One of the salt bridges E264-K331' (inter-monomer) and a restraint of 5 Å between  $C\alpha$  of G304 and I354 (intra-monomer) places the N-terminal  $\beta$ R1-strand near the terminal ends of the core, which it can shield from water.

Additional backbone restraints (such as inter-strand  $C\alpha - C\alpha$  distances) were used to connect the monomer units to a dimer, stabilize the monomer fold, and constrain loop mobility in this finite model of three layers.

Electrostatic interactions were not included explicitly at this level of molecular modeling. The final structural model shown in Figure 5.9 was chosen from an ensemble of annealed conformations according to minimum overall energy (Equation 2.14).

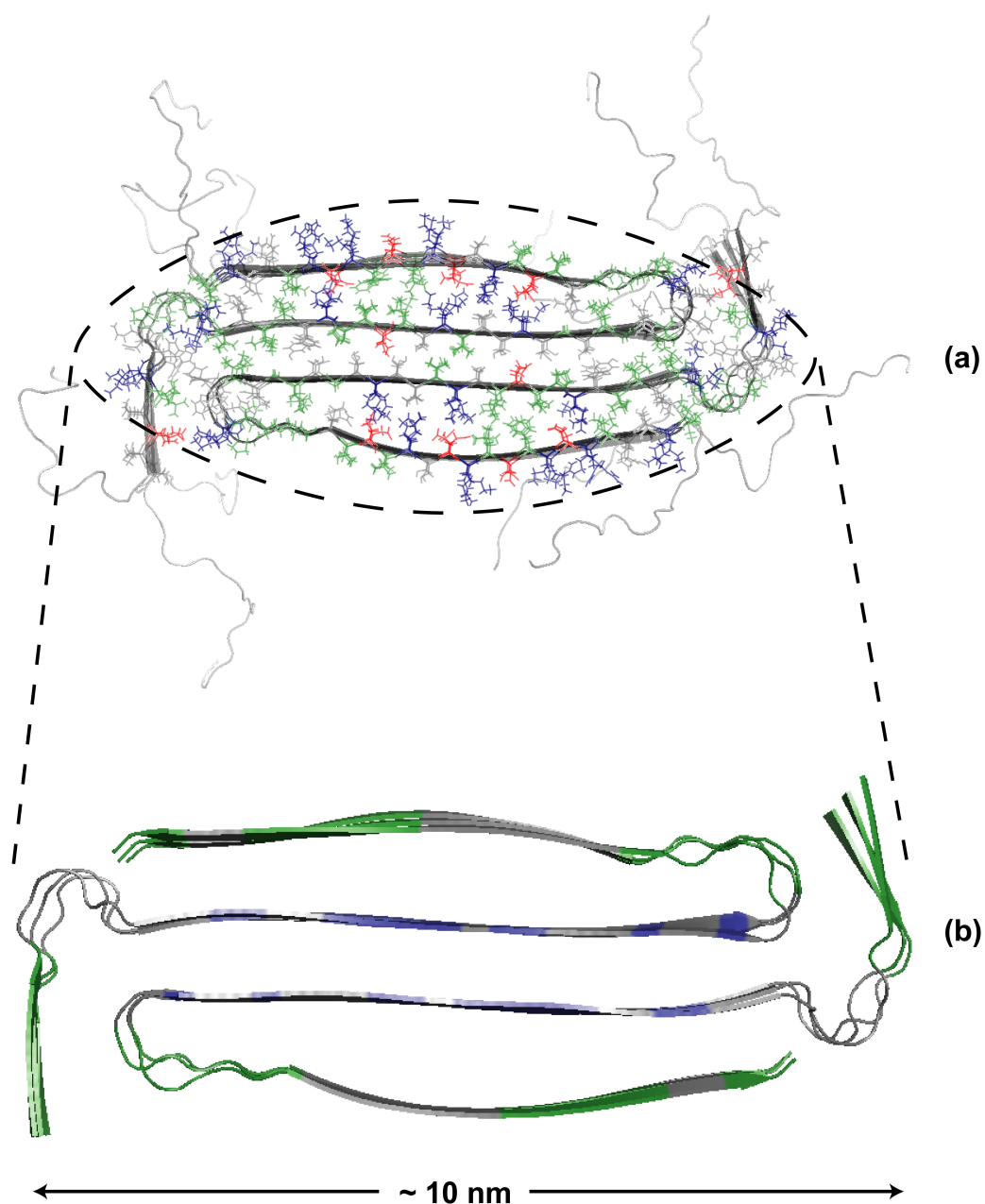


Figure 5.9: Structural model of K19 PHFs consistent with solid-state NMR data. Three dimer layers are shown along the fibril long axis: (a) 'fuzzy coat' and 'core' region (residue colors as in Figure 5.8), (b) zoom on the core region indicating hydration in colors (green - water exposed, blue - water protected).

Several merits and limitations of the model have to be highlighted. Inside the monomer favorable charge compensation is achieved, with the excess of positively charged residues located in  $\beta$ R4 pointing toward the exterior (see Figure 5.9 (a)). Existence of salt bridges seems to be indicated by two resolved side-chain  $N\zeta$  resonances of lysines (data not shown, selectively labeled variants of K19 may unambiguously prove this). Excess of positive charges on the exterior surface of the monomer can be compensated by polyanions that promote in-vitro fibrilization (in-vivo this role might be played by the hyperphosphorilation).

The antiparallel arrangement of the monomers within one fibril layer is necessary in order to protect with the short  $\beta$ R1 strands the  $\beta$ R3- $\beta$ R4 hairpin interstrand spaces from water access. In addition, clashes of negatively charged residues such as D314 of  $\beta$ R3 strands are avoided. Antiparallel K19 dimers are also suggested by previous biological experiments [256] with antibodies targeting monomer termini.

In the model presented in Figure 5.9 parallel  $\beta$ -sheets along the fibril axis are considered. Although antiparallel  $\beta$ -sheets can not be excluded only from the data obtained on molecular diluted PHFs, parallel stacking would favor formation of  $\beta$ R1 sheets and a tighter packing of the core. An undiluted PHF sample would allow to distinguish between antiparallel and parallel  $\beta$ -sheets due to different contacts present in the CHHC spectrum.

The self-consistency of the model has been checked by two independent methods. First, the experimental observed chemical shifts  $^{13}\text{C}\alpha$  and  $^{13}\text{C}\beta$  of the core have been compared to the values predicted by ShiftX [257], using the 3D structures from Figure 5.9 (b). As shown in Appendix D.3, good agreement is found for the regions of defined secondary structure (i.e.  $\beta$ R1,  $\beta$ R3 and  $\beta$ R4), particularly for those involved in the hairpin fold ( $\beta$ R3 and  $\beta$ R4). Second, the complete CHHC spectrum has been compared to prediction of intra-monomer  $^1\text{H} - ^1\text{H}$  contacts below 3.5 Å. Long-range 3D contacts that are well separated from intra-residue contribution can be identified (see Figure D.2). However, for several predictions the experimental crosspeaks are missing. Explanation relates to



the fact that these correspond to residues located in the loops (PGGGX motifs) or  $\beta$ R1 strand that might have a less defined conformation compared to the hairpin fold formed by  $\beta$ R3 and  $\beta$ R4. The same observation can be made with respect to NHC spectrum of Figure 5.6 (a).

The structural model of K19 fibrils, not only explains all ssNMR data obtained so far, but is also consistent with the cross- $\beta$  structural motif established by X-ray diffraction, mass-per-length (MPL) and fibril dimensions from scanning transmission EM (STEM) and the protease digestion sites. According to STEM the MPL of tau fibrils is approx. 4 molecules per nm in agreement with two cross- $\beta$  dimers. The cross-sectional diameter of PHFs is approx. 10 nm that can be accounted by the length of  $\beta$ R3 sheet and the two '*capping*'  $\beta$ R1 sheets at each of its ends. Protease digestion sites are located outside the  $\beta$ R3 strand, and the enzymatic kinetics at each site is consistent with the presence of structural elements such as  $\beta$ R1 and salt bridges between  $\beta$ R3 and  $\beta$ R4. Finally, the ssNMR data do not support structural models in which K19 fibrils build water-filled nanotubes [258] or that have been proposed based on a simplified interpretation of EPR measurements [245].

## 5.6 Conclusions

The ssNMR study suggests that the minimal structural unit of K19 filaments comprises K19 dimers. While N and C termini of K19 monomers are highly dynamic and solvent exposed, the rigid core consists of three  $\beta$ -strands ( $\beta$ R1,  $\beta$ R3 and  $\beta$ R4).  $\beta$ R3 and  $\beta$ R4 are arranged in a hairpin-like fold that is covered ('*capped*') by  $\beta$ R1 at each of its ends. The core dimensions found by ssNMR corroborate well with EM measurements and protease digestion studies.

The model sheds light also on the mechanisms of fibril formation and may guide the search for drugs that inhibit or dissolve the fibrils. Electrostatic interactions play a central role in stabilizing the hairpin arrangement of  $\beta$ R3 and  $\beta$ R4 inside the monomer with the key residues K311-D348, K317-E342, and K321-E342 being involved in salt-bridges.

Extrapolating the results found on K19, the mechanisms of PHFs formation by protein tau in AD seem to vary considerably from the common theme of aggregation of proteins such as A $\beta$  [246], PrP [259] and  $\alpha$ -synuclein [260] where hydrophobic sequences play the dominant role.

Fibril polymorphism and stability are other important properties that have been previously found [261, 262, 113] and are possibly associated with pathogenicity. The ssNMR data obtained so far on K19 PHFs differ also in this respect. The same fibril structure can be repeatedly obtained (three samples have been compared) and no detectable monomer fraction has been observed for a considerable period of time (six months), indicating good fibril stability.

Further studies on an undiluted sample could distinguish between the parallel or antiparallel arrangement of the  $\beta$ -sheets. Salt bridge contacts could be unambiguously proven by selectively labeling the residues involved or mutations.

In addition, drug induced fibril dissociation, oligomer and fibril formation (inhibition) and their possible association with lipid membranes can be investigated. These aspects may be relevant for pathogenic pathways involved in Alzheimer's Disease.

# Chapter 6

## Summary and outlook

The aim of this thesis was to develop multidimensional high-resolution experiments that can be incorporated in a general strategy for 3D structure determination of uniformly labeled membrane proteins or fibrils by MAS solid-state NMR spectroscopy. In particular, molecule orientation, dynamics and hydration have been investigated. The main results of Chapters 3-5 are summarized in the following and possible future studies proposed.

In Chapter 3, a method that can simultaneously probe orientation and 3D fold of membrane proteins in aligned lipid bilayers was described. Recoupling of anisotropic interactions, such as dipolar couplings (heteronuclear NC or homonuclear CC) and  $^{15}\text{N}$  CSA at high MAS were first investigated by theoretical analysis (§ 3.2) and numerical simulations (§ 3.3). These indicated that, in particular, the  $M = 2$  recoupling condition of  $^{15}\text{N}$  CSA is sensitive to the tilt angle of membrane embedded  $\alpha$ -helices. This was further used in 1D experiments on Gramicidin A and WALP23 oriented in DMPC bilayers (§ 3.5) to determine their orientation in membranes. Extension to multidimensional pulse sequences was shown in § 3.6.  $^{15}\text{N}$  CSA is recoupled ( $M = 2$ ) before  $t_1$  evolution and modulates the signal intensity in a 2D NC correlation experiment. Hence, in addition to

assignments and structural constraints that are usually obtained, orientation of membrane protein can be probed. In comparison to previous solid-state NMR experiments designed for slow MAS conditions, the method developed here can be employed for membrane proteins where specific residues are labeled, as well for uniformly labeled samples. In addition, increased resolution and signal-to-noise ratio result at high MAS. The accuracy in measuring the tilt angle is  $\pm 10^\circ$  for selectively labeled samples, but can be improved for uniformly labeled proteins, when the conformational space is restricted by multiple constraints.

Chapter 4 introduces a general strategy for the study of dynamics and structure of uniformly labeled membrane proteins reconstituted in liposomes. Besides orientation and structure that was investigated in Chapter 3, dynamics are also relevant for function. The novel concept of dynamics-based spectral editing (§ 4.3) is particularly powerful in emphasizing highly flexible parts (loops or termini extending outside the membrane) that are attached to less mobile (transmembrane) domains of membrane proteins. Because of fast dynamics, these domains can escape conventional methods of solid-state NMR that are based on dipolar-couplings (e.g., CP). Scalar-coupling interactions are not averaged out by dynamics and can be employed (e.g., INEPT and TOBSY in § 4.4) to study flexible domains. This aspect might be important for the fine tuning of protein-protein interaction such as in the case of Phospholamban (PLN) and SERCA. Application to the free PLN (§ 4.5 and § 4.6) and SERCA-bound PLN are presented (§ 4.7). In the free PLN the cytoplasmic domain (Ia) is highly flexible and water exposed while C terminal end (residues 30-53) form a transmembrane helix. Results for domain Ia are in agreement with those obtained by biophysical techniques that can study membrane proteins in lipid bilayers (e.g., EPR or FRET) but are different from studies (e.g., lsNMR) in organic solvents or micelles, suggesting that sample preparation is a critical factor. Domain Ia becomes immobilized upon interaction with SERCA. A comparison between 2D DQ/SQ spectra of free and bound PLN shows considerable changes for residues located mainly in

domain Ib and beginning of domain II. So far, data obtained on other membrane proteins (e.g., rhodopsins) indicate that the presented method might be generally applicable. Furthermore, the qualitative study of dynamics can be extended to a quantitative analysis to obtain correlation times of internal motions and order parameters, as indicated in § 2.5.2.

In Chapter 5, I studied Alzheimer's disease-like paired helical filaments (PHF) formed by the three repeat construct (K19) of protein Tau. The method developed in Chapter 4 is applied here to probe the flexible 'fuzzy coat' and the rigid 'core' of the fibrils. The through-bond correlation experiments reveal that the N and C termini are mobile (§ 5.2). Combination of dipolar-coupling and novel water-edited experiments (§ 5.3) indicates that an antiparallel dimer is the minimal structural unit (Figure 5.8 and Figure 5.9) of the fibril core. Each monomer comprises three  $\beta$ -strands and adopts a hairpin-like fold. A water filled nanotube as suggested by EPR measurements can be excluded. Specially, the water-edited experiment uses polarization transfer from protons of mobile water to protein and is able to probe the supramolecular arrangement of monomers even for fibrils with molecular dilution (mixture of 1:10 unlabeled/labeled monomers). The ssNMR data are consistent with EM dimensions, X-ray cross- $\beta$ , protease digestion and antibody labeling of fibrils. Key residues that stabilize this fold and the supramolecular assembly are identified and suggest possible ways for inhibiting PHF formation. No evidence of fibril polymorphism was found and K19 PHFs showed good stability. With the methods described in this thesis (§ 4.4 and § 5.3) drug induced fibril dissociation, oligomer and fibril formation (inhibition) and their possible association with lipid membranes could be investigated. These aspects may be relevant for pathogenic pathways involved in Alzheimer's Disease.



# Appendix A

## Spherical tensors and rotations

### A.1 Irreducible spherical tensors for NMR interactions

Irreducible spherical tensors are more convenient to express NMR Hamiltonians (Equation 2.8) when rotations between different reference frames are necessary [40, 45].

The relationship between rank 2 spherical tensors and Cartesian tensors is given by ( $k = 0, 1, 2$  and  $q = \overline{-k, k}$ ):

$$\hat{T}_{k,q} = \sqrt{2k+1} \sum_{q_1=-1}^1 \sum_{q_2=-1}^1 (-1)^q \begin{pmatrix} 1 & 1 & k \\ q_1 & q_2 & q \end{pmatrix} \hat{T}_{1,q_1} \hat{T}_{1,q_2} \quad (\text{A.1})$$

where  $\hat{T}_{1,0} = \hat{T}_z$ ,  $\hat{T}_{1,\pm 1} = \mp(1/\sqrt{2})(\hat{T}_x \pm i\hat{T}_y)$  and the Wigner's 3-j symbol are used (the same definition is valid for both space (A) and spin (T) rank 2 tensors).



## A.2 Euler rotations and reduced Wigner elements

Definition of Euler rotations and angles (Brink, [164]):

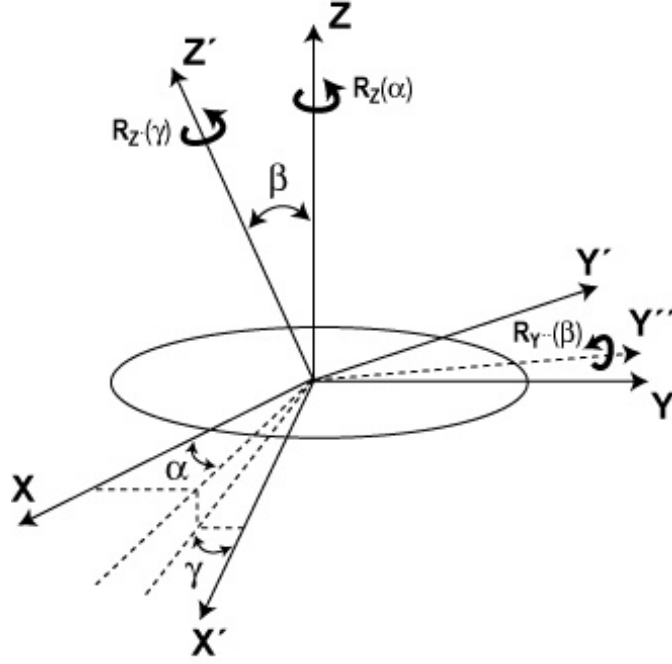


Figure A.1: Rotation  $R(\alpha, \beta, \gamma) = R_{Z'}(\gamma)R_{Y''}(\beta)R_Z(\alpha)$  between two reference systems  $(X, Y, Z)$  and  $(X', Y', Z')$ . Euler angles can vary as  $\alpha = [0, 2\pi]$ ,  $\beta = [0, \pi]$  and  $\gamma = [0, 2\pi]$ .

Reduced Wigner elements of rank 2 ( $d_{p,q}^{(2)}(\beta)$ ) used in Equation 2.9 (Ref. [45]):

$d_{p,q}^{(2)}(\beta)$	p = -2	p = -1	p = 0	p = 1	p = 2
q = -2	$\left(\frac{1+\cos\beta}{2}\right)^2$	$-\frac{1+\cos\beta}{2}\sin\beta$	$\sqrt{\frac{3}{8}}\sin^2\beta$	$-\frac{1-\cos\beta}{2}\sin\beta$	$\left(\frac{1-\cos\beta}{2}\right)^2$
q = -1	$\frac{1+\cos\beta}{2}\sin\beta$	$\frac{-1+\cos\beta}{2} + \cos^2\beta$	$\sqrt{\frac{3}{8}}\sin 2\beta$	$\frac{1+\cos\beta}{2} - \cos^2\beta$	$-\frac{1-\cos\beta}{2}\sin\beta$
q = 0	$\sqrt{\frac{3}{8}}\sin^2\beta$	$\sqrt{\frac{3}{8}}\sin 2\beta$	$\frac{3\cos^2\beta-1}{2}$	$\sqrt{\frac{3}{8}}\sin 2\beta$	$\sqrt{\frac{3}{8}}\sin^2\beta$
q = 1	$\frac{1-\cos\beta}{2}\sin\beta$	$\frac{1+\cos\beta}{2} - \cos^2\beta$	$\sqrt{\frac{3}{8}}\sin 2\beta$	$\frac{-1+\cos\beta}{2} + \cos^2\beta$	$-\frac{1+\cos\beta}{2}\sin\beta$
q = 2	$\left(\frac{1-\cos\beta}{2}\right)^2$	$\frac{1-\cos\beta}{2}\sin\beta$	$\sqrt{\frac{3}{8}}\sin^2\beta$	$\frac{1+\cos\beta}{2}\sin\beta$	$\left(\frac{1+\cos\beta}{2}\right)^2$

# Appendix B

## MAS on oriented samples

### B.1 AHT for $^{15}\text{N}$ CSA recoupling

Average Hamiltonian theory (AHT) [40] can be used to calculate the signal intensity of the recoupled interaction as a function of the orientation angles. Most generally the zeroth order AHT for a given interaction  $\Lambda$  ( $\overline{\mathcal{H}}^{(0),\Lambda}$ ) can be expanded into a series [63]:

$$\overline{\mathcal{H}}^{(0),\Lambda} = \sum_{l=0}^2 \sum_{m=-l}^l \sum_{\lambda=0}^2 \sum_{\mu=-\lambda}^{\lambda} \overline{\mathcal{H}}_{l,m;\lambda,\mu}^{(0),\Lambda} \quad (\text{B.1})$$

where the  $\overline{\mathcal{H}}_{l,m;\lambda,\mu}^{(0),\Lambda}$  terms contain the  $A_{l,m}^{RAS,\Lambda}$  space and  $T_{\lambda,\mu}^{\Lambda}$  spin spherical tensor components [45]. The symmetry based  $R18_1^7$  and  $R18_2^5$  pulse sequences [169] select only the terms  $\{l, m; \lambda, \mu\} = \{2, \pm 2; 1, \pm 1\}$  or  $\{l, m; \lambda, \mu\} = \{2, \pm 2; 1, \mp 1\}$  (shortly the  $M = 2$  condition of Figure 3.2), yielding the the zeroth order AHT:

$$\overline{\mathcal{H}}^{(0),\Lambda} = k \left\{ A_{2,2}^{RAS,\Lambda} T_{1,-1}^{\Lambda} - A_{2,-2}^{RAS,\Lambda} T_{1,1}^{\Lambda} \right\} \quad (\text{B.2})$$

where  $k$  is the r.f. pulse sequence scaling factor, and  $\Lambda$  can be either CSA or heteronuclear dipolar interaction. In the case of an oriented sample (Figure 3.1) defined by the Euler angles from Equation 3.1 and for the general situation of an asymmetric tensor (i.e.

$\Lambda = CSA$ ) it can be shown that the RAS space components of the above equation (see also Equation 3.4) can be expressed as a function of PAS space components in the form ( $\theta_R = 90^\circ$  for an alignment using rolled films):

$$A_{2,2}^{RAS,\Lambda}(\alpha_\Lambda, \beta_\Lambda, \theta, \varphi, \varphi_R) = k \left\{ a_0(\beta_\Lambda, \theta, \varphi, \varphi_R, \theta_R) A_{2,0}^{PAS,\Lambda} + a_2(\alpha_\Lambda, \beta_\Lambda, \theta, \varphi, \varphi_R) A_{2,2}^{PAS,\Lambda} \right\} \quad (B.3)$$

with the coefficients  $a_0$  and  $a_2$  retaining only the angular dependence ( $d_{ij}$  refer to the reduced Wigner elements given in Appendix A.2, superscript omitted)

$$a_0(\beta_\Lambda, \theta, \varphi, \varphi_R) = \sum_{j=-2}^2 d_{0j}(\beta_\Lambda) \left\{ \frac{1}{2} d_{j2}(\theta) \cos(j\varphi + 2\varphi_R) - id_{j1}(\theta) \sin(j\varphi + \varphi_R) + \sqrt{\frac{3}{8}} d_{j0}(\theta) \cos(j\varphi) \right\} \quad (B.4)$$

and

$$a_2(\alpha_\Lambda, \beta_\Lambda, \theta, \varphi, \varphi_R) = \sum_{j=-2}^2 d_{2j}(\beta_\Lambda) \left\{ \frac{1}{2} d_{j2}(\theta) \cos(j\varphi + 2\alpha_\Lambda + 2\varphi_R) - id_{j1}(\theta) \sin(j\varphi + 2\alpha_\Lambda + \varphi_R) + 2\sqrt{\frac{3}{8}} d_{j0}(\theta) \cos(j\varphi + 2\alpha_\Lambda) - id_{j-1}(\theta) \sin(j\varphi + 2\alpha - \varphi_R) + \frac{1}{2} d_{j-2}(\theta) \cos(j\varphi + 2\alpha_\Lambda - 2\varphi_R) \right\} \quad (B.5)$$

Equations B.3-B.5 indicate that for symmetric tensors (dipolar,  $A_{2,2}^{PAS,D} = 0$ ) or CSA tensors with very small asymmetry parameters ( $^{15}\text{N}$  CSA,  $A_{2,2}^{PAS,CSA} \ll A_{2,0}^{PAS,CSA}$ ) the influence of the Euler PAS angle  $\alpha_\Lambda$  is canceled or negligible, respectively (not considered in numerical analysis from § 3.3).

Finally, the time dependence in the laboratory frame of the recoupled NMR signal as a function of the tilt ( $\theta$ ) and azimuthal ( $\varphi$ ) angles can be obtained from the expectation value of the detect operator  $D_\Lambda$ :

$$I_\Lambda(\theta, \phi, t) = \frac{1}{4\pi^2} \int_{\theta-\Delta}^{\theta+\Delta} \int_0^{2\pi} Tr \left\{ D_\Lambda e^{it\bar{\mathcal{H}}^{(0),\Lambda}} \rho_\Lambda(0) e^{-it\bar{\mathcal{H}}^{(0),\Lambda}} \right\} g(\tilde{\theta}) \sin(\tilde{\theta}) d\tilde{\theta} d\varphi_R \quad (B.6)$$

where  $\rho_\Lambda(0)$  represents the initial density matrix, and a Gaussian angular distribution  $g(\tilde{\theta})$  with a standard deviation  $\Delta$  (mosaic spread) around an average value  $\langle\theta\rangle$  has been assumed for the molecular tilt angle  $\langle\tilde{\theta}\rangle$ . If cylindrical symmetry around the molecular director axis  $\vec{a}$  (see Figure 3.1) can be assumed, a further integration  $\int_0^{2\pi} I_\Lambda(\theta, \phi, t) d\phi$  over the azimuthal angle  $\phi$  would render the signal modulation dependent only of the tilt angle  $I_\Lambda(\theta, t)$ .

To demonstrate the agreement between the analytical derivation presented here and the numerical analysis performed in § 3.3 (Figure 3.3) the case of a symmetric  $^{15}\text{N}$  CSA tensor (i.e.  $A_{2,2}^{PAS,CSA} = 0$ , see also Equation 3.2) was considered, assuming identical PAS and MOL frames ( $\beta_{CSA-N} = 0^\circ$ , i.e. Equation 3.5 for  $M = \pm 2$  valid). The results are shown in Figure B.1.

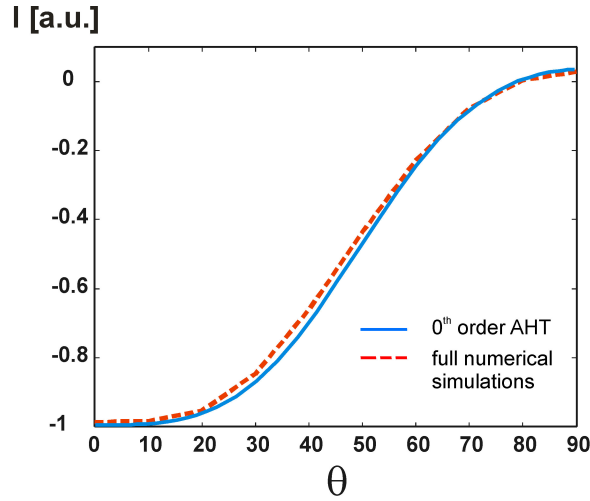


Figure B.1: Comparison between zeroth order Average Hamiltonian theory calculation and complete numerical simulation of the signal intensity function of the tilt angle  $\theta$  at the minimum dephasing point ( $t_{CSA-N} = 0.55$  ms) for the  $^{15}\text{N}$  CSA ( $\beta_{CSA-N} = 0^\circ$ ) recoupling experiment of Figure 3.5 using  $R18_2^5$  sequence at 6 kHz MAS and 600 MHz  $^1\text{H}$  magnetic field. Cylindrical symmetry was assumed for azimuthal angle  $\phi$ .

For simplicity cylindrical symmetry around the angle  $\varphi$  and perfect alignment (i.e.  $\Delta = 0^\circ$ ) have been assumed. The time was fixed to the value assumed in Figure 3.3 for the minimum dephasing point. The analytical derivation and integral calculation of Equations B.2-B.6 have been performed using Mathematica 4.1 (Wolfram Research Inc., Champaign, IL). Full numerical simulations using the piece-wise constant Hamiltonian approach as described in § 3.3 and the same  $^{15}\text{N}$  CSA parameters as mentioned above have been performed in GAMMA [43]. As visible in Figure B.1, both approaches led to similar results.

## B.2 $^{31}\text{P}$ spinning sidebands

A comparison between simulated and measured  $^{31}\text{P}$  spinning sidebands for lipids in their liquid crystalline phase can be used to check lipid bilayer alignment and to estimate the mosaic spread of reconstituted peptides.

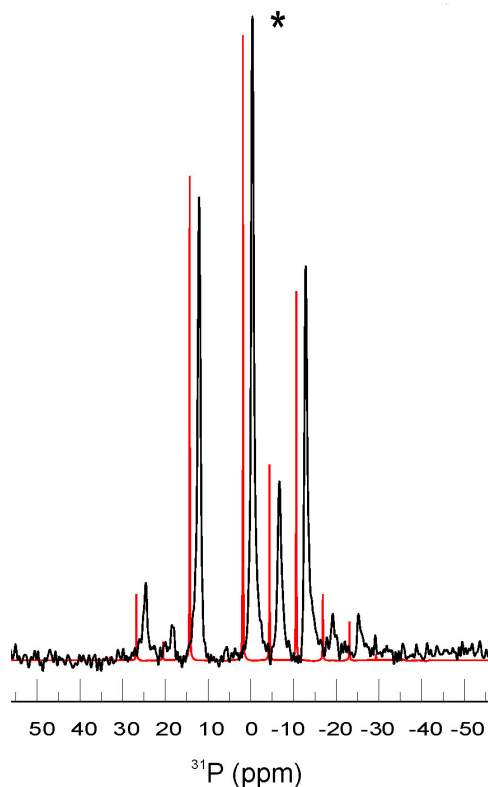


Figure B.2:  $^{31}\text{P}$  spinning sidebands for oriented samples of DMPC lipid bilayers and WALP23 (1 kHz MAS, 400 MHz  $^1\text{H}$  field, 40 °C, 16:1 L/P). In red simulated spinning sidebands (average tilt angle  $\theta = 0^\circ$ , mosaic spread  $\Delta = \pm 8^\circ$ ). A symmetric  $^{31}\text{P}$  CSA tensor [24] was considered:  $\sigma_\perp = -15.9$  and  $\sigma_\parallel = 31.9$  in ppm (asterisk indicates the isotropic line).

Simulation of the spinning sidebands has been performed in GAMMA [43] with a Floquet formalism [42] (see GAMMA program in Appendix B.3) and the Euler transformations described in Equation 3.1. Example of a spinning sideband spectrum for randomly oriented samples can be seen in Figure C.3.

## B.3 GAMMA simulation programs

```

/*****r1852-csa-maoss.cc*****/
* Program to simulate CSA recoupling under MAS for an oriented sample *
* * * * *
* R185_2 rf pulse sequence (Carravetta et al., CPL 2001, 342, 353-361) *
* R element 180 pulse, R(-R) = (180/50)(180/-50), {(180/50)(180/-50)}xND *
* rf=4.5*omegar, ND=9 corresponds to 2 rotor periods *
* * * * *
* MAOSS sample described by 5 reference frames: PAS, MOL, MEM, RAS, LAB. *
* The calculation is based on piecewise-constant Hamiltonian integration *
* Consider only the CSA Hamiltonian for one spin system *
* * * * *
* 20.06.2003 *
* written by Ovidiu Andronesi, MPIBPC *
*****/

# include "gamma.h"

int main (int argc, char*argv[])
{
    spin_system A(1); //1 spin system

    //B0 field
    coord B(0,0,1); //set B0 field direction along z
    double ppm; //size of B0 field

    //CSA interaction
    spin_T TTS = T_CS2(A,0,B); //CS spin tensor
    space_T CS_PAS,CS_MOL,CS_MEM,CS_RAS,CS_LAB; //CSA space tensor in PAS, MOL, MEM, RAS, LAB frames
    double sixx,siyy,sizz; //sigmaxx,sigmayy,sigmazz PAS values

    //r.f. field and MAS
    double omegarf; //r.f. field amplitude
    double RFphase; //r.f. field phase
    double carrier,offset; //carrier position
    double omegar; //MAS rate

    //Euler angles
    double theta0,spread; //average tilt angle and the mosaic spread

```

```

double      b;                                //the gaussian width
double      fgauss;                           //the gaussian distribution function

double      alpha,beta,gamma;                 //Set up the Euler rotation angles PAS->MOL
double      phiMM,thetaMM,gammaMM;            //MOL->MEM
double      phiMR,thetaMR,gammaMR;            //MEM->RAS
double      phiRL,ma;                          //RAS->LAB

ma = 54.73561;                                //Magic angle

//Number of points
int         NR;                                //Number of rotor periods
int         ND;                                //Number of detected points for 2 rotor periods (ND=9)
int         NC;                                //Number of calculated points for 2 rotor periods (NC>ND)
                                                //NC=720 to calculate in steps of 1 degree of MAS rotation

double      sf;                                //normalization factor
int         p=1;                              //counter for the input lines
string      outFileName;                      //Output filename dephasing curve

//Input parameters
query_parameter (argc,argv,p++, "outname"      = " ", outFileName);
query_parameter (argc,argv,p++, "Nr of rotations" = " ", NR);
query_parameter (argc,argv,p++, "Nr of detections [9]" = " ", ND);
query_parameter (argc,argv,p++, "Nr of calculations NC>ND" = " ", NC);
query_parameter (argc,argv,p++, "sigmaxx [ppm]" = " ", sixx);
query_parameter (argc,argv,p++, "sigmayy [ppm]" = " ", siyy);
query_parameter (argc,argv,p++, "sigmazz [ppm]" = " ", sizz);
query_parameter (argc,argv,p++, "ppm [ppm]" = " ", ppm);
query_parameter (argc,argv,p++, "offeset [ppm]" = " ", offset);
query_parameter (argc,argv,p++, "omegar [Hz]" = " ", omegar);
query_parameter (argc,argv,p++, "omegarf [Hz]" = " ", omegarf);
query_parameter (argc,argv,p++, "alpha [deg]" = " ", alpha);
query_parameter (argc,argv,p++, "beta [deg]" = " ", beta);
query_parameter (argc,argv,p++, "gamma [deg]" = " ", gamma);
query_parameter (argc,argv,p++, "theta0 [deg]" = " ", theta0);
query_parameter (argc,argv,p++, "spread [deg]" = " ", spread);
query_parameter (argc,argv,p++, "gauss distr. [deg]" = " ", b);

outFileName = outFileName+".dat";

int         NP = int((NR*ND)/2)+1;              //number of points in the dephasing curve
block_1D    spect(NP),specsum(NP),specsumL(NP),data(NP); //set data blocks

```



```

sixx = sixx*ppm;
siyy = siyy*ppm;           //calculate CSA for N15 at the B0 field specified by the ppm value
sizz = sizz*ppm;

carrier = (sixx+siyy+sizz)/3;    //put r.f. carrier on resonance
carrier = carrier + offset;      //put r.f. carrier off resonance

//define CSA space tensor in the PAS frame
matrix  s1(3,3);
        s1.put_h(sixx, 0, 0);  s1.put_h( 0., 0, 1);  s1.put_h( 0., 0, 2);
                                s1.put_h(siyy, 1, 1);  s1.put_h( 0., 1, 2);
                                s1.put_h(sizz, 2, 2);

CS_PAS = A2(s1);

//Operators
gen_op  sigma  = Iz(A,0);      //density matrix - longitudinal CSA recoupling sequence
gen_op  detect = Iz(A,0);      //detect operator

gen_op  H,H_cs,H_offset,H_onres,H_rf; //Hamiltonians
gen_op  S,P;                    //Propagators

gen_op  U[ND];                  //ND Propagators for two rotor periods

//time increments
double  dwtime  = 2./omegar;
int      intervall = int (NC/ND); //NC increment points per ND

//number of orientations
int      cmax = 12*1154;        //maximum number of orientations for the Cheng sampling method
int      smax = 12*1154;

        sf = 0;
        H_offset = carrier*Iz(A,0); //consider on resonance irradiation

// N.B.: for the Euler rotation from the PAS to the MOL frame for 15N
// we can take the X axis of the MOL frame the same as PAS, hence
// only the beta angle is needed for the transformation, i.e. alpha and gamma can be set to 0
// usually CS_mol = CS_pas.rotate(0.,17.,0.) for 15N in alpha-helix

CS_MOL = CS_PAS.rotate(alpha,beta,gamma); //PAS->MOL Euler rotation

```

```

/* -----MAOSS loops----- */
* calculate the CSA interaction in the Lab frame for all orientations *
* calculate the propagators for two rotor periods *
* evolve the density matrix under these propagators *
* sum up the contribution of all orientations *
*-----*/

for (int c=1;c<cmx;c+=int(cmx/(50.+2.*spread))) //MOL->MEM Euler rotation
{
    cout <<"c/cmx =" << 100*c/cmx << " of 100"<<"\r" << flush; //output the running state of the program

    thetaMM = theta0 + spread * (2. * c/cmx - 1.); //tilt angle
    fgauss = exp(-pow((thetaMM-theta0),2)/(2*pow(b,2))); //gaussian distribution

    phiMM = double(360./(12*1154.) * ((107*c)%(12*1154))); //consider cylindrical symmetry
    //for the azimuthal angle phiMM in [0,360]
    gammaMM = double(360./(12*1154.) * ((271*c)%(12*1154))); //gamma in [0,360]

    CS_MEM = CS_MOL.rotate(phiMM,thetaMM,gammaMM);

    for (int i=0; i<NP; i++) //initialize data
    {
        specsum(i) = 0.;
    }

    for (int s=1;s<smax;s+=50) //MEM->RAS Euler rotation
    {
        thetaMR = 90.; //angle between membrane normal and rotor axis
        phiMR = 0.; //phiMR = gammaMM
        //either phiMR or gammaMM can be skipped
        gammaMR = double(360./(12*1154.) * ((271*s)%(12*1154))); //gamma in [0,360]

        CS_RAS = CS_MEM.rotate(phiMR,thetaMR,gammaMR);

        S = Ie(A,0); //identity matrix
        //intialize propagators

    }

    //calculation for two rotor periods
    for (int m=0;m<ND;m++) //ND=9 number of detection points per two rotor period for R18^5_2
    {
        int beg = int (m*NC/ND); //beg = m*intervall;
        S = Ie(A,0); //initialize propagator
    }
}

```

```

for (int i=beg;i<beg+intervall;i++)          //RAS->LAB rotation
{
    //calculate propagators for each detected point in LAB frame

    phiRL = omegar/norm(omegar)*double(720.) * i/NC; //consider 2 rotor periods (720 degrees)

    CS_LAB = CS_RAS.rotate(phiRL,ma,0.);

    H_cs    = CS_LAB.component(0,0)*TTS.component(0,0);          //CSA Hamiltonian
    H_cs    = H_cs + CS_LAB.component(2,0)*TTS.component(2,0);
    H_onres = H_cs - H_offset;

    if      (i <= (beg + (intervall/2))) {RFphase= 50*PI/180;}
    else if ((beg + (intervall/2)) < i)  {RFphase=310*PI/180;}

    H_rf = sin(RFphase)*omegarf*Ix(A,0)+cos(RFphase)*omegarf*Iy(A,0); //r.f. field Hamiltonian

    H      = H_onres + H_rf;          //complete Hamiltonian

    P = prop (H,dwtime/NC);          //propagator for the piecewise-constant Hamiltonian
    S = P*S;          //propagator for one detected point

} //RAS-LAB and NC

U[m] = S;          //propagators over 2 rotor periods
//the Hamiltonian is periodic over 2 rotor periods

} //ND

sigma    = Iz(A,0);          //initialize the start density matrix for each orientation
spect(0) = trace(sigma,detect);          //first point

//calculate evolution for NR rotor periods for one orientation in LAB frame
//use the periodicity of the Hamiltonian over 2 rotor periods
//calculate ND points for each 2 rotor periods
for (int n=1; n<=int((NR*ND)/2); n++) //NR
{
    int i = int(((2*n)-1)/ND);          //counts the number of rotor periods

    if (i%2==0)          //odd rotor periods (!!i starts from 0, 0=first period)
    {
        int m = (n-1) - ND*int(i/2);          //m runs from 0 to [ND/2]-1 for odd periods
        evolve_ip(sigma,U[m]);
    }
}

```

```

else if (i%2==1)                                //even rotor periods
{
    int m = (n-1) - ND*int((i-1)/2);             //m runs from [ND/2] to ND for even periods
    evolve_ip(sigma,U[m]);
}

    spect(n) = trace(sigma,detect);

} //loop NR and LAB->RAS

    specsum = specsum + spect;                    //sum up orientations in RAS frame

} //loop RAS->MEM

    specsum = fgauss*sin(thetaMM*PI/180.) * specsum;

    specsumL = specsumL + specsum;                //sum up orientations in MEM frame

    sf = sf + fgauss*sin(thetaMM*PI/180.);        //calculate normalization factor
} //loop MEM->MOL

    specsumL = specsumL/(sf*int(smax/50));

//arrange time axis in ms
double tr = 1./omegar;                          //rotor period
double dw = 2*(tr/ND)*1000.;                    //dwell time in ms
double cpt = NR*tr*1000.;                       //cp time in ms

cout<<" "<<"\n";
cout<<"dw = " << dw*1000. << " us"<<"\n";
cout<<"cpt = " << cpt << " ms"<<"\n";

//writes the dephasing data points
for (int i=0; i < NP; i++)
{
    data(i) = complex(i*dw, Re(specsumL(i)));
}

    GP_xy(outFileName,data);

return 0;
}

```

```

/*=====ssbmaoss-floq.cc=====*/
*           Program to simulate spinning sidebands           *
*                                                                 *
* Description: Simulation of the MAS sideband pattern for a spin 1/2 system *
*           consider only CSA interaction and assume an oriented sample *
*           use 5 reference systems: PAS, MOL, MEM, RAS, LAB *
*           The MAS time dependence is described using Floquet Theory *
*                                                                 *
* Date:           16.03.2003 *
*                                                                 *
* Author:         Ovidiu Andronesi *
*           Max-Planck-Institute for Biophysical Chemistry *
*=====*/

#include "gamma.h"
int main (int argc, char *argv[])
{
    spin_system  A(1);                //Set up a 1 spin system called 'A'
    coord        B(0,0,1);            //vector of the magnetic field along z
    spin_T       TTS = T_CS2(A,0,B);   //CSA spin tensor

    double       sixx,siyy,sizz;      //sigmaxx,sigmayy,sigmazz,PAS values in ppm

    double       omegar;              //MAS rotation frequency
    double       sw, carrier;         //spectral window and carrier frequency
    double       minFreq, maxFreq;    //Spectral range

    double       theta0,spread,b;     //angle of average orientation, spread and std. deviation
    double       fgauss;              //Gauss distribution
    double       alpha,beta,gamma;    //Euler angles for PAS->MOL->MEM->RAS->LAB transformations
    double       thetaPM,thetaMR;
    double       phiPM,phiMR;
    double       gammaPM,gammaMR;

    int          p=1;
    int          N;                   //Floquet dimension
    int          NP = 4096;           //Number of points in spectrum
    string       outFileNames;       //Output filename
    int          lb;                  //line broadening

    //Input parameters
    query_parameter (argc,argv,p++,"name of output file      = ", outFileNames);
    query_parameter (argc,argv,p++,"Floquet dimension N,[N>=2] = ", N);

```



```

fsigma.put_block(sigma, 0, 0);          //initial Floquet density matrix
detect = Im(A,0);

//transformation from the 15N PAS to the MOL frame
CS_mol = CS_pas.rotate(alpha,beta,gamma);
//CS_mol = CS_pas.rotate(0.,17.,0.);      //for ideal alpha-helix

//Time and orientation independent component of the CS Hamiltonian
H_0 = CS_pas.component(0,0) * TTS.component(0,0);

//-----MAOSS loop -----//
//Nr of orientations for Cheng algorithm
int bmax = 12*1154;
int smax = 12*1154;
//Loop through spread in steps of about 1/10 degree
for (int b=1; b<bmax; b+=int(bmax/(50.+2*spread)))           //MOL->MEM transformation
{
    cout << "b/bmax = "<< 100*b/bmax <<" of 100" << "%\r" << flush;

    thetaPM = theta0 + spread * (2. * b/bmax - 1.);           //MAOSS
    fgauss = (1./(b*sqrt(2.*PI)))*exp(-(pow((thetaPM-theta0),2))/(2*b*b)); //gaussian distribution

    phiPM = double(360./(12*1154.) * ((107*b)%(12*1154)));    //phi in [0,360]
    gammaPM = double(360./(12*1154.) * ((271*b)%(12*1154)));  //gamma in [0,360]

    CS_M = CS_mol.rotate(phiPM,thetaPM,gammaPM);

    for (int i=0; i<NP; i++)
    {
        spect(i) = 0.;
    }

    for (int s=1;s<smax;s+=100)                               //MEM->RAS transformation
    {
        thetaMR = 90.;                                         //angle between membrane
                                                                    //normal and rotor axis (90 for foils)
                                                                    //may be different for other orientations!!

        phiMR = 0.;                                           //phiMR = gammaPM and can be skipped
        gammaMR = double(360./(12*1154.) * ((271*s)%(12*1154))); //gamma in [0,360]

        CS_R = CS_M.rotate(phiMR,thetaMR,gammaMR);
    }
}

```

---

```

//define rank 1 and 2 components of CSA Hamiltonian
H_1 = CS_R.component(2,1) * TTS.component(2,0);
H_1 = (1/sqrt(3.))*H_1;

H_2 = CS_R.component(2,2) * TTS.component(2,0);
H_2 = (1/sqrt(6.))*H_2;

//define the Floquet Hamiltonian
//includes RAS->LAB transformation and MAS

flop_op HAMFLOQ(N,A.HS(),omegar);           //Hamilton Floquet Matrix
HAMFLOQ.put_sdiag(adjoint(H_2),-2);         //set side diagonal # -2
HAMFLOQ.put_sdiag(adjoint(H_1),-1);         //set side diagonal # -1
HAMFLOQ.put_sdiag(H_0,0);                   //set main diagonal
HAMFLOQ.put_sdiag(H_1,1);                   //set side diagonal # 1
HAMFLOQ.put_sdiag(H_2,2);                   //set side diagonal # 2
HAMFLOQ.add_omega();                         //Add omegas on diagonal

//calculate contribution of one orientation
spec_maspowder (fsigma, detect, HAMFLOQ, minFreq, maxFreq, NP, spect);

//sum all MEM orientations (weight is one for 90 degree MEM orientation)
spect+= spect;
}

//weight and sum all MOL orientations
spect *= fgauss;
specsum += spect;

} //MAOSS loop

//Fourier transformation and line broadening
specsum = IFFT(specsum);
exponential_multiply(specsum,-lb);
specsum = FFT(specsum);

//arrange chemical shift axis in ppm for 15N at 600 MHz
for (int i=0; i<NP; i++)
{
    data(i) = complex((int(carrier) + int(sw*(1.*i/NP - 0.5)))/60.8, Re(specsum(i)));
}
GP_xy(outFileName,data);
}

```



## B.4 1D and 2D BRUKER pulse programs

```
;r1852c-1d.oca

;1D pulse program for 15N CSA recoupling using
;R18^5_2 sequence for CSA recoupling
;Ref.: Carravetta et al., CPL 2001, 342, 353-361
;written by Ovidiu Andronesi
;15.07.2003

;cnst31      : spinning speed
;p11         : 180 pulse r.f.=4.5*MAS
;l5          : 9 = 2 rotor periods
;d3          : constant time

"p11=(1s/cnst31)/9"
"d4 = d3-2*p11*l5"

#include<protection1d.oca>

1  ze
2  d1
   2u fq=0:f2
   2u pl2:f2
;90 pulse on 1H
   p2:f2 ph1
;cp 1H -> 15N
   2u pl5:f1 pl6:f2
   (p15 ph2):f1 (p15:spf0 pl6 ph0):f2
;start 1H decoupling
   2u pl12:f2
   2u cpds2:f2
;R18^5_2 15N CSA recoupling
;mixing along Z
   2u pl1:f1      ;90 pulse for 15N
   p1:f1 ph3
   2u pl11:f1     ;CSA recoupling
3  p11:f1 ph4
   p11:f1 ph5
   lo to 3 times l5 ;increment R18^5_2 recoupling time
   d4              ;delay for constant time
   2u pl1:f1
```

```
p1:f1 ph6          ;90 pulse for 15N
;aquisition
  gosc ph31
  1m do:f2
  lo to 2 times ns
  100m wr #0
HaltAcqu 1m
exit
```

```
ph0 = 0
ph1 = 1 1 1 1   1 1 1 1
      3 3 3 3   3 3 3 3
ph2 = 1
ph3 = 0 0 0 0   2 2 2 2
ph4 = (8192) 1138
ph5 = (8192) 7054
ph6 = 0 1 2 3
ph31 = 0 1 2 3   2 3 0 1
        2 3 0 1   0 1 2 3
```

```
;nc-r1852-spc5-2d.oca

;2D pulse program for 15N/13C correlations
;encode molecular orientation by 15N CSA modulation and
;transfer to isotropic 13C chemical shifts to identify secondary structure

;recoupling blocks used
;R18(5,2) sequence for 15N CSA recoupling
;SPECIFIC CP for N-Ca transfer
;SPC5 sequence for Ca-Cb DQ transfer
;written by Ovidiu Andronesi
;15.07.2003

;cnst31      : spinning speed
;p11         : 180 pulse for R18~5_2 at rf=4.5*MAS - R element=180 pulse
;p14         : 90  pulse for SPC5   at rf=5*MAS   - POST element
;l5          : 9 = 2 rotor periods, increment for R18~5_2 CSA recoupling
;l6          : 10 = 4 rotor periods, increment for SPC5 DQ transfer
;d3          : constant time for R18~5_2 CSA recoupling

"p11=(1s/cnst31)/9"
"p12=(1s/cnst31)/20"
"d4=d3-2*p11*15"

#include<protection2d.oca> ;protection file

1 ze
2 d1
   1m rpp6           ;reset phase pointers for SPC5
   1m rpp7
;90 pulse on 1H
   2u p12:f2
   p2:f2 ph1
;cp 1H -> 15N
   2u p15:f3 p16:f2
   (p15 ph2):f3 (p15:spf0 p16 ph0):f2
;start 1H decoupling with p113 power level
   2u p113:f2
   2u cpds2:f2
;R18~5_2 15N CSA recoupling along Z
   2u p11:f3
```

```

p1:f3 ph3          ;90 pulse on 15N
d4                ;constant time delay
2u pl11:f3
3 p11:f3 ph25      ;R18^5_2
p11:f3 ph26
lo to 3 times l5   ;increment R18^5_2 recoupling time
2u pl1:f3
p1:f3 ph4          ;90 pulse on 15N
;t1 evolution 15N
d0
;SPECIFIC CP N-Ca
2u pl15:f3 pl16:f1
(p25 ph15):f3 (p25:spf1 pl16 ph16):f1
;SPC5 DQ Ca-Cb transfer along Z
2u pl3:f1
p3:f1 ph17         ;90 pulse on 13C
2u pl14:f1
4 p14*1:f1 ph6     ;SPC5 with POST element
p14*4:f1 ph7^      ;increment phase pointers
p14*3:f1 ph6^
lo to 4 times l6   ;increment SPC5 mixing time
2u pl3:f1
p3:f1 ph18         ;90 pulse on 13C
;13C t2 evolution - aquisition
5u pl12:f2         ;start 1H decoupling with pl12 power level
5u cpds2:f2
gosc ph31
1m do:f2
lo to 2 times ns
100m wr #0 if #0 zd
1m id0             ;increment t1
1m ip2             ;TPPI for t1
1m ip3
1m ip4
lo to 1 times td1
HaltAcqu 1m        ;safety address
exit

ph0 = 0
ph1 = 0 0 0 0 0 0 0 0 0 0 0 0 0 0 0 0
      0 0 0 0 0 0 0 0 0 0 0 0 0 0 0 0
      0 0 0 0 0 0 0 0 0 0 0 0 0 0 0 0
      2 2 2 2 2 2 2 2 2 2 2 2 2 2 2 2

```

```

      2 2 2 2  2 2 2 2  2 2 2 2  2 2 2 2
      2 2 2 2  2 2 2 2  2 2 2 2  2 2 2 2
      2 2 2 2  2 2 2 2  2 2 2 2  2 2 2 2
ph2   = 0
ph3   = 1 1 1 1  1 1 1 1  1 1 1 1  1 1 1 1
      1 1 1 1  1 1 1 1  1 1 1 1  1 1 1 1
      3 3 3 3  3 3 3 3  3 3 3 3  3 3 3 3
      3 3 3 3  3 3 3 3  3 3 3 3  3 3 3 3
ph25  = (8192) 1138
ph26  = (8192) 7054
ph4   = 1 1 1 1  1 1 1 1  1 1 1 1  1 1 1 1
      3 3 3 3  3 3 3 3  3 3 3 3  3 3 3 3
ph15  = 0 0 0 0  0 0 0 0  2 2 2 2  2 2 2 2
ph16  = 0
ph17  = 1 1 1 1  3 3 3 3
ph6   = (8192)    0 1638 3277 4915 6554 4096 5734 7373  819 2458
ph7   = (8192) 4096 5734 7373  819 2458    0 1638 3277 4915 6554
ph18  = 0 1 2 3
ph31  = 0 1 2 3  2 3 0 1  2 3 0 1  0 1 2 3
      2 3 0 1  0 1 2 3  0 1 2 3  2 3 0 1
      2 3 0 1  0 1 2 3  0 1 2 3  2 3 0 1
      0 1 2 3  2 3 0 1  2 3 0 1  0 1 2 3
      2 3 0 1  0 1 2 3  0 1 2 3  2 3 0 1
      0 1 2 3  2 3 0 1  2 3 0 1  0 1 2 3
      0 1 2 3  2 3 0 1  2 3 0 1  0 1 2 3
      2 3 0 1  0 1 2 3  0 1 2 3  2 3 0 1

```

# Appendix C

## PLN assignment and experimental conditions

### C.1 Scalar-coupling based pulse programs

```
;hnc-inept-tobsy_2d.oca
;2D experiment: selective N-CO/CA refocused INEPT + CO-CA/CA-CB TOBSY
;Pulse sequence for sequential assignment of dynamical protein segments
;written by Ovidiu Andronesi 20.02.2005

;f1:13C detect channel
;f2:1H channel
;f3:15N channel
;cnst2 = J_HN coupling
;cnst4 = J_NC coupling
;cnst3 = 4
;cnst5 = 4
;cnst20 = 13C carrier offset for N-CO/CA selective INEPT
;p11 = rf power for 13C 90 pulse
;p12 = rf power for 1H 90 pulse
;p13 = rf power for 15N 90 pulse
;p14 = rf power for 13C selective 90 pulse for N-CO/CA INEPT
;p1 = pulse length for 13C 90 pulse
;p2 = pulse length for 1H 90 pulse
;p3 = pulse length for 15N 90 pulse
```

```
;p4 = pulse length for 13C selective 90 for N-CO/CA INEPT
```

```
;spin-echo delays for H-N INEPT
```

```
"d4=(1s)/(4*cnst2)"
```

```
"d3=(1s)/(cnst3*cnst2)"
```

```
"d13=p3-p2" ;compensation H-N delay when p1>p2
```

```
"d14=d13/2"
```

```
;spin-echo delays for N-CO/CA INEPT
```

```
"d5=(1s)/(4*cnst4)"
```

```
"d6=(1s)/(cnst5*cnst4)"
```

```
"d15=p4-p3" ;compensation N-CO delay when p1>p3
```

```
"d16=d15/2"
```

```
"d17=p1-p2" compensation H-C delay for t1 evolution
```

```
;TOBSY P9(3,1) mixing
```

```
;cnst31 = MAS rate
```

```
;p11 = 90 pulse for TOBSY
```

```
;p11 = r.f power for TOBSY, 6xMAS
```

```
;l5 = TOBSY mixing time - l5 = 9 equals 3 rotor periods
```

```
;Ex: MAS=8.33kHz, p11=50kHz, p11=5u, l5=153~6.1ms
```

```
"p11=1s/(24*cnst31)"
```

```
#include<protection_ls.oqa> ;protection file
```

```
1 ze
```

```
2 d1 do:f2
```

```
5u fq=0:f2
```

```
5u fq=cnst20:f1
```

```
5u p11:f1
```

```
5u p12:f2
```

```
5u p13:f3
```

```
20u rpp18
```

```
20u rpp19
```

```
;90 on H
```

```
p2:f2 ph1
```

```
;H->N refocused INEPT
```

```
;spin-echo (antiphase)
```

```
d3
```

```
(p3*2 ph2):f3 (d13 p2*2 ph3):f2
```

```
d3
```

```
;Polarization Transfer
```

```

      (p3 ph4):f3    (d14 p2 ph5):f2
;spin-echo (inphase)
      d4
      (p3*2 ph6):f3 (d13 p2*2 ph7):f2
      d4
;15N t1 evolution
      d0
      (d17 p2*2 ph8):f2 (p1*2 ph9):f1
      d0
;H dec during NC inept
      2u pl13:f2
      2u cpds1:f2
;selective N->CO/CA refocused INEPT
;spin-echo (antiphase)
      d5 pl4:f1
      (d15 p3*2 ph10):f3 (p4*2 ph11):f1
      d5
;Polarization Transfer
      (d16 p3 ph12):f3    (p4 ph13):f1
;spin-echo (inphase)
      d6
      (d15 p3*2 ph14):f3 (p4*2 ph15):f1
      d6 pl1:f1
;TOBSY P9(3,1) C<->C longitudinal mixing
      p1:f1  ph16
      2u fq=0:f1
      2u pl11:f1
      2u do:f2
3  p11*1:f1 ph18
   p11*4:f1 ph19~
   p11*3:f1 ph18~
   lo to 3 times l5
   2u pl1:f1
   p1:f1 ph17
;acquisition
      2u pl12:f2
      2u cpds2:f2
      10u
      go=2 ph31
      1m do:f2
      100m wr #0 if #0 zd
      1m id0
      1m ip2

```



```

1m ip4
1m ip6
lo to 1 times td1
HaltAcqu, 1m
exit

```

```

ph1  = 1
ph2  = 1
ph3  = 1
ph4  = 0
ph5  = 0 0 2 2
ph6  = 1
ph7  = 1
ph8  = 0
ph9  = 0
ph10 = 1
ph11 = 1
ph12 = 0 2
ph13 = 0
ph14 = 1
ph15 = 1
ph16 = 1 1 1 1 3 3 3 3
ph17 = 0 0 0 0 0 0 0 0
      1 1 1 1 1 1 1 1
      2 2 2 2 2 2 2 2
      3 3 3 3 3 3 3 3
ph18 = (16384) 0      1820 3641 5461 7282 9102 10923 12743 14566
ph19 = (16384) 8192 10012 11833 13653 15474 910 2730 4551 6371
ph31 = 0 2 2 0 2 0 0 2
      1 3 3 1 3 1 1 3
      2 0 0 2 0 2 2 0
      3 1 1 3 1 3 3 1

```

```
;nhhc-inept-noesy_2d.oca
;2D experiment: direct H-N INEPT + reversed N-H INEPT + H-H NOESY + H-C refocused INEPT
;Pulse sequence for through-space contacts of dynamical protein segments
;written by Ovidiu Andronesi 20.02.2005

;f1:13C detect channel
;f2:1H channel
;f3:15N channel
;p11 = rf power for 13C 90 pulse
;p12 = rf power for 1H 90 pulse
;p13 = rf power for 15N 90 pulse
;cnst2 = J_HN coupling
;cnst3 = J_HC coupling
;cnst4 = 6
;cnst20 = 13C carrier offset during H-C refocused INEPT
;d11 H-H NOESY mixing time

;spin-echo delays for H-N INEPT
"d2=(1s)/(4*cnst2)"
"d12=p3-p2" ;compensation H-N delay when p3>p2
"d13=d12/2"

;spin-echo delays for refocused H-C INEPT
"d3=(1s)/(4*cnst3)"
"d4=(1s)/(cnst4*cnst3)"
"d14=p1-p2" ;compensation H-C delay when p1>p2
"d15=d14/2"

#include<protection_ls.oca> ;protection file

1 ze
2 d1 do:f2
   5u fq=0:f2
   5u fq=cnst20:f1
   5u p11:f1
   5u p12:f2
   5u p13:f3
;90 on H
   p2:f2 ph1
;direct H->N INEPT
;spin-echo
   d2
   (p3*2 ph3):f3 (d12 p2*2 ph2):f2
```

```
d2
;Polarization Transfer
  (p3 ph4):f3   (d13 p2 ph5):f2
;15N t1 evolution
  d0
  (p1*2 ph6):f1 (d14 p2*2 ph7):f2
  d0
;reverse N->H INEPT
;Polarization Transfer
  (p3 ph8):f3   (d13 p2 ph9):f2
;spin-echo
  d2
  (p3*2 ph10):f3 (d12 p2*2 ph11):f2
  d2
;H<->H NOESY mixing
  p2:f2 ph12
  d11
  p2:f2 ph13
;refocused H->C INEPT
;spin-echo (antiphase)
  d3
  (p1*2 ph14):f1 (d14 p2*2 ph15):f2
  d3
;Polarization Transfer
  (p1 ph16):f1   (d15 p2 ph17):f2
;spinecho (inphase)
  d4
  (p1*2 ph18):f1 (d14 p2*2 ph19):f2
  d4
;aquisition
  5u pl12:f2
  5u cpds2:f2
  5u fq=0:f1
  10u
  go=2 ph31
  1m do:f2
  100m wr #0 if #0 zd
  1m id0
  1m ip3
  1m ip4
  lo to 1 times td1
  HaltAcqu, 1m
exit
```

```
ph1  = 1
ph2  = 1
ph3  = 1
ph4  = 0
ph5  = 0 2
ph6  = 0
ph7  = 0
ph8  = 0 0 2 2
ph9  = 0
ph10 = 1
ph11 = 1
ph12 = 1 1 1 1 1 1 1 1
      3 3 3 3 3 3 3 3
ph13 = 1
ph14 = 1
ph15 = 1
ph16 = 0
ph17 = 0 0 0 0 2 2 2 2
ph18 = 1
ph19 = 1
ph31 = 0 2 2 0 2 0 0 2
      2 0 0 2 0 2 2 0
```

## C.2 3D HCC experiment

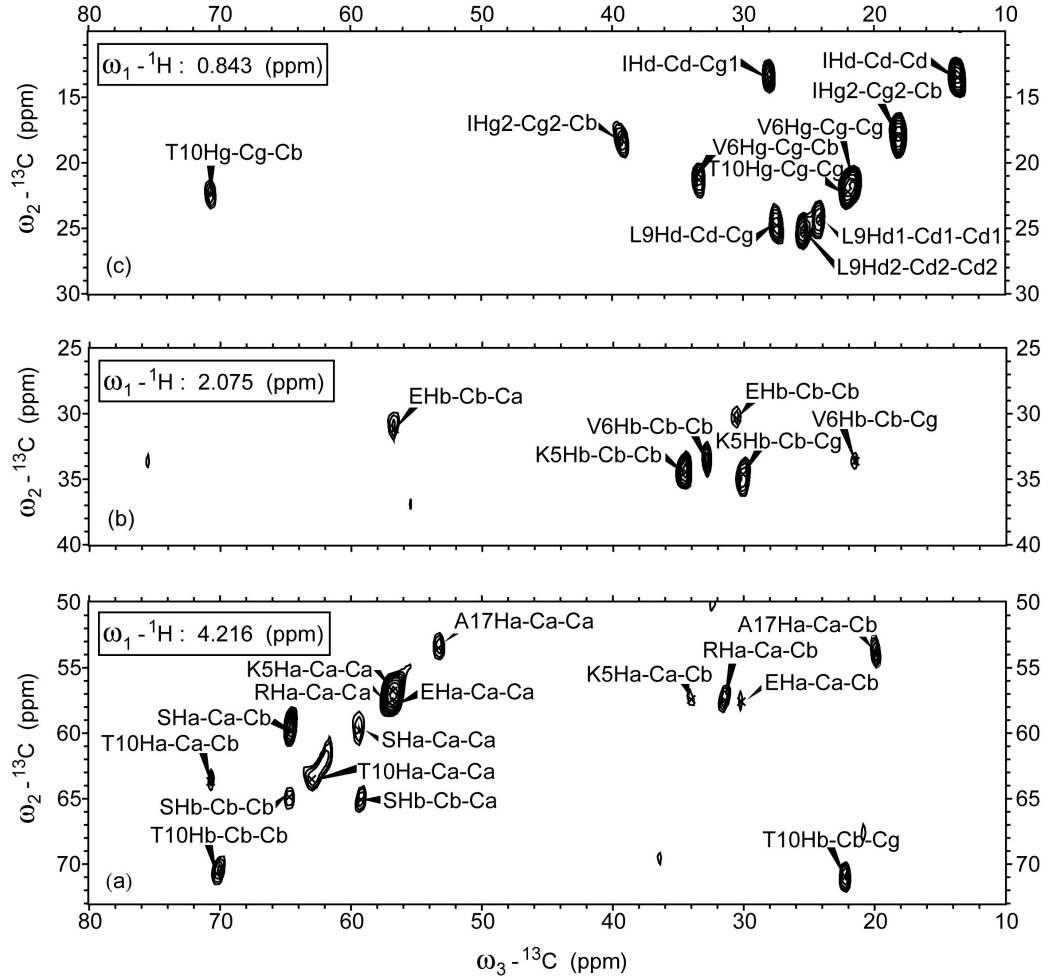


Figure C.1: 2D ( $^{13}\text{C}$ ,  $^{13}\text{C}$ ) slices from a 3D HCC spectrum of AFA-PLN in DMPC-D67 bilayers using the pulse sequence of Figure 4.5 (b): 10  $t_1$  (5 ppm  $^1\text{H}$  spectral width) and 30  $t_2$  (80 ppm  $^{13}\text{C}$  spectral width) experiments were recorded using 128 scans under the experimental conditions described in Figure 4.7. Representative slices at  $^1\text{H}$  frequencies for  $\text{H}_\alpha$  (a),  $\text{H}_\beta$  (b) and methyl groups (c) are shown.

## C.3 Assignment table

Res	N	CO	CA	CB	CG1	CG2	CD	CE	HN	HA	HB	HG1	HG2	HD	HE
<b>G1</b>			44.4							3.8					
<b>S2</b>	111.2		58.6	63.9					8.1	4.4	3.8				
<b>M3</b>	121.3		54.3	33.0	33.0			17.9	8.3	4.7	1.9	2.6			2.0
<b>E4</b>	120.6		57.4	29.9	35				8.1	4.2	1.9	2.2			
<b>K5</b>	121.2		56.6	32.9	25		29.4	42.3	8.6	4.3	1.7	1.3		1.6	3.8
<b>V6</b>	120.2		62.7	32.8	20.9	20.9			8.0	3.9	1.9	0.8	0.8		
<i>Q7</i>	122.6		55.7	32.6	31.8				8.3	4.4	2.0	2.5			
<b>Y8</b>	121.1		57.9	38.9	130.5		133.0	118.3	8.3	4.5	2.9	7.0		7.0	6.7
<b>L9</b>	122.2		55.5	42.6	27.2		25/23.7		8.2	4.3	1.5	1.5		0.8	
<b>T10</b>	113.6		62.1	70.0	21.8				7.9	4.2	4.1	1.1			
<b>R11</b>	122.0		56.4	30.7	27.2		43.5		8	4.2	1.7	1.5		3.1	
<b>S12</b>	115.3		58.6	63.9					8.1	4.4	3.8				
<b>A13</b>	125.0		52.7	19.2					8.3	4.2	1.3				
<b>I14</b>	119.0		61.4	38.7	27.6	17.6	13.7		7.9	4.0	1.8	1/1.4	0.8	0.8	
<b>R15</b>	121.5		55.2	30.7	27.2		43.5		8.0	4.2	1.7	1.5		3.1	
<b>R16</b>	122.3		56.0	30.7	27.2		43.5		8.0	4.2	1.7	1.5		3.1	
<b>A17</b>	124.8		52.7	19.2					8.3	4.2	1.3				
<b>S18</b>	114.2		58.4	63.9					8.3	4.4	3.8				
<b>T19</b>	114.9		62.0	70.0	21.8				8.6	4.2	4.1	1.1			
<b>I20</b>	123.9		61.3	38.7	27.6	17.6	13.7		8.3	4.0	1.8	1/1.4	0.8	0.8	
<b>E21</b>	124.5		56.0	29.6	35.0				8.3	4.2	1.9	2.2			
<b>M22</b>	120.2		53.6	32.3	32.6			17.2	8.2	4.7	2.0	2.5			2.0
<b>P23</b>				33.9	29.9		51.5				2.1	1.9		2.9	
<i>Q24</i>															
<i>Q25</i>		174.9	54.8	33.1			180								
<b>A26</b>	123.8	176.6	51.4	22.9											
<b>R27</b>	116.9	176.7	55.4	34.5	28.5		44.1								
<b>Q28</b>	120.6	173.8	54.2	33.4	34.4		180								
<i>K29</i>	123.6	174.5	55.0	29.9	25.7		27.7	44.1							
<i>L30</i>	121.5	61.6	40.4	27.1		23.4									
<i>Q31</i>	111.8	179.0	58.9	28.9	37.7		180								

Table C.1:  $^1\text{H}$ ,  $^{13}\text{C}$  and  $^{15}\text{N}$  chemical shifts for the cytoplasmic and transmembrane domains of AFA-PLN in DMPC-D67 lipid bilayers according to MAS solid-state NMR. Ambiguous assigned residues are given in italic letters and correspond to the light colored secondary shifts from Figure 4.12.

[illegible]

## C.4 Sample preparation

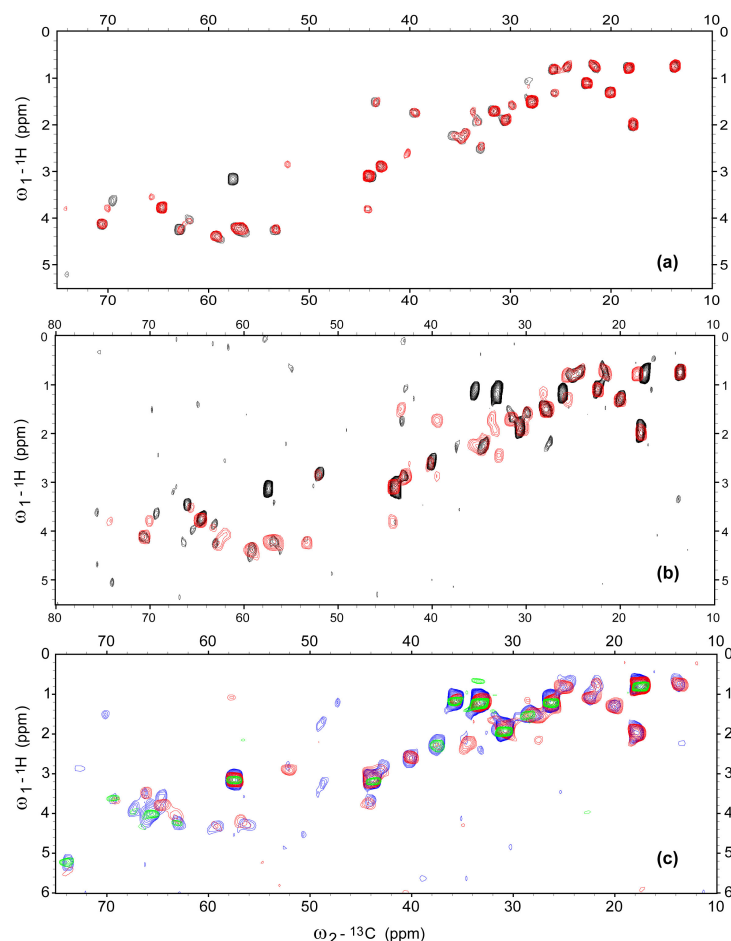


Figure C.2: 2D HC INEPT spectra on different AFA-PLN sample preparations: (a) comparison of different L/P ratios (red 20:1 vs. black 100:1) for AFA-PLN in DMPC-D67, (b) comparison of AFA-PLN in different lipid types DMPC-D67 (red) vs. DOPC/DOPE (4:1, black) for the same L/P = 20:1, (c) comparison of AFA-PLN in DOPC/DOPE lipid mixture before lyophilization (red) and after lyophilization (blue), for reference the spectrum of a sample containing only DOPC/DOPE is shown in green. The observed differences relate mainly to the lipids, either because of stronger lipid background (L/P = 100:1) or resonances due to extra  $^{13}\text{C}$  types (DOPC/DOPE).



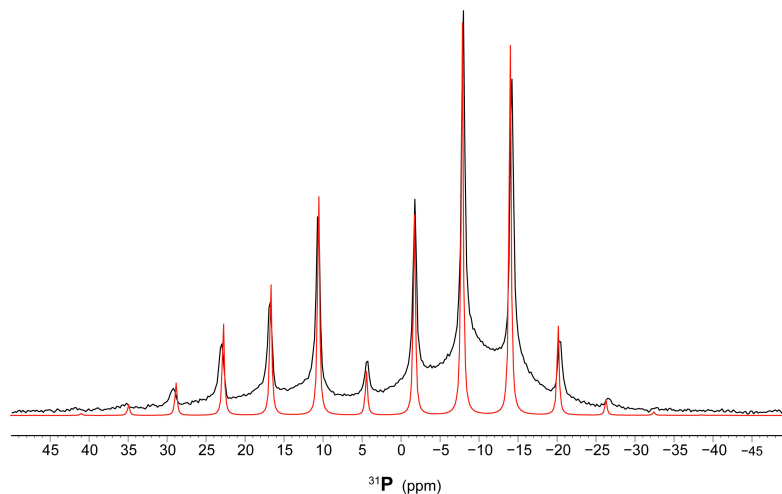


Figure C.3:  $^{31}\text{P}$  spinning-sidebands are diagnostic for formation of correct lipid bilayers: comparison between experimental (black) spinning-sidebands obtained for AFA-PLN in DMPC-D67 (L/P = 100:1) at 30 °C, 1 kHz MAS, 9.4 T  $B_0$  field and simulated (red) spinning sidebands. A symmetric  $^{31}\text{P}$  CSA tensor (rotationally averaged for lipid molecules in liquid-crystalline lipid bilayers) and a randomly oriented sample (liposomes) were considered. Simulations have been done in GAMMA [43] (see Figure B.2 and Appendix B.3).

## C.5 Dipolar-coupling based pulse sequences

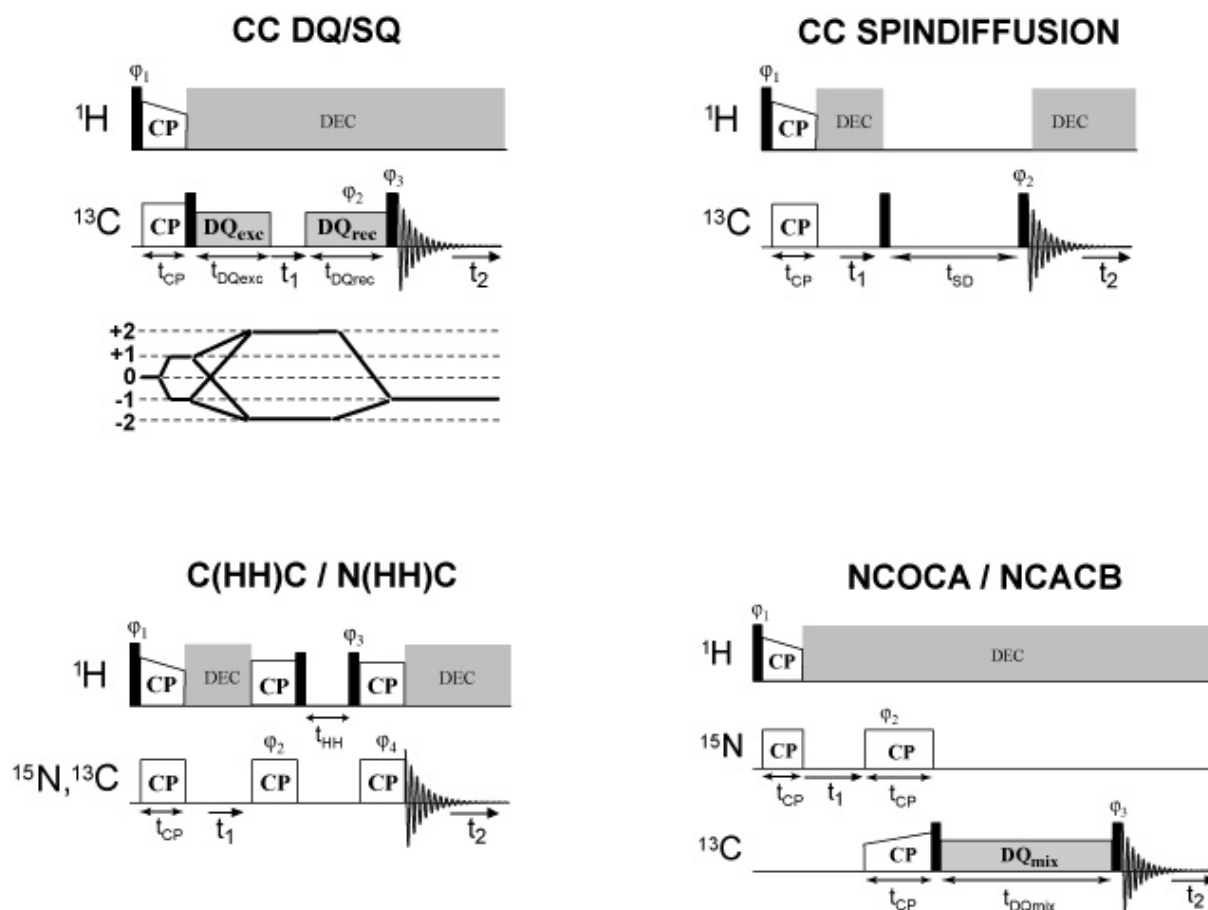


Figure C.4: Pulse sequences for dipolar-coupling based MAS solid-state NMR experiments to detect rigid protein domains (coherence transfer pathway and pulse program are given for the 2D CC DQ/SQ experiment).

```

;spc5-2qs.oqa
;2D 13C-13C DQ/SQ pulse program
;uses SPC5 DQ sequence

;cnst31      = spinning rate (Hz)
;l5          = DQexc/rec time: multiple of 80 = 4 rotor periods
;in0         = increment for DQ evolution must be rotor synchronized
;ph7         = DQ reconversion phase (has to be incremented for rotor
;             synchronization by 180*in0*cnst31 or 4k*in0/tr if 360=8k)

;Ex: MAS=7.5kHz, in0=26.67us (tr/5), SW1=124ppm (600MHz), ipp7=819
;Ex: MAS=7.5kHz, in0=13.33us (tr/10), SW1=248ppm (600MHz), ipp7=410

"p11=1s/(cnst31*20)"
"in0=1s/(cnst31*5)"

#include <protection2d.oqa>

1 ze
2 d1
   1m rpp6
   1m rpp7
   1u fq=0:f2
;90 H
   1u pl2:f2
   p2:f2 ph1
;CP H-C
   1u pl5:f1 pl6:f2
   (p15 ph2):f1 (p15:spf0 pl6 ph0):f2
;1H dec
   1u pl12:f2 pl1:f1
   1u cpds2:f2
;13C DQ excitation with spc-5
   p1:f1 ph4
   1u pl11:f1
3 p11:f1 ph6^ ipp7
   lo to 3 times l5
;t1 DQ evolution
   d0
;13C DQ reconversion with spc-5
4 p11:f1 ph7^

```

```

    lo to 4 times l5
    1u pl1:f1
    p1:f1 ph5
;aqusition
    10u
    gosc ph31
    1m do:f2
    1m ip5
    1m ip7*2048
    lo to 2 times ns
    100m wr #0 if #0 zd
    1m id0
;TPPI for DQ
    1m ip2
    1m ip4
    1m ip6*1024
;synchronization of the DQ reconversion with in0 (in0=tr/5)
    1m ip7*819
    lo to 1 times td1
exit

```

```

ph0 = 0
ph1 = 1 1 1 1    3 3 3 3
ph2 = (8) 0
ph4 = (8) 6
ph5 = 1
ph6 = (8192)    0 4096 4096 4096 4096    0    0    0
               1638 5734 5734 5734 5734 1638 1638 1638
               3277 7373 7373 7373 7373 3277 3277 3277
               4915 819 819 819 819 4915 4915 4915
               6554 2458 2458 2458 2458 6554 6554 6554
               4096    0    0    0    0 4096 4096 4096
               5734 1638 1638 1638 1638 5734 5734 5734
               7373 3277 3277 3277 3277 7373 7373 7373
               819 4915 4915 4915 4915 819 819 819
               2458 6554 6554 6554 6554 2458 2458 2458
ph7 = (8192)    0 4096 4096 4096 4096    0    0    0
               1638 5734 5734 5734 5734 1638 1638 1638
               3277 7373 7373 7373 7373 3277 3277 3277
               4915 819 819 819 819 4915 4915 4915
               6554 2458 2458 2458 2458 6554 6554 6554
               4096    0    0    0    0 4096 4096 4096

```

5734 1638 1638 1638 1638 5734 5734 5734  
7373 3277 3277 3277 3277 7373 7373 7373  
819 4915 4915 4915 4915 819 819 819  
2458 6554 6554 6554 6554 2458 2458 2458

ph31= 0 3 2 1      2 1 0 3

# Appendix D

## K19 PHFs assignment table and model validation

### D.1 Assignment table

Res	N	CA	CB	CG1	CG2	CD	CE	HA	HB	HG1	HG2	HD	HE
M	126.3	56.5	32.7	31.6			17.1	3.7	1.8	2.4			1.9
Q244	121.4	57.5	30.5	32.2				3.8	1.7	2			
T245	113	63.3	68.9	22.5				3.4	4.1	1.1			
A246	123	53.5	19.3					3.5	1.3				
P247		64	31.8	26.7		49.1		3.9	2.1	1.8		3.1	
V248	63.2	32	20.8	19.7			3.4	2.1	0.8				
P249		64	31.8	26.7		49.1		3.9	2.1	1.8		3.1	
M250	126.3	56.8	32.7	31.6			17.1	3.7	1.8	2.4			1.9
P251		64	31.8	26.7		49.1		3.9	2.1	1.8		3.1	
D252	123.5	55	39.5					3.7	2.5				

Table D.1: Chemical shifts (in ppm) for the flexible termini ( $^1\text{H}$ ,  $^{13}\text{C}$ ,  $^{15}\text{N}$ ) and rigid core ( $^{13}\text{C}$ ,  $^{15}\text{N}$ ) of the K19 PHFs as obtained from MAS ssNMR spectra shown in Figure 5.3 (a,b) and Figure 5.4 (a-d).

[illegible]

Res	N	CA	CB	CG1	CG2	CD	CE	HA	HB	HG1	HG2	HD	HE
G323	111.7	44.8											
S324	119.8	57.2	66.1										
L325	125.2	53.2	44.8	28.6		25.4							
G326	115.5	44.9											
N327	122.6	52.6	44.8										
I328	124.5	59.4	37.4	27.4	17	14.2							
H329													
H330													
K331													
P332		62.9	32.5	27.6		51							
G333	109	45.1											
G334	108.5	44.9											
G335	113.2	44.9											
Q336	116.6	53.1	28.8										
V337													
E338						183.6							
V339													
K340													
S341	109.5	56.9	66.4										
E342	117.5					183.6							
K343													
L344		54	45.8	27.3									
D345	114.4	51.7	44.2	179.6									
F346	125.8	57.4	40.5										
K347	124	54.1	35.3	25.5		30	42.3						
D348	127.1	53	42.1	179.5									
R349	127.4	56.6	33.2	27.1		43.7	159.7						
V350													
Q351													
S352	118.2	59.7	65.4										
K353													
I354		63.5	39.5	27.5	17.8	14.8							
G355													
S356													
L357	121	56.3	42.6			23.9		3.5	1.5			0.7	
D358	125.2	55.8	39.6					3.8	2.5				
N359													
I360		62.3	38.6	27.5	17.7	14.2		3.5	1.7	1.3	0.7	0.7	
T361		63	68.9	22.5				3.4	4.1	1.1			
H362	129.7	61.2	28.2										
V363		63.2	32	20.9	19.8			3.4	2.1	0.8			



Res	N	CA	CB	CG1	CG2	CD	CE	HA	HB	HG1	HG2	HD	HE
<b>P364</b>		64	31.8	26.7		49.1		3.9	2.1	1.8		3.1	
<b>G365</b>		45.4						3.8					
<b>G366</b>	107.8	45.4						3.8					
<b>G367</b>	108	45.5						3.8					
<b>N368</b>													
<b>K369</b>	125.1	58	33.7	25.5		29.3	42.2	3.9	1.6	1.2		1.5	2.8
<b>K370</b>	126.4	58	33.7	25.5		29.3	42.2	3.9	1.6	1.2		1.5	2.8
<b>I371</b>	117.7	62.2	38.6	27.5	17.7	14.2		3.5	1.7	1.3	0.7	0.7	
<b>E372</b>	126.8	57.8	30	36.2				3.6	1.9	2.1			

## D.2 Experimental conditions

Figure	B <sub>0</sub> (MHz)	MAS (kHz)	Pulse sequence parameters	2D parameters: SW <sub>1</sub> , t <sub>1</sub> , NS
Fig. 5.3 (a)	600	8.333	$^1J_{\text{HC}} = 145 \text{ Hz}$ , 6ms P9 <sub>1</sub> <sup>3</sup> TOBSY	8 ppm $^1\text{H}$ spectral width, 100 t <sub>1</sub> experiments, 272 scans
Fig. 5.3 (b)	600	9.375	t <sub>CP-HC</sub> = 250 $\mu\text{s}$ , t <sub>SD</sub> = 150 ms	80 ppm $^{13}\text{C}$ spectral width, 145 t <sub>1</sub> experiments, 560 scans
Fig. 5.4 (a)	800	8.333	$^1J_{\text{HN}} = 110 \text{ Hz}$ , $^1J_{\text{NCA}} = 25 \text{ Hz}$	27 ppm $^{15}\text{N}$ spectral width, 25 t <sub>1</sub> experiments, 5k scans
Fig. 5.4 (b)	800	8.333	$^1J_{\text{HN}} = 110 \text{ Hz}$ , $^1J_{\text{NCO}} = 25 \text{ Hz}$ , 8ms P9 <sub>1</sub> <sup>3</sup> TOBSY mixing	27 ppm $^{15}\text{N}$ spectral width, 26 t <sub>1</sub> experiments, 7k scans
Fig. 5.4 (c)	800	10	t <sub>CP-HN</sub> = 800 $\mu\text{s}$ , t <sub>CP-NCA</sub> = 1.75 ms	50 ppm $^{15}\text{N}$ spectral width, 32 t <sub>1</sub> experiments, 400 scans
Fig. 5.4 (d)	800	10	t <sub>CP-HN</sub> = 800 $\mu\text{s}$ , t <sub>CP-NCO</sub> = 2.5 ms, t <sub>DARR</sub> = 30 ms	50 ppm $^{15}\text{N}$ spectral width, 32 t <sub>1</sub> experiments, 3.3k scans
Fig. 5.6 (a)	800	10	t <sub>CP-HN</sub> = 800 $\mu\text{s}$ , t <sub>CP-NH</sub> = 65 $\mu\text{s}$ , t <sub>MIX-HH</sub> = 80 $\mu\text{s}$ , t <sub>CP-HC</sub> = 50 $\mu\text{s}$	50 ppm $^{15}\text{N}$ spectral width, 42 t <sub>1</sub> experiments, 2.6k scans
Fig. 5.6 (b)	800	12.5	t <sub>CP-HC</sub> = 250 $\mu\text{s}$ , t <sub>CP-CH</sub> = 100 $\mu\text{s}$ , t <sub>MIX-HH</sub> = 250 $\mu\text{s}$ , t <sub>CP-HC</sub> = 100 $\mu\text{s}$	70 ppm $^{13}\text{C}$ spectral width, 102 t <sub>1</sub> experiments, 1.5k scans
Fig. 5.6 (c)	800	10	$\delta = 2.5 \text{ ms}$ , t <sub>MIX-HH</sub> = 6 ms, t <sub>CP-HN</sub> = 800 $\mu\text{s}$ , t <sub>CP-NCA</sub> = 1.75 ms	70 ppm $^{13}\text{C}$ spectral width, 102 t <sub>1</sub> experiments, 1.5k scans

Table D.2: Experimental conditions, pulse sequence and 2D acquisition parameters for MAS ssNMR spectra of K19 PHFs. In all experiments the temperature was set to 5 °C.

### D.3 Chemical shifts analysis

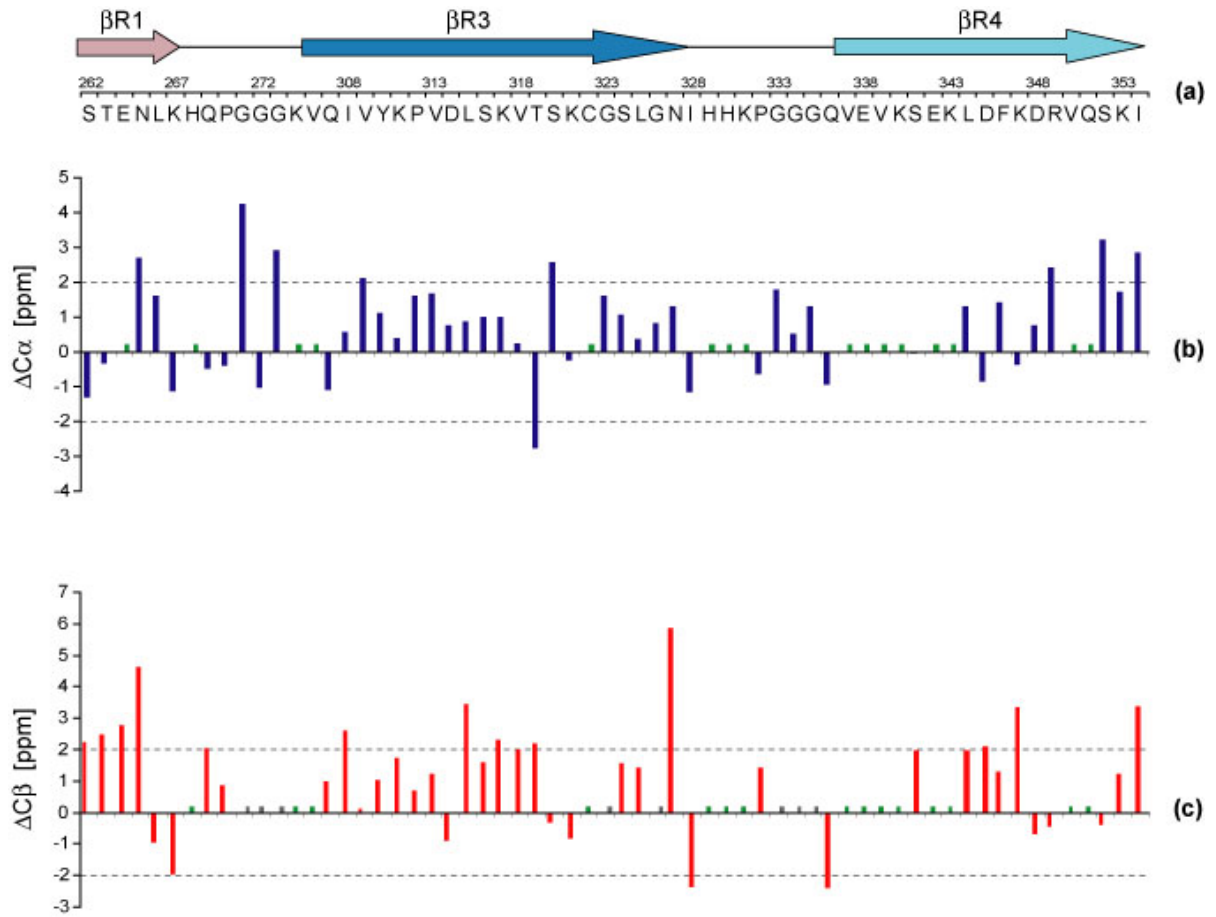


Figure D.1: Comparison of experimental and model based predicted (ShiftX, [257]) chemical shifts for the core region: (a) plot of  $\delta_{C\alpha,exp} - \delta_{C\alpha,pred}$ , unassigned residues are shown in green, and (b) plot of  $\delta_{C\beta,exp} - \delta_{C\beta,pred}$ , unassigned residues are shown in green and glycines in gray. Cutoff values of  $\pm 2$  ppm are considered, taking in account the accuracy for both the measured ( $\approx \pm 1$  ppm) and predicted ( $\approx \pm 1$  ppm) shifts. In general, good agreement is observed for the  $\beta$ -strands regions, particularly in the hairpin fold of  $\beta R3$  and  $\beta R4$ .

## D.4 CHHC analysis

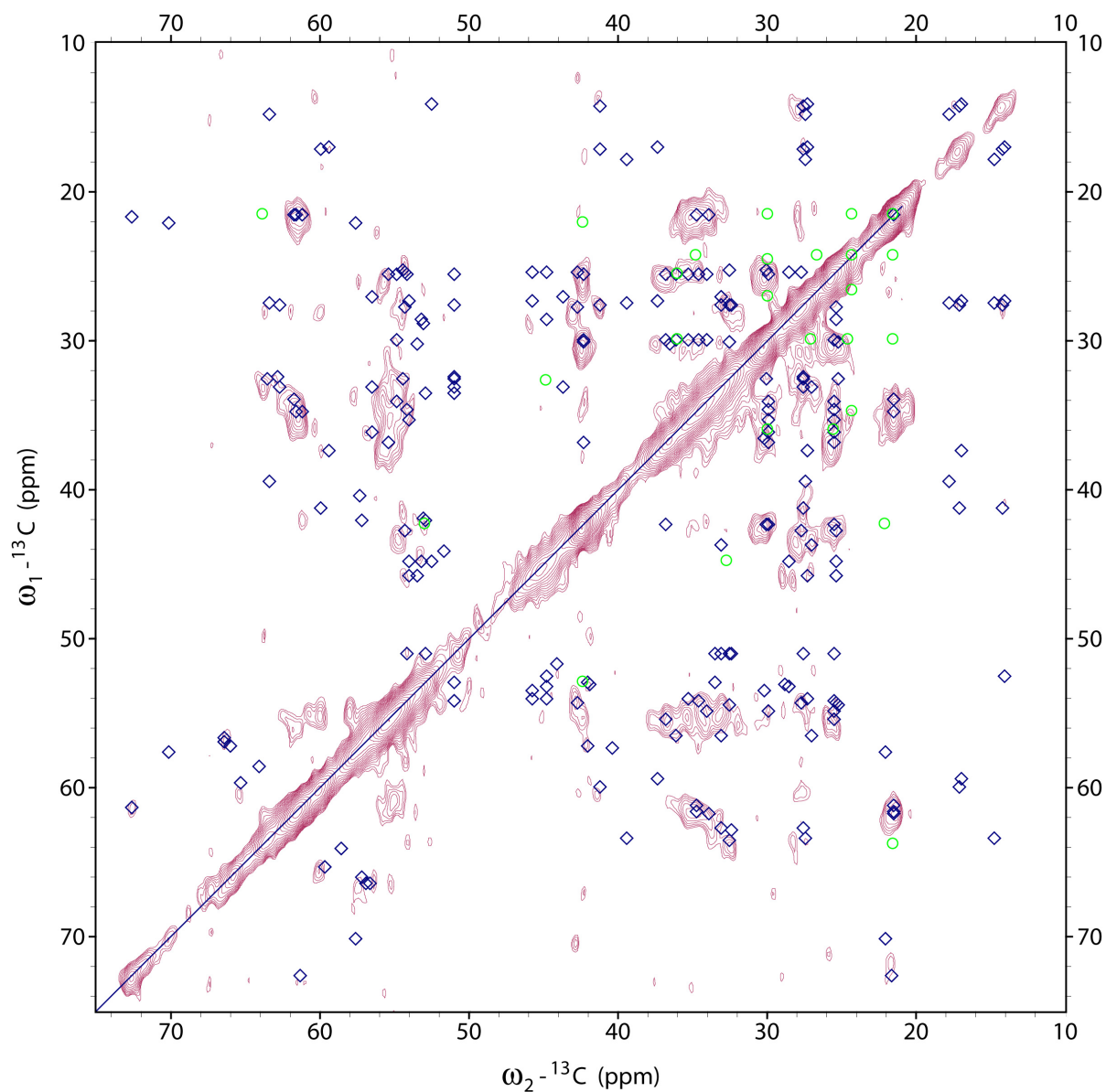


Figure D.2: Comparison of experimental and model based predicted CHHC spectrum of the core region for  $^1\text{H} - ^1\text{H}$  distances up to 3.5 Å. Intraresidue predictions are shown in blue diamonds and non-trivial long range interresidue contacts in green circles.

## D.5 Pulse program for the water-edited NCA experiment

```
;ht2f-nca_2d.oca
;water edited NCA experiment
;H T2-filter, H-H NOESY and dcp HNCA
```

```
#include <protection2d.oca>
```

```
1 ze
```

```
2 d1 do:f2
```

```
5u fq=0:f2
```

```
5u fq=cnst20:f1
```

```
5u pl16:f1
```

```
5u pl2:f2
```

```
5u pl5:f3
```

```
;proton 90 pulse
```

```
p2:f2 ph1
```

```
;H T2 filter
```

```
d6
```

```
p2*2:f2 ph10
```

```
d6
```

```
;H-H NOESY
```

```
p2:f2 ph5
```

```
d7
```

```
p2:f2 ph6
```

```
;H-N cp
```

```
(p15 ph2):f3 (p15:sp0 ph0):f2
```

```
;H dec
```

```
2u pl12:f2
```

```
2u cpds2:f2
```

```
2u pl15:f3
```

```
;15N t1 evolution
```

```
d0
```

```
;N-C cp
```

```
(p16 ph3):f3 (p16:sp1 ph4):f1
```

```
5u fq=0:f1
```

```
5u
```

```
;acquisition
```

```
go=2 ph31
1m do:f2
100m wr #0 if #0 zd
1m id0
1m ip2
lo to 2 times td1
HaltAcqu, 1m
exit

ph0= 0
ph1= 1 3
ph2= 0
ph3= 0 0 2 2
ph4= 0 0 0 0 0 0 0 0 1 1 1 1 1 1 1 1
      2 2 2 2 2 2 2 2 3 3 3 3 3 3 3 3
ph5= 1
ph6= 1 1 1 1 3 3 3 3
ph10=0
ph31=0 2 2 0 2 0 0 2 1 3 3 1 3 1 1 3
      2 0 0 2 0 2 2 0 3 1 1 3 1 3 3 1
```

# List of Tables

2.1	Hamiltonians of the NMR interactions. . . . .	10
C.1	Assignment table for AFA-PLN in DMPC-D67 lipid bilayers. . . . .	135
D.1	Assignment table of K19 PHFs. . . . .	143
D.2	Experimental conditions for MAS ssNMR on K19 PHFs. . . . .	147

# List of Figures

1.1	Models of the cell membrane and protein fibrils. . . . .	2
2.1	Phenomenon of the nuclear magnetic resonance. . . . .	5
2.2	Principles of pulsed FTNMR. . . . .	6
2.3	Magic angle spinning. . . . .	13
2.4	Cross polarization. . . . .	15
2.5	Energy transfer in the doubly rotating frame. . . . .	16
2.6	R.f. recoupling . . . . .	18
2.7	2D NMR spectroscopy . . . . .	19
2.8	Structural levels of proteins . . . . .	21
2.9	Proteins structure determination by NMR. . . . .	22
2.10	Secondary structure of proteins. . . . .	23
2.11	Correlation experiments for proteins in MAS solid-state NMR . . . . .	25
2.12	Protein dynamics. . . . .	26
3.1	Reference frames for MAS of oriented samples. . . . .	34
3.2	Simulations for recoupling interactions in oriented samples. . . . .	38
3.3	Simulation for CSA recoupling dependence of the tilt angle. . . . .	40



3.4	Influence of the azimuthal angle on CSA recoupling. . . . .	41
3.5	1D pulse sequence for CSA recoupling. . . . .	43
3.6	2D NC pulse sequence to probe orientation and structure. . . . .	44
3.7	1D and 2D recoupling experiments on powder AGG. . . . .	45
3.8	Orientation of Gramicidin A and WALP23 from $^{15}\text{N}$ CSA recoupling. . . .	48
3.9	DQ experiments on oriented WALP23. . . . .	50
3.10	Structure and orientation of WALP23. . . . .	52
4.1	Calcium regulation during the cardiac cycle . . . . .	56
4.2	Liquid-state NMR and EPR models of PLN. . . . .	58
4.3	Principle of dynamics-based spectral editing. . . . .	60
4.4	1D spectra of U- $^{13}\text{C}$ , $^{15}\text{N}$ ] AFA-PLN in DMPC-D67 bilayers. . . . .	61
4.5	Pulse sequence to detect mobile protein domains. . . . .	62
4.6	Comparison of 2D HC and CC DQ/SQ spectra. . . . .	65
4.7	2D H(C)C INEPT-TOBSY spectrum. . . . .	67
4.8	2D (H)NCACB and (H)NCOACB scalar-coupling spectra. . . . .	68
4.9	2D NCA and NCOCA dipolar-coupling spectra. . . . .	69
4.10	Overlay of the 2D HN and H(H)N INEPT-NOESY spectra. . . . .	70
4.11	2D NOESY: H(H)C and (H)N(HH)C. . . . .	71
4.12	Secondary chemical shifts plot of AFA-PLN. . . . .	72
4.13	Structural model of AFA-PLN in DMPC bilayers from ssNMR. . . . .	74
4.14	Function and regulation of SERCA. . . . .	76
4.15	Structure of SERCA and MD model of SERCA-PLN complex. . . . .	77
4.16	Dynamics of SERCA-bound AFA-PLN. . . . .	79

---

4.17	2D CC spin diffusion spectrum of SERCA-bound AFA-PLN. . . . .	80
5.1	Alzheimer's Disease intraneuronal pathogenic mechanisms. . . . .	84
5.2	Primary sequence and EM of htau40 and the K19 construct. . . . .	85
5.3	Dynamics vs. rigid parts of K19 PHFs. . . . .	87
5.4	Sequential assignment of K19 PHFs. . . . .	88
5.5	Pulse sequence of the water edited NCA experiment. . . . .	90
5.6	Distance constraints on K19 PHFs core. . . . .	91
5.7	Summary of K19 PHFs structural constraints. . . . .	92
5.8	Minimal structure unit of K19 PHFs. . . . .	94
5.9	Structural model of K19 PHFs. . . . .	96
A.1	Euler rotations. . . . .	106
B.1	Comparison of AHT and numerical simulation for $^{15}\text{N}$ CSA recoupling. . .	109
B.2	$^{31}\text{P}$ spinning sidebands for oriented samples of WALP23. . . . .	111
C.1	2D slices from 3D HCC spectrum of AFA-PLN in DMPC bilayers. . . . .	134
C.2	Sample preparation: lipid type, L/P ratio and lyophilization. . . . .	137
C.3	$^{31}\text{P}$ spinning-sidebands of AFA-PLN / DMPC sample. . . . .	138
C.4	Pulse sequences for dipolar-coupling based experiments. . . . .	139
D.1	Experimental vs. predicted K19 PHFs chemical shifts. . . . .	148
D.2	Experimental vs. predicted K19 PHFs CHHC spectrum. . . . .	149

# Index

- AHT, 9, 17, 37, 43, 107
- CP, 15, 17, 60, 61, 69
- CSA, 9, 12, 33, 38, 39, 45, 47, 107
- Dipolar coupling, 9, 12, 33, 38, 49, 60, 64, 69, 88, 107
- DQ, 18, 20, 39, 44, 49, 65, 69, 79
- Dynamics, 26, 58, 59, 88
- GAMMA, 9, 37, 110, 111, 138
- Hydration, 82, 89
- INEPT, 60, 63, 67, 68, 87
- MAS, 12, 17, 30
- NOESY, 63, 69, 73
- Oriented samples, 3, 30, 59, 111
- R.f. field, 6, 9, 10, 44, 63, 69
- Randomly oriented samples, 3, 12, 39, 45, 138
- Relaxation, 7, 12, 66
- Scalar coupling, 9, 60, 64, 88
- Spherical tensors, 11, 33, 105
- Spin diffusion, 24, 46, 49, 80, 87–89
- SQ, 20, 39
- Structure, 23, 73, 95
- TOBSY, 63, 67, 68, 87
- Zeeman interaction, 6, 9
- ZQ, 18, 20, 44, 46, 49

# Bibliography

- [1] F. Bloch, W. W. Hansen, and M. Packard. Nuclear induction. *Physical Review*, 69(3-4):127–127, 1946.
- [2] E. M. Purcell, H. C. Torrey, and R. V. Pound. Resonance absorption by nuclear magnetic moments in a solid. *Physical Review*, 69(1-2):37–38, 1946.
- [3] R. R. Ernst. Nuclear-magnetic-resonance fourier-transform spectroscopy (Nobel lecture). *Angewandte Chemie-International Edition in English*, 31(7):805–823, 1992.
- [4] K. Wuthrich. NMR studies of structure and function of biological macromolecules (Nobel lecture). *Angewandte Chemie-International Edition*, 42(29):3340–3363, 2003.
- [5] P. C. Lauterbur. All science is interdisciplinary - from magnetic moments to molecules to men (Nobel lecture). *Angewandte Chemie-International Edition*, 44(7):1004–1011, 2005.
- [6] P. Mansfield. Snapshot magnetic resonance imaging (Nobel lecture). *Angewandte Chemie-International Edition*, 43(41):5456–5464, 2004.
- [7] A. E. Ferentz and G. Wagner. NMR spectroscopy: a multifaceted approach to macromolecular structure. *Quarterly Reviews of Biophysics*, 33(1):29–65, 2000.
- [8] A. T. Brunger. X-ray crystallography and NMR reveal complementary views of structure and dynamics. *Nature Structural Biology*, 4:862–865, 1997.

- 
- [9] A. Grishaev, J. Wu, J. Trehwella, and A. Bax. Refinement of multidomain protein structures by combination of solution small-angle X-ray scattering and NMR data. *Journal of the American Chemical Society*, 127(47):16621–16628, 2005.
- [10] A. Arora, F. Abildgaard, J. H. Bushweller, and L. K. Tamm. Structure of outer membrane protein a transmembrane domain by NMR spectroscopy. *Nature Structural Biology*, 8(4):334–338, 2001.
- [11] C. Fernandez and K. Wuthrich. NMR solution structure determination of membrane proteins reconstituted in detergent micelles. *Febs Letters*, 555(1):144–150, 2003.
- [12] Bruce Alberts, Alexander Johnson, Julian Lewis, Martin Raff, Keith Roberts, and Peter Walter. *Molecular Biology of the Cell*. Garland Science, New York, 4th edition, 2002.
- [13] C. M. Dobson. The structural basis of protein folding and its links with human disease. *Philosophical Transactions of the Royal Society of London Series B-Biological Sciences*, 356(1406):133–145, 2001.
- [14] C. M. Dobson. Protein folding and misfolding. *Nature*, 426(6968):884–890, 2003.
- [15] M. Stefani and C. M. Dobson. Protein aggregation and aggregate toxicity: new insights into protein folding, misfolding diseases and biological evolution. *Journal of Molecular Medicine*, 81(11):678–699, 2003.
- [16] T. Salditt, U. Mennicke, C. Munster, and M. Vogel. X-ray and neutron diffraction from solid-supported membranes. *Biophysical Journal*, 80(1):14A–14A, 2001.
- [17] M. Adrian, J. Dubochet, J. Lepault, and A. W. McDowell. Cryo-electron microscopy of viruses. *Nature*, 308(5954):32–36, 1984.
- [18] E. R. Andrew, A. Bradbury, and R. G. Eades. Nuclear magnetic resonance spectra from a crystal rotated at high speed. *Nature*, 182(4650):1659–1659, 1958.

- 
- [19] S. O. Smith, K. Aschheim, and M. Groesbeek. Magic angle spinning NMR spectroscopy of membrane proteins. *Quarterly Reviews of Biophysics*, 29(4):395–449, 1996.
- [20] M. Baldus. Correlation experiments for assignment and structure elucidation of immobilized polypeptides under magic angle spinning. *Progress in Nuclear Magnetic Resonance Spectroscopy*, 41(1-2):1–47, 2002.
- [21] S. J. Opella, P. L. Stewart, and K. G. Valentine. Protein-structure by solid-state NMR-spectroscopy. *Quarterly Reviews of Biophysics*, 19(1-2):7–49, 1987.
- [22] F. M. Marassi and S. J. Opella. Simultaneous assignment and structure determination of a membrane protein from NMR orientational restraints. *Protein Science*, 12(3):403–411, 2003.
- [23] C. Glaubitz. An introduction to MAS NMR spectroscopy on oriented membrane proteins. *Concepts in Magnetic Resonance*, 12(3):137–151, 2000.
- [24] C. Sizun and B. Bechinger. Bilayer sample for fast or slow magic angle oriented sample spinning solid-state NMR spectroscopy. *Journal of the American Chemical Society*, 124(7):1146–1147, 2002.
- [25] F. Creuzet, A. McDermott, R. Gebhard, K. Vanderhoef, M. B. Spijkerassink, J. Herzfeld, J. Lugtenburg, M. H. Levitt, and R. G. Griffin. Determination of membrane-protein structure by rotational resonance NMR - bacteriorhodopsin. *Science*, 251(4995):783–786, 1991.
- [26] F. Castellani, B. van Rossum, A. Diehl, M. Schubert, K. Rehbein, and H. Oschkinat. Structure of a protein determined by solid-state magic-angle-spinning NMR spectroscopy. *Nature*, 420(6911):98–102, 2002.

- 
- [27] A. Lange, S. Becker, K. Seidel, K. Giller, O. Pongs, and M. Baldus. A concept for rapid protein-structure determination by solid-state NMR spectroscopy. *Angewandte Chemie-International Edition*, 44(14):2089–2092, 2005.
- [28] S. G. Zech, A. J. Wand, and A. E. McDermott. Protein structure determination by high-resolution solid-state NMR spectroscopy: Application to microcrystalline ubiquitin. *Journal of the American Chemical Society*, 127(24):8618–8626, 2005.
- [29] S. Luca, J. F. White, A. K. Sohal, D. V. Filippov, J. H. van Boom, R. Grisshammer, and M. Baldus. The conformation of neurotensin bound to its G protein-coupled receptor. *Proceedings of the National Academy of Sciences of the United States of America*, 100(19):10706–10711, 2003.
- [30] M. Etzkorn, A. Bockmann, A. Lange, and M. Baldus. Probing molecular interfaces using 2D magic-angle-spinning NMR on protein mixtures with different uniform labeling. *Journal of the American Chemical Society*, 126(45):14746–14751, 2004.
- [31] D. Marulanda, M. L. Tasayco, A. McDermott, M. Cataldi, V. Arriaran, and T. Polenova. Magic angle spinning solid-state NMR spectroscopy for structural studies of protein interfaces. resonance assignments of differentially enriched *escherichia coli* thioredoxin reassembled by fragment complementation. *Journal of the American Chemical Society*, 126(50):16608–16620, 2004.
- [32] Anatole Abragam. *Principles of Nuclear Magnetism*. Oxford University Press, New York, 13th edition, 1961.
- [33] Bodenhausen G. Ernst, Richard R. and A. Wokaun. *Principles of Nuclear Magnetic Resonance in One and Two Dimensions*. The International Series of Monographs on Chemistry. Clarendon Press, Oxford, 1987.
- [34] F. Bloch, W. W. Hansen, and M. Packard. The nuclear induction experiment. *Physical Review*, 70(7-8):474–485, 1946.

- 
- [35] F. Bloch and R. K. Wangsness. The differential equations of nuclear induction. *Physical Review*, 78(1):82–82, 1950.
- [36] N. Bloembergen, E. M. Purcell, and R. V. Pound. Nuclear magnetic relaxation. *Nature*, 160(4066):475–476, 1947.
- [37] N. Bloembergen, E. M. Purcell, and R. V. Pound. Relaxation effects in nuclear magnetic resonance absorption. *Physical Review*, 73(7):679–712, 1948.
- [38] A. G. Redfield. On the theory of relaxation processes. *IBM Journal of Research and Development*, 1(1):19–31, 1957.
- [39] Fairbrother W. G. Palmer A. G. Cavanagh, J. and N.J. Skelton. *Protein NMR Spectroscopy, Principles and Practice*. Academic Press, San Diego, 1996.
- [40] U. Haeberlen. Selective averaging. In J. S. Waugh, editor, *Advances in Magnetic Resonance, High resolution NMR in solids*. Academic Press, 1976.
- [41] T. O. Levante, M. Baldus, B. H. Meier, and R. R. Ernst. Formalized quantum-mechanical floquet theory and its application to sample-spinning in nuclear-magnetic-resonance. *Molecular Physics*, 86(5):1195–1212, 1995.
- [42] M. Baldus, T. O. Levante, and B. H. Meier. Numerical-simulation of magnetic-resonance experiments - concepts and applications to static, rotating and double rotating experiments. *Zeitschrift Fur Naturforschung Section a-a Journal of Physical Sciences*, 49(1-2):80–88, 1994.
- [43] S. A. Smith, T. O. Levante, B. H. Meier, and R. R. Ernst. Computer-simulations in magnetic-resonance - an object-oriented programming approach. *Journal of Magnetic Resonance Series A*, 106(1):75–105, 1994.
- [44] M. Bak, J. T. Rasmussen, and N. C. Nielsen. Simpson: A general simulation program for solid-state NMR spectroscopy. *Journal of Magnetic Resonance*, 147(2):296–330, 2000.



- 
- [45] Michael Mehring. *Principles of High Resolution NMR in Solids*. Springer-Verlag, Berlin Heidelberg, 1983.
- [46] M. Mehring and J. S. Waugh. Magic-angle NMR experiments in solids. *Physical Review B*, 5(9):3459–3471, 1972.
- [47] M. M. Maricq and J. S. Waugh. NMR in rotating solids. *Journal of Chemical Physics*, 70(7):3300–3316, 1979.
- [48] M. Lee and W. I. Goldburg. Nuclear-magnetic-resonance line narrowing by a rotating rf field. *Physical Review*, 140(4A):1261–1271, 1965.
- [49] I. J. Lowe. Free induction decays of rotating solids. *Physical Review Letters*, 2(7):285–287, 1959.
- [50] W. K. Rhim, D. D. Elleman, and R. W. Vaughan. Analysis of multiple pulse NMR in solids. *Journal of Chemical Physics*, 59(7):3740–3749, 1973.
- [51] D. P. Burum and W. K. Rhim. Analysis of multiple pulse NMR in solids .3. *Journal of Chemical Physics*, 71(2):944–956, 1979.
- [52] A. Bielecki, A. C. Kolbert, and M. H. Levitt. Frequency-switched pulse sequences - homonuclear decoupling and dilute spin NMR in solids. *Chemical Physics Letters*, 155(4-5):341–346, 1989.
- [53] E. Vinogradov, P. K. Madhu, and S. Vega. High-resolution proton solid-state NMR spectroscopy by phase-modulated lee-goldburg experiment. *Chemical Physics Letters*, 314(5-6):443–450, 1999.
- [54] A. Lesage, D. Sakellariou, S. Hediger, B. Elena, P. Charmont, S. Steuernagel, and L. Emsley. Experimental aspects of proton NMR spectroscopy in solids using phase-modulated homonuclear dipolar decoupling. *Journal of Magnetic Resonance*, 163(1):105–113, 2003.

- 
- [55] S. R. Hartmann and E. L. Hahn. Nuclear double resonance in rotating frame. *Physical Review*, 128(5):2042–2053, 1962.
- [56] A. Pines, M. G. Gibby, and J. S. Waugh. Proton-enhanced NMR of dilute spins in solids. *Journal of Chemical Physics*, 59(2):569–590, 1973.
- [57] S. Luca, H. Heise, and M. Baldus. High-resolution solid-state NMR applied to polypeptides and membrane proteins. *Accounts of Chemical Research*, 36(11):858–865, 2003.
- [58] A. E. Bennett, J. H. Ok, R. G. Griffin, and S. Vega. Chemical-shift correlation spectroscopy in rotating solids - radio frequency-driven dipolar recoupling and longitudinal exchange. *Journal of Chemical Physics*, 96(11):8624–8627, 1992.
- [59] M. Baldus, M. Tomaselli, B. H. Meier, and R. R. Ernst. Broad-band polarization-transfer experiments for rotating solids. *Chemical Physics Letters*, 230(4-5):329–336, 1994.
- [60] N. C. Nielsen, H. Bildsoe, H. J. Jakobsen, and M. H. Levitt. Double-quantum homonuclear rotary resonance - efficient dipolar recovery in magic-angle-spinning nuclear-magnetic-resonance. *Journal of Chemical Physics*, 101(3):1805–1812, 1994.
- [61] B. Q. Sun, P. R. Costa, D. Kocisko, P. T. Lansbury, and R. G. Griffin. Internuclear distance measurements in solid-state nuclear-magnetic-resonance - dipolar recoupling via rotor synchronized spin locking. *Journal of Chemical Physics*, 102(2):702–707, 1995.
- [62] R. Tycko. Prospects for resonance assignments in multidimensional solid-state NMR spectra of uniformly labeled proteins. *Journal of Biomolecular NMR*, 8(3):239–251, 1996.

- 
- [63] H. Levitt, Malcolm. Advances in NMR. In David M. Grant Harris and Robin K., editors, *Encyclopedia of Nuclear Magnetic Resonance*, volume Vol. 9, pages pp. 165–196. John Wiley & Sons, Ltd., Chichester, 2002.
- [64] D. P. Raleigh, M. H. Levitt, and R. G. Griffin. Rotational resonance in solid-state NMR. *Chemical Physics Letters*, 146(1-2):71–76, 1988.
- [65] K. Takegoshi, K. Nomura, and T. Terao. Rotational resonance in the tilted rotating-frame. *Chemical Physics Letters*, 232(5-6):424–428, 1995.
- [66] T. Gullion and J. Schaefer. Rotational-echo double-resonance NMR. *Journal of Magnetic Resonance*, 81(1):196–200, 1989.
- [67] A. W. Hing, S. Vega, and J. Schaefer. Transferred-echo double-resonance NMR. *Journal of Magnetic Resonance*, 96(1):205–209, 1992.
- [68] A. Brinkmann and M. H. Levitt. Symmetry principles in the nuclear magnetic resonance of spinning solids: Heteronuclear recoupling by generalized hartmann-hahn sequences. *Journal of Chemical Physics*, 115(1):357–384, 2001.
- [69] R. G. Griffin. Dipolar recoupling in MAS spectra of biological solids. *Nature Structural Biology*, 5:508–512, 1998.
- [70] J. Jeener. In *Ampere International Summer School*, Bask Polje, Yugoslavia, 1971.
- [71] R. R. Ernst. 2-dimensional spectroscopy. *Chimia*, 29(4):179–183, 1975.
- [72] W. P. Aue, E. Bartholdi, and R. R. Ernst. 2-dimensional spectroscopy - application to nuclear magnetic-resonance. *Journal of Chemical Physics*, 64(5):2229–2246, 1976.
- [73] H. Oschkinat, C. Griesinger, P. J. Kraulis, O. W. Sorensen, R. R. Ernst, A. M. Gronenborn, and G. M. Clore. 3-dimensional NMR-spectroscopy of a protein in solution. *Nature*, 332(6162):374–376, 1988.

- 
- [74] L. E. Kay, G. M. Clore, A. Bax, and A. M. Gronenborn. 4-dimensional heteronuclear triple-resonance NMR-spectroscopy of interleukin-1-beta in solution. *Science*, 249(4967):411–414, 1990.
- [75] M. Ikura, L. E. Kay, and A. Bax. A novel-approach for sequential assignment of H-1, C-13, and N-15 spectra of larger proteins - heteronuclear triple-resonance 3-dimensional NMR-spectroscopy - application to calmodulin. *Biochemistry*, 29(19):4659–4667, 1990.
- [76] G. Bodenhausen, H. Kogler, and R. R. Ernst. Selection of coherence-transfer pathways in NMR pulse experiments. *Journal of Magnetic Resonance*, 58(3):370–388, 1984.
- [77] G. Bodenhausen, R. L. Vold, and R. R. Vold. Multiple quantum spin-echo spectroscopy. *Journal of Magnetic Resonance*, 37(1):93–106, 1980.
- [78] D. J. States, R. A. Haberkorn, and D. J. Ruben. A two-dimensional nuclear overhauser experiment with pure absorption phase in 4 quadrants. *Journal of Magnetic Resonance*, 48(2):286–292, 1982.
- [79] D. Rovnyak, D. P. Frueh, M. Sastry, Z. Y. J. Sun, A. S. Stern, J. C. Hoch, and G. Wagner. Accelerated acquisition of high resolution triple-resonance spectra using non-uniform sampling and maximum entropy reconstruction. *Journal of Magnetic Resonance*, 170(1):15–21, 2004.
- [80] E. Kupce and R. Freeman. Fast multi-dimensional hadamard spectroscopy. *Journal of Magnetic Resonance*, 163(1):56–63, 2003.
- [81] S. Kim and T. Szyperski. Gft NMR, a new approach to rapidly obtain precise high-dimensional NMR spectral information. *Journal of the American Chemical Society*, 125(5):1385–1393, 2003.

- [82] L. Frydman, T. Scherf, and A. Lupulescu. The acquisition of multidimensional NMR spectra within a single scan. *Proceedings of the National Academy of Sciences of the United States of America*, 99(25):15858–15862, 2002.
- [83] L Stryer. *Biochemistry*. W.H. Freeman and Co., New York, 4th edition, 1995.
- [84] P. Guntert. Structure calculation of biological macromolecules from NMR data. *Quarterly Reviews of Biophysics*, 31(2):145–237, 1998.
- [85] J. L. Markley, A. Bax, Y. Arata, C. W. Hilbers, R. Kaptein, B. D. Sykes, P. E. Wright, and K. Wuthrich. Recommendations for the presentation of NMR structures of proteins and nucleic acids - IUPAC-IUBMB-IUPAB inter-union task group on the standardization of data bases of protein and nucleic acid structures determined by NMR spectroscopy. *Journal of Biomolecular NMR*, 12(1):1–23, 1998.
- [86] S. Luca, D. V. Filippov, J. H. van Boom, H. Oschkinat, H. J. M. de Groot, and M. Baldus. Secondary chemical shifts in immobilized peptides and proteins: A qualitative basis for structure refinement under magic angle spinning. *Journal of Biomolecular NMR*, 20(4):325–331, 2001.
- [87] A. Lange, K. Seidel, L. Verdier, S. Luca, and M. Baldus. Analysis of proton-proton transfer dynamics in rotating solids and their use for 3D structure determination. *Journal of the American Chemical Society*, 125(41):12640–12648, 2003.
- [88] A. T. Brunger, P. D. Adams, G. M. Clore, W. L. DeLano, P. Gros, R. W. Grosse-Kunstleve, J. S. Jiang, J. Kuszewski, M. Nilges, N. S. Pannu, R. J. Read, L. M. Rice, T. Simonson, and G. L. Warren. Crystallography and NMR system: A new software suite for macromolecular structure determination. *Acta Crystallographica Section D-Biological Crystallography*, 54:905–921, 1998.

- 
- [89] C. D. Schwieters, J. J. Kuszewski, N. Tjandra, and G. M. Clore. The XPLOR-NIH NMR molecular structure determination package. *Journal of Magnetic Resonance*, 160(1):65–73, 2003.
- [90] J. P. Linge, M. Habeck, W. Rieping, and M. Nilges. Aria: automated noe assignment and NMR structure calculation. *Bioinformatics*, 19(2):315–316, 2003.
- [91] W. Gronwald and H. R. Kalbitzer. Automated structure determination of proteins by NMR spectroscopy. *Progress in Nuclear Magnetic Resonance Spectroscopy*, 44(1-2):33–96, 2004.
- [92] D. S. Wishart and B. D. Sykes. Chemical-shifts as a tool for structure determination. In *Nuclear Magnetic Resonance, Pt C*, volume 239 of *Methods in Enzymology*, pages 363–392. 1994.
- [93] G. Cornilescu, F. Delaglio, and A. Bax. Protein backbone angle restraints from searching a database for chemical shift and sequence homology. *Journal of Biomolecular NMR*, 13(3):289–302, 1999.
- [94] M. P. Williamson, T. F. Havel, and K. Wuthrich. Solution conformation of proteinase inhibitor-iiia from bull seminal plasma by H-1 nuclear magnetic-resonance and distance geometry. *Journal of Molecular Biology*, 182(2):295–315, 1985.
- [95] M. Sattler, J. Schleucher, and C. Griesinger. Heteronuclear multidimensional NMR experiments for the structure determination of proteins in solution employing pulsed field gradients. *Progress in Nuclear Magnetic Resonance Spectroscopy*, 34(2):93–158, 1999.
- [96] N. K. Goto and L. E. Kay. New developments in isotope labeling strategies for protein solution NMR spectroscopy. *Current Opinion in Structural Biology*, 10(5):585–592, 2000.

- [97] Y. S. Jung and M. Zweckstetter. Mars - robust automatic backbone assignment of proteins. *Journal of Biomolecular NMR*, 30(1):11–23, 2004.
- [98] V. Tugarinov, R. Muhandiram, A. Ayed, and L. E. Kay. Four-dimensional NMR spectroscopy of a 723-residue protein: Chemical shift assignments and secondary structure of malate synthaseGG. *Journal of the American Chemical Society*, 124(34):10025–10035, 2002.
- [99] M. Kainosho. Isotope labelling of macromolecules for structural determinations. *Nature Structural Biology*, 4:858–861, 1997.
- [100] K. Seidel, A. Lange, S. Becker, C. E. Hughes, H. Heise, and M. Baldus. Protein solid-state NMR resonance assignments from (C-13, C-13) correlation spectroscopy. *Physical Chemistry Chemical Physics*, 6(22):5090–5093, 2004.
- [101] B. J. van Rossum, F. Castellani, J. Pauli, K. Rehbein, J. Hollander, H. J. M. de Groot, and H. Oschkinat. Assignment of amide proton signals by combined evaluation of HN, NN and HNCA MAS-NMR correlation spectra. *Journal of Biomolecular NMR*, 25(3):217–223, 2003.
- [102] N. Bloembergen. On the interaction of nuclear spins in a crystalline lattice. *Physica*, 15(3-4):386–426, 1949.
- [103] D. Suter and R. R. Ernst. Spin diffusion in resolved solid-state NMR-spectra. *Physical Review B*, 32(9):5608–5627, 1985.
- [104] Kurt Wuthrich. *NMR of Proteins and Nucleic Acids*. Wiley-Interscience, New York, first edition, 1986.
- [105] A. Lange, S. Luca, and M. Baldus. Structural constraints from proton-mediated rare-spin correlation spectroscopy in rotating solids. *Journal of the American Chemical Society*, 124(33):9704–9705, 2002.

- [106] J. Pauli, M. Baldus, B. van Rossum, H. de Groot, and H. Oschkinat. Backbone and side-chain C-13 and N-15 signal assignments of the alpha-spectrin sh3 domain by magic angle spinning solid-state NMR at 17.6 tesla. *Chembiochem*, 2(4):272–281, 2001.
- [107] T. A. Egorova-Zachernyuk, J. Hollander, N. Fraser, P. Gast, A. J. Hoff, R. Cogdell, H. J. M. de Groot, and M. Baldus. Heteronuclear 2D-correlations in a uniformly C-13, N-15 labeled membrane-protein complex at ultra-high magnetic fields. *Journal of Biomolecular NMR*, 19(3):243–253, 2001.
- [108] A. Bockmann, A. Lange, A. Galinier, S. Luca, N. Giraud, M. Juy, H. Heise, R. Montserret, F. Penin, and M. Baldus. Solid state NMR sequential resonance assignments and conformational analysis of the 2 x 10.4 kda dimeric form of the bacillus subtilis protein crh. *Journal of Biomolecular NMR*, 27(4):323–339, 2003.
- [109] T. I. Igumenova, A. J. Wand, and A. E. McDermott. Assignment of the backbone resonances for microcrystalline ubiquitin. *Journal of the American Chemical Society*, 126(16):5323–5331, 2004.
- [110] K. Seidel, M. Etzkorn, H. Heise, S. Becker, and M. Baldus. High-resolution solid-state NMR studies on uniformly C-13,N-15 -labeled ubiquitin. *Chembiochem*, 6(9):1638–1647, 2005.
- [111] O. C. Andronesi, S. Becker, K. Seidel, H. Heise, H. S. Young, and M. Baldus. Determination of membrane protein structure and dynamics by magic-angle-spinning solid-state NMR spectroscopy. *Journal of the American Chemical Society*, 127(37):12965–12974, 2005.
- [112] A. B. Siemer, C. Ritter, M. Ernst, R. Riek, and B. H. Meier. High-resolution solid-state NMR spectroscopy of the prion protein het-s in its amyloid conformation. *Angewandte Chemie-International Edition*, 44(16):2441–2444, 2005.



- [113] H. Heise, W. Hoyer, S. Becker, O. C. Andronesi, D. Riedel, and M. Baldus. Molecular-level secondary structure, polymorphism, and dynamics of full-length alpha-synuclein fibrils studied by solid-state NMR. *Proceedings of the National Academy of Sciences of the United States of America*, 102(44):15871–15876, 2005.
- [114] F. M. Marassi and S. J. Opella. NMR structural studies of membrane proteins. *Current Opinion in Structural Biology*, 8(5):640–648, 1998.
- [115] S. J. Opella, F. M. Marassi, J. J. Gesell, A. P. Valente, Y. Kim, M. Oblatt-Montal, and M. Montal. Structures of the m2 channel-lining segments from nicotinic acetylcholine and nmda receptors by NMR spectroscopy. *Nature Structural Biology*, 6(4):374–379, 1999.
- [116] F. Tian and T. A. Cross. Cation binding induced changes in N-15 csa in a membrane-bound polypeptide. *Journal of Magnetic Resonance*, 135(2):535–540, 1998.
- [117] J. K. Denny, J. F. Wang, T. A. Cross, and J. R. Quine. Pisema powder patterns and pisa wheels. *Journal of Magnetic Resonance*, 152(2):217–226, 2001.
- [118] M. F. Mesleh, S. Lee, G. Veglia, D. S. Thiriot, F. M. Marassi, and S. J. Opella. Dipolar waves map the structure and topology of helices in membrane proteins. *Journal of the American Chemical Society*, 125(29):8928–8935, 2003.
- [119] P. Luginbuhl and K. Wuthrich. Semi-classical nuclear spin relaxation theory revisited for use with biological macromolecules. *Progress in Nuclear Magnetic Resonance Spectroscopy*, 40(3):199–247, 2002.
- [120] A. Krushelnitsky and D. Reichert. Solid-state NMR and protein dynamics. *Progress in Nuclear Magnetic Resonance Spectroscopy*, 47(1-2):1–25, 2005.
- [121] G. Lipari and A. Szabo. Model-free approach to the interpretation of nuclear magnetic-resonance relaxation in macromolecules .1. theory and range of validity. *Journal of the American Chemical Society*, 104(17):4546–4559, 1982.

- 
- [122] G. Lipari and A. Szabo. Model-free approach to the interpretation of nuclear magnetic-resonance relaxation in macromolecules .2. analysis of experimental results. *Journal of the American Chemical Society*, 104(17):4559–4570, 1982.
- [123] D. A. Torchia. Solid-state NMR-studies of protein internal dynamics. *Annual Review of Biophysics and Bioengineering*, 13:125–144, 1984.
- [124] A. G. Palmer, J. Williams, and A. McDermott. Nuclear magnetic resonance studies of biopolymer dynamics. *Journal of Physical Chemistry*, 100(31):13293–13310, 1996.
- [125] W. Hans Spiess. Rotation of molecules and nuclear spin relaxation. In P. Diehl, E. Fluck, and R. Kosfeld, editors, *NMR Basic Principles and Progress, Dynamic NMR Spectroscopy, Vol. 15*. Springer-Verlag, 1978.
- [126] G. A. Morris and R. Freeman. Enhancement of nuclear magnetic-resonance signals by polarization transfer. *Journal of the American Chemical Society*, 101(3):760–762, 1979.
- [127] M. Baldus, R. J. Iuliucci, and B. H. Meier. Probing through-bond connectivities and through-space distances in solids by magic-angle-spinning nuclear magnetic resonance. *Journal of the American Chemical Society*, 119(5):1121–1124, 1997.
- [128] F. Moll and T. A. Cross. Optimizing and characterizing alignment of oriented lipid bilayers containing gramicidin-d. *Biophysical Journal*, 57(2):351–362, 1990.
- [129] M. R. R. de Planque and J. A. Killian. Protein-lipid interactions studied with designed transmembrane peptides: role of hydrophobic matching and interfacial anchoring (review). *Molecular Membrane Biology*, 20(4):271–284, 2003.
- [130] T. Salditt. Lipid-peptide interaction in oriented bilayers probed by interface-sensitive scattering methods. *Current Opinion in Structural Biology*, 13(4):467–478, 2003.

- 
- [131] C. Fernandez, C. Hilty, G. Wider, P. Guntert, and K. Wuthrich. NMR structure of the integral membrane protein ompx. *Journal of Molecular Biology*, 336(5):1211–1221, 2004.
- [132] T. A. Cross and S. J. Opella. Solid-state NMR structural studies of peptides and proteins in membranes. *Current Opinion in Structural Biology*, 4(4):574–581, 1994.
- [133] B. Bechinger. The structure, dynamics and orientation of antimicrobial peptides in membranes by multidimensional solid-state NMR spectroscopy. *Biochimica Et Biophysica Acta-Biomembranes*, 1462(1-2):157–183, 1999.
- [134] F. M. Marassi, J. J. Gesell, and S. J. Opella. Recent developments in multidimensional NMR structural studies of membrane proteins. In *Modern Techniques in protein NMR*, volume 16 of *Biological Magnetic Resonance*, pages 121–145. 1998.
- [135] N. Tjandra and A. Bax. Direct measurement of distances and angles in biomolecules by NMR in a dilute liquid crystalline medium. *Science*, 278(5340):1111–1114, 1997.
- [136] A. Bax, G. Kontaxis, and N. Tjandra. Dipolar couplings in macromolecular structure determination. In *Nuclear Magnetic Resonance of Biological Macromolecules, Pt B*, volume 339 of *Methods in Enzymology*, pages 127–174. 2001.
- [137] R. R. Ketchum, W. Hu, and T. A. Cross. High-resolution conformation of gramicidin-a in a lipid bilayer by solid-state NMR. *Science*, 261(5127):1457–1460, 1993.
- [138] A. C. Zeri, M. F. Mesleh, A. A. Nevzorov, and S. J. Opella. Structure of the coat protein in fd filamentous bacteriophage particles determined by solid-state NMR spectroscopy. *Proceedings of the National Academy of Sciences of the United States of America*, 100(11):6458–6463, 2003.
- [139] L. M. McDowell and J. Schaefer. High-resolution NMR of biological solids. *Current Opinion in Structural Biology*, 6(5):624–629, 1996.

- 
- [140] L. K. Thompson. Solid-state NMR studies of the structure and mechanisms of proteins. *Current Opinion in Structural Biology*, 12(5):661–669, 2002.
- [141] S. Luca, J. F. White, A. K. Sohal, D. Fillipov, J. H. van Boom, R. Grisshammer, and M. Baldus. Studying the conformation of neurotensin bound to its G-protein-coupled receptor NTS-1 by 2D solid-state NMR. *Biophysical Journal*, 84(2):137A–137A, 2003.
- [142] S. O. Smith, T. Kawakami, W. Liu, M. Ziliox, and S. Aimoto. Helical structure of phospholamban in membrane bilayers. *Journal of Molecular Biology*, 313(5):1139–1148, 2001.
- [143] C. M. Gabrys, J. Yang, and D. P. Weliky. Analysis of local conformation of membrane-bound and polycrystalline peptides by two-dimensional slow-spinning rotor-synchronized MAS exchange spectroscopy. *Journal of Biomolecular NMR*, 26(1):49–68, 2003.
- [144] R. Q. Fu, M. Cotten, and T. A. Cross. Inter- and intramolecular distance measurements by solid-state MAS NMR: Determination of gramicidin a channel dimer structure in hydrated phospholipid bilayers. *Journal of Biomolecular NMR*, 16(3):261–268, 2000.
- [145] S. O. Smith and M. Eilers. Helix-helix association in membrane proteins. *Biophysical Journal*, 80(1):352A–352A, 2001.
- [146] J. Yang and D. P. Weliky. Solid-state nuclear magnetic resonance evidence for parallel and antiparallel strand arrangements in the membrane-associated HIV-1 fusion peptide. *Biochemistry*, 42(40):11879–11890, 2003.
- [147] D. J. Hirsh, J. Hammer, W. L. Maloy, J. Blazyk, and J. Schaefer. Secondary structure and location of a magainin analogue in synthetic phospholipid bilayers. *Biochemistry*, 35(39):12733–12741, 1996.

- 
- [148] S. J. Opella and J. S. Waugh. 2-dimensional C-13 NMR of highly oriented polyethylene. *Journal of Chemical Physics*, 66(11):4919–4924, 1977.
- [149] G. S. Harbison and H. W. Spiess. Two-dimensional magic-angle-spinning NMR of partially ordered systems. *Chemical Physics Letters*, 124(2):128–134, 1986.
- [150] M. Demura, M. Minami, T. Asakura, and T. A. Cross. Structure of bombyx mori silk fibroin based on solid-state NMR orientational constraints and fiber diffraction unit cell parameters. *Journal of the American Chemical Society*, 120(6):1300–1308, 1998.
- [151] C. Glaubitz and A. Watts. Magic angle-oriented sample spinning (maoss): A new approach toward biomembrane studies. *Journal of Magnetic Resonance*, 130(2):305–316, 1998.
- [152] J. Herzfeld and A. E. Berger. Sideband intensities in NMR-spectra of samples spinning at the magic angle. *Journal of Chemical Physics*, 73(12):6021–6030, 1980.
- [153] C. Glaubitz, I. J. Burnett, G. Grobner, A. J. Mason, and A. Watts. Deuterium-MAS NMR spectroscopy on oriented membrane proteins: Applications to photointermediates of bacteriorhodopsin. *Journal of the American Chemical Society*, 121(24):5787–5794, 1999.
- [154] G. Grobner, I. J. Burnett, C. Glaubitz, G. Choi, A. J. Mason, and A. Watts. Observations of light-induced structural changes of retinal within rhodopsin. *Nature*, 405(6788):810–813, 2000.
- [155] F. M. Marassi and S. J. Opella. A solid-state NMR index of helical membrane protein structure and topology. *Journal of Magnetic Resonance*, 144(1):150–155, 2000.

- 
- [156] J. Wang, J. Denny, C. Tian, S. Kim, Y. Mo, F. Kovacs, Z. Song, K. Nishimura, Z. Gan, R. Fu, J. R. Quine, and T. A. Cross. Imaging membrane protein helical wheels. *Journal of Magnetic Resonance*, 144(1):162–167, 2000.
- [157] J. A. Killian. Gramicidin and gramicidin lipid interactions. *Biochimica Et Biophysica Acta*, 1113(3-4):391–425, 1992.
- [158] T. A. Cross, A. Arseniev, B. A. Cornell, J. H. Davis, J. A. Killian, R. E. Koeppe, L. K. Nicholson, F. Separovic, and B. A. Wallace. Gramicidin channel controversy - revisited. *Nature Structural Biology*, 6(7):610–611, 1999.
- [159] R. R. Ketchum, B. Roux, and T. A. Cross. High-resolution polypeptide structure in a lamellar phase lipid environment from solid state NMR derived orientational constraints. *Structure*, 5(12):1655–1669, 1997.
- [160] E. Strandberg, S. Morein, D. T. S. Rijkers, R. M. J. Liskamp, P. C. A. van der Wel, and J. A. Killian. Lipid dependence of membrane anchoring properties and snorkeling behavior of aromatic and charged residues in transmembrane peptides. *Biochemistry*, 41(23):7190–7198, 2002.
- [161] P. C. A. van der Wel, E. Strandberg, J. A. Killian, and R. E. Koeppe. Geometry and intrinsic tilt of a tryptophan-anchored transmembrane alpha-helix determined by h-2 NMR. *Biophysical Journal*, 83(3):1479–1488, 2002.
- [162] E. Strandberg, S. Ozdirekcan, D. T. S. Rijkers, P. C. A. van der Wel, R. E. Koeppe, R. M. J. Liskamp, and J. A. Killian. Tilt angles of transmembrane model peptides in oriented and non-oriented lipid bilayers as determined by h-2 solid-state NMR. *Biophysical Journal*, 86(6):3709–3721, 2004.
- [163] S. Auge, H. Mazarguil, M. Tropis, and A. Milon. Preparation of oriented lipid bilayer on ultrathin polymers for solid-state NMR analyses of peptide-membrane interactions. *Journal of Magnetic Resonance*, 124(2):455–458, 1997.

- 
- [164] D.M. Brink and G.R. Satchler. *Angular Momentum*. Oxford University Press, 1961.
- [165] K. Schmidt-Rohr and H.W. Spiess. *Multidimensional Solid-state NMR and Polymers*. Academic Press, London/San Diego, 1994.
- [166] F. M. Marassi. NMR of peptides and proteins in oriented membranes. *Concepts in Magnetic Resonance*, 14(3):212–224, 2002.
- [167] W. Mai, W. Hu, C. Wang, and T. A. Cross. Orientational constraints as 3-dimensional structural constraints from chemical-shift anisotropy - the polypeptide backbone of gramicidin-a in a lipid bilayer. *Protein Science*, 2(4):532–542, 1993.
- [168] M.; Eden M.; Levitt M. H. Glaubitz, C.; Carravetta. Perspectives on solid-state NMR in biology. In deGroot H. J. M. Kiihne, S., editor, *Focus on Structural Biology*, volume Vol. 1 of *Focus on Structural Biology*, pages pp 71–81. Kluwer Academic Publishers, Dordrecht, The Netherlands, 2001.
- [169] M. Carravetta, M. Eden, X. Zhao, A. Brinkmann, and M. H. Levitt. Symmetry principles for the design of radiofrequency pulse sequences in the nuclear magnetic resonance of rotating solids. *Chemical Physics Letters*, 321(3-4):205–215, 2000.
- [170] M. Baldus, A. T. Petkova, J. Herzfeld, and R. G. Griffin. Cross polarization in the tilted frame: assignment and spectral simplification in heteronuclear spin systems. *Molecular Physics*, 95(6):1197–1207, 1998.
- [171] M. Hohwy, H. J. Jakobsen, M. Eden, M. H. Levitt, and N. C. Nielsen. Broad-band dipolar recoupling in the nuclear magnetic resonance of rotating solids: A compensated c7 pulse sequence. *Journal of Chemical Physics*, 108(7):2686–2694, 1998.
- [172] V. B. Cheng, H. H. Suzukawa, and Wolfsber.M. Investigations of a nonrandom numerical-method for multidimensional integration. *Journal of Chemical Physics*, 59(8):3992–3999, 1973.

- 
- [173] X. Zhao, M. Eden, and M. H. Levitt. Recoupling of heteronuclear dipolar interactions in solid-state NMR using symmetry-based pulse sequences. *Chemical Physics Letters*, 342(3-4):353–361, 2001.
- [174] A. E. Bennett, C. M. Rienstra, M. Auger, K. V. Lakshmi, and R. G. Griffin. Heteronuclear decoupling in rotating solids. *Journal of Chemical Physics*, 103(16):6951–6958, 1995.
- [175] M. Hohwy, C. M. Rienstra, C. P. Jaroniec, and R. G. Griffin. Fivefold symmetric homonuclear dipolar recoupling in rotating solids: Application to double quantum spectroscopy. *Journal of Chemical Physics*, 110(16):7983–7992, 1999.
- [176] T. G. Oas, C. J. Hartzell, F. W. Dahlquist, and G. P. Drobny. The amide N-15 chemical-shift tensors of 4 peptides determined from C-13 dipole-coupled chemical-shift powder patterns. *Journal of the American Chemical Society*, 109(20):5962–5966, 1987.
- [177] O. C. Andronesi, J. R. Pfeifer, L. Al-Momani, S. Ozdirekcan, D. T. S. Rijkers, B. Angerstein, S. Luca, U. Koert, J. A. Killian, and M. Baldus. Probing membrane protein orientation and structure using fast magic-angle-spinning solid-state NMR. *Journal of Biomolecular NMR*, 30(3):253–265, 2004.
- [178] Y. J. Wang and O. Jardetzky. Probability-based protein secondary structure identification using combined NMR chemical-shift data. *Protein Science*, 11(4):852–861, 2002.
- [179] P. R. Costa, J. D. Gross, M. Hong, and R. G. Griffin. Solid-state NMR measurement of psi in peptides: a nccn 2q-heteronuclear local field experiment. *Chemical Physics Letters*, 280(1-2):95–103, 1997.



- 
- [180] L. Sonnenberg, S. Luca, and M. Baldus. Multiple-spin analysis of chemical-shift-selective (C-13, C-13) transfer in uniformly labeled biomolecules. *Journal of Magnetic Resonance*, 166(1):100–110, 2004.
- [181] D. H. MacLennan, M. Asahi, and A. R. Tupling. The regulation of serca-type pumps by phospholamban and sarcolipin. In *Na,K-ATPase and Related Cation Pumps*, volume 986 of *Annals of the New York Academy of Sciences*, pages 472–480. 2003.
- [182] J. P. Schmitt, M. Kamisago, M. Asahi, G. H. Li, F. Ahmad, U. Mende, E. G. Kranias, D. H. MacLennan, J. G. Seidman, and C. E. Seidman. Dilated cardiomyopathy and heart failure caused by a mutation in phospholamban. *Science*, 299(5611):1410–1413, 2003.
- [183] I. T. Arkin, P. D. Adams, K. R. Mackenzie, M. A. Lemmon, A. T. Brunger, and D. M. Engelman. Structural organization of the pentameric transmembrane  $\alpha$ -helices of phospholamban, a cardiac ion-channel. *Embo Journal*, 13(20):4757–4764, 1994.
- [184] H. K. B. Simmerman, Y. M. Kobayashi, J. M. Autry, and L. R. Jones. A leucine zipper stabilizes the pentameric membrane domain of phospholamban and forms a coiled-coil pore structure. *Journal of Biological Chemistry*, 271(10):5941–5946, 1996.
- [185] Y. Kimura, K. Kurzydowski, M. Tada, and D. H. MacLennan. Phospholamban inhibitory function is activated by depolymerization. *Journal of Biological Chemistry*, 272(24):15061–15064, 1997.
- [186] L. G. Reddy, L. R. Jones, and D. D. Thomas. Depolymerization of phospholamban in the presence of calcium pump: A fluorescence energy transfer study. *Biochemistry*, 38(13):3954–3962, 1999.

- [187] T. L. Kirby, C. B. Karim, and D. D. Thomas. Electron paramagnetic resonance reveals a large-scale conformational change in the cytoplasmic domain of phospholamban upon binding to the sarcoplasmic reticulum Ca-ATPase. *Biochemistry*, 43(19):5842–5852, 2004.
- [188] P. Pollesello, A. Annala, and M. Ovaska. Structure of the 1-36 amino-terminal fragment of human phospholamban by nuclear magnetic resonance and modeling of the phospholamban pentamer. *Biophysical Journal*, 76(4):1784–1795, 1999.
- [189] S. Lamberth, H. Schmid, M. Muenchbach, T. Vorherr, J. Krebs, E. Carafoli, and C. Griesinger. NMR solution structure of phospholamban. *Helvetica Chimica Acta*, 83(9):2141–2152, 2000.
- [190] J. Zamoon, A. Mascioni, D. D. Thomas, and G. Veglia. NMR solution structure and topological orientation of monomeric phospholamban in dodecylphosphocholine micelles. *Biophysical Journal*, 85(4):2589–2598, 2003.
- [191] A. Mascioni, C. Karim, J. Zamoon, D. D. Thomas, and G. Veglia. Solid-state NMR and rigid body molecular dynamics to determine domain orientations of monomeric phospholamban. *Journal of the American Chemical Society*, 124(32):9392–9393, 2002.
- [192] T. Toyofuku, K. Kurzydowski, M. Tada, and D. H. MacLennan. Amino-acids glu(2) to ile(18) in the cytoplasmic domain of phospholamban are essential for functional association with the Ca<sup>2+</sup>-ATPase of sarcoplasmic-reticulum. *Journal of Biological Chemistry*, 269(4):3088–3094, 1994.
- [193] R. L. Cornea, L. R. Jones, J. M. Autry, and D. D. Thomas. Mutation and phosphorylation change the oligomeric structure of phospholamban in lipid bilayers. *Biochemistry*, 36(10):2960–2967, 1997.

- [194] S. A. Tatulian, L. R. Jones, L. G. Reddy, D. L. Stokes, and L. K. Tamm. Secondary structure and orientation of phospholamban reconstituted in supported bilayers from polarized attenuated total-reflection ftir spectroscopy. *Biochemistry*, 34(13):4448–4456, 1995.
- [195] J. H. Li, D. J. Bigelow, and T. C. Squier. Conformational changes within the cytosolic portion of phospholamban upon release of Ca-ATPase inhibition. *Biochemistry*, 43(13):3870–3879, 2004.
- [196] C. B. Karim, T. L. Kirby, Z. W. Zhang, Y. Nesmelov, and D. D. Thomas. Phospholamban structural dynamics in lipid bilayers probed by a spin label rigidly coupled to the peptide backbone. *Proceedings of the National Academy of Sciences of the United States of America*, 101(40):14437–14442, 2004.
- [197] S. O. Smith, D. Song, S. Shekar, M. Groesbeek, M. Ziliox, and S. Aimoto. Structure of the transmembrane dimer interface of glycophorin a in membrane bilayers. *Biochemistry*, 40(22):6553–6558, 2001.
- [198] E. Hughes and D. A. Middleton. Solid-state NMR reveals structural changes in phospholamban accompanying the functional regulation of Ca<sup>2+</sup>-ATPase. *Journal of Biological Chemistry*, 278(23):20835–20842, 2003.
- [199] E. E. Metcalfe, J. Zamoon, D. D. Thomas, and G. Veglia. H-1/N-15 heteronuclear NMR spectroscopy shows four dynamic domains for phospholamban reconstituted in dodecylphosphocholine micelles. *Biophysical Journal*, 87(2):1205–1214, 2004.
- [200] W. W. Ying, S. E. Irvine, R. A. Beekman, D. J. Siminovitch, and S. O. Smith. Deuterium NMR reveals helix packing interactions in phospholamban. *Journal of the American Chemical Society*, 122(45):11125–11128, 2000.
- [201] P. C. Dave, E. K. Tiburu, K. Damodaran, and G. A. Lorigan. Investigating structural changes in the lipid bilayer upon insertion of the transmembrane domain of the

- membrane-bound protein phospholamban utilizing p-31 and h-2 solid-state NMR spectroscopy. *Biophysical Journal*, 86(3):1564–1573, 2004.
- [202] K. K. Kumashiro, K. Schmidt-Rohr, O. J. Murphy, K. L. Ouellette, W. A. Cramer, and L. K. Thompson. A novel tool for probing membrane protein structure: Solid-state NMR with proton spin diffusion and x-nucleus detection. *Journal of the American Chemical Society*, 120(20):5043–5051, 1998.
- [203] M. Baldus and B. H. Meier. Total correlation spectroscopy in the solid state. the use of scalar couplings to determine the through-bond connectivity. *Journal of Magnetic Resonance Series A*, 121(1):65–69, 1996.
- [204] David Neuhaus and Michael P. Williams. *The Nuclear Overhauser Effect in Structural and Conformational Analysis*. Methods in Stereochemical Analysis. Wiley-VCH, New York, second edition, 2000.
- [205] E. H. Hardy, R. Verel, and B. H. Meier. Fast MAS total through-bond correlation spectroscopy. *Journal of Magnetic Resonance*, 148(2):459–464, 2001.
- [206] A. Bax, R. Freeman, and S. P. Kempell. Natural abundance C-13-C-13 coupling observed via double-quantum coherence. *Journal of the American Chemical Society*, 102(14):4849–4851, 1980.
- [207] A. J. Shaka, P. B. Barker, and R. Freeman. Computer-optimized decoupling scheme for wideband applications and low-level operation. *Journal of Magnetic Resonance*, 64(3):547–552, 1985.
- [208] B. M. Fung, A. K. Khitrin, and K. Ermolaev. An improved broadband decoupling sequence for liquid crystals and solids. *Journal of Magnetic Resonance*, 142(1):97–101, 2000.
- [209] M. Nilges. Structure calculation from NMR data. *Current Opinion in Structural Biology*, 6(5):617–623, 1996.

- 
- [210] C. Toyoshima and G. Inesi. Structural basis of ion pumping by  $\text{Ca}(2+)\text{-ATPase}$  of the sarcoplasmic reticulum. *Annual Review of Biochemistry*, 73:269–292, 2004.
- [211] J. V. Moller, B. Juul, and M. leMaire. Structural organization, ion transport, and energy transduction of p-type atpases. *Biochimica Et Biophysica Acta-Reviews on Biomembranes*, 1286(1):1–51, 1996.
- [212] M. C. Hutter, J. Krebs, J. Meiler, C. Griesinger, E. Carafoli, and V. Helms. A structural model of the complex formed by phospholamban and the calcium pump of sarcoplasmic reticulum obtained by molecular mechanics. *Chembiochem*, 3(12):1200–1208, 2002.
- [213] C. Toyoshima, M. Asahi, Y. Sugita, R. Khanna, T. Tsuda, and D. H. MacLennan. Modeling of the inhibitory interaction of phospholamban with the  $\text{Ca}^{2+}$  ATPase. *Proceedings of the National Academy of Sciences of the United States of America*, 100(2):467–472, 2003.
- [214] C. Toyoshima, M. Nakasako, H. Nomura, and H. Ogawa. Crystal structure of the calcium pump of sarcoplasmic reticulum at 2.6 angstrom resolution. *Nature*, 405(6787):647–655, 2000.
- [215] K. Obara, N. Miyashita, C. Xu, L. Toyoshima, Y. Sugita, G. Inesi, and C. Toyoshima. Structural role of countertransport revealed in  $\text{Ca}^{2+}$  pump crystal structure in the absence of  $\text{Ca}^{2+}$ . *Proceedings of the National Academy of Sciences of the United States of America*, 102(41):14489–14496, 2005.
- [216] D. L. Stokes and N. M. Green. Structure and function of the calcium pump. *Annual Review of Biophysics and Biomolecular Structure*, 32:445–468, 2003.
- [217] H. S. Young, L. R. Jones, and D. L. Stokes. Locating phospholamban in co-crystals with  $\text{Ca}^{2+}\text{-ATPase}$  by cryoelectron microscopy. *Biophysical Journal*, 81(2):884–894, 2001.

- [218] H. S. Young and D. L. Stokes. The mechanics of calcium transport. *Journal of Membrane Biology*, 198(2):55–63, 2004.
- [219] J. Zamoon, F. Nitu, C. Karim, D. D. Thomas, and G. Veglia. Mapping the interaction surface of a membrane protein: Unveiling the conformational switch of phospholamban in calcium pump regulation. *Proceedings of the National Academy of Sciences of the United States of America*, 102(13):4747–4752, 2005.
- [220] B. Mueller, C. B. Karim, I. V. Negrashov, H. Kutchai, and D. D. Thomas. Direct detection of phospholamban and sarcoplasmic reticulum Ca-ATPase interaction in membranes using fluorescence resonance energy transfers. *Biochemistry*, 43(27):8754–8765, 2004.
- [221] A. Lange, K. Giller, S. Hornig, M.F. Martin-Eaucclair, O. Pongs, S. Becker, and M. Baldus. Toxin-induced conformational changes in a potassium channel revealed by solid-state NMR. *Nature*, in press, 2006.
- [222] D. H. MacLennan, M. Abu-Abed, and C. Kang. Structure-function relationships in Ca<sup>2+</sup> cycling proteins. *Journal of Molecular and Cellular Cardiology*, 34(8):897–918, 2002.
- [223] L. G. Reddy, L. R. Jones, S. E. Cala, J. J. Obrian, S. A. Tatulian, and D. L. Stokes. Functional reconstitution of recombinant phospholamban with rabbit skeletal Ca<sup>2+</sup>-ATPase. *Journal of Biological Chemistry*, 270(16):9390–9397, 1995.
- [224] C. B. Karim, C. G. Marquardt, J. D. Stamm, G. Barany, and D. D. Thomas. Synthetic null-cysteine phospholamban analogue and the corresponding transmembrane domain inhibit the Ca-ATPase. *Biochemistry*, 39(35):10892–10897, 2000.
- [225] M. Etzkorn and et al. Molecular structure and intrinsic dynamics of a 7-transmembrane protein receptor in native membranes seen by solid-state NMR. *manuscript in preparation*.

- 
- [226] R. A. Santarella, G. Skiniotis, K. N. Goldie, P. Tittmann, H. Gross, E. M. Mandelkow, E. Mandelkow, and A. Hoenger. Surface-decoration of microtubules by human tau. *Journal of Molecular Biology*, 339(3):539–553, 2004.
- [227] V. M. Y. Lee, M. Goedert, and J. Q. Trojanowski. Neurodegenerative tauopathies. *Annual Review of Neuroscience*, 24:1121–1159, 2001.
- [228] M. S. Forman, J. Q. Trojanowski, and V. M. Y. Lee. Neurodegenerative diseases: a decade of discoveries paves the way for therapeutic breakthroughs. *Nature Medicine*, 10(10):1055–1063, 2004.
- [229] M. P. Mattson. Pathways towards and away from alzheimer’s disease. *Nature*, 430(7000):631–639, 2004.
- [230] H. Braak, E. Braak, and M. Strothjohann. Abnormally phosphorylated tau-protein related to the formation of neurofibrillary tangles and neuropil threads in the cerebral-cortex of sheep and goat. *Neuroscience Letters*, 171(1-2):1–4, 1994.
- [231] M. von Bergen, S. Barghorn, J. Biernat, E. M. Mandelkow, and E. Mandelkow. Tau aggregation is driven by a transition from random coil to beta sheet structure. *Biochimica Et Biophysica Acta-Molecular Basis of Disease*, 1739(2-3):158–166, 2005.
- [232] J. Hardy. Amyloid, the presenilins and alzheimer’s disease. *Trends in Neurosciences*, 20(4):154–159, 1997.
- [233] S. Oddo, A. Caccamo, M. Kitazawa, B. P. Tseng, and F. M. LaFerla. Amyloid deposition precedes tangle formation in a triple transgenic model of Alzheimer’s disease. *Neurobiology of Aging*, 24(8):1063–1070, 2003.
- [234] S. Oddo, L. Billings, J. P. Kesslak, D. H. Cribbs, and F. M. LaFerla. A beta immunotherapy leads to clearance of early, but not late, hyperphosphorylated tau aggregates via the proteasome. *Neuron*, 43(3):321–332, 2004.

- [235] R. Kaye, E. Head, J. L. Thompson, T. M. McIntire, S. C. Milton, C. W. Cotman, and C. G. Glabe. Common structure of soluble amyloid oligomers implies common mechanism of pathogenesis. *Science*, 300(5618):486–489, 2003.
- [236] H. Braak and E. Braak. Neuropathological staging of Alzheimer-related changes. *Acta Neuropathologica*, 82(4):239–259, 1991.
- [237] P. Friedhoff, M. von Bergen, E. M. Mandelkow, and E. Mandelkow. Structure of tau protein and assembly into paired helical filaments. *Biochimica Et Biophysica Acta-Molecular Basis of Disease*, 1502(1):122–132, 2000.
- [238] S. Barghorn and E. Mandelkow. Toward a unified scheme for the aggregation of tau into alzheimer paired helical filaments. *Biochemistry*, 41(50):14885–14896, 2002.
- [239] M. von Bergen, P. Friedhoff, J. Biernat, J. Heberle, E. M. Mandelkow, and E. Mandelkow. Assembly of tau protein into alzheimer paired helical filaments depends on a local sequence motif ((306)VQIVYK(311)) forming beta structure. *Proceedings of the National Academy of Sciences of the United States of America*, 97(10):5129–5134, 2000.
- [240] M. von Bergen, S. Barghorn, L. Li, A. Marx, J. Biernat, E. M. Mandelkow, and E. Mandelkow. Mutations of tau protein in frontotemporal dementia promote aggregation of paired helical filaments by enhancing local beta-structure. *Journal of Biological Chemistry*, 276(51):48165–48174, 2001.
- [241] D. A. Kirschner, C. Abraham, and D. J. Selkoe. X-ray-diffraction from intraneuronal paired helical filaments and extraneuronal amyloid fibers in alzheimer-disease indicates cross-beta conformation. *Proceedings of the National Academy of Sciences of the United States of America*, 83(2):503–507, 1986.
- [242] J. Berriman, L. C. Serpell, K. A. Oberg, A. L. Fink, M. Goedert, and R. A. Crowther. Tau filaments from human brain and from in vitro assembly of recom-



- binant protein show cross-beta structure. *Proceedings of the National Academy of Sciences of the United States of America*, 100(15):9034–9038, 2003.
- [243] L. C. Serpell, M. Sunde, and C. C. F. Blake. The molecular basis of amyloidosis. *Cellular and Molecular Life Sciences*, 53(11-12):871–887, 1997.
- [244] C. M. Wischik, M. Novak, P. C. Edwards, A. Klug, W. Tichelaar, and R. A. Crowther. Structural characterization of the core of the paired helical filament of alzheimer-disease. *Proceedings of the National Academy of Sciences of the United States of America*, 85(13):4884–4888, 1988.
- [245] M. Margittai and R. Langen. Template-assisted filament growth by parallel stacking of tau. *Proceedings of the National Academy of Sciences of the United States of America*, 101(28):10278–10283, 2004.
- [246] A. T. Petkova, Y. Ishii, J. J. Balbach, O. N. Antzutkin, R. D. Leapman, F. Delaglio, and R. Tycko. A structural model for Alzheimer’s beta-amyloid fibrils based on experimental constraints from solid state NMR. *Proceedings of the National Academy of Sciences of the United States of America*, 99(26):16742–16747, 2002.
- [247] C. P. Jaroniec, C. E. MacPhee, V. S. Bajaj, M. T. McMahon, C. M. Dobson, and R. G. Griffin. High-resolution molecular structure of a peptide in an amyloid fibril determined by magic angle spinning NMR spectroscopy. *Proceedings of the National Academy of Sciences of the United States of America*, 101(3):711–716, 2004.
- [248] C. Smet, A. Leroy, A. Sillen, J. M. Wieruszeski, I. Landrieu, and G. Lippens. Accepting its random coil nature allows a partial NMR assignment of the neuronal tau protein. *Chembiochem*, 5(12):1639–1646, 2004.
- [249] A. Sillen, A. Leroy, J. M. Wieruszeski, A. Loyens, J. C. Beauvillain, L. Buee, I. Landrieu, and G. Lippens. Regions of tau implicated in the paired helical fragment core as defined by NMR. *Chembiochem*, 6(10):1849–1856, 2005.

- [250] A. Sillen, J. M. Wieruszeski, A. Leroy, A. Ben Younes, I. Landrieu, and G. Lippens. High-resolution magic angle spinning NMR of the neuronal tau protein integrated in alzheimer's-like paired helical fragments. *Journal of the American Chemical Society*, 127(29):10138–10139, 2005.
- [251] D. Eliezer, P. Barre, M. Kobaslija, D. Chan, X. H. Li, and L. Heend. Residual structure in the repeat domain of tau: Echoes of microtubule binding and paired helical filament formation. *Biochemistry*, 44(3):1026–1036, 2005.
- [252] M. D. Mukrasch, J. Biernat, M. von Bergen, C. Griesinger, E. Mandelkow, and M. Zweckstetter. Sites of tau important for aggregation populate beta-structure and bind to microtubules and polyanions. *Journal of Biological Chemistry*, 280(26):24978–24986, 2005.
- [253] H. T. Edzes and E. T. Samulski. Cross relaxation and spin diffusion in proton NMR of hydrated collagen. *Nature*, 265(5594):521–523, 1977.
- [254] H. T. Edzes and E. T. Samulski. Measurement of cross-relaxation effects in proton NMR spin-lattice relaxation of water in biological-systems - hydrated collagen and muscle. *Journal of Magnetic Resonance*, 31(2):207–229, 1978.
- [255] W. L. DeLano. Use of Pymol as a communications tool for molecular science. *Abstracts of Papers of the American Chemical Society*, 228:U313–U314, 2004.
- [256] H. Wille, G. Drewes, J. Biernat, E. M. Mandelkow, and E. Mandelkow. Alzheimer-like paired helical filaments and antiparallel dimers formed from microtubule-associated protein-tau invitro. *Journal of Cell Biology*, 118(3):573–584, 1992.
- [257] S. Neal, A. M. Nip, H. Y. Zhang, and D. S. Wishart. Rapid and accurate calculation of protein H-1, C-13 and N-15 chemical shifts. *Journal of Biomolecular NMR*, 26(3):215–240, 2003.

- 
- [258] M. F. Perutz, J. T. Finch, J. Berriman, and A. Lesk. Amyloid fibers are water-filled nanotubes. *Proceedings of the National Academy of Sciences of the United States of America*, 99(8):5591–5595, 2002.
- [259] F. Tagliavini, F. Prelli, L. Verga, G. Giaccone, R. Sarma, P. Gorevic, B. Ghetti, F. Passerini, E. Ghibaudi, G. Forloni, M. Salmona, O. Bugiani, and B. Frangione. Synthetic peptides homologous to prion protein residues 106-147 form amyloid-like fibrils in-vitro. *Proceedings of the National Academy of Sciences of the United States of America*, 90(20):9678–9682, 1993.
- [260] K. Ueda, H. Fukushima, E. Masliah, Y. Xia, A. Iwai, M. Yoshimoto, D. A. C. Otero, J. Kondo, Y. Ihara, and T. Saitoh. Molecular-cloning of cDNA encoding an unrecognized component of amyloid in Alzheimer-disease. *Proceedings of the National Academy of Sciences of the United States of America*, 90(23):11282–11286, 1993.
- [261] A. T. Petkova, R. D. Leapman, Z. H. Guo, W. M. Yau, M. P. Mattson, and R. Tycko. Self-propagating, molecular-level polymorphism in Alzheimer’s beta-amyloid fibrils. *Science*, 307(5707):262–265, 2005.
- [262] C. Ritter, M. L. Maddelein, A. B. Siemer, T. Luhrs, M. Ernst, B. H. Meier, S. J. Saupe, and R. Riek. Correlation of structural elements and infectivity of the Het-s prion. *Nature*, 435(7043):844–848, 2005.

## Curriculum Vitae

### Personal data

Name	Ovidiu-Cristian Andronesi
Date and place of birth	19.6.1974, Bucharest, Romania
Citizenship	Romanian

### Studies

1980-1988	'Sfantul Andrei' Primary and Secondary School, Bucharest, Romania
1988-1992	'Sfantul Sava' College, Bucharest, Romania
1992-1997	B.Sc. in Physics at Bucharest University, Romania
1997-1999	M.Sc. in Physics at Bucharest University, Romania
1995-1998	Preclinical medical studies at 'Carol Davila' University of Medicine and Pharmacy, Bucharest, Romania
1998-1999	Nuffic and Socrates scholarships at Leiden University, The Netherlands
1999-2001	Clinical medical studies at 'Carol Davila' University of Medicine and Pharmacy, Bucharest, Romania
Jul.-Dec. 2001	Beginning of PhD in the NMR-based Structural Biology Department of Max Planck Institute for Biophysical Chemistry, Göttingen, Germany
Jan.-Sept. 2002	Final year and M.D. license exam at 'Carol Davila' University of Medicine and Pharmacy, Bucharest, Romania
Oct. 2002 - Apr. 2006	Continuation of PhD in the NMR-based Structural Biology Department of Max Planck Institute for Biophysical Chemistry, Göttingen, Germany

### Previous experience

1999-2002	Teaching and research assistant in the Biophysics Department of 'Carol Davila' University of Medicine and Pharmacy, Bucharest, Romania
-----------	--

## Lebenslauf

### Persönliche Daten

Name	Ovidiu-Cristian Andronesi
Geburtstag und -ort	19.6.1974, Bukarest, Rumänien
Staatsangehörigkeit	rumänisch

### Studium

1980-1988	'Sfantul Andrei' Grundschule und Gymnasium, Bukarest, Rumänien
1988-1992	'Sfantul Sava' Kollegium, Bukarest, Rumänien
1992-1997	Physikstudium an der Universität Bukarest, Rumänien
1997-1999	Master in Physik an der Universität Bukarest, Rumänien
1995-1998	Vorklinisches Medizinstudium an der 'Carol Davila' Universität für Medizin und Pharmazie in Bukarest, Rumänien
1998-1999	Nuffic und Socrates Stipendium an der Universität Leiden, Niederlande
1999-2001	Klinisches Medizinstudium an der 'Carol Davila' Universität für Medizin und Pharmazie in Bukarest, Rumänien
Jul.-Dez. 2001	Beginn des Doktorstudiums in der Abteilung für NMR-basierte Strukturbiologie, Max Planck Institut für Biophysikalische Chemie, Göttingen, Deutschland
Jan.-Sept. 2002	Abschluß des Medizinstudiums und Staatsexamen an der 'Carol Davila' Universität für Medizin und Pharmazie in Bukarest, Rumänien
Okt. 2002 - Apr. 2006	Fortsetzung des Doktorstudiums in der Abteilung für NMR-basierte Strukturbiologie, Max Planck Institut für Biophysikalische Chemie, Göttingen, Deutschland

### Vorherige Tätigkeiten

1999-2002	Wissenschaftlicher Assistent der Abteilung Biophysik an der 'Carol Davila' Universität für Medizin und Pharmazie in Bukarest, Rumänien
-----------	--